Mª Del Carmen Ortega Liébana

Light-Emitting Carbon Nanodots. Synthesis and Development of Novel Applications

Departamento

Ingeniería Química y Tecnologías del Medio Ambiente

Director/es

Santamaria Ramiro, Jesus
Hueso Martos, Jose Luis

EXTRACTO

El presente documento es un extracto de la tesis original depositada en el Archivo Universitario.

En cumplimiento del artículo 14.6 del Real Decreto 99/2011, de 28 de enero, por el que se regulan las enseñanzas oficiales de doctorado, los autores que puedan verse afectados por alguna de las excepciones contempladas en la normativa citada deberán solicitar explícitamente la no publicación del contenido íntegro de su tesis doctoral en el repositorio de la Universidad de Zaragoza. Las situaciones excepcionales contempladas son:

• Que la tesis se haya desarrollado en los términos de un convenio de confidencialidad con una o más empresas o instituciones.
• Que la tesis recoja resultados susceptibles de ser patentados.
• Alguna otra circunstancia legal que impida su difusión completa en abierto.

Tesis Doctoral   [Extracto]

LIGHT-EMITTING CARBON NANODOTS. SYNTHESIS AND DEVELOPMENT OF NOVEL APPLICATIONS

Autor

Mª Del Carmen Ortega Liébana

Director/es

Santamaria Ramiro, Jesus
Hueso Martos, Jose Luis

UNIVERSIDAD DE ZARAGOZA

Ingeniería Química y Tecnologías del Medio Ambiente

2018

"Light-Emitting Carbon Nanodots. Synthesis and Development of Novel Applications"
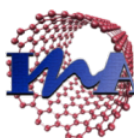
This thesis dissertation is submitted to the Department of Chemical Engineering and Environmental Technologies at the University of Zaragoza, Spain in partial fulfillment of the requirements for the degree of Doctor

María del Carmen Ortega Liébana

Zaragoza, 2018

**Departamento de Ingeniería
Química y Tecnologías
del Medio Ambiente
Universidad** Zaragoza

El **Profesor Jesús Santamaría Ramiro**, Catedrático de Universidad, y el **Doctor José Luis Hueso Martos**, ambos pertenecientes al Departamento Ingeniería Química y Tecnologías del Medio Ambiente y al Instituto de Nanociencia de Aragón de la Universidad de Zaragoza,

CERTIFICAN

Que la presente memoria titulada:

"**Light-Emitting Carbon Nanodots. Synthesis and Development of Novel Applications**"

se ha desarrollado y elaborado bajo su supervisión por **Dña. María del Carmen Ortega Liébana**, en el Departamento de Ingeniería Química y Tecnologías del Medio Ambiente de la Universidad de Zaragoza y en el Instituto de Nanociencia de Aragón. En consecuencia, autorizamos su presentación en la modalidad de compendio de publicaciones.

Y para que así conste, firmamos este certificado en Zaragoza a 23 de mayo del 2018.

Prof. Jesús Santamaría Ramiro   Dr. José Luis Hueso Martos

The PhD thesis **"Light-emitting carbon nanodots. Synthesis and development of novel applications"** *is presented by compendium of the following publications:*

1. **M.C. Ortega-Liebana**, M.M. Encabo-Berzosa, M.J. Ruedas-Rama, J.L. Hueso. "Nitrogen-induced transformation of vitamin C into multifunctional up-converting carbon nanodots in the Visible-NIR range". Chemistry A European Journal, 2017, 23: 3067-3073. Hot Paper. IF: 5.317 (29/166 Chemistry Multidisciplinary). Selected as Front Cover. Highlighted as Hot Paper by the Journal and in the ChemistryViews portal. *Article 1*

2. **M.C. Ortega-Liebana**, J.L. Hueso, S. Ferdousi, K.L. Yeung, J. Santamaria. "Nitrogen-doped luminescent carbon nanodots for optimal photo-generation of hydroxyl radicals and visible-light expanded photo-catalysis". Diamond and Related Materials, 2016, 65: 176-182. IF: 2.561 (91/275 Materials Science, Multidisciplinary). *Article 2*

3. **M.C. Ortega-Liebana**, M.M. Encabo-Berzosa, A. Casanova; M. D. Pereboom, J.O. Alda, J.L. Hueso, J. Santamaria. "Upconverting carbon nanodots as near-infrared activated phototheranostic agents: Dual funtion in bioimaging and photodynamic therapy"- in preparation. *Article 3*

4. **M.C. Ortega-Liebana**, J.L. Hueso, A. Larrea, V. Sebastian, J. Santamaria. "Feroxyhyte nanoflakes coupled to up-converting carbon nanodots: a highly active, magnetically recoverable, Fenton-like photocatalyst in the visible-NIR range". Chemical Communications, 2015, 51: 16625-16628. IF: 6.567 (21/163 Chemistry, Multidisciplinary). *Article 4*

5. **M.C. Ortega-Liebana**, J.L. Hueso, S. Ferdousi, R. Arenal, S. Irusta, K.L. Yeung, J. Santamaria. "Extraordinary sensitizing effect of co-doped carbon nanodots derived from mate herb: Application to enhanced photocatalytic degradation of chlorinated wastewater compounds under visible light". Applied Catalysis B: Environmental, 2017, 218: 68-79. IF: 9.446 (1/49 Engineering Environmental). *Article 5*

6. **M.C. Ortega-Liebana**, N.X. Chung, R. Limpens, L. Gomez, J.L. Hueso, J. Santamaria, T. Gregorkiewicz. "Uniform luminescent carbon nanodots prepared by rapid pyrolysis of organic precursors confined within nanoporous templating structures". Carbon, 2017, 117: 437-446. IF: 6.337 (32/275 Materials Science, Multidisciplinary). *Article 6*

7. **M.C. Ortega-Liebana**, J.L. Hueso, R. Fernandez-Pacheco, S. Irusta, J. Santamaria. "Luminescent mesoporous nanorods as photocatalytic enzyme-like peroxidase surrogates"- under review in Chemical Science. *Article 7*

La Tesis Doctoral *"Light-emitting carbon nanodots. Synthesis and development of novel applications"* *se presenta bajo la modalidad de compendio de las siguientes publicaciones:*

1. **M.C. Ortega-Liebana**, M.M. Encabo-Berzosa, M.J. Ruedas-Rama, J.L. Hueso. "Nitrogen-induced transformation of vitamin C into multifunctional up-converting carbon nanodots in the Visible-NIR range". Chemistry A European Journal, 2017, 23: 3067-3073. Hot Paper. IF: 5.317 (29/166 Chemistry Multidisciplinary). Selected as Front Cover. Highlighted as Hot Paper by the Journal and in the ChemistryViews portal. *Article 1*

2. **M.C. Ortega-Liebana**, J.L. Hueso, S. Ferdousi, K.L. Yeung, J. Santamaria. "Nitrogen-doped luminescent carbon nanodots for optimal photo-generation of hydroxyl radicals and visible-light expanded photo-catalysis". Diamond and Related Materials, 2016, 65: 176-182. IF: 2.561 (91/275 Materials Science, Multidisciplinary). *Article 2*

3. **M.C. Ortega-Liebana**, M.M. Encabo-Berzosa, A. Casanova; M. D. Pereboom, J.O. Alda, J.L. Hueso, J. Santamaria. "Upconverting carbon nanodots as near-infrared activated phototheranostic agents: Dual funtion in bioimaging and photodynamic therapy"- in preparation. *Article 3*

4. **M.C. Ortega-Liebana**, J.L. Hueso, A. Larrea, V. Sebastian, J. Santamaria. "Feroxyhyte nanoflakes coupled to up-converting carbon nanodots: a highly active, magnetically recoverable, Fenton-like photocatalyst in the visible-NIR range". Chemical Communications, 2015, 51: 16625-16628. IF: 6.567 (21/163 Chemistry, Multidisciplinary). *Article 4*

5. **M.C. Ortega-Liebana**, J.L. Hueso, S. Ferdousi, R. Arenal, S. Irusta, K.L. Yeung, J. Santamaria. "Extraordinary sensitizing effect of co-doped carbon nanodots derived from mate herb: Application to enhanced photocatalytic degradation of chlorinated wastewater compounds under visible light". Applied Catalysis B: Environmental, 2017, 218: 68-79. IF: 9.446 (1/49 Engineering Environmental). *Article 5*

6. **M.C. Ortega-Liebana**, N.X. Chung, R. Limpens, L. Gomez, J.L. Hueso, J. Santamaria, T. Gregorkiewicz. "Uniform luminescent carbon nanodots prepared by rapid pyrolysis of organic precursors confined within nanoporous templating structures". Carbon, 2017, 117: 437-446. IF: 6.337 (32/275 Materials Science, Multidisciplinary). *Article 6*

7. **M.C. Ortega-Liebana**, J.L. Hueso, R. Fernandez-Pacheco, S. Irusta, J. Santamaria. "Luminescent mesoporous nanorods as photocatalytic enzyme-like peroxidase surrogates"- under review in Chemical Science. *Article 7*

A mi Familia

"Science is not only a disciple of reason but, also, one of romance and passion" – Stephen Hanwking.

Acknowledgements. Agradecimientos

Me gustaría empezar este trabajo agradeciendo a todas la personas que me han ayudado tanto profesionalmente como personalmente durante estos años de mi formación pre-doctoral.

En primer lugar quiero agradecer a Prof. Jesús Satamaría y Dr. José Luis Hueso, mis directores, por toda su paciencia, tiempo, dedicación y brindar en mi la oportunidad de comenzar mi carrera investigadora. Gracias Jesús, por hacer que el grupo NFP sea mi segunda familia y por enseñarme a superarme y mejorar siempre con la mayor excelencia. Gracias José Luis por guíar mi investigación día a día y por forjar en mi la diversidad científica que te caracteriza. Sois los mejores referentes que puedo tener.

No quisiera olvidarme de todas las colaboraciones que han surgido en este trabajo. Al Dr. Raúl Arenal, por dedicarme mas tiempo del que tiene. Gracias Raúl por confiar en mi trabajo, me has ensañado tanto profesionamente como personalmente, tengo suerte de contar con el mejor del LMA. Al Dr. Rodrigo Fernández-Pacheco, por su paciencia en las medidas y los análisis de EELS de mis millones de muestras y por estar dispuesto siempre hacer cosas nuevas. Me habéis enseñado a ver el mundo "nano" desde otra perspectiva. También me gustaría agradecer al Dr. Victor Sebastian por estar dispuesto siempre a ayudarme y hacer cosas con nosotros. A la Dr. Silvia Irusta por su trabajo en las medidas de XPS y por enseñarme a tartar los resultados obtenidos. Al Prof. Octavio Alda y al Dr. Alvaro Casanova por su dedicación en la aplicación de mis nanoparticulas en terápia fotodinámica y por todas las sugerencias e ideas que nos han aportado para futuros experimentos.

De las mejores experiencias de las que puedes disfrutar en los años de tesis son las estancias. Y en los meses que he pasado fuera he tenido la suerte de estar en dos grupo excepcionales. Gracias al Prof. King Lun Yeung y Dr. Shammi Ferdousi por haberme aceptado en su grupo en HKUST y ampliar mi formación en el área de la fotocatálisis, fue una gran aventura lo vivido en esos meses. *I would like to thanks Prof. King Lun Yeung and Dr. Sahmmi Ferdousi for giving me the oportunity of accept me in their laboratory at HKUST and expanding my training in the field of photocatalysis, It*

was a great adventure and experience what I lived during those months. De igual forma, gracias al Prof. Boukany y a la Dr. Lea Rems por vuestra paciencia y ayuda en la puesta a punto en el uso de la técnica de electroporación para garantizar la entreda de nanopartículas en las células durante mi estancia en TUDelft. *I would like to thanks Prof. Boukany and Dr. Lea Rems for your patience and help in the development of the use of electroporation technique to ensure the delivery of the nanoparticles into the cells during my time in TUDelft.*

¿Y qué sería un doctorado sin sus compañeros de aventuras y sin esas reuniones de grupo? Gracias a todos los doctores del grupo NFP, Gema Martinez, Reyes Mallada, Pili Pina, Silvia Irusta, Nuria Navascues (por tu entraga día tras día, eres nuestra salvadora), Carlos Bueno (tu ayuda ha sido fundamental en el montaje fotocatalítico con irradiación LED), Manuel Arruebo, Gracia Mendoza (prometo no llevarte más un sábado a la Zona), Miguel Urbiztondo, Victor, Alberto, Laura Usón, Nacho, Adriana, Vanesa, Teresa, Paco Balas, Pilar Lobera, por vuestra disponibilidad y por recibirme siempre con la mejor de vuestras sonrísas. A mis chic@s del lab 8, Iván, Ane y Martin. A este último, por ser un apoyo fundamental durante estos años, me llevo un gran persona como amigo, y perdona por tantos males que te doy!!. A mi Hakan, que aún siendo doctor, ha sido uno de mis pilares durante esta ultima etapa, gracias por estar ahí y espero que pronto volvamos vernos en algún lugar del mundo. A ti Fer, por aguantarme todos los días, por tus terapias de cómo ligar con tus amigos y por ser uno de los responsables por los que he salido del Actur :). A Leyre, gracias por contar con nosotros para establecer colaboración con tu grupo de Holanda y por tu disponibilidad para reencontrarnos. A Marta la Fuente, por estar ahí cuando lo he necesitado y por su tiempo en las medidad con el Raman. Y como no a mis chicas, MMar eres mi gran amiga, tengo la suerte de tener a la mejor scienctific blogger, gracias por apoyarme y por todo este tiempo… y por lo que vendrá. A mi Núri, eres la persona que no puede faltar en mi vida, no tengo palabras para describir todo lo vivido, te debo muchas cosas, vente pronto a Zaragoza que nos espera una o dos copa de vino para ahogar nuestras penas, si se pueden llamar penas!!. A mi Ana Malumbres, que me has enseñado a ser única y valorar la naturalidad de las cosas, gracias por estar siempre ahí, que sería de nosotras sin ese grupo de whatsapp que nos mantiene en contacto todos los días. A mi Marieta, María Sancho, eres la ilusión en persona, gracias por esos momentos de risas y trabajo. Los mejores ratos, indiscutiblemente, has sido

gracias a todos los mencionados es estas líneas, a los que han pasado por el grupo y a los que aun están, Sara, Kike, Isabel, Roberta, Cris, Bea y Diego, gracias porque habéis hecho que mi realidad durante estos años sea inmejorable.

Grácias, al Dr. Scott Mitchell y al Dr. Alfonso Ibarra, a todos los que formáis parte del INA y del Departamento de Ingeniería Química (a Pilar Sanchez por ayudarme siempre con toda la documentación y a mis profesoras de docencia) …porque ha sido un placer compartir con vosotros todo este tiempo.

También me gustaría agradecer a todo la gente de la Universidad de Jaén y la Universidad de Córdoba que apostó por los inícios de mi carrera investigadora y con los que compartí grande momentos, sobre todo a la Prof. Sofía Salido que me animó para venirme a la Universidad de Zaragoza e instauró en mi la semilla de la investigación.

Gracias a mis compañeras de piso y a mis amigas de Jaén, sobre todo a Mamen por estar siempre ahí. Por vuestro ánimo, vuestra comprensión y por todas las charlas que compartimos en las que todo tiene solución.

Que sería de mi sin mi familia. Gracias, papá y mamá por vuestros valores y disciplina, por todo lo que me habéis enseñado y por aporyarme día tras día incluso en la distancia. Todo ello a contribuido a que sea como soy y que todo lo que tenga sea gracias a vosotros. A ti mamá, eres la persona que más admiro. Gracias a mi Hermano y a Carmen, que son mi mayor apoyo, por estar constantemente pendiente de mi y ayudarme en cada momento, y sobre todo por darme a dos sobrinos guapísimos, Alberto y Jorge, que son la alegría de la casa. Mención especial a mi abuela María, y gracias a mis tíos, primos y amigos de mis padres, por apoyarme siempre.

Summary. Resumen

Fluorescent **Carbon Nanodots**, "CNDs", are a new type of carbon nanomaterials that have emerged recently, and have attracted intense interest as a potential alternative to classical semiconductor Quantum Dots. CNDs possess high biocompatibility, easy and low-cost synthesis, good colloidal stability and appealing optical properties. CNDs also hold a huge potential as novel and versatile luminescent nanomaterials for a wide range of applications such as bioimaging, drug delivery, chemical sensing, photocatalysis, and as sensitizers for photovoltaic solar cells.

This Thesis deals first with the development of different strategies to produce non-toxic, inexpensive carbon nanoparticles with good and tunable emission properties spanning an activation window from the ultraviolet (UV) to the near infrared (NIR). On the other hand, the prepared CNDs have been applied in different fields: theranostics, sensing and catalysis. The aims of this PhD Thesis have been: (i) to synthesize fluorescent CNDs from abundant and inexpensive precursors by improving state-of-the-art methods and by the development of novel synthesis strategies; (ii) to understand and optimize the structural and optical properties of the as-synthesized CNDs; and (iii) to use the CNDs as fluorescent **Biomarkers** and **Photodynamic Therapy** agents, as luminescent **Nanosensors** and as photosensitisers in **Catalytic** applications.

After an introductory section, the thesis is structured in three blocks:

I. Synthesis of CNDs, evaluation of different synthesis methods: hydrothermal treatment, pyrolysis of organic compounds and flash-thermal pyrolysis of carbon precursors contained in the channels of inorganic mesoporous templates.

II. Characterization of CNDs: evaluation of their structural and optical properties with special attention to the role of functional groups generated in the CNDs and the chemical composition of the different precursors to induce an enhanced response in the visible-NIR range.

III. Applications of CNDs: evaluation of their role as biomarkers, theranostic agents, and ion sensors, especially in the NIR range. Evaluation as sensitizers/light harvesters able to expand the response of other photocatalysts or to mimic the enzymatic activity of peroxidase.

Finally, a conclusion section contains the main conclusions reached in this work.

…………………………………

Los **Carbon Nanodots**, "CNDs", son un nuevo tipo de nanomateriales de carbono fluorescentes que han despertado un gran interés como alternativa potencial a los clásicos semiconductores fluorescentes, los denominados Quantum Dots. Los CND se pueden obtener mediante rutas sintéticas fáciles y de bajo coste, manifiestando alta biocompatibilidad, buena estabilidad coloidal y atractivas propiedades ópticas. Además, los CND presentan un enorme potencial como novedosos y versátiles nanomateriales luminiscentes en una amplia gama de aplicaciones, como en la creación de imágenes biológicas, en la administración de fármacos, en la detección química, en fotocatálisis heterogénea y como sensibilizadores en células solares fotovoltaicas.

En primer lugar, esta Tesis Doctoral trata del desarrollo de diferentes estrategias para producir nanopartículas de carbono no tóxicas y económicas con optimizadas propiedades de emisión que abarcan un amplio rango de foto-activación, desde el ultravioleta (UV) hasta el infrarrojo cercano (NIR). Por otro lado, los CND preparados se han aplicado en diferentes campos: como teranósticos, como sensores y en catálisis. En consiguiente, los objetivos de esta tesis doctoral han sido: (i) sintetizar, mediante la mejora de los métodos de vanguardia y mediante el desarrollo de nuevas estrategias sintéticas, CND fluorescentes a partir de precursores de fácil disponibilidad en la naturaleza y de bajo coste; (ii) comprender y optimizar las propiedades estructurales y ópticas de los CND sintetizados; y (iii) usar los CND como **Biomarcadores** fluorescentes y agentes de **Terapia Fotodinámica**, como **Nanosensores** luminiscentes y como fotosensibilizadores en aplicaciones **Catalíticas**.

Después de una sección introductoria, la tesis se ha estructurado en tres bloques:

I. Síntesis de CNDs, evaluando diferentes métodos sintéticos: tratamiento hidrotermal, pirólisis de compuestos orgánicos y ultrarapida pirólisis térmica de precursores de carbono contenidos en los canales de templantes mesoporosos inorgánicos.

II. Caracterización de los CND: evaluación de las propiedades estructurales y ópticas de los CNDs obtenidos, con especial atención al papel que juegan los grupos

funcionales y la composición química de los diferentes precursores utilizados en la síntesis para inducir una respuesta mejorada en el rango visible-NIR.

III. Aplicaciones de los CND: evaluación de estos como biomarcadores, agentes teranóstico y como sensores de iones, especialmente en el rango NIR. Además, se llevó acabo también su evaluación como sensibilizadores/recolectores de luz capaces de expandir la respuesta de otros fotocatalizadores o imitar la actividad enzimática de la enzima peroxidasa natural.

Finalmente, una sección de conclusión engloba las principales conclusiones alcanzadas en este trabajo.

CONTENTS

Contents

X

List of Abbreviations

Key abbreviations and symbols used in this PhD thesis are defined here. Some less important ones are defined in the main body of the text.

AA   L- ascorbic Acid

AuNRs   Gold Nanorods

CA   Citric Acid

CB   Conduction Band

CNDs   Carbon Nanodots

CNTs   Carbon Nanotubes

DCP   Dichlorophenol

DHR   Dihydrorhodamine R123

EDTA   Ethylenediaminetetraacetic acid

E$_g$ Energy Band Gap

EN   Ethanolamine

Fe-NFs   Feroxyhyte nanoflakes

FTIR   Furier Transform Infrared Spectroscopy

GC-MS   Gas Chromatography to Mass Spectrometry

GO   Graphene oxide

GOx   Glucose Oxidase

GQDs   Graphene Quantum Dots

HE   Hydroethidine

HOMO   Highest Occupied Molescular Orbital

HTC   Hydrothermal Carbonization

IFE   Inner filter effect

IR   Infrarred

LMS   Luminescent Mesoporous Silica

LOD   Limit of detection

LUMO   Lowes Unoccupied Molecular Orbital

M   Molar

Methanol   MeOH

MO   Methyl Orange

MB   Methylene Blue

Contents

MW   Microwave

MWNTs   Multi-Walled Carbon Nanotubes

NaTA   Disodium Terephthalate

NCs   Nanoclusters

N-doped   Nitrogen doped

NDs   Nanodiamonds

NIR   Near infrared

NPs   Nanoparticles

PEG   Polyethyleneglycol

Pdots   Polymer Dots

PDT   Photodynamic Therapy

PL   Photoluminescence

PQDs   Perouskite Quantum Dots

QDs   Semiconductor Quantums Dots

QY   Quantum Yield

RE-UCNPs   Rare-earth Upconversion Nanoparticles

rGO   Reduced Graphene Oxide

RH   Rhodamine 123

SDA   Structure-directing Agent

Si   Silicon

SiCNPs   Silicon Carbide Nanoparticles

SiQDs   Silicon Quantum Dots

SPR   Surface Plasmon Resonance

SWNTs   Single-Walled Carbon Nanotubes

TEM   Transmission Electron Microscopy

TMB   3,3',5,5'-tetramethylbenzidine

TiO$_2$ Titanium Dioxide

UPLC   Ultra Performance Liquid Chromatography

UV   Ultraviolet

UV-vis   Ultraviolet-Visible

VB   Valence Band

XPS   X-ray Photoelectron Spectroscopy

II. OBJETIVES AND STRUCTURE

The focus of the research presented in this thesis has been the development of different synthetic routes to fabricate luminescent carbon nanoparticles with tunable emission properties. The emission ranges of these CNDs spanning a window from the ultraviolet (UV) to the near infrared (NIR) have been modified by tailoring variables related to the chemical composition of the CNDs and their physical structure. In addition, this Thesis has pursened the development of applications where the outstanding properties of the different CNDs, especially those associated to their optical response in the NIR range can be leveraged. The fields of application have included theranostics, bioimaging and photocatalys.

Accordingly, the main *objetives* of arising in this thesis have been the following:

1. Exploration and development of novel, reproducible and reliable synthesis strategies of CNDs that enable the modification and tuning of their bulk and surface compositions as well as their photoluminescence properties, while using as raw materials readily available, environmentally benign or recyclable precursors.

2. Exploitation of the optical response of the CNDs in the visible-NIR range as potential bioimaging labels with reduced cytotoxicity and good internalization capability.

3. Study of the remotely-triggered response of CNDs in the cell media cultures to evaluate their potential role as simultaneaously active bioimaging and therapeutic agents through the in situ generation of reactive oxygen species (ROS).

4. Exploitation of the capability of CNDs to act as luminescent sensors to respond selectively to the presence of certain ions *via* quenching mechanisms.

5. Expand and enhance the photocatalytic response of well-established photocatalytic supports by taking advantage of the role of CNDs as potential photosensitizers with absorption capabilities in the visible-NIR range.

6. Evaluation of the biocatalytic activity of supported CNDs within a mesoporous nanoplatfrom to mimic the functions of natural peroxidase enzymes upon photoactivation, as well as gaining knowledge of peroxidase-like mechanisms linked to the generation of reactive oxygen species (ROS).

Keeping these goals in mind, the main achievements of this thesis have been structured using the compendium of peer-reviewed articles published (or currently under evaluation). The information of these articles has been organized in two major blocks as shown below in *Thesis Structure Diagram*. The first block addresses different synthesis strategies to synthesize light-emitting carbon nanodots, namely, hydrothermal synthesis (published in ***Articles 1-3***), pyrolytic carbonization of plants (published in ***Articles 4-5***), or the flash-thermal pyrolysis of organic precursors encased within mesoporous templates (gathered in ***Articles 6-7***).

The second block of this Thesis refers to the main fields of applications explored for each of the synthesized CNDs. The CNDs obtained by hydrothermal synthesis have been tested in different applications that are summarized in the *Scheme 1*. The CNDs synthesized by pyrolytic carbonization of plants were coupled to different photocatalytic supports for application in environmental photocatalysis in the UV-vis-NIR range (see *Scheme 2*). Finally, the CNDs synthesized by flash-thermal pyrolysis of inorganic mesoporous templates have been applied as photo-activated peroxidase-mimicking surrogates for biocatalytic processes (see *Scheme 3*).
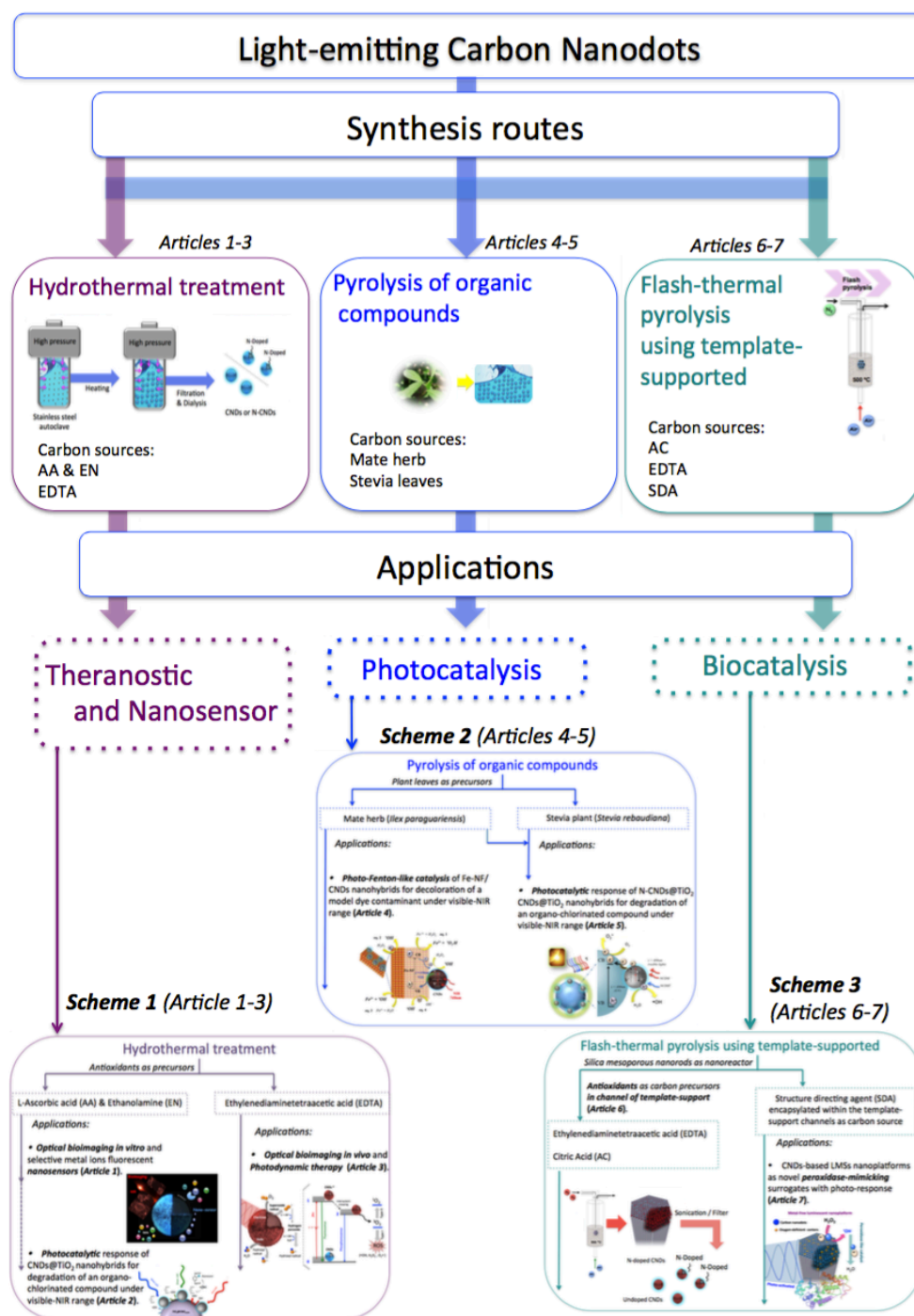
Thesis Structure Diagram. Schematic summary of the subjects tackled in this thesis: **Synthesis** of **light-emitting Carbon Nanodots** and their corresponding **Applications**.

A more detailed description provided in *Scheme 1* highlights the main applications presented in **Articles 1-3** corresponding to the CNDs synthesized by hydrothermal methods. **Articles 1** and **2** evaluated the influence of including a second co-reactant, where the latter included a heteroatom. In contrast, **Article 3** attempts to reach the same result using a single molecular precursor with heteroatoms. In **Article**

1, the obtained CNDs were first applied to image tumor cells in the visible range and, more importantly, in the NIR region in which minimal tissue or water absorption and maximum penetration depth are expected. In addition, the Nitrogen-containing CNDs (N-CNDs) showed high selectivity and sensitivity towards the detection of copper ions in solution, especially in the study of quenching mechanism under excitation in the NIR range. Likewise, **Article 2**, also evaluates the optical response of these N-doped CNDs to selectively generate highly reactive oxidative hydroxyls ($^{\bullet}$OH) upon irradiation with different light-emitting diodes (LEDs) in the visible-NIR range. The role of the N-doped CNDs as sensitizers to maximize solar light harvesting and expand the photo-catalytic response of a commonly used UV-active semiconductor such as TiO_2 was successfully tested in the visible-light mediated degradation of an organo-chlorinated compound. Finally, **Article 3**, we have successfully reported a dual role of CNDs synthesized in a single step from a single precursor for simultaneous bioimaging and photodynamic therapy (PDT) of tumor cells under NIR irradiation at 808 nm. The antitumor activity arises due to the light-stimulated production of reactive oxidative species-ROS, namely $^{1}O_2$ and H_2O_2.
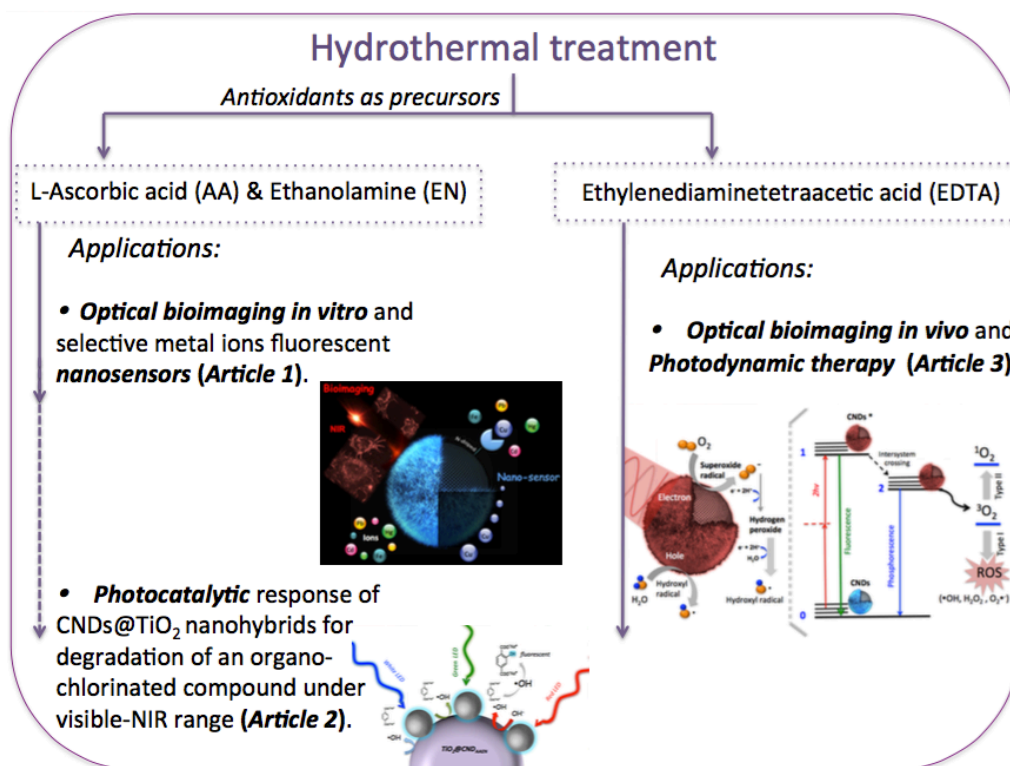
Scheme 1. Schematic summary of *articles 1-3* reported in this thesis. **Hydrothermal synthesis** of **light-emitting Carbon Nanodots** and their of application as **Theranostics Agents (Bioimaging + Photodynamic Therapy)** and **Nanosensors.**

Articles 4-5 of this doctoral thesis are highlighted in *Scheme 2* and refer to the main applications of the CNDs synthesized by pyrolytic carbonization of plant leaves. In both works and continuing the work developed in the *Article 3*, the obtained CNDs were employed as nanostructured photosensitizers and deployed onto the surface of conventional photocatalytic supports to expand their response towards the visible-NIR range for solar-driven pollution abatement. In **Article 4**, we demonstrated the enhanced photocatalytic response of a novel Fenton-like heterogeneous catalyst (magnetically recoverable) obtained through the assembly of superparamagnetic feroxyhyte nanoflakes to CNDs pyrolized from mate herbs. Furthermore, in **Article 5**, we evaluated the tunable PL response of two types of CNDs, derived from stevia and mate, with different levels of N and P doping after assembling with TiO_2 to form heterogeneous photocatalysts that were highly active in the visible-light and NIR-driven photodegradation of a persistent chlorinated organic compound.
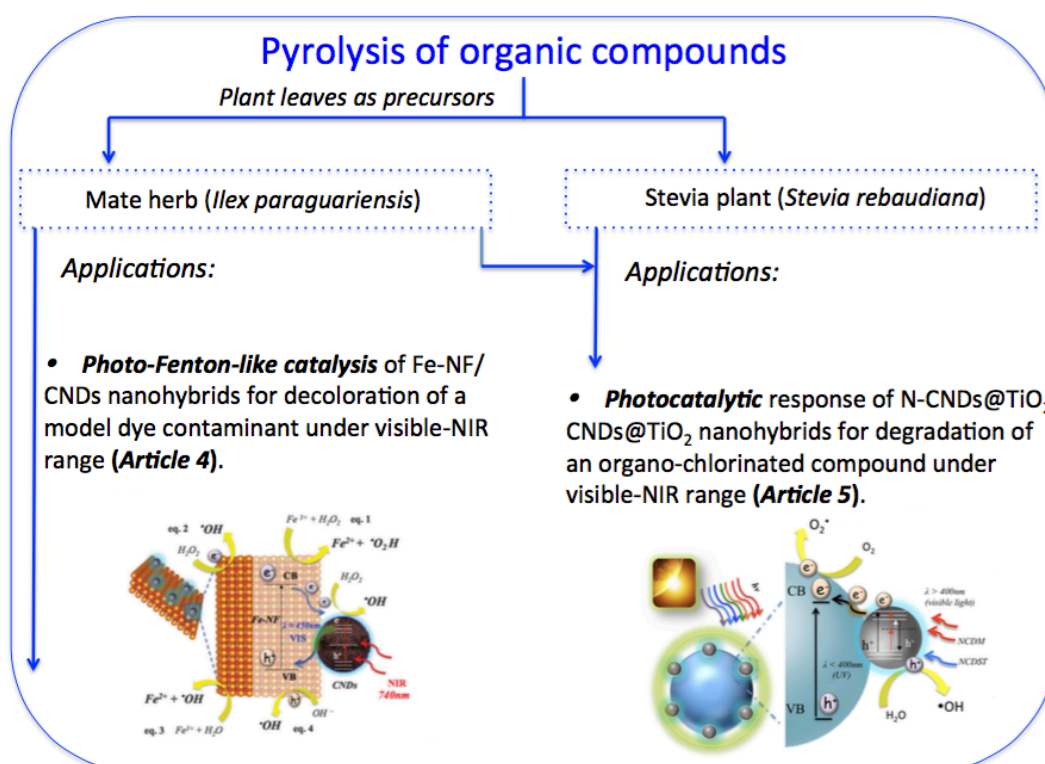
Scheme 2. Schematic summary of *articles 4-5* reported in this thesis. **Pyrolysis of organic compounds synthesis** of **light-emitting Carbon Nanodots** and their application in **environmental Catalysis.**

Finally, as shown in *Scheme 3*, referring to ***Articles 6-7*** of this thesis, we highlight the synthesis of luminescent CNDs retrieved from ordered mesoporous silica nanorods, which are used as confining templates. A rapid thermal decomposition

(pyrolysis) within the confined dimensions of their pores leads to a highly uniform size distribution of CNDs. These CNDs were synthesized in an extremely short time period (between 2-5 min of reaction) by immersion in a fluidized-bed reactor that provided heating homogeneity and ensured fast heat transfer. In this regard, in **Article 6**, we use this approach with two natural sources, to obtain undoped and nitrogen-doped luminescent CNDs, depending on the carbon source used. In **Article 7**, the structure-directing agent (SDA) within the channels of the mesoporous template was used as a carbon source to generate strong blue PL centers attributed to silicon and carbon-based sites within the mesoporous silica nanorod platform. In addition, these luminescent mesoporous nanorods were also successfully tested as robust photocatalysts able to display peroxidase-like activity in a wider range of pH conditions compared to the natural enzyme.
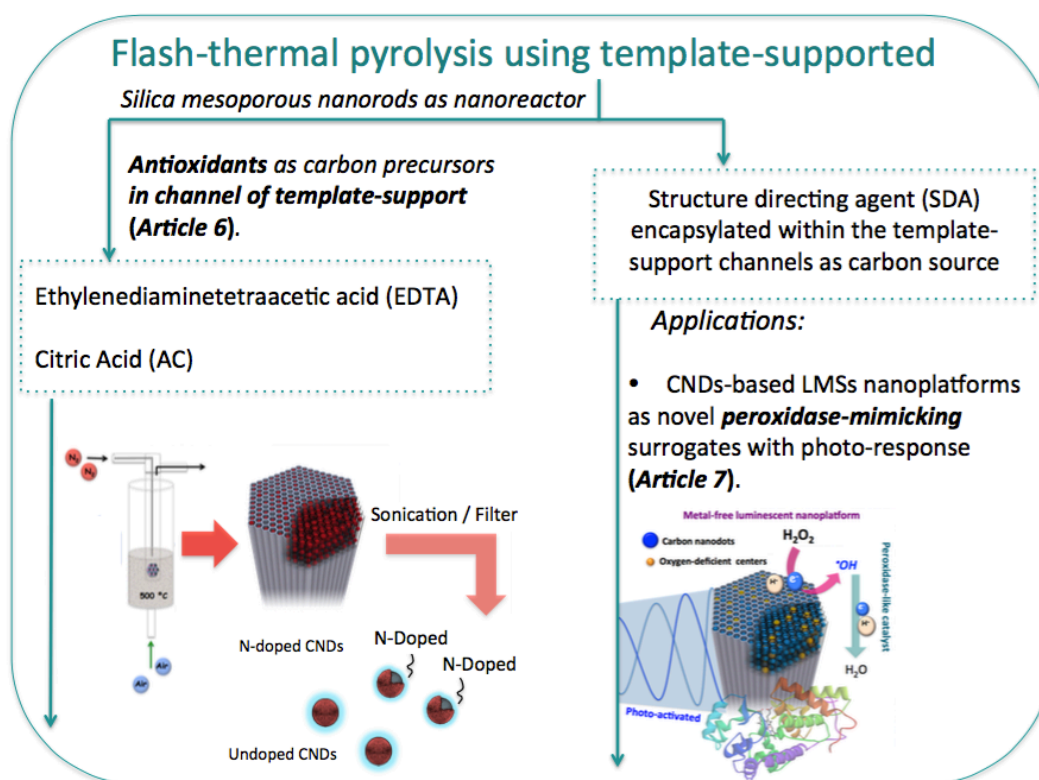
Scheme 3. Schematic summary of *articles 6-7* reported in this thesis. **Flash-thermal pyrolysis** using **supported-synthesis procedure** of **light-emitting Carbon Nanodots** and their application in **Biocatalysis**.

III. METHODOLOGY

III.1 Synthesis of freestanding Carbon Nanodots

In this section we describe the three synthesis strategies developed throughout the course of this thesis, making especial emphasis on the goal of functionalizing/doping the CNDs with heteroatoms such as nitrogen. We also aim to describe the advantages and limitations of each of these methods to obtain CNDs from different organic precursors.

The first synthetic route explored in this thesis has been the ***hydrothermal (or solvothermal) carbonization (HTC)*** method. This is a feasible way to make X-CNDs, and can be considered as an "environmentally friendly transformation tool" to transform raw materials with complex compositions into valuable products. The main advantage of using the HTC method to obtain X-CQDs is reflected in the widely available precursors that are not only restricted to materials existing in nature, but also extended to many organic small molecules containing carbon and doping hetereatoms (i.e. N, S, P). In comparison to the HTC method, it was reported that the microwave (MW) method has a similar reaction mechanism but greatly increases the reaction efficiency, and significantly reduces the reaction time. However, we had tried to synthesize these nanomaterials *via* MW, and did not obtain satisfactory results.

The second synthesis strategy consisted of the ***pyrolytic carbonization*** of natural plants. Compared with other "Botom-up" methods such as MW synthesis, pyrolysis of organic compounds is more cost effective, because it does not need special equipment or any solvent. This method was developed to extend the doping categories and greatly shorten the reaction time compared to the HTC route.

Finally, to further enhance the control of the process to yield CNDs that are homogeneous in size and shape, a novel approach combining the use of ***flash thermal treatment*** and inorganic mesoporous silica nanorods as ***confining templates*** has been successfully developed.

III.1.1 Hydrothermal synthesis

Hydrothermal carbonization (HTC), which is one type of solvothermal carbonization process is regarded as a direct and efficient synthetic approach that works through polymerization and carbonization reactions. It has been widely applied to prepare numerous materials due to the high reactivity of the reactants, easy control of the solution parameters and limited energy consumption. Typically, a solution of organic precursor is sealed and reacted in a hydrothermal reactor at high temperature. Hsu el al. proposed for first time the mechanism for the formation of CNDs by hydrothermal synthesis[118], see *Figure 47*. CNDs formation was suggested to proceed *via* four stages, including dehydration, polymerization, carbonization, and passivation. Initially, the molecules assemble as a result of hydrogen bonding. Then, during heating (dehydration), polymerization occurs, leading to a short single burst of nucleation. The resulting nuclei then intergrew by the diffusion of solutes toward the particle surfaces.

Polymerization   *Carbonization*   *Passivation*
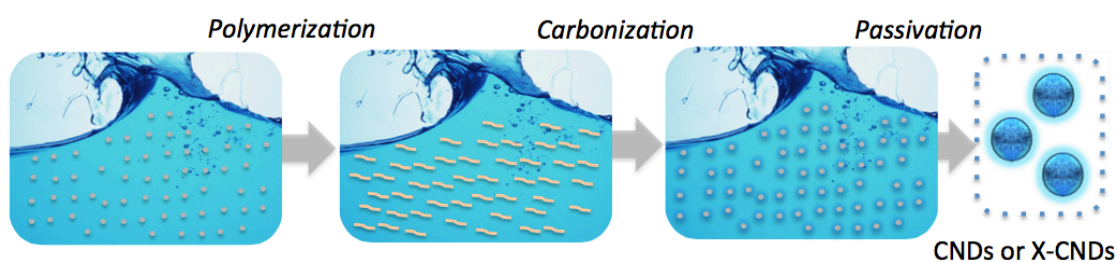
CNDs or X-CNDs

Figure 47. Schematic illustration of growth model for CNDs or X-CNDs by hydrothermal synthesis.

It has been previously reported that the use of precursor molecules containing a large number of carboxylic moieties was strongly beneficial to develop highly luminescent CNDs[352-355]. Likewise, the presence of additional doping heteroatoms could have positive effects on the optical response of the generated CNDs[137, 142, 223, 348, 356-359]. Therefore, we initially performed a series of experiments exploring the effect of of adding ethanolamine (EN) as a co-reactant containing a short chain terminal amine group during the hydrothermal carbonization of vitamin C (L-ascorbic acid (AA)), ***Article 1***.

Once we demostrated that the presence of N atoms induced substantial modifications on the final response of the CNDs, another series of synthesis

experiments using a single precursor containing N atoms were performed. Ethylenediaminetetraacetic acid (EDTA), a low-cost and naturally abundant amino-acid like compound was utilized as single-source precursor for this purpose. Its molecular structure includes a C-N bond connecting a nitrogen atom to the carbon chain from which the CNDs doped is produced, without the need of a co-reactant, **Article 3**. As discussed in section I.6.2, besides conventional (i.e. down-converted) PL, N-doped CNDs synthesized with both approaches were shown to possess excellent up-conversion properties.

III.1.1.1 *One-step hydrothermal synthesis with addition of a co-reactant*

The hydrothermal synthesis of the CNDs is summarized in the *Figure 48-a*. A first synthesis of CNDs was carried out in the absence of the amine co-fed precursor (hereafter labelled as CND_{AA}, see *Figure 48 b-1*) to clearly establish the influence of adding N species during the carbonization of AA in the presence of a co-fed N-containing precursor (hereafter denoted as $N-CNDs_{AAEN}$, *Figure 48 b-2*).

The typical experimental procedure to synthesize the un-doped CNDs is described as follows (see *Figure 48*). First, 1M solution of AA, as the carbon source, and 10 mL triple distilled water were mixed in a beaker with a magnetic stirrer. Subsequently, the suspension was transferred into a 25 mL Teflon-lined stainless-steel autoclave and was heated at a constant temperature of 250 ^{o}C for 4 hours. Finally, the resulting solution was cooled to room temperature and centrifuged at 6000 rpm for 10 min to separate the supernatant liquid containing fluorescent CNDs from the solid black precipitate. The solution containing carbon nanomaterials was filtered through a 0.10 μmm PTFE membrane (WhatmanTH) membrane to further remove large particles. The brownish-yellow supernatant was then dialyzed against ultrapure water through a dialysis membrane for 5 h. An analogous procedure was carried out to synthesize the N-doped CNDs but replacing the initial 1M solution of AA by a solution containing a 3:1 molar ratio (EN:AA). These synthesis conditions correspond to the minimum reaction times and temperatures at which both $CNDs_{AA}$ and $N-CNDs_{AAEN}$ were obtained. Shorter temperatures or times failed to retrieve homogeneous and reproducible luminescent nanocarbons with the desired optical response. Higher EN concentrations did not render a successful generation of carbogenic dots under the conditions employed.
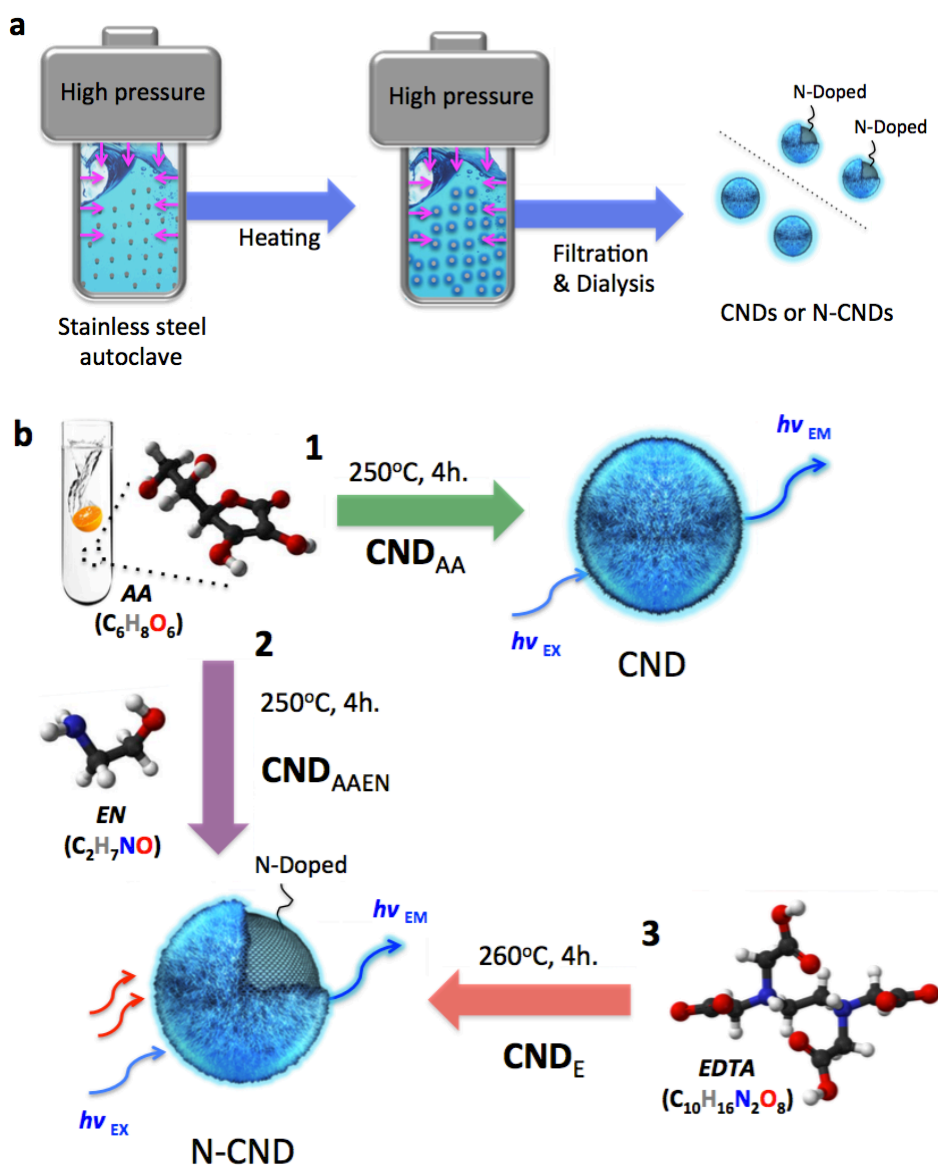
Figure 48. a) Schematic illustration of the hydrothermal synthesis carried out in a teflon-lined stainless autoclave at constant temperatura for CNDs or X-CNDs; and b) Hydrothermal carbonization of: 1) Ascorbic acid at 250°C in the absence or in the presence of ethanolamine to obtain un-doped (CND_{AA}) and 2) N-modified carbon nanodots (CND_{AAEN}); 3) Hydrothermal treatment of Ethylenediaminetetraacetic acid at 260°C to obtain N-modified cabon nanodots (CND_E).

We investigated the formation mechanism of CNDs exploring different temperature ranges. As shown in *Figure 49*, higher reaction temperatures (above 230 °C) favored the generation of a higher fraction of carbogenic dots. In contrast, lower temperatures led to dehydration and polymerization of the starting precursors without reaching the temperature required to induce the formation of the CNDs. Therefore, at lower temperatures, small fluorophore molecules with PL were obtained (see *Figure*

49) but exhibited a fluorophore-like behavior as previously described by other authors[116].
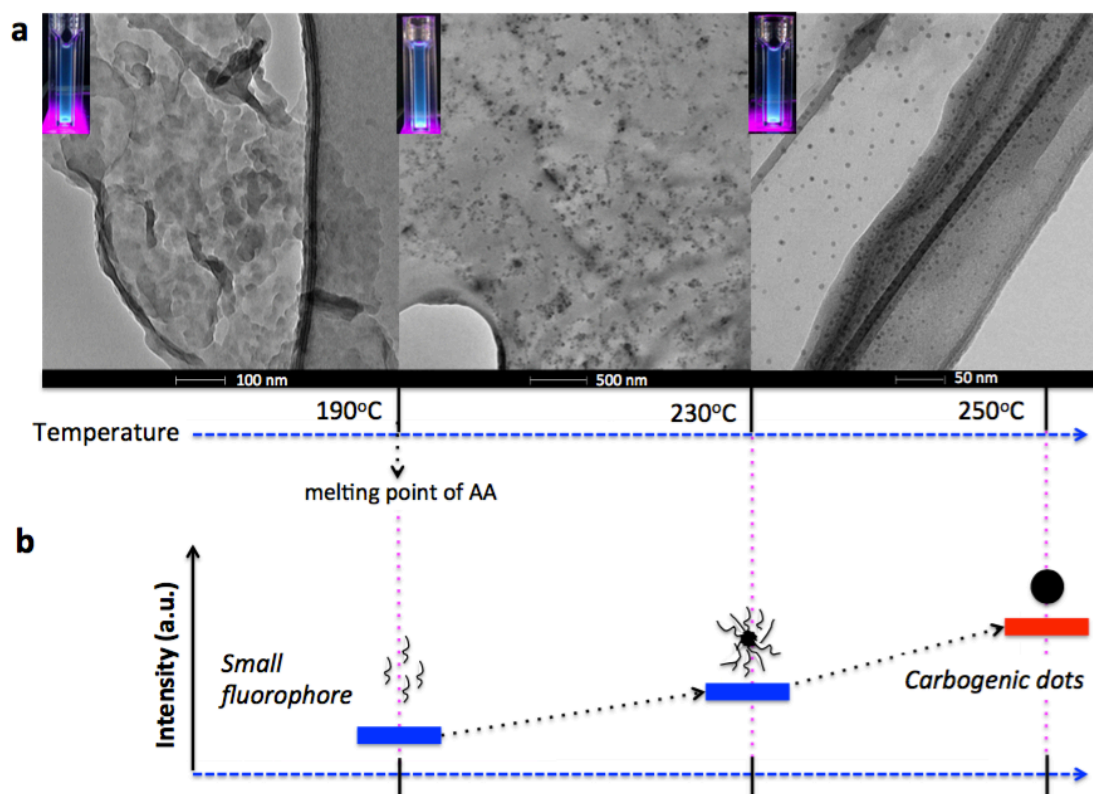
Figure 49. (a) Transmission electron microscopy (TEM) images of the photoactive species produced at different temperatures during from the hydrothermal synthesis of mixture of AA and EN; The insets show images of the suspensions obtained in each experiment under UV light illumination (λ_{exc} = 365 nm); and (b) Schematic representation of the emission characteristics of photoactive species produces from thermal treatment of mixture of AA and EN. During thermal tratment, the organic fluorophores (depicted as black threads) are consumed for the buildup of the carbogenic core (black sphere) so that the PL component that corresponds to the carbogenic core (red bars) increases at the expense of the component that arises from the organic fluorophores (blue bars).

To sum up, regarding HTC methodology with two simultaneous co-reactants, it was concluded that controlling the temperature was a critical step governing the final PL behaviour and nucleation of small CNDs. Furthermore, the presence of the second amine co-reactant further influenced the final PL properties of the CNDs, especially when compared with the undoped counterpart. These results are further developed in *Articles 1-2* of this Thesis.

III.1.1.2 One-step hydrothermal synthesis with a single-source precursor

N-doped carbon nanodots were also synthesized with a single carbon source, which contained the heteroatom of interest (hereafter labelled as CND$_E$, see *Figure 48*

b-3). Briefly, 1M solution of EDTA, and 10 mL triple distilled water were mixed in a beaker with a magnetic stirrer, the solution was then transferred into a 25 mL Teflon-lined stainless-steel autoclave and was heated to a constant temperature of 260 $^{\circ}$C for 4 hours. The resulting solution was purified following the previously described protocol (*vide supra*). These synthesis conditions correspond to the threshold reaction times and temperatures required to rendering a successful production of the CNDs$_E$. The selection of a different set of T or reaction times yielded to less homogeneous and non-reproducible luminescent nanocarbons with the desired optical response (see *Figure 50*).
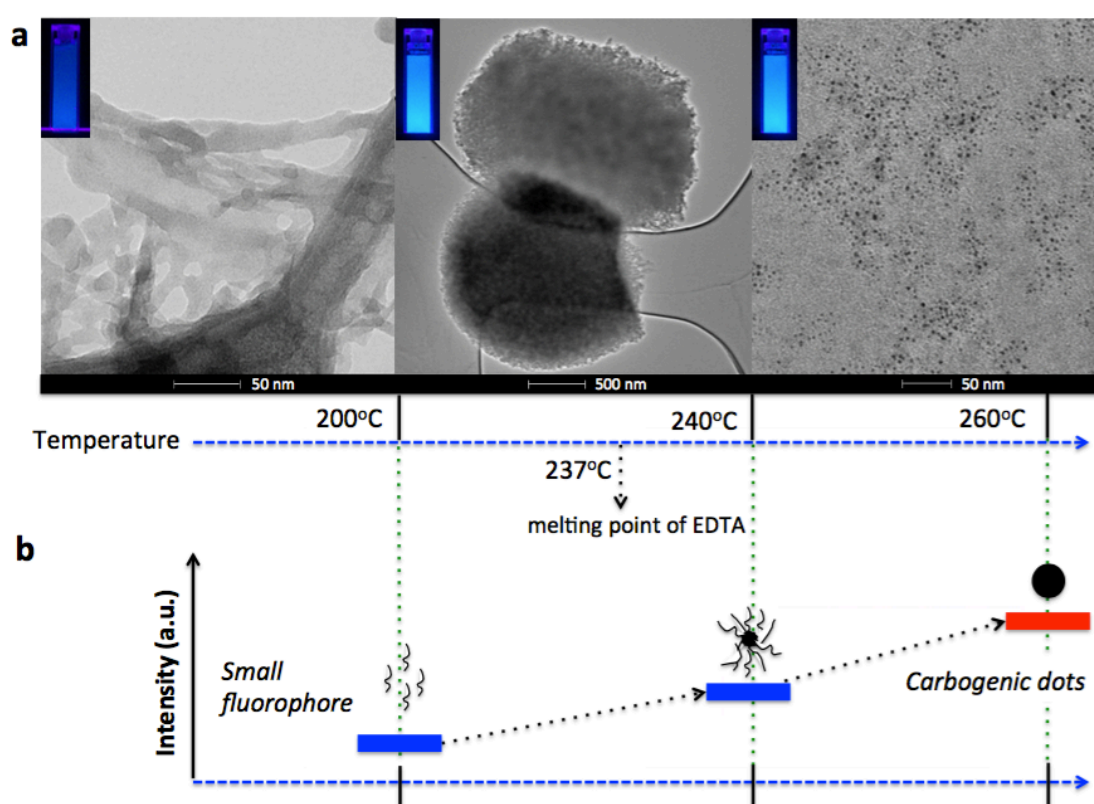
Figure 50. (a) Transmission electron microscopy (TEM) images of the photoactive species produced at different temperaturas from the hydrothermal synthesis of EDTA; The insets show images of the suspensions obtained in each experiment under UV light illumination (λ_{exc} = 365 nm); and (b) Schematic representation of the emission characteristics of photoactive species produces from thermal treatment of EDTA. During thermal tratment, the organic fluorophores (depicted as black threads) are consumed for the buildup of the carbogenic core (black sphere) so that the PL component that corresponds to the carbogenic core (red bars) increases at the expense of the component that arises from the organic fluorophores (blue bars).

To the best of our knowledge, there are no reports on the effect of heating time and temperature on PL properties of CNDs using EDTA as the only precursor. As shown in *Figure 50*, the nucleation of carbogenic dots from EDTA depends on the synthesis conditions. These results are further developed in ***Article 3*** of this Thesis.

III.1.2 Pyrolytic carbonization

Pyrolytic carbonization has been widely adopted for the preparation of carbon nanodots, *via* pyrolysis or carbonization of carbon precursors under high temperature conditions[133]. First, the carbon source is heated to a sufficiently high temperature, loading to the formation of black pyrolytic materials from which the CNDs can be separated and purified. Generally, this method requires a high concentration of alkali or strong acid to cleave bonds in the carbon precursors to obtain nanoscale colloidal particles. However, in this work we report a large-scale aproach for synthesizing water-soluble CNDs from inexpensive and abundant plant leaves as recyclable green wastes. No strong acid treatment or further surface modification was necessary in the process. The CNDs exhibited good water-solubility, small particle size, strong blue luminescence and good colloidal stability.
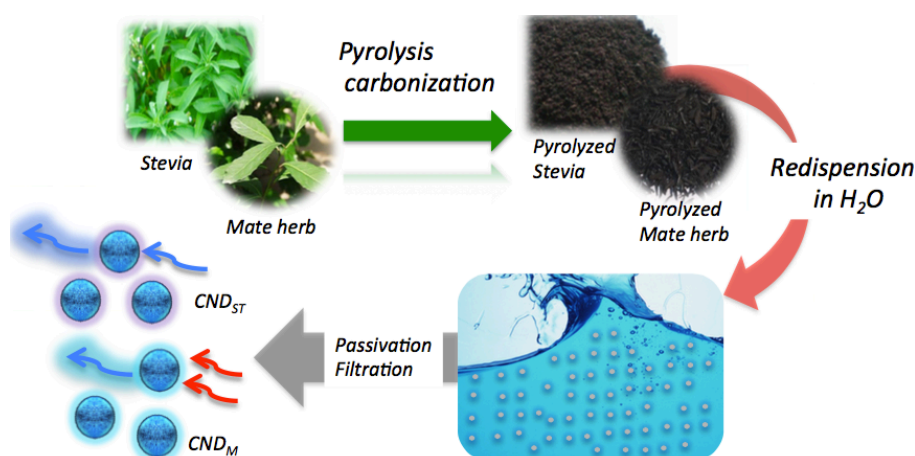
Figure 51. Schematic synthesis of CNDs from pyrolysis of plant leaves.

CNDs were prepared by pyrolysis of Mate herb (*Ilex paraguariensis*), ***Article 4-5***, and stevia leaves (*Stevia rebaudiana*), ***Article 5***. Typically, the plants were first dried in an oven at 100°C prior to grinding into a fine powder. Then, 1.2 g of the dried and powdered mate and stevia leaves were thermally treated in air for 2h at 300 ^{o}C and 250 ^{o}C, respectively (see *Figure 51*). Black carbonized powder was cooled to room temperature, dispersed in ultrapure water (15 mL) and centrifuged at 6000 rpm for 10 min to remove large or agglomerated particles. The remaining supernatant was filtered through a 0.1 µm PTFE membrane (WhatmanTH) to give a brownish yellow suspension of CNDs. No presence of additional agglomerates was detected in the final suspension. The CNDs from mate and stevia leaves were named as CND_M and CND_{ST},

respectively. It was observed that other heating temperatures did not render CNDs as indicated by the absence of photoluminescence (at temperatures above 300 ^{o}C ash is produced). According to the literature 250-300 ^{o}C was enough for the preparation of CNDs[116].

Furthermore, no external surface passivation agents or further modification was necessary in their preparation. Since the plant leaves and extracts abound with carbon, nitrogen and oxygen elements, we have observed that carbon nanodots from different plant sources contain different levels of doping with nitrogen and phosphor. Thus, by selecting suitable precursors it is possible to tailor the resulting green CNDs with different optical response as up-converters or down-converters.

III.1.3 Flash-thermal pyrolysis in fluidized-bed reactors with confining templantes

Discrete CNDs with tunable and uniform sizes can be prepared *via* confined pyrolysis of an organic precursor in nanoreactors. We embarked in this more difficult route because it is of great importance to control the size of CNDs during the preparation process in order to get uniform properties. The *supported synthetic procedure* involves three main steps: (i) absorbing the organic precursor into porous nanoreactors via capillary force, (ii) pyrolysis of the organic precursor confined in the nanoreactors, (iii) release of the as-synthesized CNDs by ultra-sonication in water. The size and size-distribution of the CNDs produced from this method are dictated by the texture parameters of the nanoreactors. In this regard, mesoporous silica (MS)[109, 114], zeolites[360] and polymeric core-shell nanoparticles[111, 112, 361] have already been used as confining nanoreactors in the production of CNDs. Porous silicas are the most widely used nanoreactors thanks to their inorganic nature that provides, thermal stability and easy removal of the product CNDs, as well as the possibility to select pore structures with different characteristics.

We report the synthesis of undoped and nitrogen-doped luminescent carbon nanodots by rapid pyrolysis using ordered mesoporous silica (MS) nanorods as confining templates, *Article 6*. The structure of the silica hosting matrix (ordered mesoporous silica nanorods) allowed the synthesis of different undoped and N-doped CNDs simply by changing the nature of the precursor hosted within the pores. Fort he

first time, we used immersion of the loaded template in a fluidized-bed reactor for rapid (flash) pyrolysis in order to ensure to fast heat transfer and heating to the desired reaction temperature, see *Figure 52*. Also as an alternative procedure, we have used directly the surfactant molecules (structure-directing agent (SDA)), confined within the ordered mesoporous channels during its synthesis, as carbon precursors to obtain CNDs by direct carbonization, **Article 7**. Again, the flash pyrolysis method produced strong PL centers attributed to silicon and carbon-based sites within of MS nanorods.
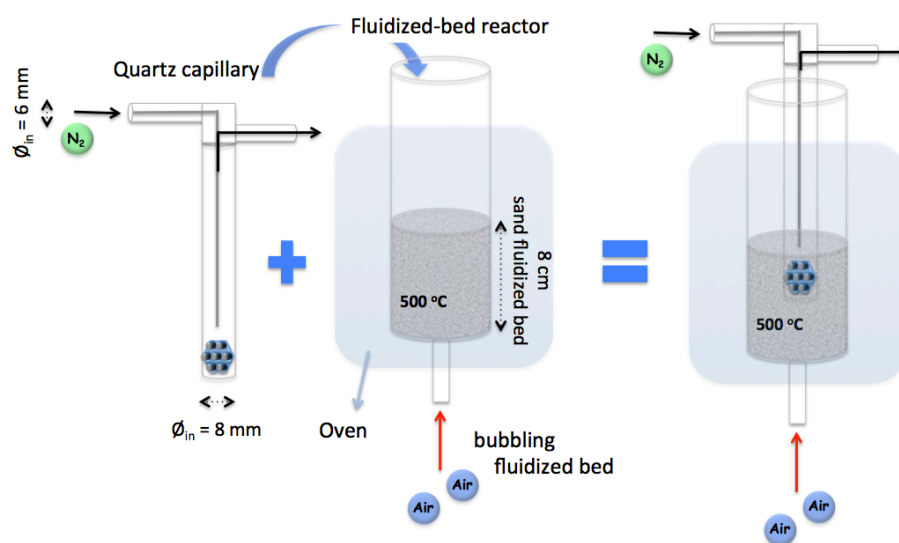
Figure 52. Flash pyrolysis treatment by immersion in a fluidized-bed reactor. The sample to pyrolyzed is placed in a quartz capillary well ($\emptyset_{in}$ = 8 mm) designed with inlet-outlet outfits ($\emptyset_{in}$ = 6 mm) for inert gas feeding (flow rate 3 L h^{-1}). The capillary tube was introduced inside a fluidized sand bed (8 cm bed height) used to induce flash heating of the sample. The fluidized bed was kept at the temperature, in this case at 500°C, and desired time, inducing rapid carbonization under controlled conditions.

III.1.3.1 *Rapid pyrolysis of organic precursors in confining mesoporous templates*

These silica-based nanostructures have been successfully used to: (i) load two different organic precursors such as citric acid (CA), or ethylenediaminetetraacetic acid (EDTA), (ii) induce their thermal decomposition (pyrolysis) within the confined dimensions of their porous walls, and (iii) render a highly uniform size distribution of CNDs (see *Figure 53*) with average sizes below 4 nm.

The ordered SBA-15 mesoporous silica nanorods were prepared according to previously reported procedures[362, 363]. In brief, 1.2 g of P123 and 0.014g of NH$_4$F were first dissolved at 20°C in 40 mL of HCl (1.75M) solution under stirring. Upon complete

dissolution, 2.75 mL of TEOS and 8.5 mL heptane were added drop-wise and left under stirring for 8 min. The aged precursor mixture was hydrothermally heated at 100°C for 24 hours in a Teflon-lined autoclave. In the case where a different precursors was embedded in the SBA-15 pores, the porous structure had to be vacant. To this end, the removal of the SDA confined within the ordered mesoporous channels was carried out by calcination with a heating ramp of 1°C min^{-1} up to 550 $^{\circ}$C and a dwell time of 6 h in flowing air (in the next procedure, section III.1.3.2, this step will not carried out). The solid product was then filtered, washed three times with distilled water, and dried at 60 $^{\circ}$C overnight.
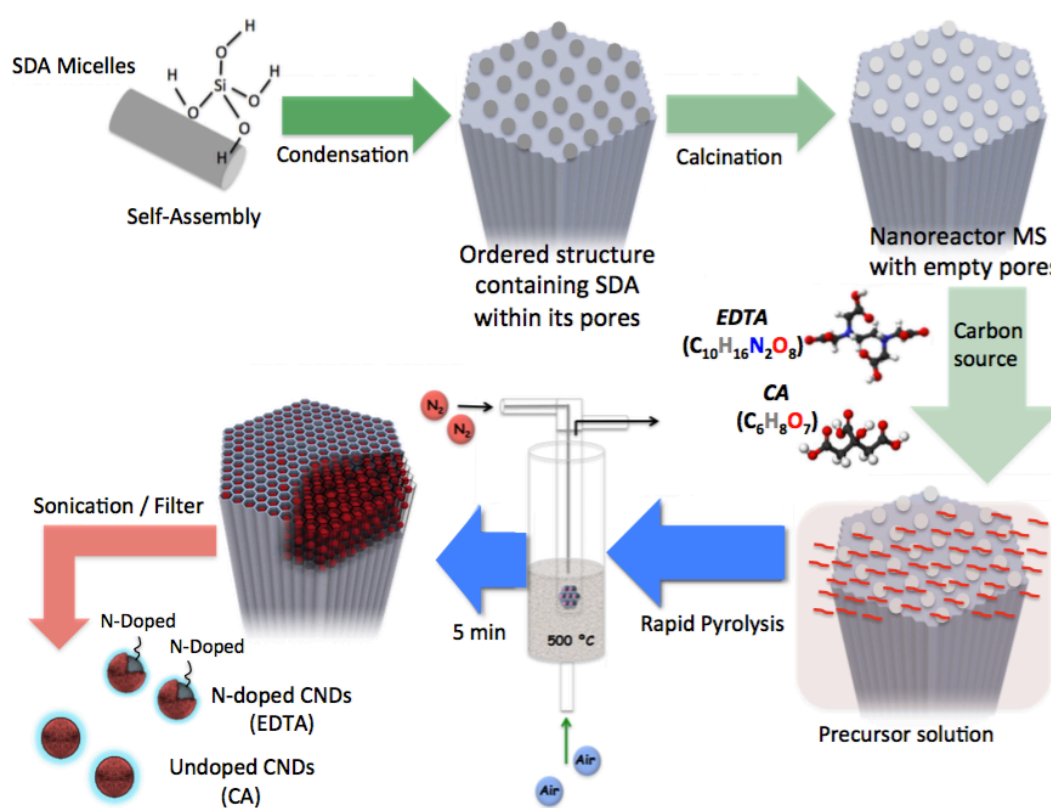
Figure 53. Scheme describing the different steps carried out to synthesize the mesoporous silica nanorods, used as templates. The empty nanochannels were loaded with either citric acid (CA) or EDTA, and the rapid pyrolysis treatment carried out in the fluidized bed reactor at 500 $^{\circ}$C render confined undoped and N-doped CNDs, respectively.

Once the nanoreactor template was synthesized, in a typical experiment, 200 mg of this calcined silica nanorods and 100 mg of the selected organic precursor (citric acid (CA) or EDTA) were mixed and sonicated in 0.5 mL of a solution containing NaCl, LiCl and KNO$_3$ (mass ratio 20:5:5). The mixture was dried in an oven at 60°C for 10 min and a fraction of the resulting powder (20 mg) was placed in a quartz capillary ($\varnothing_{in}$ = 8

mm) designed with inlet-outlet outfits ($\emptyset_{in}$ = 6 mm) for inert gas feeding (nitrogen flow rate 3 L h^{-1}). The capillary tube was immersed in a sand bubbling fluidized bed (8 cm bed height). Fluidization was achieved with air (flow feeding rate 15 L h^{-1}) (see *Figure 53*). This fluidized bed configuration promotes a rapid and homogeneous heating to the desired temperatura (500 ^{o}C) of immersed objects, leading to a rapid pyrolysis process of the contents of a tubular reactor loaded with the mesoporous solids. The sample was kept inside the fluidized bed at 500 ^{o}C for 5 min and then allowed to cool down to room temperatura (see *Figure 53*). After the flash pyrolysis process, a brownish-pale yellow solid was obtained.

As shown in the *Figure 54*, the optimal mass ratio of MS template to organic precursor was 2:1, for both AC and EDTA. For mass ratios of 2:0.5 and 2:1.5, fewer CNDs were generated in the structure and the excess of carbon induced collapse of the MS structure, respectively.
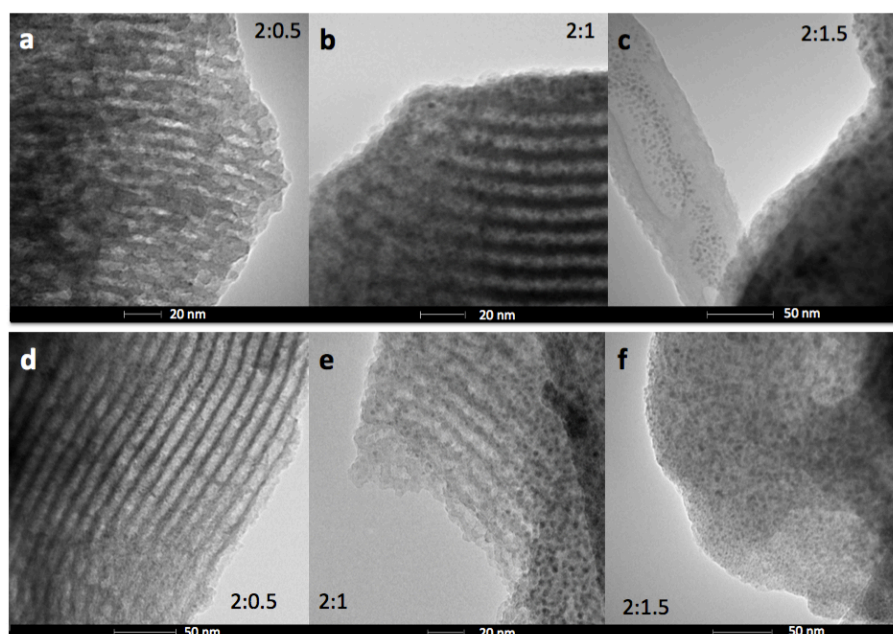
Figure 54. Transmission electron microscopy (TEM) images of SBA-15 nanorods after flash-pyrolysis silica structures loaded with carbon precursos with different mass ratios. a-c) Using CA as carbon precursor; and d-f) Using EDTA as carbon precursor.

To extract the CNDs confined in mesoporous templates most works in the literature report the use of an alkaline solution for eching of the silica structure[109], followed by neutralization by HNO$_3$ and dyalysis against double distilled water through a dialysis membrane to remove NaOH excess. However, the template was difficult to

be etched off completely, separation and purification was hard, and the yield was low. In addition, the procedure did not allow the possibility of reusing the templante for successive synthesis. In contrast, our powdered solid was extensively rinsed and ultra-sonicated in water for 15 min to facilitate the release of the carbon nanostructures generated within the silica nanoreactor. The supernatant containing the CNDs was passed through a 10 nm cut-off filter. The nanoreactor could then be reused, and the final yellow solution containing the CNDs was stored without any further treatment for subsequent use. As expected, from EDTA, as a carbon source, N-doped CNDs were obtained. In such a way, that the CNDs synthesized from CA, as carbon source, presented carboxylated groups on their surface. Consequently, the CNDs prepared from CA and EDTA was hereafter named as CND_{AC} (for undoped-) and CND_{EF} (for N-doped-), respectively. These results are discussed in **Article 6** of this Thesis.

The key feature of this method has been the employment of MS nanorods as supports, which not only confines the growth ot the CNDs to a narrow size distribution within the pores of MS nanorods, but also prevents the aggregation of the nanosized CNDs. The second main novelty correspond to the rapid heating process provided by the use of a fluidized-bed reactor.

III.1.3.2 Rapid pyrolysis of structure-directing agent confined in mesoporous templates

Here, we take advantage of the existence of the SDA in the mesoporous structure as a source of carbon. In a tipycally procedure, the ordered mesoporous silica (MS) nanorods were synthesized using Pluronic P123 as SDA and Tetraethylorthosilicate (TEOS) as silicon source following a hydrothermal approach as mencioned in section III.1.3.1. In order to induce the generation of light-emitting centers within the silica nanorods, these were placed in a thin wall 8 mm diameter quartz tube, which was immersed in a sand fluidized-bed reactor at 500 ^{o}C (see *Figure 52*). The samples were flash-heated to the bed temperature in less than 40 s. This flash heating protocol induced luminescent sites within the MS nanorods while keeping their ordered structure. Furthermore, the selection of different reaction ambients derived in different photoluminescence responses of the resulting materials (*Figure 55*). Thus, flushing the samples with nitrogen during pyrolysis led to the preferential

generation of carbogenic dots (sample hereafter refered as LMS@C) due to the *in situ* carbonization of the SDA encapsulated within the mesoporous channels.
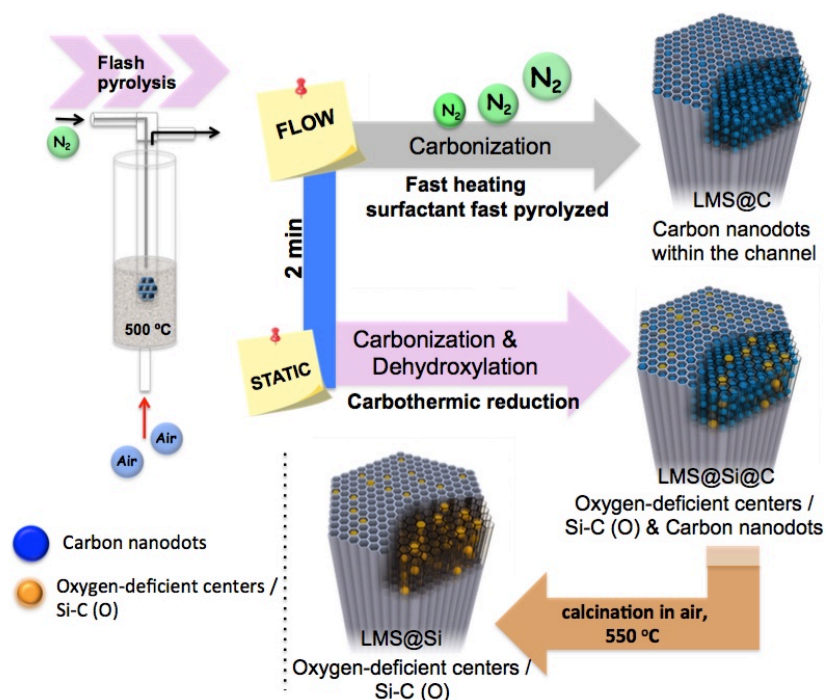
Figure 55. A flash heating of SDA-containing silica nanorods induced the generation of different light-emitting centers within its structure. The conditions could be tailored to obtain only carbon dots in the silica structure (LMS@C) or carbon dots plus silica-based emitting species (LMS@Si@C). A third set of samples containing only luminescent silicon-based species (LMS@Si) was obtained by a slow oxidation post-treatment of the LMS@Si@C sample in a conventional furnace. Different reaction atmospheres (flowing N_2 or static air) were used to tailor the preferential formation of the different luminescent sites during the flash-thermal treatments.

Interestingly, the partial reduction of silica units generated defect-luminescent features in the structure stemming from oxygen-deficient silica centers[364]. These could be present simultaneously with carbon-doped silica domains[365] (sample referred as LMS@Si@C). In order to identify whether the emission could be attributed to defect-silica and/or carbon-doped silica sites, an additional calcination step in air was carried out using a slower (5 $^{\circ}$C/min) temperature ramp in order to remove all carbonaceous species (CNDs and residues from the pyrolysis of the SDA still present in the pores) from samples LMS@C and LMS@Si@C (*Figure 55*). After the removal of carbon nanodots, the luminescence was attributed to partially reduced silica emission centers or Si-C-O domains. The luminescence could be clearly discerned, with characteristic emission peaks clearly distinguishable from the carbon nanodots typical luminescent features[366]. This sample containing only silicon-related emitting species was labeled as LMS@Si for subsequent use and evaluation (*Figure 55*). *Figure 56* shows an

explanatory scheme on the calcination stages for each nanomaterial of interest. For more details of these results, see *Article 7* of this Thesis.
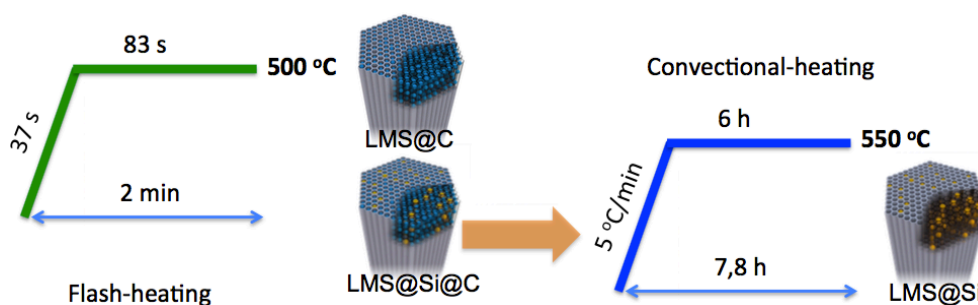
Figure 56. Scheme of the calcination steps for LMS@C, LMS@Si@C and LMS@Si.

In addition, we also investigated the formation of emitting centers under different temperatures and treatment times. As a representative example, for the condition of LMS@C under flowing N_2, *Figure 57*, shows that by increasing the time the 2 min to 30 min at 500 ^{o}C, the mesoporous structure was maintained without collapse.
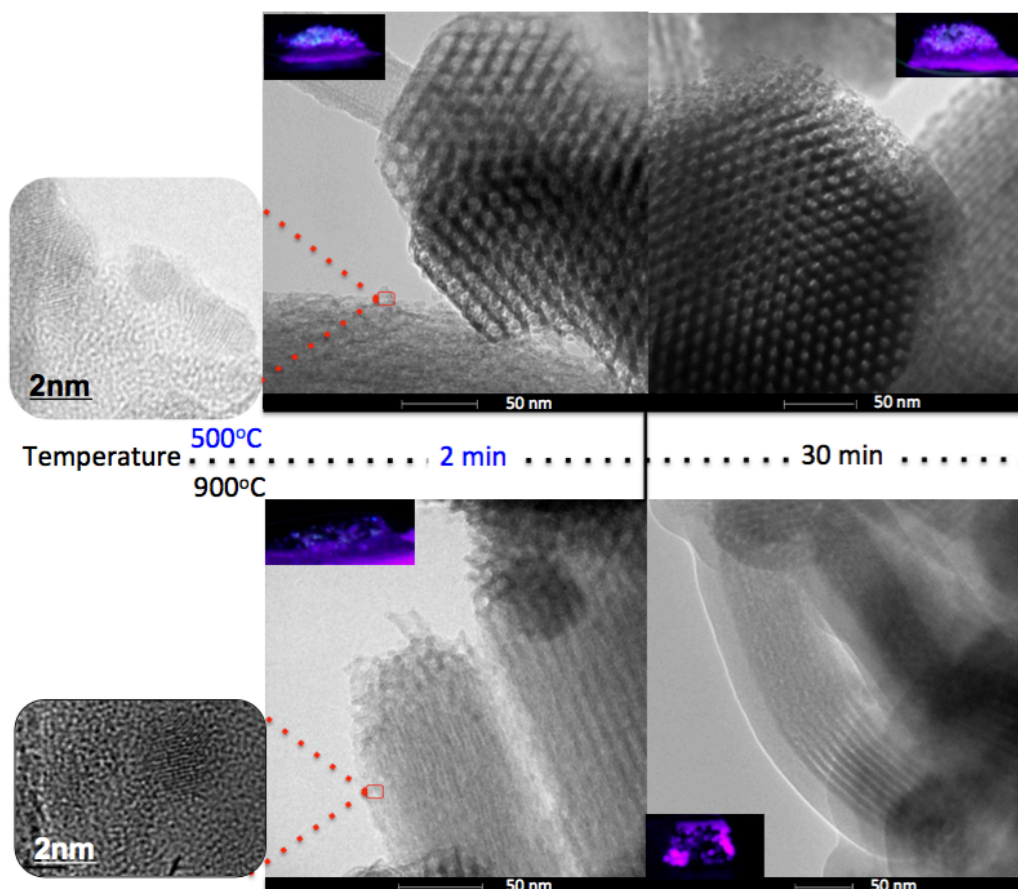
Figure 57. Transmission electron microscopy (TEM) and High resolution TEM images of different condition of temperatures and times for the condition of LMS@C procedure; (insets: Digital photographs corresponding to the powdered LMSs with a UV lamp (λ_{exc} = 365 nm).

However, the generation efficiency of carbon nanodots was less efficient at 30 min. On the other hand, when the experiment was made to 900 ^{o}C. The collapse of the MS structure was observed after a time of 30 min. Even so, in short times, 2 min, a luminescent carbogenic core could be observed. Finally, to corroborate that the generation of luminescent centers was due to the use of the flash pyrolysis method, slow conventional calcination treatments were carried out for comparison under identical reaction atmospheres and temperatures. None of the control experiments under conventional heating conditions rendered any luminescent nanostructures. This was attributed to the slower heating rates that provided sufficient time for the carbon-containing species to exit the mesoporous structure before inducing partial carbothermic reduction of the support.

III.2   Assembly of Carbon Nanodots create to heterogeneous photocatalysts nanohybrids

Although there are previous reports describing the *in situ* synthesis of CNDs-based composites[367], they normally exhibit certain drawbacks. For instance, the size of the CNDs and their homogeneity on the heterogeneous photocatalyst support (i.e., TiO$_2$ and iron-based nanoparticles) are difficult to control *in situ* procedures. Therefore, an alternative approach where the CNDs are first synthesized and then deployed onto the targeted supports has been exploited in this work to ensure a more homogeneous nanohybrid configuration.

III.2.1   Coupling to TiO$_2$ nanoparticles

The assembly protocols of different CNDs including CND$_{AAEN}$, CND$_M$ and CND$_{ST}$ onto anatase-phase nanoparticles were similar in all cases and have been described in *Articles 2 and 5*. It is worth mentioning that the initially acquired commercial TiO$_2$ supports included a thin layer of organic material after inspection by TEM (see *Figure 58-a*). In order to prevent issues with the deployment of the CNDs, a pretreatment at 180 ^{o}C for 1 h was carried out prior to the addition of the carbon nanodots. Additional TEM images confirmed that the thermal pre-treatment was enough to get rid of the outer monolayer of organic/amorphous material around the TiO$_2$ NPs. Furthermore,

the attachment of CNDs was more efficient (*Figure 58-b*) and the photocatalytic response was better. For all these reasons, all the subsequent preparation of CNDs@TiO$_2$ involved this pre-treatment.
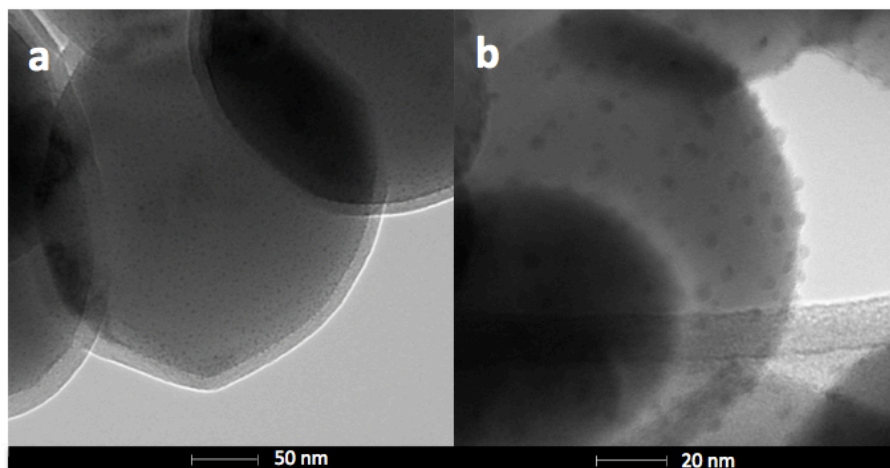
Figure 58. Transmission electron microscopy (TEM) of CNDs deposited on commercial Anatase TiO$_2$: (a) without pre-calcination; and (b) pre-calcined.

Typically, 0.5 g Anatase TiO$_2$ powders (previously calcined at 180 ^{o}C for 1h) were dispersed in a mixture of 2.6 mL CNDs solution (1 mg/mL) and 2.4 mL deionized water, and stirred vigorously for 30 min (see *Figure 59*). The resulting suspension was dried under vacuum at 65 ^{o}C for 90min and stored at ambient conditions until further use.
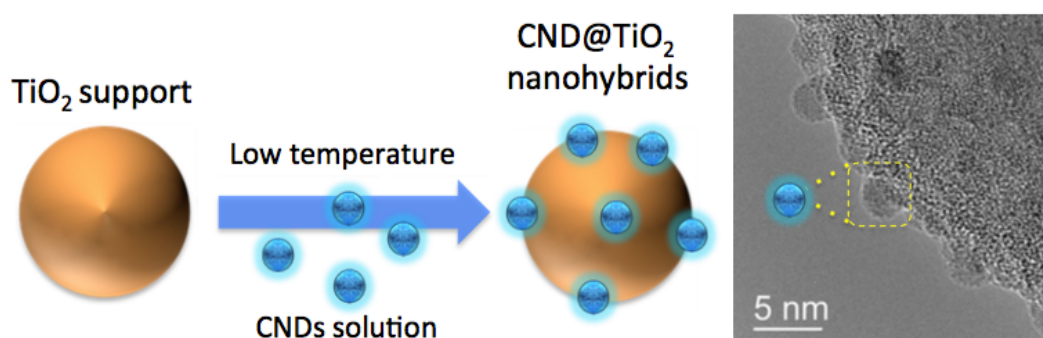
Figure 59. Scheme of the coupling of TiO$_2$ support with CNDs to generate CNDs@TiO$_2$ and High resolution TEM images of CNDs@TiO$_2$ nanohybrids.

III.2.2 Coupling to recoverable magnetic nanoparticles

Similarly, the CNDs were first synthesized followed by deposition on to the iron-based inorganic support. In this case, superparamagnetic feroxyhyte nanoflakes were

prepared by continuous gas-slug microfluidics. L-lysine was used for their stabilization, helping through physical mixing to also stabilize of coupling the CNDs. The feroxyhyte nanoflakes represent a scarcely explored iron-based (δ-FeOOH) phase (Fe-NFs) with a graphene-like layered nanostructure (**Article 4**). The high availability of exposed area in the suspended feroxyhyte nanoflakes (Fe-NFs) (estimated at 80 $m^2 g^{-1}$ for the pseudo-planar configuration) facilitates the assembly of the CNDs, while their superparamagnetic nature enables their reutilization via magnetic recovery.

The facile self-assembly procedure used to form the Fe-NF/CND$_M$ nanohybrid photocatalysts involved a simple dispersion of the Fe-NFs in a solution of CNDs under vigorous stirring, followed by vacuum-assisted drying at low temperatura (see *Figure 59*). Typically, 0.2 g Fe-NFs were suspended in a mixture of 1 mL CNDs (0.5 mg/mL) and 1 mL deionized water, and stirred vigorously for 30 min. Then, the suspension was dried at 65°C in a vacuum-driven oven during 60 min.
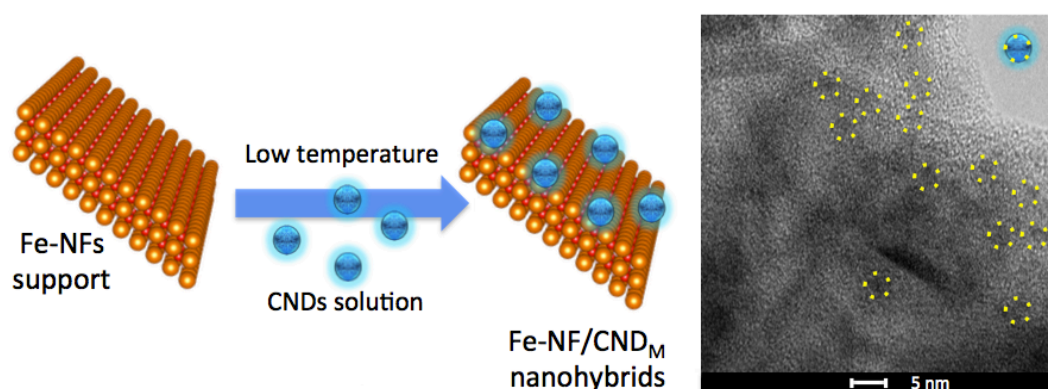
Figure 59. Schematic coupling of Fe-NFs support with CNDs to generate Fe-NF/CND$_M$ and High resolution TEM images of an example of Fe-NF/CND$_M$ nanohybrids.

III.3 Surface chemistry/characterization of light-emitting Carbon Nanodots

CNDs reported in this thesis primarily consist of C, H, N and O elements, which are present in the form of various functional groups, and provide good water solubility with scope for further functionalization. CNDs showned quasispherical or spherical shaped less than 10 nm in diameter, depending on their preparation conditions and precursors. In addition, the obtained CNDs can be described in terms of a carbogenic core with surface functional groups, where the advantage of green sources over chemical entities was that of these methods did not require separate reactants for

doping, post-modifications or surface passivation because of the presence of various carbohydrates, protein and other biomolecules which provide self-passivation to green CNDs. Although many researchers have demonstrated the existence of crystalline sp^2-carbon-containing sections, and some studies suggest the existence of diamond-like structure formed by sp^3 carbons[97], most CNDs have poor or partial crystallinity. In our case, we have been able to synthesize CNDs with an amorphous to a nanocrystalline core with predominantly sp^2 carbon, the lattice spacings of which are consistent with graphitic crystalline. This section briefly describes surface chemistry of the synthesized green CNDs.

Besides the presence of a carbogenic core with different kinds of carbon hybridization, CNDs also contain different surface functional groups. The analysis of the elemental composition and surface functional groups of CNDs has been carried out by X-ray photoelectron spectroscopy (XPS) analysis (see *Figure 60*). XPS characterization is in common use to explore the chemical composition and configuration of X-CNDs almost without any exception as it is a powerful surface-sensitive quantitative spectroscopic technique that measures the elemental composition, chemical state and electronic state of the elements within CNDs. Typically, the surface composition of the samples was analyzed by x-ray photoelectron spectroscopy (XPS) with an Axis Ultra DLD (Kratos Tech.). The spectra were excited by a monochromatic Al Kα source (1486.6 eV) run at 12kV and 10mA and pass energy of 20eV was used. The binding energies were referenced to the internal C 1s (284.2 or 294.3 eV) standard. Analyses of the peaks were performed with CasaXPS software, using a weighted sum of Lorentzian and Gaussian component curves after Shirley background subtraction.

We studied the detailed surface composition and bonding information on the doped nitrogen atoms in the CNDs by XPS spectra, which indicated the presence of N, C and O elements and corresponding N 1s, C 1s and O 1s peaks at about 399.3 eV a type species named N_6 (attributed to pyridine), terminal C-N or amide groups; and 400.9 eV a type species named N_5 (due to pyrrolic, pyridones or nitroso groups) or the presence of protonated primary amines ($-NH_3^+$), confirming the doping of N into the raw materials (see *Figure 60 a-b*). The O 1s spectra assume the presence of two types of C/O species. As shown in *Figure 60-c*, a firts one appearing at around 532.4 is usually

associated to oxygen atoms bonded to C through sp^2 orbitals (carbonyl group, O=C). The second contribution at around 530.9 eV is usually attributed to oxygen bonded to carbon through aliphatic sp^3 orbitals, (H)O-C/O-C. Finally, the evaluation of the C 1s regions confirmed the presence of multiple C=O, C-O and/or C-N surface groups (*Figure 60-d*).
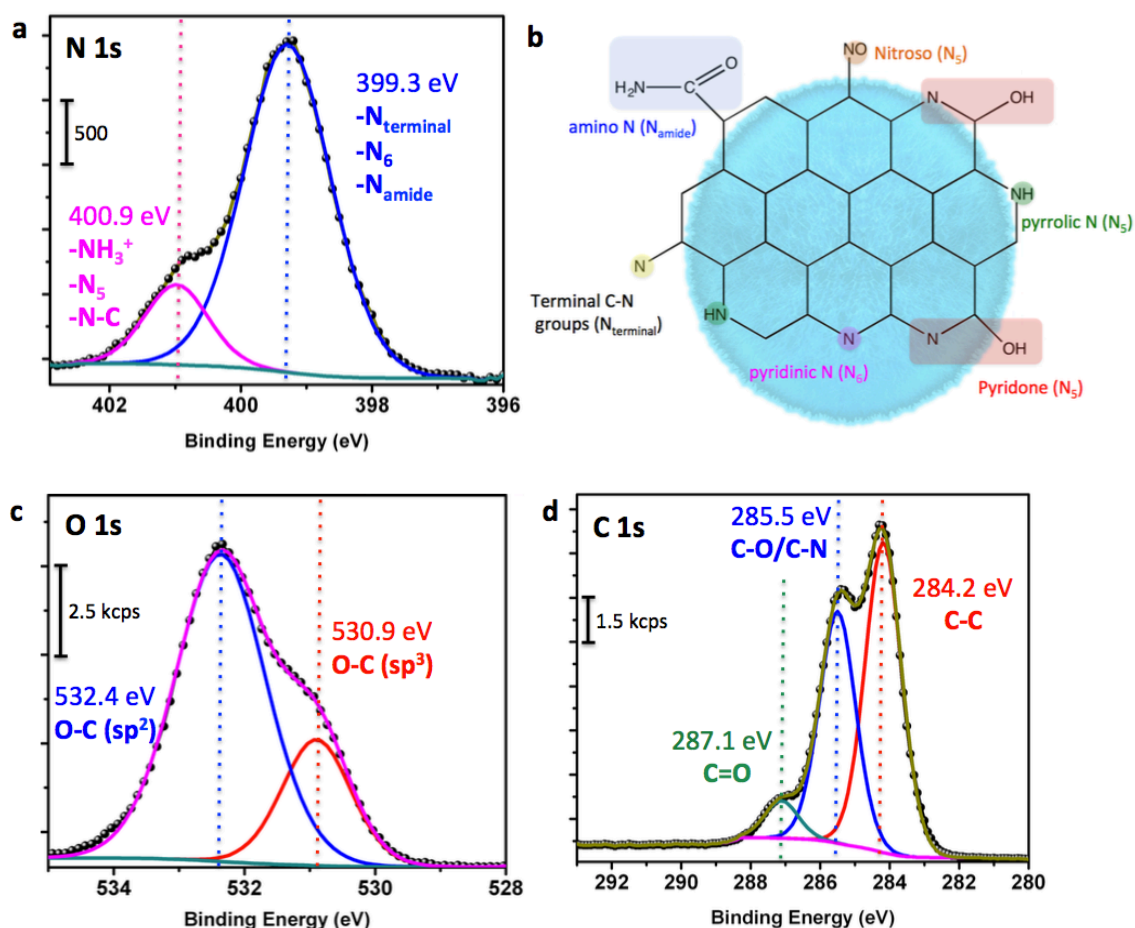
Figure 60. Surface chemistry analysis of the N doped CNDs: (a) Fitted X-ray photoemission spectra in the N 1s region of the N-CNDs; (d) Some nitrogen funtional forms possibly present in carbonaceous materials; and (c)-(d) Fitted X-ray photoemission spectra in the O 1s and C 1s region, respectively.

Based on the above discussion, unless the carbon source contains C-N bands, oxidized CNDs generally feature carboxylic moieties at their surface, with overall oxygen contents ranging from 5-35 wt%, depending upon the experimental conditions. Therefore, we can conclude that N-doped CNDs consist of core with predominantly sp^2 carbon and with N groups in the surface.

III.4 Photo-physical properties of freestanding Carbon Nanodots

III.4.1 Measurement of Optical Absorption and Photoluminescence (PL)

The optical absorption spectra and steady-state fluorescence emission spectra of different CNDs solutions in distilled water were collected on a JASCO FP-6500 spectrofluorometer equipped with a 450 W xenon lamp for excitation, with temperature controller ETC-273T at 25 ^{o}C, using 5×10 mm cuvettes and a LS55 Fluorescence Spectrometer (PerkinElmer) equipped with a xenon arc lamp as the light source and a quartz cell (10 x 10 mm). The excitation wavelengths used in the experiments to record the emission spectra were 365 and 800 nm.

III.4.2 Measurement of Quantum yields (QYs)

The fluorescence quantum yield (QY), "Φ", of different CNDs in aqueous solution were computed according to the *equation 1*[368]:

$$\Phi_S = \Phi_R \times F_S \times (1\text{-}10^{-AR\,(\lambda ex)}) \times n_S^2)/\,F_R \times (1\text{-}10^{-AS\,(\lambda ex)}) \times n_R^2) \qquad \text{(eqn. 1)}$$

The subscript S refers to the CND samples, R stands for the selected reference fluorophore (quinine sulfate, 0.1 M H_2SO_4) with known quantum yield (0.54), F stands for the corrected, integrated fluorescence spectra, A(λ_{exc}) denotes the absorbance at the used excitation wavelength λ_{exc}, and n represents the refractive index of the solvent. To minimize inner filter effects, the absorbance at the excitation wavelength λ_{exc} was kept under 0.1. The measurements were performed using 10 mm optical path length cuvettes under right-angle (L-) arrangement and "magic angle" conditions. The averages and standard uncertainties of Φ are computed from independent Φ measurements (2 conc. of sample×2 conc. of reference×2 excitation wavelengths λ_{exc}).

Typically, the fluorescence QY value of CNDs was calculated by comparing the integrated PL intensities (excited at 360 nm) and absorbance values (at ~340-345 nm) for two different concentrations of CNDs with those of quinine sulphate. Quinine sulphate (QY = 0.54 at 360 nm) was dissolved in 0.1 M HSO_4 (refractive index, 1.33) and CNDs were dissolved in water (refractive index, 1.33).

III.4.3   Measurement of Time-resolved Photolumicescence decay (lifetime decay)

Time resolved photoluminescence decay traces were fitted using FluoFit 4.4 package (Picoquant GmbH). In all cases, PL decay traces were recorded at 450, 460 and 470 nm emission wavelengths, and the three decay traces were fitted globally with the decay times linked as shared parameters, whereas the pre-exponential factors were local adjustable parameters. The experimental decay traces were fitted to multi-exponential functions via a Levenberg-Marquard algorithm-based nonlinear least-squares error minimization deconvolution method. In all cases, three different exponential terms were used to fit the experimental decay traces. The quality of fittings was evaluated by the reduced chi-squared method, X^2, the weighted residuals and the correlation functions. In all cases, the best fits of the decay traces required a sum of three exponential decay functions to reach low X^2 values as well as random distributions of the weighted residuals and auto-correlation function, indicators of the goodness of the fits. To compare the emission lifetime of the different CNDs at different concentrations and different pH media it was necessary to determinate their average lifetime using the *equation 2*:

$$\tau_{ave} = \sum a_i \tau_i^2 / \sum a_i \tau_i \qquad\qquad (eqn.\ 2)$$

In which, a_i are pre-exponential factors and τ_i the lifetimes obtained in the multi-exponential fitting of the decay curves of CNDs emission.

Fluorescence decay traces of the different CNDs were recorded in the Time Correlated Single Photon Counting (TCSPC) mode using the FluoTime 200 fluorometer (PicoQuant, GmbH). Briefly, the samples were excited by a 405 nm Picosecond Pulsed Diode Laser (Edinburgh EPL405) with a 10 MHz repetition rate. The full width at half maximum of the laser pulse was ~90 ps. The fluorescence was collected after crossing through a polarizer set at the magic angle, and a 2 nm bandwidth monochromator. Fluorescence decay histograms were collected using a TimeHarp200 board, with a time increment per channel of 36 ps, at the emission wavelengths of 450, 460, and 470 nm. The histograms of the instrument response function (IRF) was determined using LUDOX scatterer, and sample decays were recorded until they typically reached 2×10^4 counts in the peak channel, since it is well known that complex decays can be well

described by the simplest exponential models if the fitting is carried out from experimental data with a low number of condensation particle counter (CPC).

III.5 Experimental setups for the evaluation of photocatalytic properties

III.5.1 Heterogeneous photocatalysis with Carbon Nanodots coupling to TiO$_2$ semiconductor

The experimental setups will be divided into two parts, according to the irradiation source: **(1)** Under irradiation of <u>visible light</u>, **Articles 2** and **5**, system used during my Postgraduate Internship at the Hong Kong University of Science and Technology (HKUST); and **(2)** under the irradiation of selective wavelenths with light-emitting diodes (LEDs) (LED ENGIN, LZ4 model) at <u>740 nm (red LED)</u>, **Article 5**. Thus, the photocatalytic activity of the CND@TiO$_2$ nanohybrids was evaluated by degradation of 2,4-Dichlorophenol (2,4-DCP) under visible light or under specific near-infrared (NIR) irradiation. In the typical experiment:

1. Experimental setup for photocatalytic processes under visible light (Hg lamp, cutoff filter for $\lambda < 420$ nm) were performed on a 100 mL reactor open to the air (see *Figure 61*). In a standard procedure, 0.2 mg mL^{-1} nanohybrids were mixed with 0.025 mM 2,4-DCP aqueous solution (pH around 7), in a total volumen of 100 mL, which was stirred for 12-20 h to reach adsorption equilibrium between 2,4-DCP and photocatalyst before irradiation. Temperature was kept at 20-22 $^{\circ}$C using a fans cooling system and the assays were sheltered from the ambient light. A small fraction of the stirred suspension (about 3 mL) was taken at different times intervals under irradiation and filtered through a 0.22 μm filter. The liquid was analyzed using an ultra performance liquid chromatography (UPLC) or Gas Chromatography coupled to Mass Spectrometry (GC-MS).
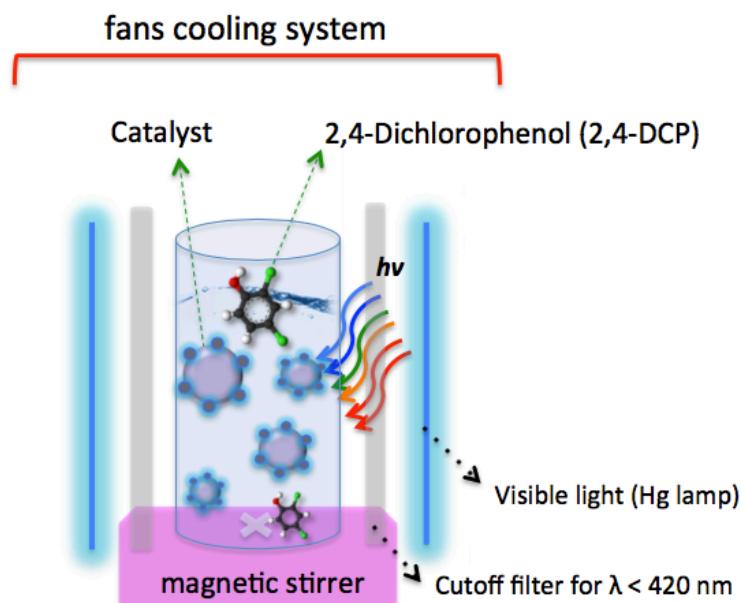
Figure 61. Schematic experimental setup for photocatalytic processes under visible light (Hg lamp, cutoff filter for λ < 420 nm) performed on a 100 mL reactor open to the air.

2. Experimental setup for photocatalytic processes under NIR light LED irradiation were carried out suspending 0.6 mg of catalyst, CNDs@TiO$_2$ nanohybrids or plain TiO$_2$ nanoparticles as control, in 3 mL of 0.025 mM 2,4-DCP solution at pH around 7 (final concentrations were 0.025 mM 2,4-DCP and 0.2 mg mL^{-1} catalyst). The suspensions were magnetically stirred under dark for 3 h, prior to the irradiation with one red light emitting LED, in order to guarantee the establishment of an adsorption/desorption equilibrium. Temperature was kept at 20-22 $^{\circ}$C using a cooling system Synjet® coupled to a LED irradiating device (see *Figure 62*) and the assays were sheltered from the ambient light. Different aliquots of 180 µL were taken at several selected time intervals. Then, the sample was centrifugation and air dried to redissolved in 600 µL methanol (MeOH) for it analysis by GC-MS, following the decreasing of the maximum absorption peak of the 2,4-DCP and generation of different intermediates (see section III.6.2). All the photocatalytic procedures of 2,4-DCP, including plain TiO$_2$ nanoparticles and others control approaches, were performed following the same experimental conditions. At least three assays were carried out for each tested solid and different CNDs@TiO$_2$ batches were tested in order to certify the reproducibility of the photocatalytic effect depending on the synthesized materials.
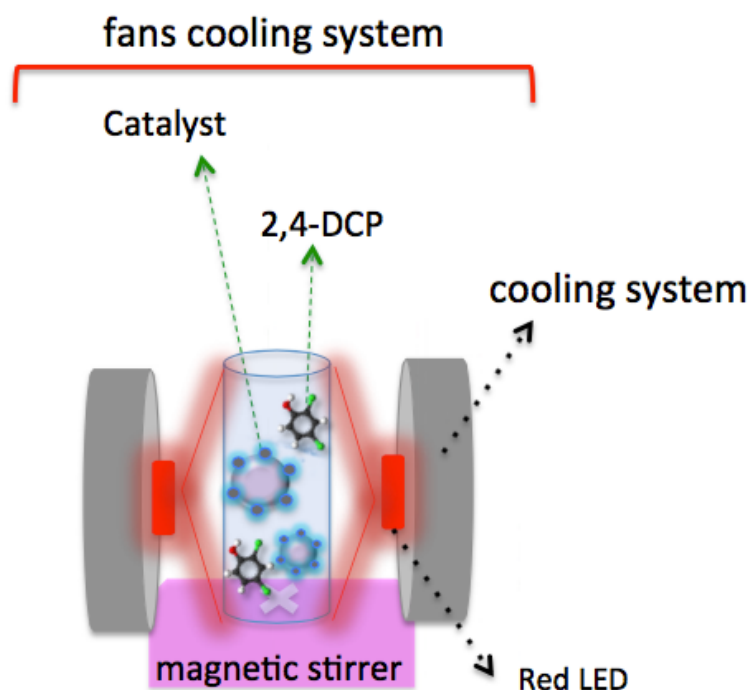
Figure 62. Schematic experimental setup for photocatalytic processes under white LED irradiation performed on a 3 mL quartz cuvette.

In addition, a series of quenching experiments in the presence of 1-butanol and ethylenediaminetetraacetic acid disodium salt (EDTA-Na$_2$) (a hydroxyl and hole scavenger, respectively)[369] were also performed to assess the role of these oxidative radicals in the overall degradation of 2,4-DCP. Thus, the experiments photocatalytic procedures as previously reported was carried out containing 1mM of EDTA-Na$_2$ or 1mM 1-butanol, as appropriate.

III.5.2 Photo-Fenton processes enabled by Carbon Nanodots with recoverable magnetic nanoparticles hybrids

The Photo-Fenton like assays were evaluated by measuring the decomposition rate of methyl orange (MO) as model dye in aqueous solution in the presence of two different LEDs (LED ENGIN, LZ4 models) emitting either at 532 nm (10 W) or 740 nm (6.3 W), respectively. In a typical reaction for mineralization, 0.6 mg of catalyst (Fe-NF/CNDs) was dispersed in 3 mL of MO solution (25 µM), see **Article 4**. Temperature was kept at 20-22 ^{o}C using a cooling system Synjet® coupled to a LED irradiating device (see *Figure 63*). Prior to irradiation with LEDs, the suspension was magnetically stirred

in the dark for 30 minutes to ensure the a proper adsorption/desorption equilibrium, followed by addition of H_2O_2 (2 mM). Different aliquots were taken at selected time intervals and analyzed by UV-Vis spectroscopy (V-67, Jasco Company) following the decreasing of the maximum absorption peak of the dye after retrieval magnetically of the catalyst. The pH of the solution was adjusted using solutions of sulfuric acid (H_2SO_4, 95-87%, Sigma-Aldrich) and sodium hydroxide (NaOH, ACS reagent, ≥97%, Sigma-Aldrich). All the MO degradation assays were sheltered from the ambient light and performed following the same experimental conditions. At least three assays were carried out for each tested solid and different Fe-NF/CND batches were tested in order to certify the reproducibility of the photocatalytic effect depending on the synthesized material.
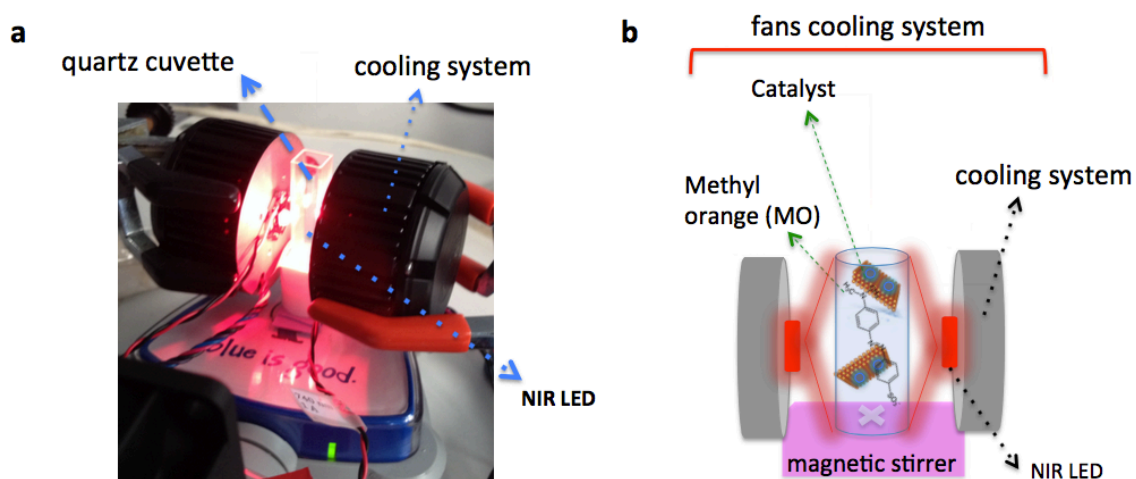
Figure 63. (a) Photo of experimental setup using e.i., NIR LED; and (b) Scheme of experimental setup for Photo-Fenton like under light LED irradiation performed on a 3 mL quartz cuvette.

Additionally, a set of experiments to indirectly demonstrate the formation of hydroxyl radicals and their active role in the MO degradation process beyond a reversible photo-switching mechanism were also carried out. We evaluated the photocatalytic mechanism to induce the generation of hydroxyl radicals with the presence of increasing concentrations of methanol (MeOH) (a well-known hydroxyl radical scavenger)[370] was also carried out for the most favorable conditions (pH = 2.8; LED visible; Fe-NF/CND hybrid). Different volumetric ratios MeOH:H_2O (0:1/0.25:0.75/0.5:0.5) were tested under our photocatalytic decoloration conditions

in order to evaluate the inhibition of the dye mineralization in the presence of increasing concentrations of MeOH.

III.6 Techniques for the detection of reactive intermediates in photocatalytic reactions

III.6.1 Experiment to detection of reactive oxygen species (ROS) as hydroxyl radicals formed upon irradiation in photocatalytic processes

The detection of hydroxyl radicals ($^{\bullet}$OH) under irradiation (depending on the excitation source used in the experiment) was carried out with the aid of terephthalic acid (TA, 3 mL, 5 mM) as described above, which selectively reacts to generate a fluorescent product (2-hydroxy terephthalic acid) emitting at ca. 425 nm (see *Figure 67*). We found it was important to select basic conditions (pH $\sim$ 7-9) or alternatively use disodium terephthalate (NaTA) to conduct the experiments in water due to the limited solubility of TA in water. NaTA is a non-fluorescent molecule that may stoichiometrically react with $^{\bullet}$OH to produce its fluorescent derivative (see *Figure 64*). The fluorescence intensity of this derivative correlates with the level of $^{\bullet}$OH radical formation[371]. The preparation of NaTA was carried out by neutralization of 0.8 g of TA with 50 mL of aqueous 0.05 N NaOH solution with constant stirring for 1 h. Then, 8.3 g of NaOH were added to reach 14% by weight concentration and favor the precipitation of the desired product. Under these conditions, the precipitate NaTA was filtered and dried in an oven at 110 ° C for 12 hours.

In order to evaluate the photo-activity of the CNDs and their potential role as broad-spectrum nano-sensitizers, the light-induced formation of hydroxyl groups was systematically evaluated after the selective irradiation of TiO_2 and $CND@TiO_2$ nanohybrids with different LEDs exciting at selected wavelengths from the UV-Vis (white LED) to the visible-NIR ranges (green and red LEDs, respectively), see *Figure 64*. Typically, a thermostatic bath and/or a cooling system Synjet® coupled to LED emitter were also set at 19-22 °C to ensure a homogeneous suspension temperature and discard the influence of water evaporation events caused by local overheating of the solution. After irradiation at different time intervals, the mixture solution was centrifuged to remove the catalyst nanostructures. The fluorescence emission

spectrum of the generated 2-hydroxy disodium terephtalate in the supernatant was subsequently measured at an excitation wavelength of 315 nm.
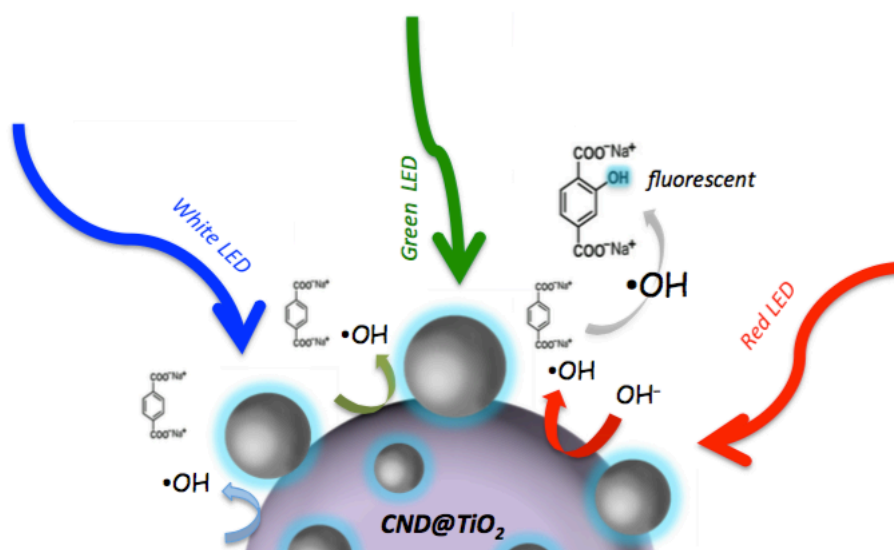
Figure 64. Schematic representation of the LED-induced generation of hydroxyl radicals after selective irradiation with a white LED source (λexc = 450 + 550 nm), a green LED (λexc = 532 nm) and a red LED (λexc = 740 nm). The reaction of the non-fluorescent terephthalic acid probe with hydroxyl OH radicals to yield a fluorescent derivative emitting at 425 nm is shown.

III.6.2 Degradation of reaction intermediates by Gas Chromatography coupled to Mass Spectrometry (GC-MS)

The organic pesticides are the most widespread persistent organic pollutants used in agriculture worldwide. These pollutants are able to move in the environment and in low concentrations over a long period of time, but through bioaccumulation they can have hazardous effects on the biota of the region. Therefore, the persistent chlorinated organic compound, as 2,4-Dichlorophenol (2,4-DCP), is present in numerous pesticides formulation. The use of photocatalytic technologies which use sunlight and photocatalysts to break down potentially harmful organic molecules into simple molecules and non-toxic. So, it is important to study the mechanism of degradation of the organic molecule, to establish which intermediates are obtained.

During CND@TiO$_2$ nanohybrids photocatalytic process to degradation of 2,4-DCP, different intermediates are generated (***Article 5***). First, aliquots of the photocatalytic process were taken at different times. Then, it were centrifuged to remove the catalyst, and the supernatant that contained the intermediates of the degradation of

119

2,4-DCP. This solution was air dried and redissolved 600 xx µL methanol (MeOH) prior to Gas Chromatography coupled to Mass Spectrometry (GC-MS).

The GC-MS instrument (GC-MS Shimadzu QP-2010SE) used for the analysis of reaction intermediates was equipped with a Zebron capillary GC column (30 m x 250 µm, 0.25 µm). A NIST/EPA/NIH mass spectral library (NIST14) was used for identification of m/z values. Helium (purity>99.999%) was used as a carrier gas with a flow rate of 1.0 mL min^{-1}, and a 1 µL sample was injected at a split mode. According to previous reports, the temperature of injection was set to 300°C. The column temperature was first kept at 60°C for 2 min, and raised up to a final temperature of 280°C at a rate of 10°C min^{-1}. The detector was a quadrupole mass spectrometer and the temperatures of the ion source and interface were 200 and 250°C, respectively.

III.7 Peroxidase-like processes enabled by photoactivity of Carbon Nanodots and Si-based luminescent centers in mesoporous silica nanorods

Enzyme peroxidase belongs to the family of oxidoreductases that play a critical role in different metabolic activities in living organisms. Typically, the catalytic reaction of peroxidases involves the oxidation of an electron-donor substrate with the simultaneous reduction of H_2O_2 or occasionally alkyl hydroperoxide (see *Figure 65-a*). Horseradish peroxidase (HRP) containing the iron protoporphyrin IX cofactor (commonly referred to as the heme group)[372] is process the most abundant peroxidase isoenzyme, which functions like a ping-pong ball, bouncing back and forth from an intermediate state (E*) to its ground state (E). Consequently, one substrate (A) converts to the product (C) and releases before the second substrate (B) binds to the enzyme. The overall process of this double displacement reaction is highlighted in *Figure 65-b*.

The peroxidase-like activity of a desired material can be evaluated by measuring the concentration of H_2O_2 using a vaiety of chromogenic substrates. In general, the peroxidase-catalyzed oxidation of TMB + H_2O_2 system involves H_2O_2 using a variety of chromogenic substrates such as hydroquinone, 1,2,3-trihydroxybenzene (THB) or pyrrogallol, o-phenylenediamine (OPD), 2,2′-azino-bis-(3-ethylbenzothiozoline-6-sulfonic) acid (ABTS), and 3,3′,5,5′-tetramethylbenzidine (TMB).

However, owing to the low carcinogenicity and high absorption coefficient of its reaction products, TMB serves as the most-studied chromogen for HRP mimics[331], in acidic and neutral conditions. In general, the peroxidase-catalyzed oxidation of TMB + H_2O_2 system involves two electron transfer steps. In the first step, a one electron oxidation generates a TMB radical cation. Two of these intermediate radical cations then form a blue-colored charge-transfer complex (λ = 370 & 652 nm), a diagnostic for HRP mimic, as shown in *Figure 65-c*. The cation radical (under mild acidification) is further oxidized in the second electron transfer step, producing diimine derivative of TMB (TMBDI: λ = 450nm). This explains the presence of three absorption bands in the TMB oxidized byproduct.

a

$$AH_2 \; + \; H_2O_2 \xrightarrow{\text{Peroxidases}} A \; + \; 2H_2O$$

$$AH_2 \; + \; ROOH \xrightarrow{\text{Peroxidases}} A \; + \; ROH \; + \; 2H_2O$$

b

$$E \xrightarrow{A} EA \rightleftharpoons E^*C \xrightarrow{C} E^* \xrightarrow{B} E^*B \rightleftharpoons ED \xrightarrow{D} E$$

c
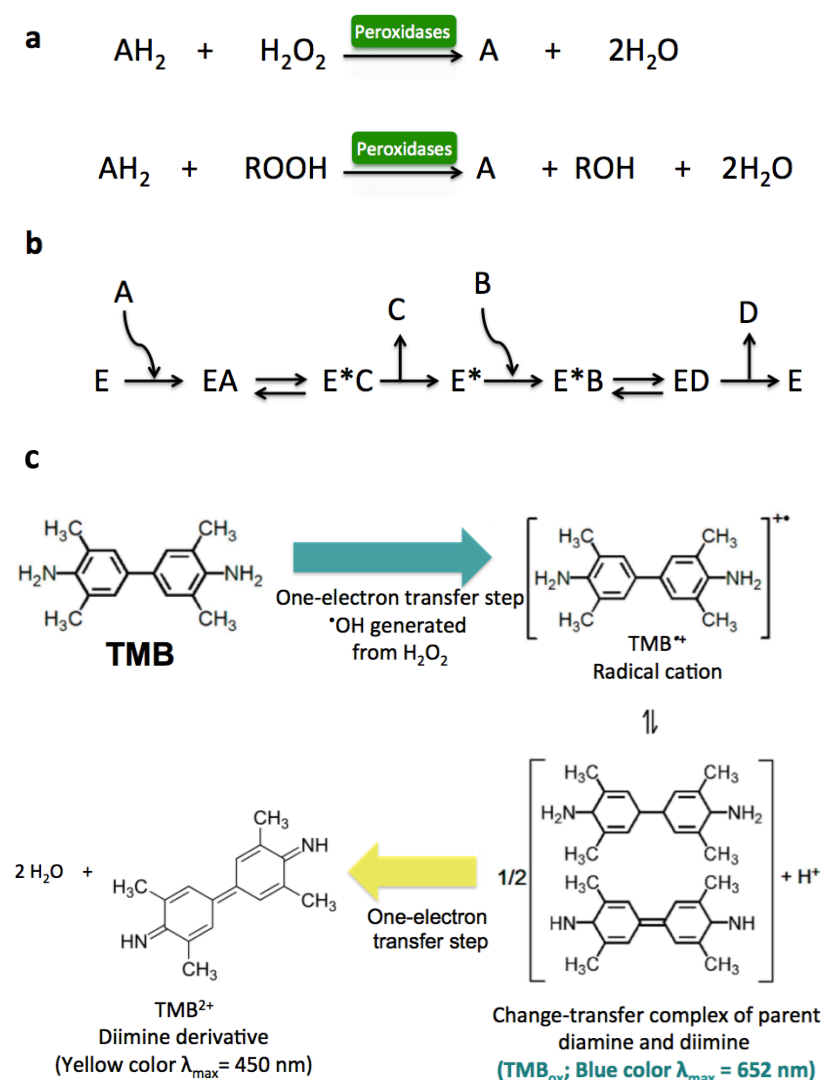
Figure 65. (a) Representative reactions catalyzed by Peroxidases; Schematic for: (b) ping-pong mechanism; and (c) Peroxidase-catalyzed two electron oxidation of TMB into TMB-Diimine.

121

The peroxidase enzymatic assays using TMB have been thoroughly explained in **Article 7**. Typically, the experiments were carried out at room temperature in MW24 cell culture plates and upon irradiation with a blue LED (λ_{exc} = 405 nm), see Figure *66-a*.
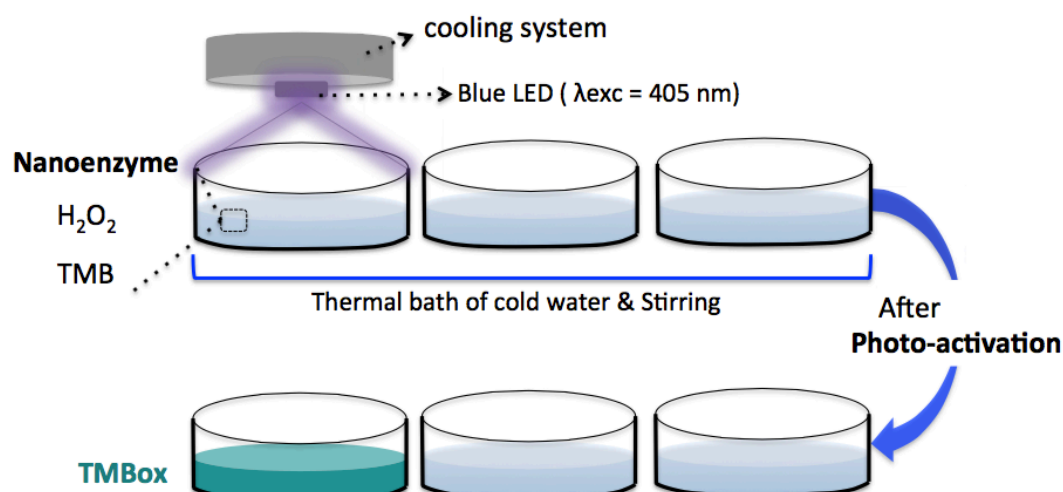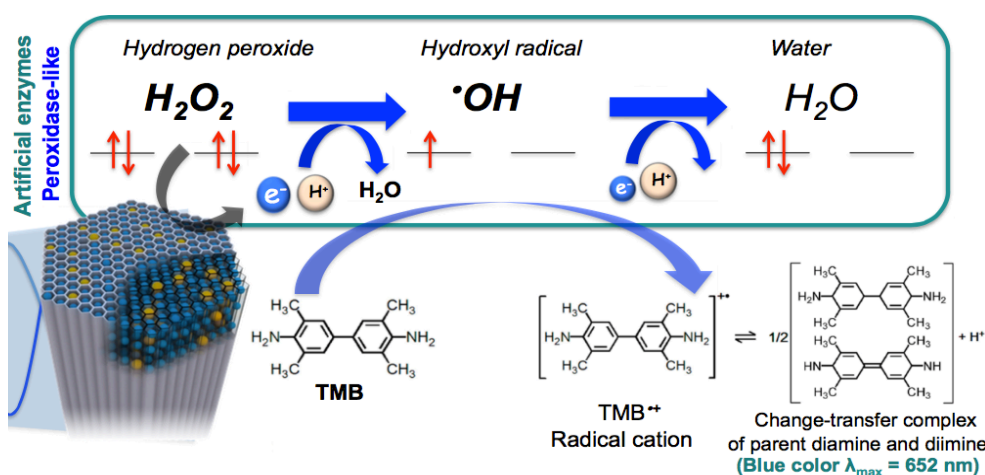
Figure 66. Scheme of: (a) experimental setup for peroxidase enzymatic assays using TMB performed in MW24 cell culture plates; and (b) illustration of the photocatalytic mechanism behind the oxidation of TMB likely induced by hydroxyl radicals generated upon the blue LED photoactivation of H_2O_2 in the presence of the different LMSs samples.

The peroxidase-like activity of the as-prepared luminescent mesoporous (LMS) nanostructures (as described in section III.1.3.2) was tested *via* the catalytic oxidation of the peroxidase substrate TMB in the presence of H_2O_2 (see *Figure 66-b*). The reactions were carried out in 2.0 mL of a 0.2 M sodium acetate buffer solution, pH 7.4, containing ~4 µg·mL^{-1} of the catalysts in the presence of 10 mM H_2O_2 and 0.16 mM

TMB as the substrates (8 µL of 40 mM TMB and 200 µL of 100 mM H_2O_2, stock solution, respectively).   The blue solutions appearing along with the reaction proceeding were monitored in time scan mode at 652 nm using a UV-Vis spectroscopy equipment. All the peroxidase enzymatic procedure, includind the control approaches, were performed following the same experimental conditions. At least three assays were carried out for each tested solid and different catalysts batches were tested in order to certify the reproducibility of the photocatalytic effect depending on the synthesized materia.

III.7.1   Determination of the Kinetic parameters in peroxidase-like processes

All kinetic of peroxidase-like assays were carried out at room temperature in 2.0 mL MW24 cell culture plates and irradiation with a blue LED at 405 nm. Unless otherwise stated, a 0.2 M NaAc solution (pH 7.4) was used as the reaction buffer (total volume = 2 mL). The reaction kinetic measurements were carried out in time course mode by monitoring the absorbance variation of 652 nm. The initial experiments were performed with 4 µg·mL^{-1} of LMS nanostructures in the presence of 50 mM H_2O_2 and using TMB as the substrate. Additional experiments varying TMB and H_2O_2 concentrations were tuned to 0.01-0.02-0.05-0.08-0.10-0-12 mM and 10-20-30-50-100-300 mM, respectively. After the addition of LMS catalyst to the substrates (TMB and H_2O_2), the absorbance values (with especial attention to the maximum at 652 nm) were monitored as function of time in 1 minute intervals. These "absorbance *vs* time" plots were then used to obtain the slope at the initial point (Slope$_{Initial}$) of each reaction by conducting the first derivation of each curve using OriginPro 8.0 software. The initial reaction velocity (v) was calculated by Slope$_{Initial}$/($\varepsilon_{TMB-652nm}$ x l), where $\varepsilon_{TMB-652nm}$ is the molar extinction coefficient of TMB at 652 nm, which equals 39000 M^{-1} cm^{-1}[345]. The plots of v against substrate concentrations were fitted using nonlinear regression of the Michaelis-Menten equation[341]. The apparent kinetic parameters were calculated based on the Michaelis-Menten equation (see equation 3) using the Lineweaver-Burk plot:

$$1/v = K_m/V_{max} \ (1/[S] + 1/K_m) \qquad\qquad (eqn. 3)$$

where Vmax represents the maximal reaction velocity, [S] is the concentration of substrate, and K_m is the Michaelis constant. Parameters K_m and V_{max} were obtained from the double reciprocal plot.

III.7.2 Determination to mechanism of peroxidase enzymatic assays

The peroxidase-mimicking activity of the LMS nanostructures was initially determined from their catalytic ability to decompose H_2O_2 into $^{\bullet}OH$ radicals. A fluorimetric method to detect the interaction of these $^{\bullet}OH$ radicals with terephtalic acid (TA)[250] was selected and optimized (see *Figure 67*). It is important to note that basic pH conditions (7-9) are first required to promote the stabilization of disodium terephthalate (NaTA), for more detail see section III.6.1. NaTA is a non-fluorescent molecule that may stoichiometrically react with $^{\bullet}OH$ to produce its fluorescent derivative (see *Figure 68*). For detecting $^{\bullet}OH$, as-prepared LMS (0.004 mg mL^{-1}) was redispersed in the probe NaTA solution (2 mL, 5 mM). After irradiation (typically 5 minutes) with a blue-emitting LED at 405 nm, the mixture suspension was centrifuged to remove the solid nanocatalysts. The fluorescence emission spectrum of the generated 2-hydroxy disodium terephtalate in the supernatant was subsequently monitored under the excitation wavelength of 315 nm.
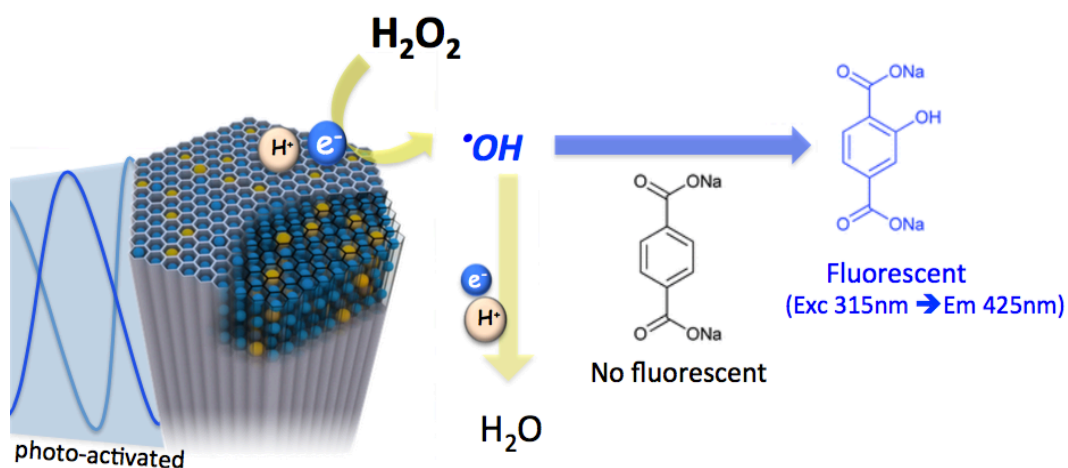
Figure 67. Schematic illustration of the colorimetric assay performed to identify the presence of hydroxyl radicals using disodium terephthalate (NaTA) with LMS nanostructures as catalyst: The reaction occurs between hydroxyl radicals generated *in situ* in the presence of the LMS catalysts under blue-LED irradiation and the NaTA molecule that forms a selectively hydroxylated fluorescent derivative.

III.8 Experiment to evaluate metal ion nanosensor applications of freestanding Carbon Nanodots

III.8.1 Quenching and interference experiments for detection of copper

The quenching by copper ions (Cu^{2+}) was initially described using the Stern-Volmer formalism (see *equation 4*), where I_0 represents the PL intensity of the CNDs in the absence of Cu^{2+}; I corresponds the PL intensity observed in the presence of Cu^{2+} and K_{S-V} is the Stern-Volmer constant[373], (**Article 1**).

$$I_0/I = 1 + K_{S-V}[Cu^{2+}] \qquad \text{(eqn. 4)}$$

Although a linear dynamic response could be determined for copper (II) concentrations between 0.1-10 µM, the existence of a downward curvature suggests that all the surface of the CNDs are not equally accessible to the quenchers or an uneven functional group distribution. Therefore, a modified Stern-Volmer model (*equation 5*) was used to assess whether only a fraction of Cu^{2+} was being quenched.

$$I_0/\Delta I = 1/(f_a K_a [Cu^{2+}]) + 1/f_a \qquad \text{(eqn. 5)}$$

Where $\Delta I = (I_0 - I)$, f_a is the fraction of initial fluorescence that is accessible to the quencher and K_a is the Stern-Volmer quenching constant of the accessible fraction. For the quenching experiments, CNDs solutions were incubated for 15 minutes with different targeted concentrations of ions ranging from 1×10^{-9} to 1×10^{-4} M. Fe^{3+}, Hg^{2+}, Pb^{2+}, Cd^{2+}, Ag^+ and Zn^{2+} ions were checked individually in the same concentration ranges and as crossed-interferences in the presence of Cu^{2+} at equimolar concentrations of 1 and 10 µM. The PL intensity of samples was systematically evaluated under excitation at 400 nm and 740 nm.

III.9 Experiments to evaluate bio-applications of freestanding Carbon Nanodots

III.9.1 Cell culture

Here, we have used four types of cell lines. The tumoral cell lines U251MG and HeLa cells, and the somatic cell lines (human dermal fibroblast and HaCat keratinocytes) were cultured in Dulbecco's modifies Eagle's medium (DMEM, Gibco) supplemented with 10% fetal bovine serum (FBS, Gibco), 1% penicillin/streptomycin and 1% amphotericin at 37 °C under a 5% CO_2-humidified atmosphere with normoxic conditions. Meanwhile, osteoblasts were cultured in OGM™ medium (Lonza) under the above mentioned culture conditions.

III.9.2 Cell viability assays

The *in vitro* cytotoxicity of freestanding carbon nanodots (**Articles 1 and 3**) was determined by AlamarBlue assay (Invitrogen). Typically, the CNDs solutions used in the assay were obtained by diluting the stock solution in culture cell medium. The final concentration of water in the medium did not cause any osmotic imbalance. Human U251MG glioma cells were culture in Dulbecco's modifies Eagle's medium (DMEM, GIBCO) with 10% fetal bovine serum (FBS, GIBCO), 1% penicillin/streptomycin and 1% amphotericin overnight. Then, cells were seeded into 96-well culture plate at a concentration of 7 x 10^3 cells per well in 100 µL of the above medium. After incubation at 37 ^{o}C in a 5% CO_2-humidified incubator for 24 h, the medium was changed to 100 µL medium with CNDs (500 to 37.5 µg mL^{-1} (serial dilutions)) and cells were cultured for another 24 h in contact with the different concentrations of CNDs. For studying the citotoxicity we used Alamar-Blue assay. This method is based on the reduction of resazurin to resorufin by mitochondrial oxidoreductases (see *Figure 68*). After the CNDs incubation we removed the medium and washed with PBS. Then, cells were treated with 10% (v/v) of resazurin dye reagent prepared in DMEM medium. The plate was then placed in a 37°C/5% CO_2 incubator for 3 h. After that the plate was read at 530 nm excitation and 590 nm emission wavelengths using a Synergy HT (Biotek) plate reader. Results are represented as percentage of the control (cells without CNDs treatments).
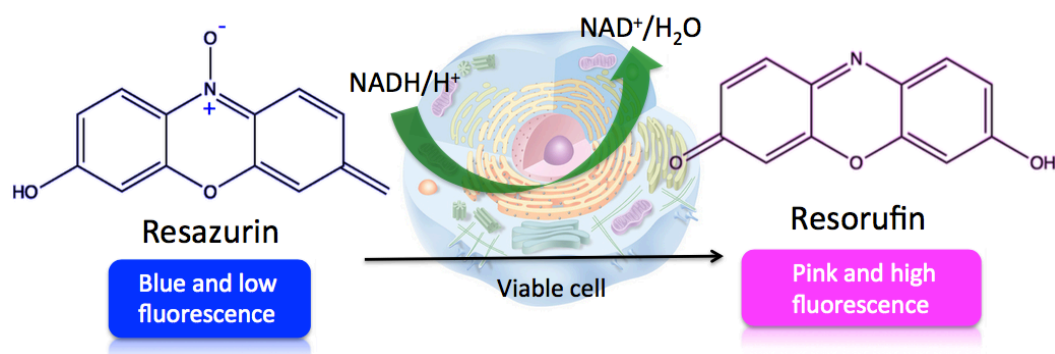
Figure 68. Schematic evaluation of cell healthe by Alamar-Blue cell viability reagent, which functions as a cell health indicator by using the reducing power of living cells to quantitatively measure the proliferation of various human and animal cell lines, bacteria, plant, and fungi allowing you to establish relative cytotoxicity of agents within various chemical classes. When cells are alive they maintain a reducing environment within the cytosol of the cell. Resazurin, the active ingredient of Alamar-Blue reagent, is a non-toxic, cell permeable compound that is blue in color and virtually non-fluorescent. Upon entering cells, resazurin is reduced to resorufin, a compound that is pink in color and highly fluorescent. Viable cells continuously convert resazurin to resorufin, increasing the overall fluorescence and color of the media surrounding cells.

III.9.3   Internalization and confocal microscopy bioimaging in the visible-NIR ranges

The internalization and *in vitro* emission of freestanding CNDs was evaluated as following:

In the *Article 1*, the CNDs solutions used in the assays (20 and 200 µg/mL) were obtained by diluting the stocks solution in culture cell medium. The final concentration of water in the medium did not cause any osmotic imbalance. First, Human U251MG glioma cells were used and cultured as mentioned above. Briefly, cells were subsequently seeded on sterile cover-slips at a density of 50000 cells per well and were incubated during 24 h with CNDs (20 and 200 µg/mL). Subsequently, cells were washed twice with PBS and fixed with 4% paraformaldehyde. The cover-slips were mounted and the samples were observed in an Olympus FV10-i OilType confocal microscopy with a laser excitation source at 488 nm and analysed with the microscopy software. Analogous settings were utilized for both the control experiments (without CNDs) and the treated samples. Likewise, the experiments for the NIR imaging were carried out with the aid of a Leica SP5 HyD multi-photon microscope combining the flexibility of confocal imaging with the deep tissue imaging capability of multiphoton (or two-photon) microscopy. The titanium-sapphire infrared laser was tuned and optimized at 740 nm.

On the other hand, in the **Article 3**, four different cell types was used at two different time points (4 and 24 h) and two nanoparticle concentrations (50 and 400 µg/mL). The CNDs solutions used in the assays were obtained by diluting the stocks in culture cell medium. The final concentration of water in the medium employed did not cause any osmotic imbalance. First, different cells types were cultured as mentioned above. Briefly, cells were seeded on sterile cover-slips at a density of 40000 cells per well and were incubated during 24 h to facilitate substrate adhesion. After that, medium was removed and CNDs solutions were added to cultured cells. At the two time points of interest (4 and 24 h) medium containing CNDs was removed and cells were washed twice with PBS, in order to eliminate non-internalized nanoparticles, and fixed with 4% paraformaldehyde. Subsequently, the cover-slips were mounted and the samples were observed in an Olympus FV10-i OilType confocal microscopy with a laser excitation source at 473 nm and analyzed with the microscopy software. Analogous settings were employed for both the control experiments (without CNDs) and the treated samples.

III.9.4 Experiment setup for Photodynamic Therapy (PDT) with freestanding Carbon Nanodots

The cell death study by generation of Reactive Oxygen Species (ROS) by NIR-activated carbon nanodots was based on cells morphological analysis using double labeling with annexin V and propidium iodide (AV/IP), that allows to divide cells into four populations: live cells (negative for both dyes), necrotic (AV-, IP+), early apoptotic (AV+, IP-) and late apoptotic/necroptotic cells (positive for both dyes). In summary, cells were incubated with the CNDs at the concentrations of 100 and 400 µg/mL and subsequently irradiated with a NIR laser (808 nm, 2 W/cm^2) coupled to fiber collimation (THOLABSS F220SMA-780, 780nm, f=11.07mm) during 10 min. Then, the cell viability was analyzed with an ImageStreamX-Image flow cytometry (Amnis, Seatle, WA). This flow cytometry, has integrated 3 lasers and a microscopy (60x magnification) to simultaneously produce 12 images of each cell directly in flow, at rates exceeding 15.000 cells/min. Enables quantification of cell shape changes, internalization, apoptosis, nuclear translocation, co-localization, cell-cell interactions, etc. In addition, cells without nanoparticles and not irradiated were used as control. Also the effects of

CNDs without laser and laser effect without CNDs incubation were studied. Cytometer results were analyzed using *IDEAS®* software that allows the differentiation between late apoptotic and necroptotic populations through "Contrast_Morphology *vs* Intensity_Threshold" morphocytometric parameters separation.

III.9.5 *In vitro* evaluation by flow cytometry of the production of reactive oxygen species (ROS) by Carbon Nanodots under NIR irradiation

III.9.5.1 *Evaluation of Hydrogen peroxide and Superoxide radical*

The intracellular general ROS production was detected by the oxidation-sensitive fluorescent probe dye. Specifically, hydrogen peroxide production was measured using: (a) Dihydrorhodamine 123 (DHR, Sigma-Aldrich); and (b) superoxide anion formation was studied using Hydroethidine (HE, Sigma-Aldrich). It is important to remark that ROS production measurement was carried out in live cells, which were selected using propidium iodide (0.025 mM, Sigma Aldrich) incubation during 15 min. After that, individual fluorescence cell intensity was analyzed using an ImageStreamX image cytometer (Amnis, Seattle, WA), measuring the emission between 520-617 nm under a 488 nm laser.

Superoxide radical anion ($^{\bullet}O_2^-$) is a free radical formed by single electron donation to oxygen. Like all free radical, it is highly reactive and will dismute rapidly to H_2O_2. Here we propose two selective methods for the detection of these radicals in cells by flow cytometry:

(a) DHR 123 is an uncharged and non-fluorescent ROS indicator that can passively diffuse across membranes where it is oxidized to cationic Rhodamine 123 (HR 123) which localizes in the mitochondria and exhibits green fluorescence (λ_{exc}=505 nm; λ_{em}= 529 nm), see *Figure 69*. The lipophilicity of DHR facilitates its diffusion across cell membranes. Upon oxidation of DHR to the fluorescent RH, one of the two equivalent amino groups tautomerizes into an imino, effectively trapping RH within cells.

129
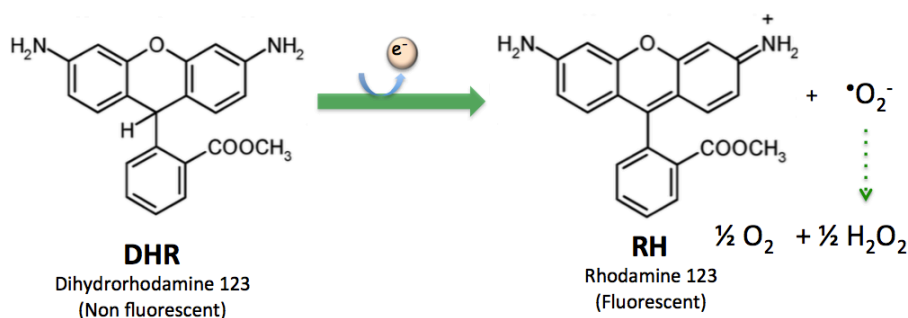
Figure 69. Selective detection in cells of hydrogen peroxide under oxidation of DHR to give fluorescent cationic RH.

(b) HE has been used as a fluorescent probe for detecting $^{\bullet}O_2^-$ due to its reported relative specificity for this ROS. Indeed, HE is the most popular fluorogenic probe used for detecting intracellular these radical. The reaction between superoxide and HE generates a highly specific red fluorescent product, 2-hydroxyethidium (2-OH-E^+). Although there is controversy in this, since it has been discussed about the formation of another red fluorescent porduction, the ethidium (E^+), in biological systems. HE, a two-electron reduction product of ethidium (E^+), was thought to react specifically with the superoxide radical anion ($^{\bullet}O_2^-$) and get oxidized back to E^+. However, recently, Kalyanaraman et al.[374] found that, in a pure superoxide-generating enzymatic system, HE was not oxidized to E^+; rather, a hydroxylated product that has fluorescence characteristics similar to that of E^+ was formed. The structure of the hydroxylated product was determined to be 2-hydroxyethidium (2-OH-E^+), as shown in *Figure 70*.
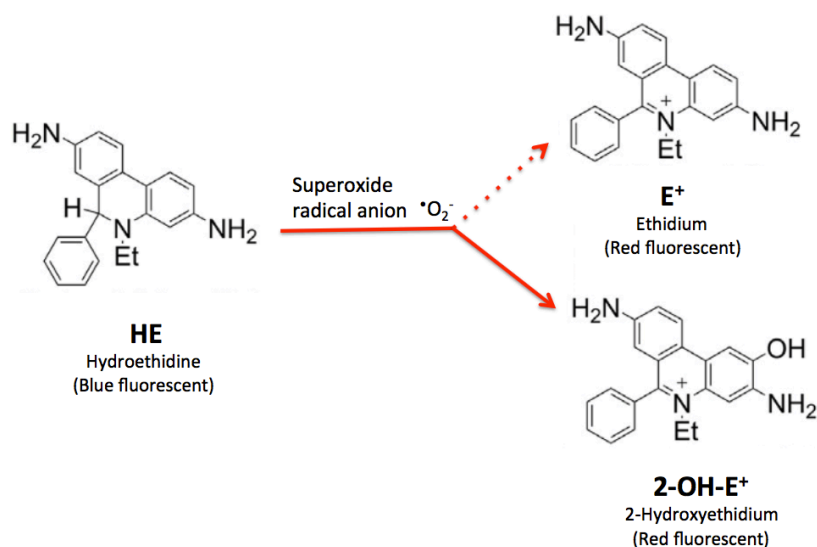
Figure 70. Superoxide radical anion reacts with hydroethidine to produce 2-Hydroxyethidium but not Ethidium.

130

Briefly, U251MG were seeded onto 48-well microplate and incubated with CNDs at two different concentrations (100 and 400 µg/mL) during 24 h. After that, cells were irradiated during 10 min using a NIR laser (808 nm, 2 W/cm^2) coupled to fiber collimation (THOLABSS F220SMA-780, 780nm, f=11.07mm), as shown in *Figure 71*. Subsequently, cells were stained with DHR123 or HE, and cellular fluorescence intensity was analyzed with an ImageStreamX image cytometer, measuring the fluorescence emission at 480-560 nm (DHR) or 595-660 nm (HE) under excitation at 488 nm. Cells without nanoparticles and not irradiated were used as control. Also the effects of CNDs without laser and laser without CNDs incubation were studied.
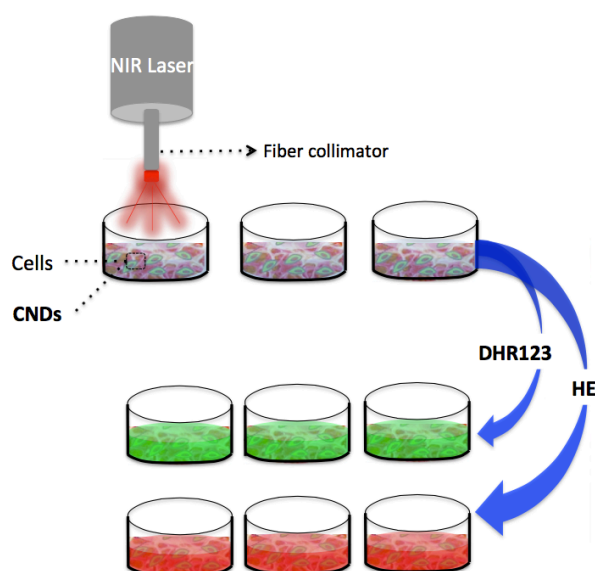
Figure 71. Scheme of experimental setup for evaluation of ROS with DHR 123 or HE in cells using CNDs and a NIR laser in MW48 cell culture plates.

IV.   COMPILATION OF SCIENTIFIC ARTICLES

IV.1 Article 1. Nitrogen-induced transformation of vitamin C into multifunctional up-converting carbon nanodots in the Visible-NIR range

Cover Picture:
J. L. Hueso et al.
Nitrogen-Induced Transformation of Vitamin C into Multifunctional
Up-Converting Carbon Nanodots in the Visible–NIR Range

COVER PICTURE

M. C. Ortega-Liebana,
M. M. Encabo-Berzosa,
M. J. Ruedas-Rama, J. L. Hueso*

■■ – ■■

Nitrogen-Induced Transformation of Vitamin C into Multifunctional Up-Converting Carbon Nanodots in the Visible–NIR Range

CHEMISTRY
A European Journal

www.chemeurj.org

A Journal of
ChemPubSoc
Europe
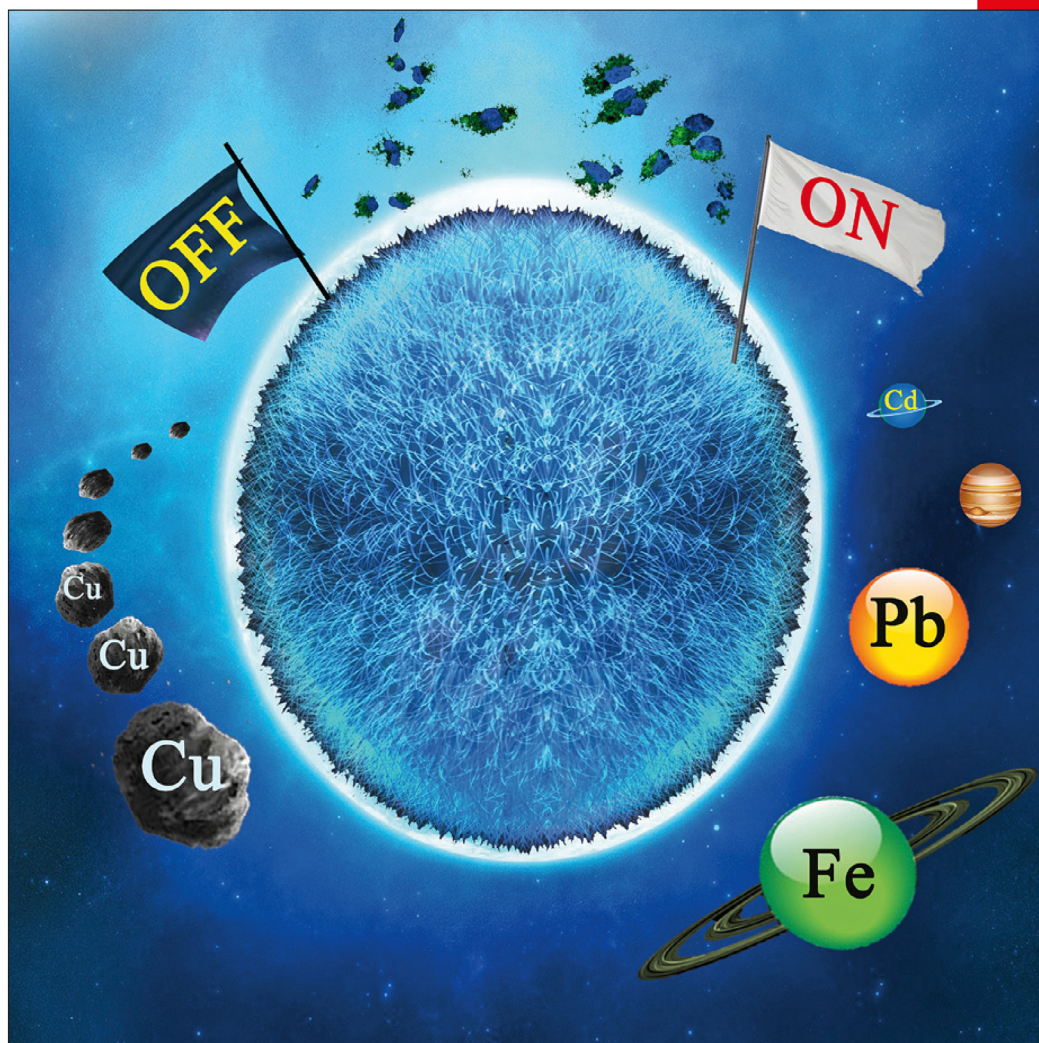
2017–23/00

Cover Picture:
J. L. Hueso et al.
Nitrogen-Induced Transformation of Vitamin C into Multifunctional
Up-Converting Carbon Nanodots in the Visible–NIR Range

Supported by
ACES

WILEY-VCH

Luminescent carbon nanolights derived from ascorbic acid (vitamin C) and N-doped with amine groups offer a selective quenching response towards copper ("ionic asteroids") even in the presence of other interfering "ionic-planet entities". Other interesting properties include their potential use as pH sensors or as biocompatible labels in the visible–NIR range. More information can be found in the Full Paper by J. L. Hueso et al. on page ■■ ff. (DOI: 10.1002/chem.201604216).

■ **Nanomaterials** |*Hot Paper*|

Nitrogen-Induced Transformation of Vitamin C into Multifunctional Up-converting Carbon Nanodots in the Visible–NIR Range

M. Carmen Ortega-Liebana,[a, b] M. Mar Encabo-Berzosa,[a, b] M. Jose Ruedas-Rama,[c] and Jose L. Hueso*[a, b]

Abstract: Water-soluble, biocompatible, and photoluminescent carbon nanodots have been obtained from the rationalized carbonization of vitamin C, a well-known antioxidant molecule in the presence of an amine co-reactant. Herein, we describe the positive influence of N-doping to induce a unique pH-dependent lifetime decay response that would be potentially attractive in biological backgrounds with intrinsic fluorescence fluctuations. In addition, the selectivity and sensitivity of the *N*-containing carbon nanoprobes towards the detection of copper ions at ppm levels is critically enhanced in comparison with the un-doped counterpart, especially in the near-infrared (NIR) range. Finally, the up-converting properties have been also successfully applied to image tumor cells in the visible range and remarkably, in the NIR region in which minimal tissue or water absorption and maximum penetration depth are expected.
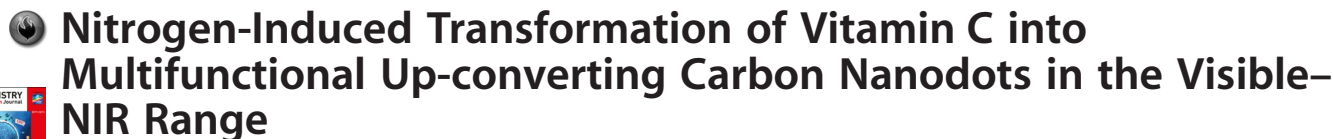
Introduction

Semiconducting quantum dots (QDs) and up-converting rare-earth-based nanoparticles (UCNPs) represent two of the most widespread fluorescent systems successfully developed for sensing and imaging applications.[1,2] Recently, new types of luminescent carbon-based structures including graphene dots, carbon nanotubes (CNTs) or carbogenic nanodots (hereafter CNDs) have emerged as competitive alternatives to overcome the major concerns arising from QDs and UCNPs:[3–13] i) the inherent toxicity of certain components that burdens their biomedical applications; a threat on both biological and environmental levels, ii) the requirement of multiple and tedious steps during synthesis and purification, iii) the requirement of high-boiling solvents and ligand exchange to make them water-soluble or optically active in the near-infrared (NIR) range. In this regard, CNDs exhibit appealing properties such as an inexpensive and abundant variety of potential precursors, high resistance to photo-bleaching, wide emission spectra in the whole UV/Vis–NIR range, good colloidal stability in water and minimal cytotoxicity. Remarkably, certain types of CNDs have also shown up-converting properties to convert longer wavelength radiation from the NIR range into shorter wavelength emitting in the visible range thereby expanding the potential application of these carbogenic dots in bioimaging, sensing, photocatalysis, solar cells and theranostics.[3, 14–29]

Different bottom-up and top-down synthetic approaches have been recently developed and reviewed elsewhere.[30–33] Among them, the hydrothermal carbonization of low-cost raw materials is considered as one of the most simple, straightforward and cost-effective methods to successfully obtain CNDs. Furthermore, the simultaneous or subsequent addition of co-reactants containing N, P or S groups has been identified as a crucial step to provide CNDs with up-converting properties, even though the origin of such optical behavior is not fully understood yet.[5, 34] Nevertheless, there is still room to further explore and optimize the full potential of these nanomaterials and their applications. Herein, we report on the effect of adding ethanolamine (EN) as a co-reactant containing a short chain terminal amine group during the hydrothermal carbonization of vitamin C (ascorbic acid (AA)). Interestingly, we have observed a different and sensitive optical response upon pH variations or as selective probe for copper ion detection in comparison with its un-doped counterpart. Furthermore, the presence of N species has also enabled an up-converting response successfully applied to the direct imaging of cells in the NIR window in which minimal tissue damage or water absorption and maximum penetration depth is expected.[35,36]

[a] M. C. Ortega-Liebana, M. M. Encabo-Berzosa, Dr. J. L. Hueso
Department of Chemical Engineering and Environmental Technology
Institute of Nanoscience of Aragon (INA)
University of Zaragoza, 50018 Zaragoza (Spain)
E-mail: jlhueso@unizar.es

[b] M. C. Ortega-Liebana, M. M. Encabo-Berzosa, Dr. J. L. Hueso
Networking Research Center on Bioengineering
Biomaterials and Nanomedicine (CIBER-BBN), 28029 Madrid (Spain)

[c] Dr. M. J. Ruedas-Rama
Department of Physical Chemistry, Faculty of Pharmacy
University of Granada, 18701 Granada (Spain)

⌨ Supporting information and the ORCID identification number(s) for the author(s) of this article can be found under http://dx.doi.org/10.1002/chem.201604216.

Results and Discussion

Synthesis and morpho-chemical characterization of the CNDs

The hydrothermal synthesis of the CNDs is summarized in the Scheme 1 and further detailed in the Experimental Section. A first synthesis of CNDs was carried out in the absence of the amine precursor (hereafter labelled as CND, see Scheme 1) to clearly establish the influence of adding N species during the carbonization of AA (hereafter denoted as *N*-CNDs, Scheme 1).
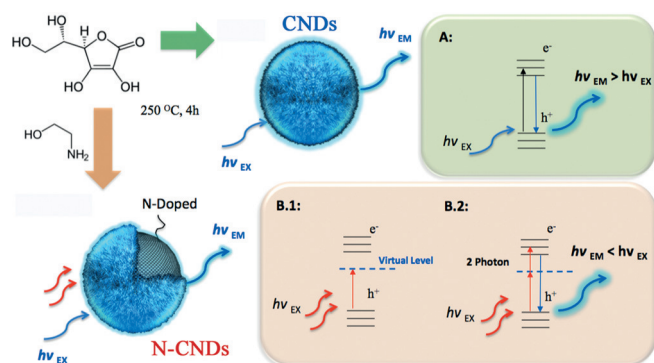
Scheme 1. Hydrothermal carbonization of ascorbic acid at 250 °C in the absence and the presence of ethanolamine to obtain un-doped (CNDs) and *N*-modified carbon nanodots (*N*-CNDs). The colored charts (right) display the down-conversion and up-conversion mechanisms for each type of luminescent carbon dot.

Typically, an aqueous solution containing 10 mL of a 1 M solution of the organic precursor (AA or EN/AA 3:1 molar ratio) was mixed and magnetically stirred in a beaker for 10 minutes and then transferred into a Teflon-lined stainless-steel autoclave that was heated at 250 °C for 4 hours. Figure 1 a/b shows the morphologies and particle size distributions obtained by transmission electron microscopy (TEM) after purification (see Experimental Section). The CNDs retrieved from the hydrothermal carbonization of AA exhibited a quite homogeneous size distribution of 5.6 ± 1.1 nm (see Figure S1, Supporting Information) whereas the *N*-CNDs rendered smaller mean diameters of 3.3 ± 1.7 nm (see Figure S2, Supporting Information).

The evaluation of the surface chemistry carried out by XPS showed an enrichment of nitrogen-containing groups in the *N*-CNDs with two main contributions centred at around 399 and 401 eV, respectively (Figure 1 d). The former contributions have been previously assigned to N species present in terminal and bridge positions of carbon networks (-C-N-H/-C-N-C).[37] Likewise, the latter contribution is attributable to pyrrol-type rings (N_5) or alternatively to the presence of protonated primary amines (-NH_3^+).[38] These *N*-species accounted for up to 6% of the atomic composition at the surface level in comparison with the undoped CNDs (Figure 1 d). The O1s region revealed an increment of the fraction of oxygen species bonded to carbon species with sp^3 configuration (typically aliphatic) at around 531 eV.[37] Finally, the evaluation of the C1s regions (Fig-
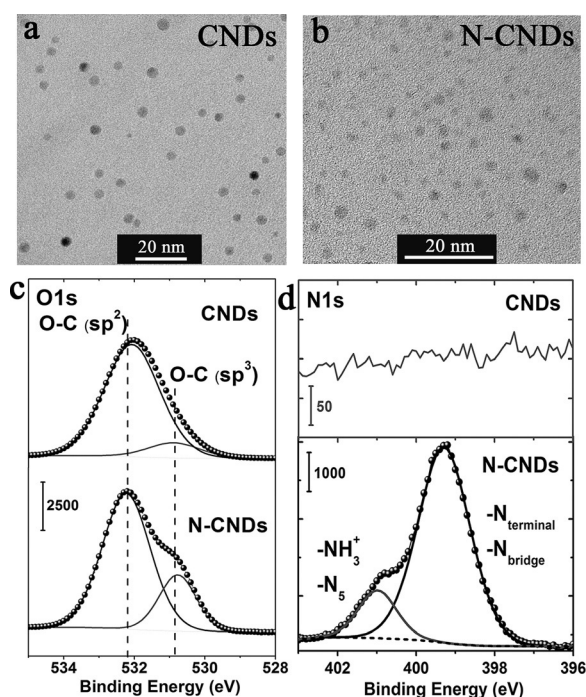
Figure 1. a) TEM image of the un-doped carbon dots synthesized with ascorbic acid. b) TEM image of the N-doped carbon dots modified with ethanolamine. c) XP spectra and fittings corresponding to the O1s region for both doped and un-doped CNDs. d) XP spectra and fittings corresponding to the N1s region for both CNDs.

ures S3 and S4, Supporting Information) and additional FT-IR spectroscopic analyses (Figure S5, Supporting Information) confirmed the presence of multiple C=O, C—O and C—OH surface groups. Interestingly, the absence of amide bond signatures also corroborated that N is predominantly present in the *N*-CNDs as dopant or as terminal amine group. The role of amine precursors with shorter alkyl chains as N-doping inducer has been also claimed in previous works.[39]

Optical properties of the CNDs: up-conversion and pH-dependent lifetime decays

Figures 2 a/b show the wavelength-dependent photo-luminescent (PL) response of both carbon nanoparticles. A tunable PL emission downshifting from blue to green has been observed at longer excitation wavelengths and correspond to the expected behavior of a semiconducting quantum dot (see Scheme 1, chart A). This down-conversion has been more accused in the un-doped CNDs thereby accounting for a narrower and more homogeneous size and composition distribution with predominant response in the UV region and quantum yields (QYs) of 12% using quinine sulfate as reference (see Experimental Section). Remarkably, the *N*-CNDs exhibited up-conversion capabilities after the excitation in the NIR range (Figure 2 b) and slightly higher QY values of 15%. In contrast, minimal or negligible PL response was detected in the 500–700 nm range in which absorption events to induce down- or up-conversion were minimized for both samples. Although the underlying mechanism has not been fully understood yet, it has
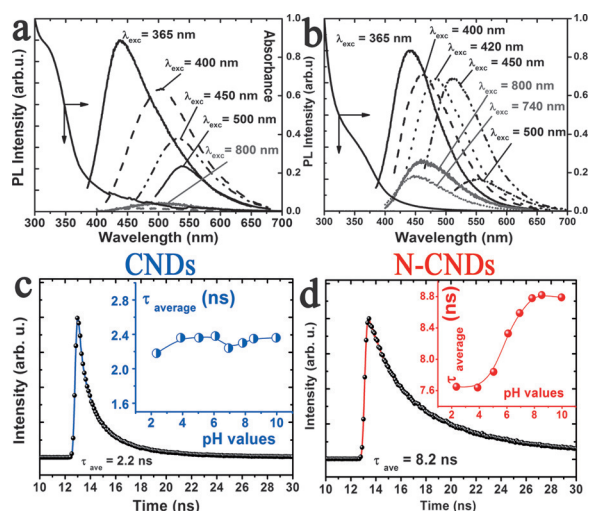
Figure 2. a) UV/Vis absorbance spectrum and wavelength-dependent photoluminescence emission spectra of the un-doped CNDs. b) UV/Vis absorbance and wavelength-dependent photoluminescence emission spectra of the N-CNDs displaying both down and up-conversion. c) Time-resolved fluorescence-decay curve of the un-doped CNDs exciting at 470 nm (inset: evolution of the average lifetimes at different pH values). d) Time-resolved fluorescence-decay curve of the N-CNDs exciting at 470 nm (inset: pH-dependent evolution of the average lifetime).

been claimed that N atoms can provide additional energy levels to accommodate intermediate electronic transitions upon excitation with longer wavelength photons and favor the absorption of a second photon prior to the radiative recombination decay and facilitate the final emission of a single photon at shorter wavelengths (Figure 2b and Scheme 1, Chart B).

Another important effect of the addition of ethanolamine as co-reactant was observed in the variation of the time-resolved PL emission decays (Figures 2c/d). These PL decays are correlated with the radiative and non-radiative pathways that an exciton undergoes to achieve electron-hole recombination and can be modified by changes on the surface environment.[1,40] The N-CNDs exhibited longer average PL lifetimes of 8.23 ± 0.06 ns in comparison with the PL lifetime averages of 2.24 ± 0.01 ns of the un-doped nanoparticles. A sum of three-exponential functions was required to adjust the PL decay traces (see also Experimental Section). The shortest fitting components have been previously attributed to intrinsic recombination of populated core states whilst the longer (slower) fitting components have been usually attributed to surface defects that give rise to trap and surface states. The major contribution of these latter components in the N-CNDs account for the induced variation at their surface composition as also suggested from XPS analysis (Figure 1). After the exponential fitting analyses of the PL decays, the intensity-weighted average lifetime (τ_{ave}) were calculated at different pH values (see Tables S1 and S2, Supporting Information). Interestingly, the calculated τ_{ave} of the N-CNDs showed a dependency on the pH value of the media, decreasing from 8.8 ns at alkaline conditions (pH > 8) to 7.6 ns when the pH was set below 4.5 (see inset in Figure 2d). A linear response was identified in the pH range 4.5–8.0, at

which a great potential application for pH determination in biological samples such as endosomes (pH 5–6.5) or some tumour cells (pH 6.4–6.9) can be envisioned.[1,40]

Although this linear range is similar to other pH-related nanosensors,[1] the measurements based on average lifetimes offer several advantages in comparison with fluorescent-based analyses, especially in terms of the acquisition of a reliable and unique signal regardless of the CNDs local concentration changes and the fluctuations associated to the intrinsic background fluorescence typically observed in biological samples. This fact minimizes the requirement of ratiometric nanoprobes[24] or multi-channel/multi-color detection systems[40] and provides the N-CNDs with a remarkable potential for pH sensing applications.[24]

Selective detection of copper ions in the visible-NIR range

The carbon dots were also systematically investigated as potential nanoprobes for the detection of ions and the presence of the amine co-reactant rendered an enhanced selective response towards the presence of copper ions (Figures 3a/b) in
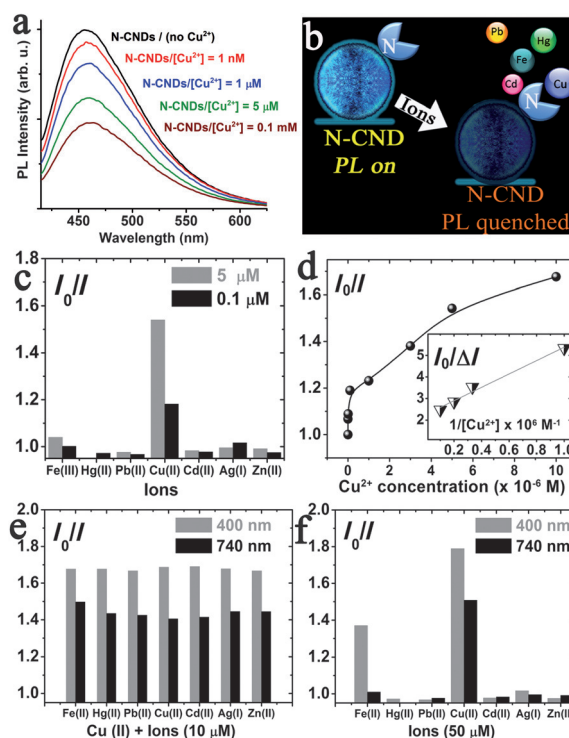
Figure 3. a) Photoluminescence spectra of N-CNDs in the presence of different concentrations of Cu^{2+} ($\lambda_{exc} = 400$ nm) in aqueous media. b) Scheme of the PL quenching effect induced by the presence of copper ions. c) Selectivity of the N-CNDs for Cu^{2+} in comparison with other tested ionic species ($\lambda_{exc} = 400$ nm). d) Collisional quenching of the PL intensity of the CNDs by Cu^{2+} using the Stern–Volmer formalism and its modified approximation considering a fractional accessibility of quenchers (inset). e) PL response of the N-CNDs in the presence of Cu^{2+} and a second interference ion (equimolar concentrations of 10 μM). Excitation wavelengths selected at 400 nm and 740 nm, respectively. f) Evaluation of the preferential interference of Fe-II ions at concentrations higher than 30 μM and how the inner filter effect can be dramatically diminished upon excitation at 740 nm, taking advantage of the up-converting capabilities of the N-CNDs.

comparison with the un-doped CNDs. The N-CNDs showed a selective quenching efficiency in the presence of Cu^{2+} whereas the other selected ionic species did not cause any significant change in the fluorescence intensity of the N-CNDs for the evaluated concentrations (up to 10^{-4} M) (Figure 3c). Only the presence of Fe^{3+} ions caused certain optical changes or interference at concentration levels higher than 3×10^{-5} M when using an excitation wavelength of 400 nm (Figures 3e/f). This influence has been previously attributed to inner filter effects[41] caused by its strong absorption in that wavelength range and in the case of our up-converting N-CNDs could be minimized after selecting an excitation wavelength of 740 nm (Figure 3f).[3] The quenching mechanism was described by the Stern–Volmer formalism and a modified approximation accounting for a fractional accessibility of the quenchers[42] (Figure 3d and Experimental Section). A linear response range towards the Cu^{2+} detection was determined between 0.1–10 μM (Figure 3d) with a limit of detection of 0.1 μM and a 44% of accessible fraction to quenchers (see Experimental Section). This response as selective nanoprobe for copper ions fits within the range of previously reported fluorescent nanoparticles[3,18,41,43,44] and meets the detection limit criteria established by the environmental protection agency (EPA) as a priority pollutant.[2,3,43,44]

Evaluation as biocompatible cell biomarkers in the visible-NIR range

Finally, taking into account the greater biocompatibility of carbon nanodots in comparison with other nanostructured semiconductors containing heavy metals, the N-CNDs were also successfully evaluated as fluorescent biomarkers of U251MG glioma cells both under visible and near-infrared excitation sources (Figure 4 and Supporting Information Figure S6). The N-CNDs exhibited good cell permeability, minimal cytotoxicity at concentration levels below 0.5 mg mL^{-1} (Figure S7, Supporting Information) and a remarkable fluorescent signal upon multiphoton excitation at 740 nm thereby corroborating the up-converting response of the N-CNDs and opening an impor-
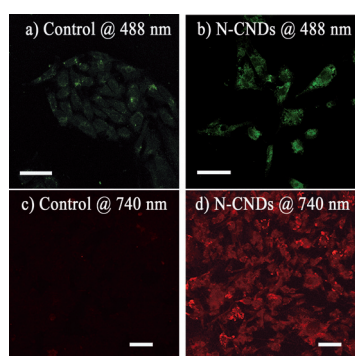
Figure 4. Confocal fluorescence imaging of human U251MG glioma cells: a) Control without carbon dots and b) after 24 h incubation with N-CNDs (0.02 mg mL^{-1}) and exciting at 488 nm. c) Control and d) after 24 h incubation with N-CNDs (0.2 mg mL^{-1}) and multi-photon excitation at 740 nm. All the scale bars correspond to 50 μm.

tant synthetic alternative to expensive and less stable NIR dyes and the potential capability to monitor multiple cell processes and induce therapeutic treatments with minimal tissue damages and maximum penetration depth.

Conclusion

In this study, we have shown a simple and cost-effective hydrothermal assisted method to induce the transformation of vitamin C (ascorbic acid) into multifunctional carbon nanodots with different and appealing optical properties such as expanded photoluminescence in the visible-NIR range (down and up-conversion behavior) for cell bioimaging, pH dependent lifetime decay response or enhanced selectivity towards the detection of copper ions, even in the presence of highly interfering ion counterparts such as iron that can be selectively minimized in the NIR detection range. Furthermore, the crucial influence of ethanolamine in the N-doping process of the carbon dots to enhance these properties is clearly demonstrated.

Experimental Section

Materials

L-Ascorbic acid (AA), ethanolamine (EN), lead (II) nitrate (Pb(NO$_3$)$_2$), cadmium nitrate tetrahydrate (Cd(NO$_3$)$_2$·4H$_2$O), iron (III) sulfate monohydrate (Fe$_2$(SO$_4$)$_3$), silver nitrate (AgNO$_3$), zinc sulfate heptahydrate (ZnSO$_4$·7H$_2$O), mercury (II) chloride (HgCl$_2$) and copper (II) sulfate (CuSO$_4$) were obtained from Sigma–Aldrich. All chemicals were of analytical purity grade. 10 KDa molecular weight cut off (MWCO) membranes (Amicon Ultra-15, Millipore) were also obtained from Sigma–Aldrich.

Synthesis and purification of carbon dots

To synthesize the un-doped carbon nanodots, 1 M solution of L-ascorbic acid, as the carbon source, and 10 mL triple distilled water were mixed in a beaker with a magnetic blender, the solution was then transferred into a 25 mL Teflon-lined stainless-steel autoclave and was heated at a constant temperature of 250 °C for 4 hours. The resulting solution was cooled at room temperature and was centrifuged at 6000 rpm for 10 min to remove agglomerated particles. The supernatant containing carbon nanomaterials was filtered through a 0.10 μm PTFE membrane (WhatmanTH) membrane to further remove large particles. The brownish yellow supernatant was then dialyzed against ultrapure water through a dialysis membrane for 5 h. An analogous procedure was carried out to synthesize the N-doped carbon nanodots but replacing the initial 1 M solution of L-ascorbic acid by a solution containing a 3:1 molar ratio (ethanolamine:ascorbic acid). These synthesis conditions correspond to the minimum reaction times and temperatures at which both CNDs and N-CNDs were obtained. Lower T or times failed to retrieve homogeneous and reproducible luminescent nanocarbons with the desired optical response. Higher ENconcentrations did not render a successful generation of carbogenic dots.

Characterization techniques

The morphologies and particle size distributions were determined by transmission electron microscopy (TEM) (FEI Tecnai T20 and F30,

operated at 200–300 kV, respectively). To prepare the samples, the nanoparticle suspensions were diluted with water prior to casting on a holey carbon TEM grid. The functionalization of the CNDs surface was analyzed by Fourier transform infrared (FTIR) spectroscopy (Bruker Vertex 70 FTIR spectrometer) and X-ray photoelectron spectroscopy (XPS) with an Axis Ultra DLD (Kratos Tech.). A monochromatic Al κα source (1486.6 eV) was employed with multiple runs at 12 kV, 10 mA and pass energy of 20 eV was used. The binding energies were calibrated to the internal C1s (284.2 eV) standard. Analyses of the peaks were performed with CasaXPS software, using a weighted sum of Lorentzian and Gaussian component curves after Shirley background subtraction. Steady-state fluorescence emission spectra were collected on a JASCO FP-6500 spectrofluorometer equipped with a 450 W xenon lamp for excitation, with temperature controller ETC-273T at 25 °C, using 5×10 mm cuvettes and a LS55 Fluorescence Spectrometer (PerkinElmer) equipped with a xenon arc lamp as the light source and a quartz cell (10×10 mm). The excitation wavelengths used in the experiments to record the emission spectra were 400 and 740 nm. Both excitation and emission slits were 3 nm. Fluorescence decay traces of the different CNDs were recorded in the Time Correlated Single Photon Counting (TCSPC) mode using the FluoTime 200 fluorometer (PicoQuant, GmbH). Briefly, the samples were excited by a 405 nm Picosecond Pulsed Diode Laser (Edinburgh EPL405) with a 10 MHz repetition rate. The full width at half maximum of the laser pulse was around 90 ps. The fluorescence was collected after crossing through a polarizer set at the magic angle, and a 2 nm bandwidth monochromator. Fluorescence decay histograms were collected using a TimeHarp200 board, with a time increment per channel of 36 ps, at the emission wavelengths of 450, 460, and 470 nm. The histograms of the instrument response function (IRF) was determined using LUDOX scatterer, and sample decays were recorded until they typically reached 2×10^4 counts in the peak channel, since it is well known that complex decays can be well described by the simplest exponential models if the fitting is carried out from experimental data with a low number of CPC.

Quantum yield calculations

The fluorescence quantum yields Φ of the different CNDs in aqueous solution were computed according to Eqn. 1.[45]

$$\Phi_S = \Phi_R \times F_S \times \left(1 - 10^{-A_R(\lambda_{exc})}\right) \times n_S^2 / F_R \times \left(1 - 10^{-A_S(\lambda_{exc})}\right) \times n_R^2 \tag{1}$$

The subscript S refers to the CND samples, R stands for the selected reference fluorophore (quinine sulfate, 0.1 M H_2SO_4) with known quantum yield (0.54), F stands for the corrected, integrated fluorescence spectra, $A(\lambda_{exc})$ denotes the absorbance at the used excitation wavelength λ_{exc}, and n represents the refractive index of the solvent. To minimize inner filter effects, the absorbance at the excitation wavelength λ_{exc} was kept under 0.1. The measurements were performed using 10 mm optical path length cuvettes under right-angle (L-) arrangement and "magic angle" conditions. The averages and standard uncertainties of Φ are computed from independent Φ measurements (2 conc. of sample×2 conc. of reference×2 excitation wavelengths λ_{exc}).

Time-resolved photoluminescence decays at different pH values

Time resolved photoluminescence decay traces were fitted using FluoFit 4.4 package (Picoquant GmbH). In all cases, PL decay traces

were recorded at 450, 460 and 470 nm emission wavelengths, and the three decay traces were fitted globally with the decay times linked as shared parameters, whereas the pre-exponential factors were local adjustable parameters. The experimental decay traces were fitted to multi-exponential functions via a Levenberg–Marquard algorithm-based nonlinear least-squares error minimization deconvolution method. In all cases, three different exponential terms were used to fit the experimental decay traces. The quality of fittings was evaluated by the reduced chi-squared method, χ^2, the weighted residuals and the correlation functions. In all cases, the best fits of the decay traces required a sum of three exponential decay functions to reach low χ^2 values as well as random distributions of the weighted residuals and auto-correlation function, indicators of the goodness of the fits (Figures S8 and S9 for CND and N-CND respectively, Supporting Information). To compare the emission lifetime of the different CNDs at different concentrations and different pH media it was necessary to determinate their average lifetime using the Eqn. 2[46]:

$$\tau_{ave} = \sum a_i \, \tau_i^2 \Big/ \sum a_i \, \tau_i \tag{2}$$

in which a_i are pre-exponential factors and τ_i the lifetimes obtained in the multi-exponential fitting of the decay curves of CNDs emission.

Quenching and interference experiments for detection of copper

The quenching by Cu^{2+} ions was initially described using the Stern–Volmer formalism (see Eqn. 3), in which I_0 represents the PL intensity of the N-CNDs in the absence of Cu^{2+}; I corresponds the PL intensity observed in the presence of Cu^{2+} and K_{S-V} is the Stern–Volmer constant.

$$I_0/I = 1 + K_{S-V} \, [Cu^{2+}] \tag{3}$$

Although a linear dynamic response could be determined for copper (II) concentrations between 0.1–10 μM, the existence of a downward curvature suggests that all the surface of the CNDs are not equally accessible to the quenchers or an uneven functional group distribution. Therefore, a modified Stern–Volmer model (Eqn. 4) was used to assess whether only a fraction of Cu^{2+} was being quenched[42,46]

$$I_0/\Delta I = 1/(f_a K_a \, [Cu^{2+}]) + 1/f_a \tag{4}$$

in which $\Delta I = (I_0 - I)$, f_a is the fraction of initial fluorescence that is accessible to the quencher and K_a is the Stern–Volmer quenching constant of the accessible fraction. For the quenching experiments, CNDs were incubated for 15 minutes with different targeted concentrations of ions ranging from 1×10^{-9} to 1×10^{-4} M. Fe^{3+}, Hg^{2+}, Pb^{2+}, Cd^{2+}, Ag^+ and Zn^{2+} ions were checked individually in the same concentration ranges and as crossed-interferences in the presence of Cu^{2+} at equimolar concentrations of 1 and 10 μM. The samples were systematically excited at 400 nm and 740 nm.

Cell viability assays

The N-CNDs solutions used in the assay were obtained by diluting the stock solution in culture cell medium. The final concentration of water in the medium did not cause any osmotic imbalance. Human U251MG glioma cells were culture in Dulbecco's modified Eagle's medium (DMEM, GIBCO) with 10% fetal bovine serum (FBS,

GIBCO), 1% penicillin/streptomycin and 1% amphotericin overnight. Then, cells were seeded into 96-well culture plate at a concentration of 7×10^3 cells per well in 100 μL of the above medium. After incubation at 37°C in a 5% CO_2-humidified incubator for 24 h, the medium was changed to 100 μL medium with C-dots (500 to 37.5 μg mL^{-1} (serial dilutions)) and cells were cultured for another 24 h in contact with the different concentrations of N-CNDs. For studying the citotoxicity we used Alamar-Blue assay (Invitrogen). This method is based on the reduction of resazurin to resorufin by mitochondrial oxidoreductases. After the N-CNDs incubation we removed the medium and washed with PBS. Then, cells were treated with 10% (v/v) of resazurin dye reagent prepared in DMEM medium. The plate was then placed in a 37°C/5% CO_2 incubator for 3 h. After that, the plate was read at 530 nm excitation and 590 nm emission wavelengths using a Synergy HT (Biotek) plate reader. Results are represented as percentage of the control (cells without N-CNDs treatments).

Cell cultures and confocal microscopy bioimaging in the visible–NIR ranges

N-CNDs were diluted to 0.5 mg mL^{-1} concentrations for a stock solution. The N-CNDs solutions used in the assays (0.05 and 0.2 mg mL^{-1}) were obtained by diluting the stocks solution in culture cell medium. The final concentration of water in the medium did not cause any osmotic imbalance. Human U251MG glioma cells were cultured in Dulbecco's modifies Eagle's medium (DMEM, GIBCO) with 10% fetal bovine serum (FBS, GIBCO), 1% penicillin/streptomycin and 1% amphotericin overnight. Cells were subsequently seeded on sterile cover-slips at a density of 50000 cells per well and were incubated during 24 h with the N-CNDs (0.05 and 0.2 mg mL^{-1}). Subsequently, cells were washed twice with Phosphate Buffer Solution (PBS) and fixed with 4% paraformaldehyde. The cover-slips were mounted and the samples were observed in an Olympus FV10-i OilType confocal microscopy with a laser excitation source at 488 nm and analysed with the microscopy software. Analogous settings were utilized for both the control experiments (without N-CNDs) and the samples. Likewise, the experiments for the NIR imaging were carried out with the aid of a Leica SP5 HyD multi-photon microscope combining the flexibility of confocal imaging with the deep tissue imaging capability of multiphoton (or two-photon) microscopy. The titanium–sapphire infrared laser was tuned and optimized at 740 nm.

Acknowledgements

[1] M. J. Ruedas-Rama, A. Orte, E. A. H. Hall, J. M. Alvarez-Pez, E. M. Talavera, Chem. Commun. 2011, 47, 2898–2900.

[2] J. Zhang, B. Li, L. M. Zhang, H. Jiang, Chem. Commun. 2012, 48, 4860–4862.

[3] A. Salinas-Castillo, M. Ariza-Avidad, C. Pritz, M. Camprubi-Robles, B. Fernandez, M. J. Ruedas-Rama, A. Megia-Fernandez, A. Lapresta-Fernandez, F. Santoyo-Gonzalez, A. Schrott-Fischer, L. F. Capitan-Vallvey, Chem. Commun. 2013, 49, 1103–1105.

[4] J. H. Shen, Y. H. Zhu, X. L. Yang, C. Z. Li, Chem. Commun. 2012, 48, 3686–3699.

[5] S. J. Zhu, Y. B. Song, X. H. Zhao, J. R. Shao, J. H. Zhang, B. Yang, Nano Res. 2015, 8, 355–381.

[6] P. Roy, P. C. Chen, A. P. Periasamy, Y. N. Chen, H. T. Chang, Mater. Today 2015, 18, 447–458.

[7] S. N. Baker, G. A. Baker, Angew. Chem. Int. Ed. 2010, 49, 6726–6744; Angew. Chem. 2010, 122, 6876–6896.

[8] C. T. Chien, S. S. Li, W. J. Lai, Y. C. Yeh, H. A. Chen, I. S. Chen, L. C. Chen, K. H. Chen, T. Nemoto, S. Isoda, M. W. Chen, T. Fujita, G. Eda, H. Yamaguchi, M. Chhowalla, C. W. Chen, Angew. Chem. Int. Ed. 2012, 51, 6662–6666; Angew. Chem. 2012, 124, 6766–6770.

[9] Y. Q. Dong, H. C. Pang, H. B. Yang, C. X. Guo, J. W. Shao, Y. W. Chi, C. M. Li, T. Yu, Angew. Chem. Int. Ed. 2013, 52, 7800–7804; Angew. Chem. 2013, 125, 7954–7958.

[10] H. P. Liu, T. Ye, C. D. Mao, Angew. Chem. Int. Ed. 2007, 46, 6473–6475; Angew. Chem. 2007, 119, 6593–6595.

[11] K. Lingam, R. Podila, H. J. Qian, S. Serkiz, A. M. Rao, Adv. Funct. Mater. 2013, 23, 5062–5065.

[12] S. Liu, J. Q. Tian, L. Wang, Y. W. Zhang, X. Y. Qin, Y. L. Luo, A. M. Asiri, A. O. Al-Youbi, X. P. Sun, Adv. Mater. 2012, 24, 2037–2041.

[13] H. Tetsuka, R. Asahi, A. Nagoya, K. Okamoto, I. Tajima, R. Ohta, A. Okamoto, Adv. Mater. 2012, 24, 5333–5338.

[14] X. Guo, C. F. Wang, Z. Y. Yu, L. Chen, S. Chen, Chem. Commun. 2012, 48, 2692–2694.

[15] S. Karthik, B. Saha, S. K. Ghosh, N. D. P. Singh, Chem. Commun. 2013, 49, 10471–10473.

[16] C. H. Lee, R. Rajendran, M. S. Jeong, H. Y. Ko, J. Y. Joo, S. Cho, Y. W. Chang, S. Kim, Chem. Commun. 2013, 49, 6543–6545.

[17] D. Y. Pan, J. C. Zhang, Z. Li, C. Wu, X. M. Yan, M. H. Wu, Chem. Commun. 2010, 46, 3681–3683.

[18] Q. Qu, A. W. Zhu, X. L. Shao, G. Y. Shi, Y. Tian, Chem. Commun. 2012, 48, 5473–5475.

[19] J. H. Shen, Y. H. Zhu, C. Chen, X. L. Yang, C. Z. Li, Chem. Commun. 2011, 47, 2580–2582.

[20] W. B. Shi, Q. L. Wang, Y. J. Long, Z. L. Cheng, S. H. Chen, H. Z. Zheng, Y. M. Huang, Chem. Commun. 2011, 47, 6695–6697.

[21] Y. P. Sun, B. Zhou, Y. Lin, W. Wang, K. A. S. Fernando, P. Pathak, M. J. Meziani, B. A. Harruff, X. Wang, H. F. Wang, P. J. G. Luo, H. Yang, M. E. Kose, B. L. Chen, L. M. Veca, S. Y. Xie, J. Am. Chem. Soc. 2006, 128, 7756–7757.

[22] S. T. Yang, L. Cao, P. G. J. Luo, F. S. Lu, X. Wang, H. F. Wang, M. J. Meziani, Y. F. Liu, G. Qi, Y. P. Sun, J. Am. Chem. Soc. 2009, 131, 11308.

[23] S. J. Zhu, S. J. Tang, J. H. Zhang, B. Yang, Chem. Commun. 2012, 48, 4527–4539.

[24] H. Nie, M. J. Li, Q. S. Li, S. J. Liang, Y. Y. Tan, L. Sheng, W. Shi, S. X. A. Zhang, Chem. Mater. 2014, 26, 3104–3112.

[25] M. C. Ortega-Liebana, J. L. Hueso, A. Larrea, V. Sebastian, J. Santamaria, Chem. Commun. 2015, 51, 16625–16628.

[26] F. Wang, Z. Xie, H. Zhang, C. Y. Liu, Y. G. Zhang, Adv. Funct. Mater. 2011, 21, 1027–1031.

[27] L. W. Zhang, H. B. Fu, Y. F. Zhu, Adv. Funct. Mater. 2008, 18, 2180–2189.

[28] B. Kong, A. W. Zhu, C. Q. Ding, X. M. Zhao, B. Li, Y. Tian, Adv. Mater. 2012, 24, 5844–5848.

[29] M. C. Ortega-Liebana, J. L. Hueso, S. Ferdousi, K. L. Yeung, J. Santamaria, Diamond Relat. Mater. 2016, 65, 176–182.

[30] H. T. Li, Z. H. Kang, Y. Liu, S. T. Lee, J. Mater. Chem. 2012, 22, 24230–24253.

[31] P. J. G. Luo, S. Sahu, S. T. Yang, S. K. Sonkar, J. P. Wang, H. F. Wang, G. E. LeCroy, L. Cao, Y. P. Sun, *J. Mater. Chem. B* **2013**, *1*, 2116–2127.

[32] Z. F. Wang, H. D. Zeng, L. Y. Sun, *J. Mater. Chem. C* **2015**, *3*, 1157–1165.

[33] Y. B. Song, S. J. Zhu, B. Yang, *RSC Adv.* **2014**, *4*, 27184–27200.

[34] W. P. Wang, Y. C. Lu, H. Huang, A. J. Wang, J. R. Chen, J. J. Feng, *Biosens. Bioelectron.* **2015**, *64*, 517–522.

[35] H. T. Li, X. D. He, Y. Liu, H. Huang, S. Y. Lian, S. T. Lee, Z. H. Kang, *Carbon* **2011**, *49*, 605–609.

[36] H. Q. Tao, K. Yang, Z. Ma, J. M. Wan, Y. J. Zhang, Z. H. Kang, Z. Liu, *Small* **2012**, *8*, 281–290.

[37] J. L. Hueso, J. P. Espinos, A. Caballero, J. Cotrino, A. R. Gonzalez-Elipe, *Carbon* **2007**, *45*, 89–96.

[38] A. Eguizabal, L. Uson, V. Sebastian, J. L. Hueso, M. P. Pina, *RSC Adv.* **2015**, *5*, 90691–90697.

[39] X. Y. Zhai, P. Zhang, C. J. Liu, T. Bai, W. C. Li, L. M. Dai, W. G. Liu, *Chem. Commun.* **2012**, *48*, 7955–7957.

[40] A. Orte, J. M. Alvarez-Pez, M. J. Ruedas-Rama, *ACS Nano* **2013**, *7*, 6387–6395.

[41] Y. Q. Dong, R. X. Wang, G. L. Li, C. Q. Chen, Y. W. Chi, G. N. Chen, *Anal. Chem.* **2012**, *84*, 6220–6224.

[42] M. Algarra, B. B. Campos, K. Radotic, D. Mutavdzic, T. Bandosz, J. Jimenez-Jimenez, E. Rodriguez-Castellon, J. da Silva, *J. Mater. Chem. A* **2014**, *2*, 8342–8351.

[43] J. Zong, X. L. Yang, A. Trinchi, S. Hardin, I. Cole, Y. H. Zhu, C. Z. Li, T. Muster, G. Wei, *Biosens. Bioelectron.* **2014**, *51*, 330–335.

[44] M. Vedamalai, A. P. Periasamy, C. W. Wang, Y. T. Tseng, L. C. Ho, C. C. Shih, H. T. Chang, *Nanoscale* **2014**, *6*, 13119–13125.

[45] A. M. Brouwer, *Pure Appl. Chem.* **2011**, *83*, 2213–2228.

[46] J. R. Lakowicz, *Principles of Fluorescence Spectroscopy*, Third Edition ed., Springer US, **2006**.

IV.1.1 Supporting Information of Article 1

CHEMISTRY A European Journal

Nitrogen-induced transformation of vitamin C into multifunctional up-converting carbon nanodots in the visible-NIR range

M. Carmen Ortega-Liebana,[a,b] M. Mar Encabo-Berzosa, [a,b] M. Jose Ruedas-Rama, [c] and Jose L. Hueso*[a,b]

aInstitute of Nanoscience of Aragon (INA) and Department of Chemical Engineering and Environmental Technology, University of Zaragoza, 50018 Zaragoza, Spain.
bNetworking Research Center on Bioengineering, Biomaterials and Nanomedicine (CIBER-BBN), 28029 Madrid, Spain.
cDepartment of Physical Chemistry, Faculty of Pharmacy, University of Granada, 18701 Granada (Spain).
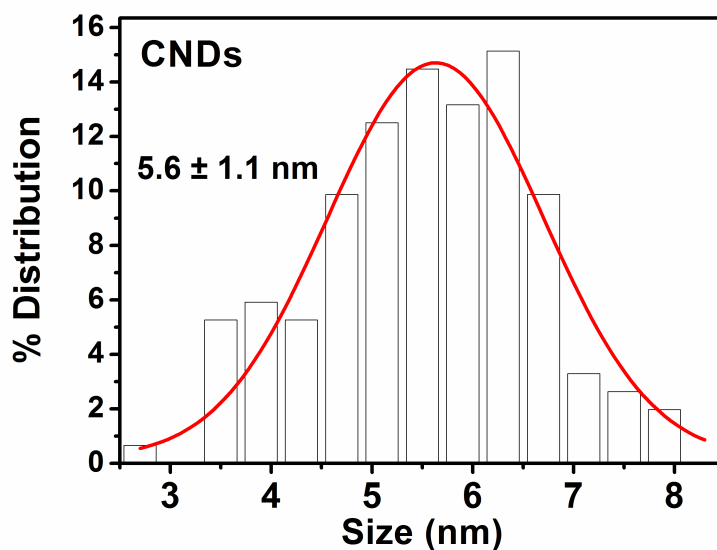
Figure S1. Particle size distribution of the CNDs synthesized from ascorbic acid.
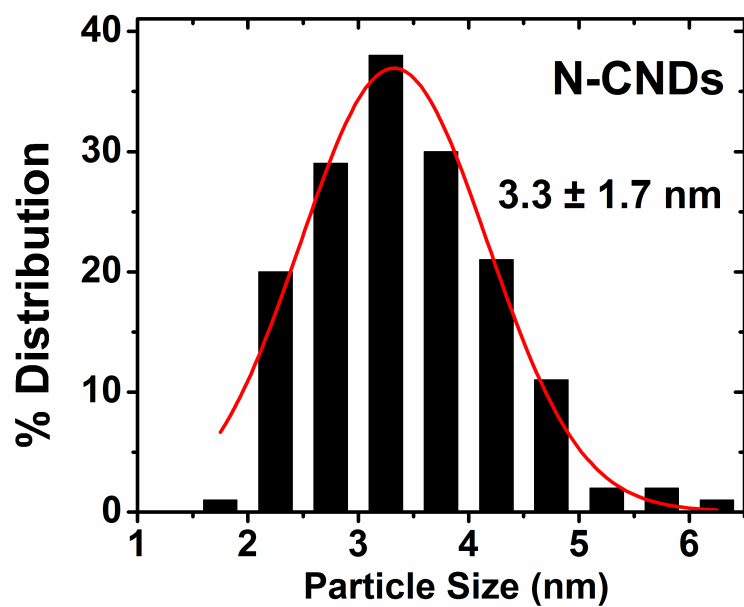
Figure S2. Particle size distribution of the N-modified carbon nanodots.
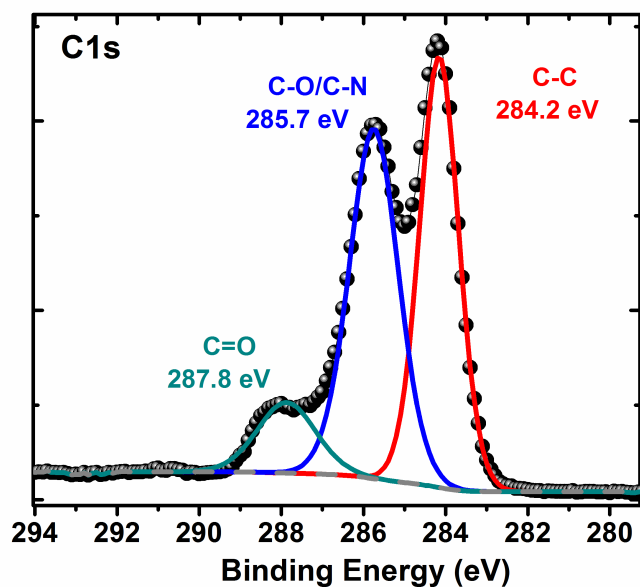
Figure S3. X-ray photoemission spectrum and fitting analysis of the C1s region corresponding to the undoped CNDs.
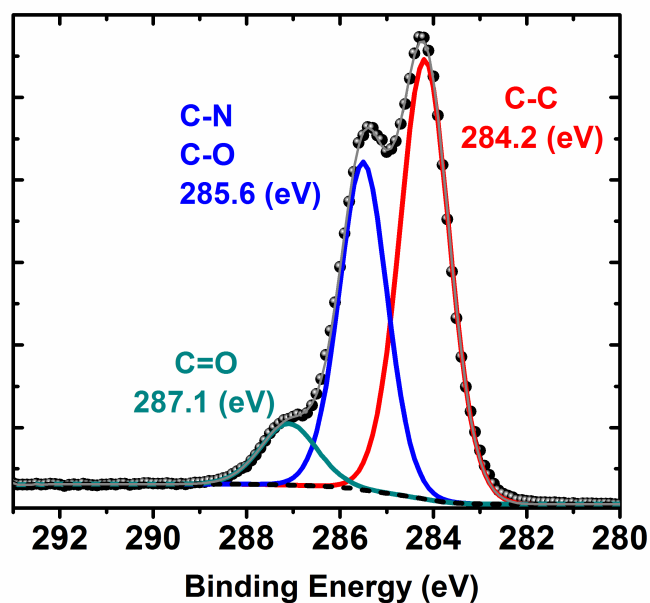
Figure S4. X-ray photoemission spectrum and fitting analysis of the C1s region corresponding to the N-doped CNDs.
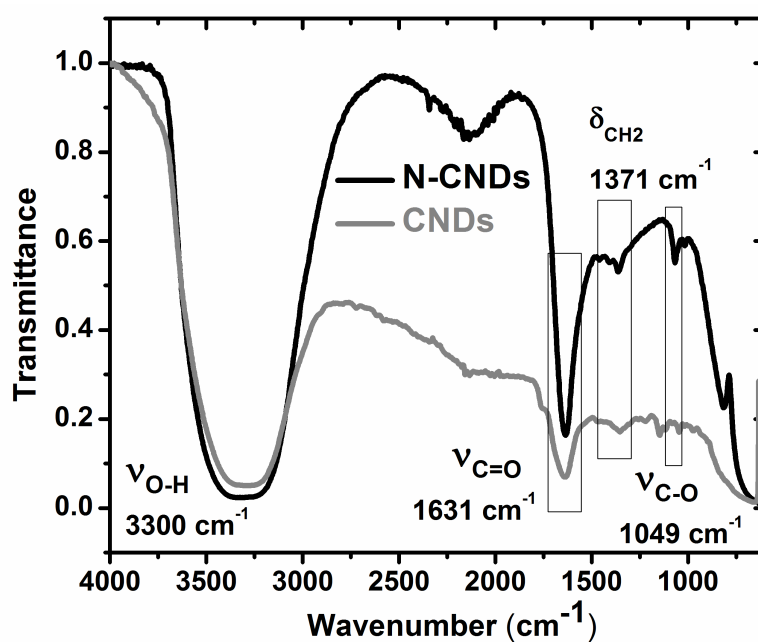
Figure S5. FT-IR analysis of the different carbon nanodots including the contribution absorption contributions at ~3300, ~1630, ~1370 and ~1049 cm^{-1} that can be ascribed to ν_{O-H}, $\nu_{C=O}$, δ_{C-H} and ν_{C-O}, respectively.

149
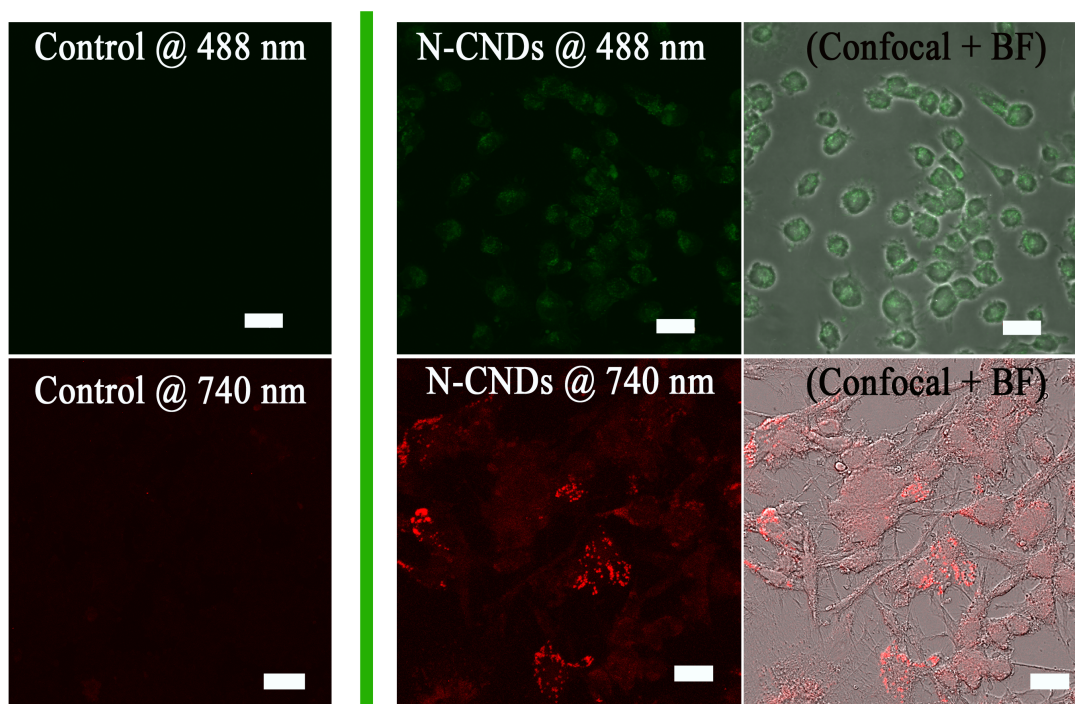
Figure S6. Confocal fluorescence microphotographs of U251MG glioma cells after 24 hours of incubation at 37 ºC using λ_{exc} = 488 nm (top-panel images) and λ_{exc} = 740 nm (down-panel images), respectively; The control images correspond to unlabeled cells. The N-CNDs were co-incubated at 0.02 and 0.2 mg mL^{-1} concentrations for the down and upconversion induced imaging in the visible and NIR ranges, respectively. The images on the right correspond to the overlay of confocal and bright field microphotographs. The detection wavelength range was 400-600 nm. All the scale bars correspond to 20 μm.
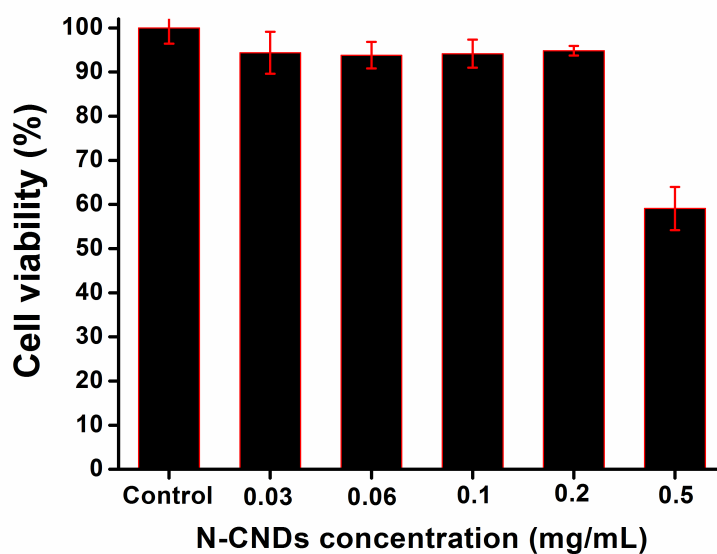
Figure S7. Evaluation of the N-doped carbon dots concentration effect on the viability of U251MG glioma cells.
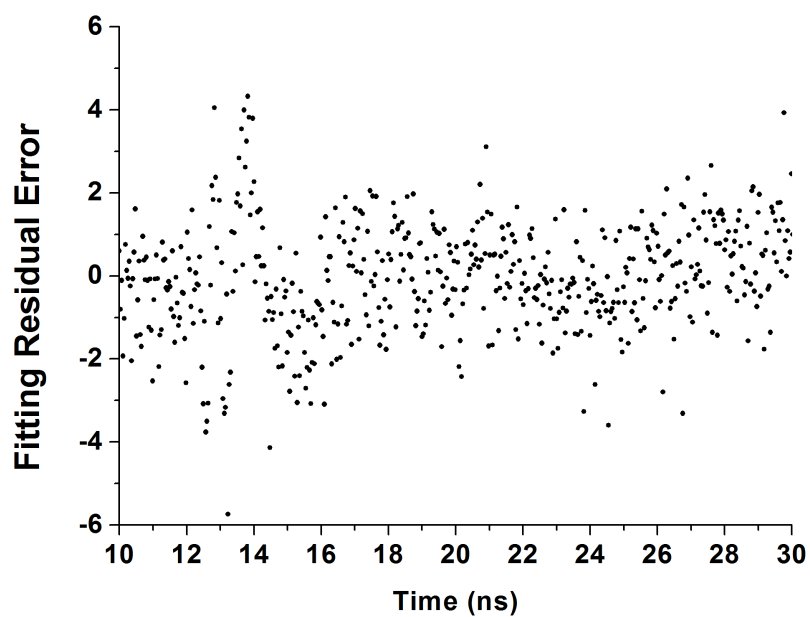
Figure S8. Residual error associated to the three-exponential fitting of the decay curve of the un-doped CNDs.
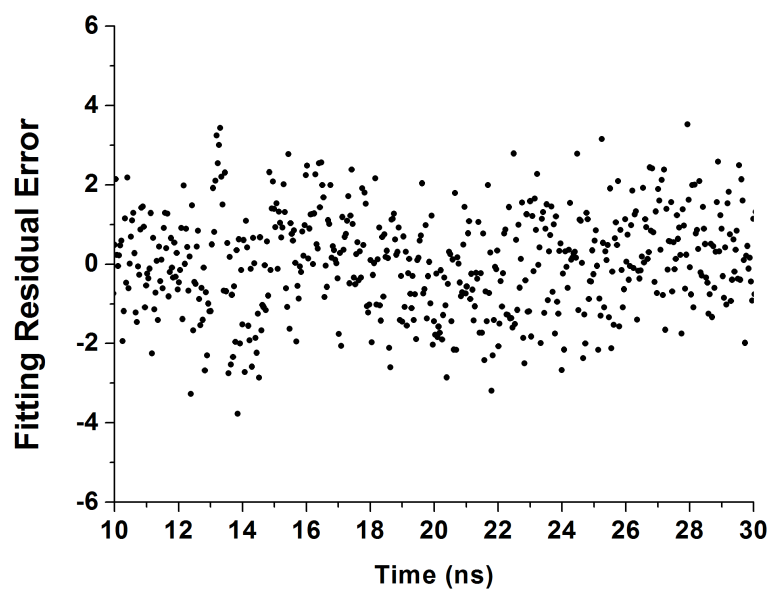
Figure S9. Residual error corresponding to the three-exponential fitting of the decay curve of the N-doped CNDs.

Table S1. Decay times and normalized pre-exponentials of the undoped CNDs at different pH values. PL decay traces collected at λ_{exc}=470 nm.

pH values	First component τ_1 [ns]	Second component τ_2 [ns]	Third component τ_3 [ns]	$\tau_{average}$ [ns]
2.34	0.22	1.40	4.39	2.18
3.88	0.23	1.46	4.66	2.36
5.04	0.24	1.47	4.66	2.36
6.09	0.24	1.50	4.76	2.38
6.93	0.23	1.39	4.66	2.24
7.83	0.25	1.47	4.67	2.30
8.53	0.23	1.49	4.60	2.35
9.96	0.21	1.46	4.55	2.36
11.60	0.19	1.34	4.15	2.16

Table S2. Decay times and normalized pre-exponentials of the N-doped CNDs at different pH values. PL decay traces collected at λ_{exc}=470 nm.

pH values	First component τ_1 [ns]	Second component τ_2 [ns]	Third component τ_3 [ns]	$\tau_{average}$ [ns]
2.34	1.32	5.10	14.77	7.65
3.88	1.26	5.04	13.76	7.64
5.04	1.31	5.35	14.43	7.84
6.09	1.30	5.45	13.58	8.33
6.93	1.36	5.70	13.47	8.59
7.83	1.37	5.96	13.38	8.78
8.53	1.46	6.51	13.94	8.82
9.96	1.44	6.46	13.86	8.79
11.60	1.43	6.17	12.39	7.72

IV.2 **Aricle 2.** Nitrogen-doped luminescent carbon nanodots for optimal photo-generation of hydroxyl radicals and visible-light expanded photo-catalysis

Nitrogen-doped luminescent carbon nanodots for optimal photo-generation of hydroxyl radicals and visible-light expanded photo-catalysis

M.C. Ortega-Liebana [a,b], Jose L. Hueso [a,b,*], S. Ferdousi [c], K.L. Yeung [c], Jesus Santamaria [a,b,*]

[a] Department of Chemical Engineering, Nanoscience Institute of Aragon (INA), University of Zaragoza, 50018 Zaragoza, Spain
[b] Networking Research Center on Bioengineering, Biomaterials and Nanomedicine, CIBER-BBN, 28029 Madrid, Spain
[c] Department of Chemical and Biomolecular Engineering, The Hong Kong University of Science and Technology (HKUST), Clear Water Bay, Kowloon, Hong Kong, China

ARTICLE INFO

ABSTRACT

Luminescent carbon nanodots (CNDs) have been obtained by hydrothermal processing of ascorbic acid (AA) and ethanolamine (EN). The resulting N-doped carbon nanostructures exhibit interesting and tunable emission capabilities with a dual behavior as down-converters and more importantly, as up-converting quantum dots. Herein, we also evaluate the optical response of these CNDs to selectively generate highly reactive oxidative hydroxyls (•OH) upon irradiation with different light-emitting diodes (LEDs) in the visible–NIR range. Finally, the role of the N-doped CNDs as nano-sensitizers to maximize the solar light harvesting and expand the photo-catalytic response of a commonly used UV-active catalyst such as TiO_2 was successfully tested in the degradation of an organo-chlorinated compound under visible light.

1. Introduction

Research on photo-luminescent semiconducting nanomaterials, generally defined as quantum dots (QDs), has attracted a vast interest and experienced rapid development in the last decades, due to their promising and diverse potential applications in optoelectronics and bio/nano-technology. Most recently, the interest of QDs is also focusing on the development of novel carbon-based materials with narrow size distributions below 10 nm, that maintain an analogous and tunable wavelength-dependent optical response associated to quantum confinement and surface state emissions [1–8]. These carbon-based nanoparticles represent a new type of fluorescent nanomaterials that include fluorescent carbon nanotubes (CNTs), graphene quantum dots (GQDs), nanodiamonds and carbon nanodots (CNDs). The latter family of carbon nanoparticles is generally formed by less ordered structures with a different ratio of carbon backbone and surface groups depending on the preparation method (generally a bottom-up approach that includes a variety of polymerization and carbonization processes of small organic molecules depending on the synthesis conditions) [2]. Nowadays, CNDs are attracting a strong interest as a valid alternative

to conventional quantum dots due to their lower fabrication costs, lower intrinsic toxicity and greater availability. Furthermore, CNDs exhibit superior versatility for surface chemical modification and great stability in multiple solvents, including the aqueous media for potential bio-applications [9–15].

Remarkably, some CNDs have recently shown unique capabilities as up-converting nanomaterials being able to sequentially absorb two or more longer wavelength photons that are emitted as shorter wavelength (and more energetic) photons [16–18]. This nonlinear optical response, traditionally observed in certain organic dyes or in inorganic lanthanide nanocrystals, has widened the potential application of CNDs in biologically related processes as biomarkers [10,19,20], biosensors [21] or Photodynamic Therapy (PDT) agents working in the NIR window where minimal background signal and deeper tissue penetration are ensured [2]. Furthermore, the potential use of CNDs as sensitizers of photo-catalytic supports [22–26] (typically TiO_2) has been also recently explored as alternative to direct carbon-doping or carbon coating of TiO_2 [27–34].

In the present work, we describe the successful synthesis of CNDs obtained after a hydrothermal heating process of ascorbic acid (AA) and ethanolamine (EN). These CNDs have been characterized and have shown appealing up-converting properties, most probably induced by the presence of N atoms doping the generated carbon nanoparticles. Furthermore, we have indirectly confirmed the up-converting capabilities of the CNDs after their assembly on commercial anatase

supports and their irradiation with different broad spectrum illumination sources. Interestingly, an improved generation of hydroxyl radicals and an expanded photo-catalytic response towards the degradation of 2,4-dichlorophenol (a persistent organo-chlorinated pesticide) have been observed in the visible–NIR range.

2. Materials and methods

2.1. Chemicals

L-Ascorbic acid (AA), ethanolamine (EN), anatase TiO_2, terephthalic acid (TA) and 2,4-dichlorophenol (2,4-DCP) were purchased from Sigma-Aldrich (analytical grade) and used without further purification.

2.2. Synthesis of carbon nanodots and assembly on TiO_2 supports

CNDs were synthesized by hydrothermal processing of AA and EN. A 1:3 molar ratio solution of both organic precursors (1 M) was mixed and magnetically stirred in a beaker for 10 min. Later on, the solution was transferred into a Teflon-lined stainless–steel autoclave and heated at 250 °C for 4 h (Fig. 1). The resulting suspension was cooled down to room temperature, centrifuged and filtered through a 0.10 μm PTFE membrane (WhatmanTH) to remove larger aggregates. The resulting brownish yellow suspension contained the carbon nanodots and was labeled as AAEN and stored at 8 °C. An aliquot of the AAEN CNDs (2 mL; 1.5 mg L^{-1}) was further assembled into an anatase (TiO_2) support (0.5 g in 2.5 mL of deionized water) using a slow temperature evaporation ramp at 65 °C for 90 min in a vacuum oven (Fig. 1). The synthesis of the nanoparticles has been carried out using the platform for Production of Biomaterials and Nanoparticles of the NANBIOSIS ICTS.

2.3. Characterization techniques

Fluorescence measurements were performed using a LS55 Fluorescence Spectrometer (PerkinElmer) equipped with a xenon arc lamp as the light source and a quartz cell (10 × 10 mm). The CND spectra were acquired in a UV–visible–NIR spectrophotometer (V-67, Jasco Company) with a quartz cell of 1 cm light path. The morphologies and particle size distributions were determined by transmission electron microscopy (TEM) (FEI Tecnai T20 and F30, operated at 200–300 kV, respectively). To prepare the samples, the nanoparticle suspensions were diluted with water prior to casting on a holey carbon TEM grid. The

functionalization of the CND surface was analyzed by Fourier transform infrared (FTIR) spectroscopy (Bruker Vertex 70 FTIR spectrometer) and X-ray photoelectron spectroscopy (XPS) with an Axis Ultra DLD (Kratos Tech.). A monochromatic Al Kα source (1486.6 eV) was employed with multiple runs at 12 kV, 10 mA and pass energy of 20 eV was used. The binding energies were calibrated to the internal C1s (284.3 eV) standard. Analyses of the peaks were performed with CasaXPS software, using a weighted sum of Lorentzian and Gaussian component curves after Shirley background subtraction. Raman analysis was carried out with the aid of a Laser Raman WiTec-Alpha 300 spectrometer using an Ar^+ ion laser exciting at 532 nm. The Raman light was collected in a backscattering geometry. The instrument was calibrated against the Stokes Raman signal of pure Si at 520 cm^{-1} using a silicon wafer crystal plane surface. Background subtraction was carried out with a second order polynomial fitted with the least squares method.

2.4. LED-assisted generation and detection of hydroxyl radicals

The generation of hydroxyl radicals (•OH) under the irradiation of selective wavelengths was carried out in the presence of three different light-emitting diodes (LEDs) (LED ENGIN, LZ4 models) at 532 nm (green LED), 740 nm (red LED) and a combination of 450 nm and 550 nm (white LED), respectively. Terephthalic acid (TA) was used as an indirect fluorescent probe that selectively reacts with hydroxyl radicals [23,35]. In a typical experiment, 0.6 mg of catalyst was dispersed in the probe solution containing TA (3 mL, 5 mM) and deposited in a cuvette with 1 cm path length. Prior to irradiation with LEDs, the suspensions were magnetically stirred in the dark for 30 min. Different aliquots were taken after selected irradiation time intervals and analyzed by fluorescence spectroscopy without retrieval of the catalyst.

2.5. Photo-catalytic experiments

The photo-catalytic capabilities of the CND–TiO$_2$ nanohybrids were evaluated by degradation of 2,4-DCP under visible light irradiation with a Xe lamp (cutoff filter for λ <420 nm). In a typical experiment, 20 mg of the CND–TiO$_2$ nanohybrids (0.5% wt. CNDs as determined by TGA) was suspended in an aqueous solution containing 2,4-dichlorophenol (2,4-DCP, 100 mL, 25 mM) and stirred overnight in dark conditions to ensure the establishment of adsorption/desorption equilibrium between 2,4-DCP and the photo-catalyst before irradiation. Multiple aliquots were progressively taken and analyzed at different irradiation times with the aid of an ultra performance liquid chromatograph
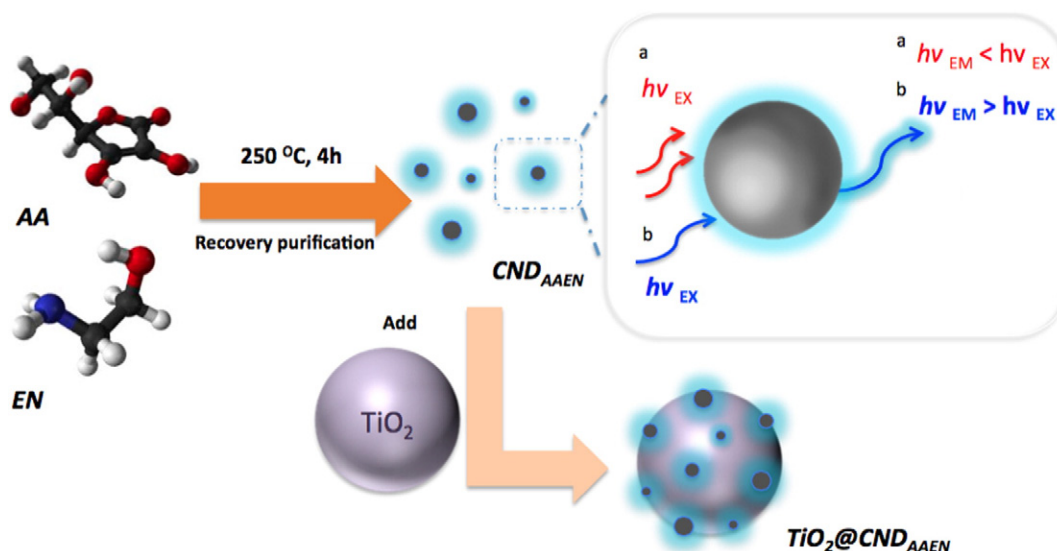
Fig. 1. Scheme of the hydrothermal processing of carbon nanodots with down-conversion (a) and up-conversion (b) properties and their assembly on TiO$_2$ supports.

(UPLC). Finally, four additional reutilization cycles were carried out with fresh suspensions of the organo-chlorinated contaminant.

3. Results and discussion

3.1. Characterization of CNDs and CND–TiO$_2$ hybrids

Fig. 2a shows a representative TEM image corresponding to the CNDs obtained after the hydrothermal processing of AA and EN at 250 °C during 4 h and after the filtration–purification step. The nanoparticle size distribution is rather homogeneous with a mean diameter of 3.3 ± 1.7 nm (inset in Fig. 2a). Nevertheless, TEM images do not provide enough resolution and perspective to clearly discern whether the CNDs exhibit a pseudo-spherical or a more planar shape. Raman analysis depicted in Fig. 2b shows that the CNDs are structurally constituted by a mixture of disordered graphitic lattice structures, generally recognized by the appearance of the so-called D band at 1360 cm^{-1} (D for defects or disordered), and graphitic-like crystalline domains commonly associated with a band at 1580 cm^{-1} known as G-band (G for graphite) [36]. It is also worth mentioning that the potential interference of the fluorescence contribution of the N-CNDs is minimal when exciting at 532 nm (see Figs. S1–S2 from the Supporting information for a comparison at equivalent spectra ranges).

The FT-IR analysis of the CNDs (see Fig. S3) shows clear absorption contributions at ~3300, ~1630, ~1370 and ~1049 cm^{-1} that can be ascribed to ν_{O-H}, $\nu_{C=O}$, δ_{C-H} and ν_{C-O}, respectively. There was no evidence of amide bonding formation, in good agreement with other recently reported CND systems [37]. Interestingly, the surface chemistry analysis carried out by XPS not only confirmed the presence of sp^2/sp^3 C–O bonds in the C1s spectrum with binding energies ranged between 285.5–287.1 eV (Fig. 2c) but also revealed the presence of N elements (Fig. 2d).

The N1s spectrum shows two clear contributions centered at ~399 and ~401 eV that can be assigned to different N-containing conformations. The former contribution at lower BEs has been previously attributed to N species present in terminal positions of carbon matrices (−N–H), aromatic rings (N6) or as part of amides (O=C–NH–) [37–39]. Likewise, the contribution at ~401 eV has been correlated with the formation of N–C bonds in pyrrol-type rings (N5) or with the presence of protonated primary amines (−NH$_3^+$) [37–40]. Taking into account the spectroscopic results retrieved from FT-IR it seems reasonable to assume that the main contribution in the ~401 eV band observed in XPS analysis could be assigned to N6 structures. This implies that N is present as a dopant, rather than forming amide chemical bonds [37]. The role of amine groups as N-doping inducers has been previously reported by other authors employing different degrees of functionalization and branching of amine precursors [37,41,42]. It has been claimed that the use of shorter alkyl chains and lower reaction temperatures favors the formation of these N-doped CND species [37].

Fig. 3a shows that the UV–Vis absorption band of the N-CNDs starts at ca. 515 nm. The photoluminescence (PL) response is wavelength-dependent and exhibits the expected behavior for a semiconducting quantum dot [2,8]. The PL emission maximum intensities progressively downshift from 440 nm to 550 nm at increasing excitation wavelengths (from 365 to 500 nm) due to the lower capability to repopulate the excited states with lower energy excitation sources. Notably, a differential up-converting effect is observed at longer excitation wavelengths of 740 and 800 nm, respectively (Fig. 3a). This up-conversion effect has been previously identified for other carbon nanoparticles and it has been attributed to their capability to absorb longer wavelength photons and emit at shorter emission wavelengths in a multi-photon absorption event [8]. Although the underlying mechanism has not been completely unveiled yet, it is commonly accepted that the presence of intermediate energy levels (provided in our case by N-doping atoms) is necessary to favor the direct or sequential absorption of two photons of lower energy to render a single
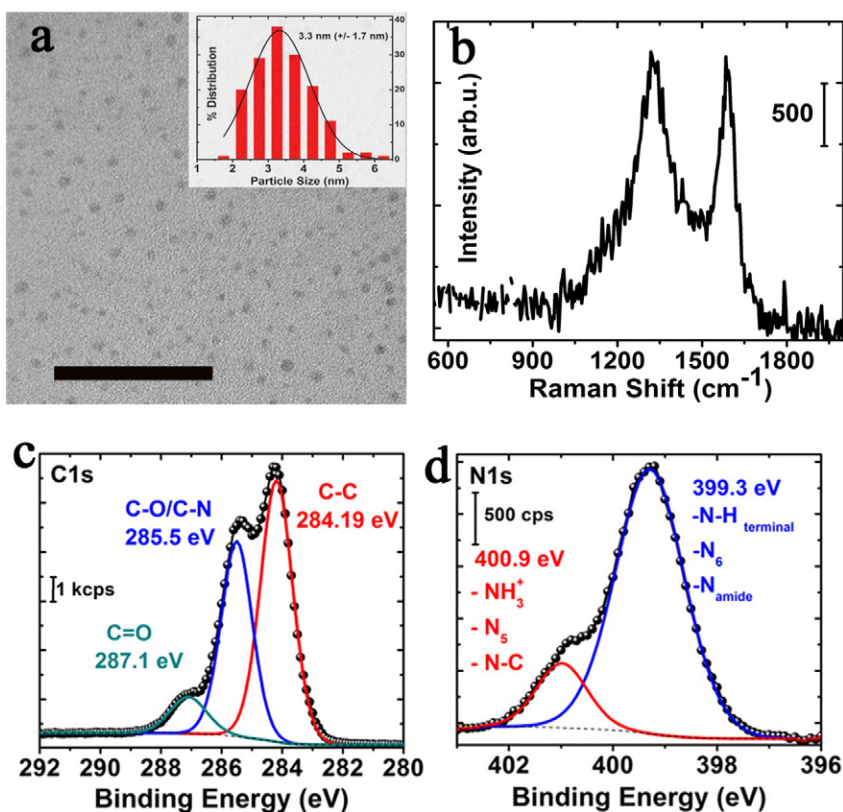
Fig. 2. a) TEM image of the CNDs after hydrothermal synthesis and purification (inset: particle size distribution estimated from TEM image counting and the scale bar corresponds to 20 nm); b) Raman spectrum of the CNDs; c)–d) X-ray photoemission spectrum corresponding to the C1s and N1s areas, respectively.
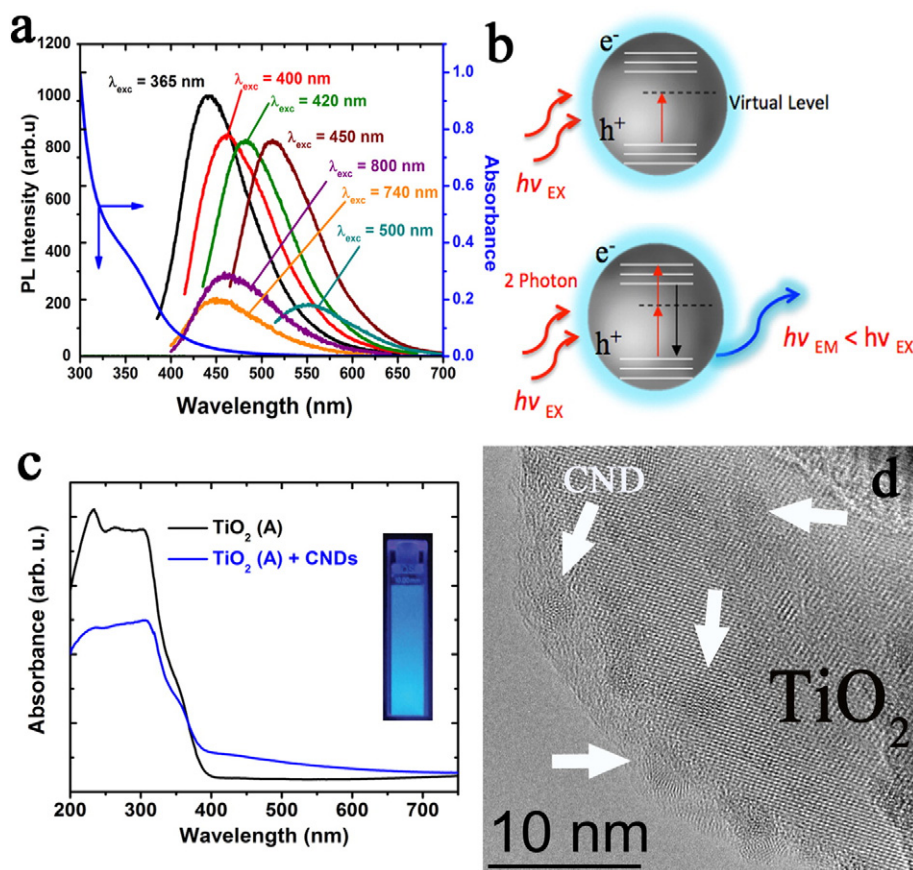
Fig. 3. a) UV–Vis absorbance spectrum and photoluminescence spectra of the CNDs in aqueous solution at different excitation wavelengths; b) up-conversion mechanism of the CNDs based on a two-photon absorption process and the existence of virtual intermediate energy levels; c) UV–Vis spectra of the anatase support before and after the assembly of the CNDs (note that the absorption spectrum does not decay completely and a significant absorbance can be observed throughout the whole visible range; the inset shows a digital image of the fluorescent suspension of CNDs in DI-water under excitation with a portable UV-light at 365 nm); d) HR-TEM image of the CND–TiO₂ nanohybrids.

emitting photon at shorter wavelengths (see Fig. 3b) [17]. This fact provides the CNDs with an enhanced photo-response in the NIR range and a great potential to expand their utilization in a broader spectrum window. This capability was further evaluated after decorating a commercial anatase support with the N-doped CNDs. Anatase is a well-known semiconductor support widely employed in photocatalysis with limited photo-response beyond the UV region, as expected from its UV–Vis absorbance spectrum (Fig. 3c). The addition of the CNDs extended the absorption response towards the visible range (Fig. 3c).

TEM images of the CND–TiO₂ hybrids further confirmed the successful and well-dispersed disposition of the carbonaceous nanoparticles onto the titania support (Fig. 3d) probably favored by the slow impregnation method assisted by vacuum drying. Interestingly, high-resolution only evidenced a clear crystalline structure for the commercial TiO₂ support but not for the CNDs that only exhibited a partial organization of atoms (Fig. 3d). Still, it was not possible to clearly determine the exact shape configuration (spherical or planar) of the CNDs that would probably require the use of AFM techniques. This pseudo-amorphous nature of the CNDs has been previously reported for other analogous nanocarbons synthesized under hydrothermal conditions [37]. Additional XPS analysis of the CND–TiO₂ hybrid confirmed the assembly of the N-doped carbon dots with the titania support through the formation of O–Ti–N linkages via N⁻ anionic species interacting with the TiO₂ lattice [43–45]. The shifting of the Ti2p (Fig. S4) and O1s core levels (Fig. S5) to lower binding energies in conjunction with the appearance of a novel N1s contribution, not observed in the original support (Fig. S6), evidenced the partial change of electronic density around certain Ti centers when interacting with less electronegative N species [43–45].

3.2. Selective generation of hydroxyl radicals under LED illumination

The photo-generation of hydroxyl radicals (•OH) has been established as a critical step to induce the redox decomposition of multiple organic contaminants or an important factor in multiple biological processes [30,32,35,46,47]. Therefore, in order to evaluate the photo-activity of the CNDs and their potential role as broad-spectrum nano-sensitizers, the light-induced formation of hydroxyl groups was systematically evaluated after the selective irradiation of TiO₂ and CND–TiO₂ nanosystems with different LEDs exciting at selected wavelengths from the UV–Vis (white LED) to the visible–NIR ranges (green and red LEDs, respectively). Terephthalic acid (TA) was selected as a chemical probe to detect the in situ formation of •OH groups [35]. TA selectively reacts with hydroxyl groups to form a fluorescent derivative (2-hydroxy-terephthalic acid: HTA) emitting at ca. 425 nm according to the reaction depicted in Fig. 4a [23,35].

Fig. 4b–c show the fluorescent intensities of the HTA derivative after one hour of irradiation with each LED wavelength for the CND–TiO₂ hybrid and the TiO₂ used as reference, respectively. Both samples can generate •OH groups under the irradiation of the white LED thanks to the contribution of near-UV wavelengths in the white light that are able to activate the TiO₂ particles. However, clear differences are observed between both samples depending on the wavelength used. Thus, anatase alone practically has no response (Fig. 4c–d) while the addition of the CNDs strongly favors a strong enhancement in the photo-generation of the hydroxyl intermediates. This enhancement can be observed with any of the three LEDs, although the effect is more dramatic in the case of the green and red LEDs where the near-UV contribution is absent (Fig. 4b–d). Still, it is worth mentioning that the use of the white
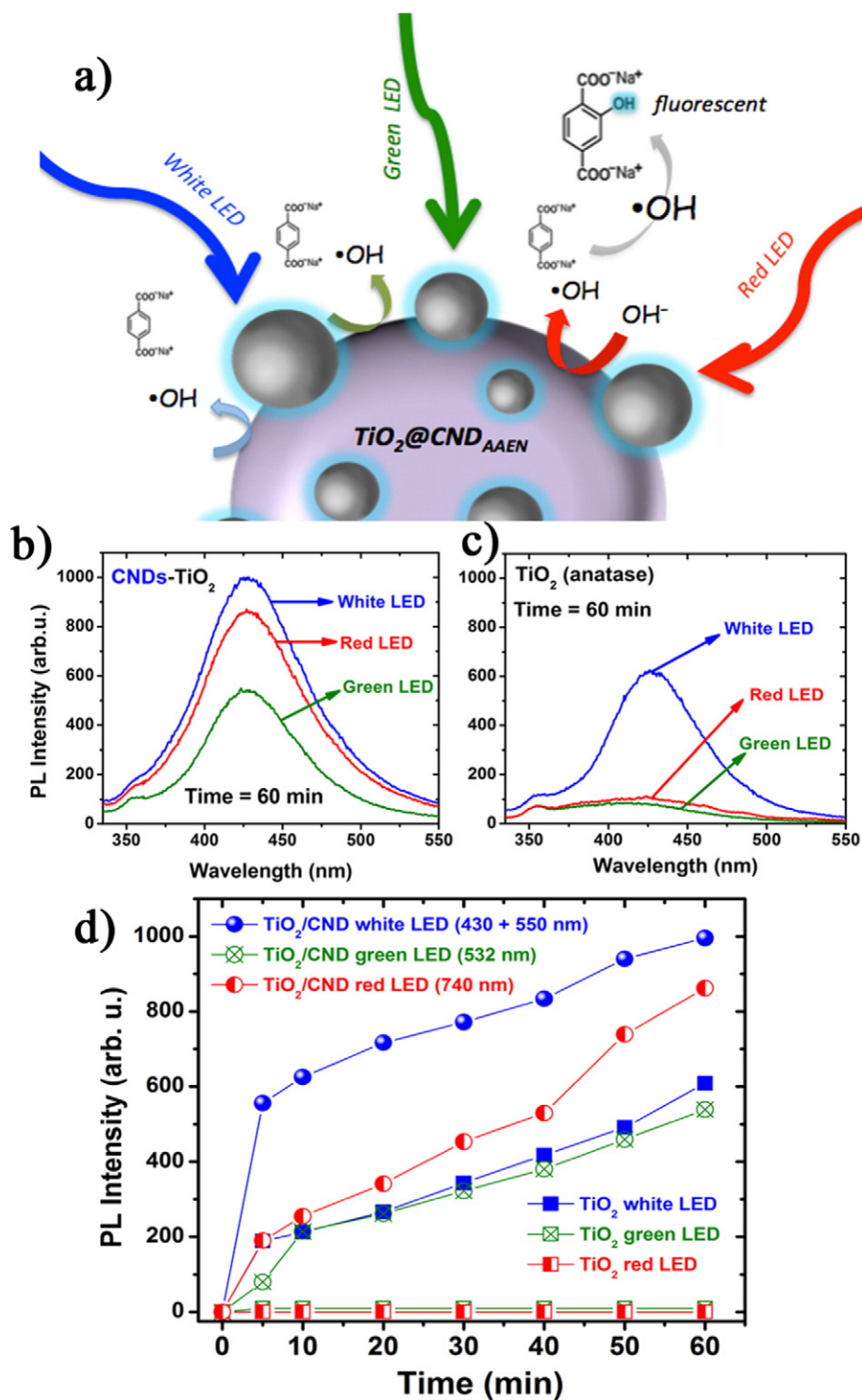
Fig. 4. a) Schematic representation of the LED-induced generation of hydroxyl radicals after selective irradiation with a white LED source (λ_{exc} = 450 + 550 nm), a green LED (λ_{exc} = 532 nm) and a red LED (λ_{exc} = 740 nm). The reaction between the non-fluorescent terephthalic acid probe with hydroxyl OH radicals to yield a fluorescent derivative emitting at 425 nm is shown; b) fluorescence emission spectra of the terephthalate derivative after 60 min of irradiation of the CND–TiO$_2$ composite with different LED wavelengths; c) fluorescence emission spectra of the terephthalate derivative after 60 min of irradiation of the TiO$_2$ support with different LED wavelengths; d) overview of the fluorescence intensity evolution against different irradiation times for all the experiments carried out in the presence (circles) and absence of CNDs (squares).

LED outperforms the photo-activity of the other LEDs, thereby demonstrating the synergism of the simultaneous activation of the anatase support and the CNDs (Fig. 4), and the active role of the CNDs as a photo-sensitizer able to expand the response of the TiO$_2$ beyond the UV region.

3.3. Enhanced photo-catalytic response in the visible range

The response of the CND–TiO$_2$ composite was further tested in the photo-catalytic degradation of an organo-chlorinated contaminant (2,4-dichlorophenol, DCP) under visible light. Fig. 5 shows the evolution

Fig. 5. Visible-light driven photo-catalytic degradation of 2,4-dichlorophenol in the absence of photocatalyst, with anatase or in the presence of the CND–TiO$_2$ composite after different irradiation times; [DCP] = 25 mM; [catalyst] = 0.2 g L^{-1}.

on the concentration of DCP at different irradiation times in the absence of catalyst (regular photolysis), in the presence of anatase and finally, in the presence of the hybrid composite combining the C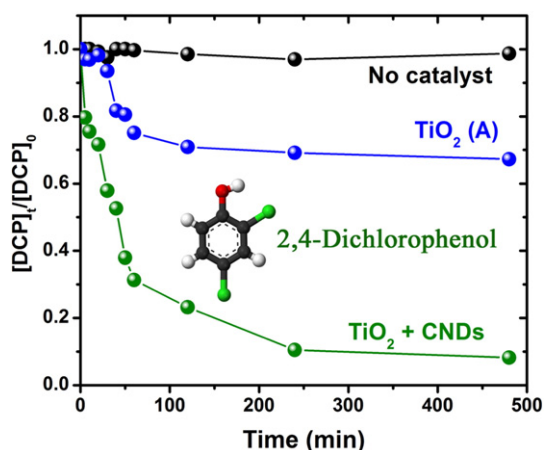NDs and the TiO$_2$ support. It is clear that the CNDs are playing a very active role as nano-sensitizers and expanding the photo-catalytic response of anatase beyond the UV-region. From the results discussed in the previous section, the capability of CNDs to co-generate highly active hydroxyl radicals in the visible–NIR range (Fig. 4) can be credited as the main factor in the enhancement in the degradation rate of the tested organo-chlorinated contaminant (up to 96% degradation) in comparison with the regular photolytic conditions (no degradation) or the non-decorated titania support (up to 30%) (Fig. 5). Furthermore, four additional cycles were carried out with fresh DCP solutions without observing any signal of photo-catalytic deactivation.

Different reports in the literature have claimed that doping with C atoms [48], coating with either carbonaceous layers [49], carbon-type nanoparticles [34] or more recently with graphene-type materials [30–33,50] can enhance the visible-light driven response of wide band gap semiconductors such as TiO$_2$. As previously pointed out, the CNDs behave as organic nano-sensitizers that can expand the absorption window of TiO$_2$ beyond the UV range (Fig. 3c) and directly transfer electrons to its Conduction Band (CB) [16,51,52]. Alternatively, a fraction of the light-emitting photons stemming from the irradiated CNDs (Fig. 3a) can directly excite and promote the generation of electron–hole pairs in the TiO$_2$ support or form overlapping intermediate energy levels that reduce the overall band gap energy of TiO$_2$ after the coordination of N terminal groups from the CNDs with the titania network (see Figs. S4–S6) [16,43]. The presence of N-doping atoms from the hydrothermal treatment of amine derivatives provides the CNDs with expanded optical response in the NIR range (Fig. 3a) and holds a great potential for multiple photo-chemical related processes that aim to exploit a wider fraction of the solar spectrum.

4. Conclusions

The most important characteristics of the CNDs developed in this work are their photo-chemical stability and their up-converting response in the NIR range induced by the presence of N-doping atoms. This response is the main contribution for the strong increase observed on the photo-degradation rate of a chlorinated pesticide under visible light, and takes place via an enhanced production of highly reactive hydroxyl radicals. Likewise, the NIR range capability opens up a promising potential for solar harvesting applications and the in situ generation of reactive oxidative species within the biological window of minimal tissue absorption and maximum depth penetration.

Prime novelty statement

Development of carbon nanoparticles with tunable optical emissions in the visible–NIR range. These optical properties are successfully applied in the selective generation of radicals and in the photo-catalytic degradation of chlorinated compounds.

Appendix A. Supplementary data

Supplementary data to this article can be found online at http://dx.doi.org/10.1016/j.diamond.2016.03.021.

References

[1] S.Y. Lim, W. Shen, Z.Q. Gao, Carbon quantum dots and their applications, Chem. Soc. Rev. 44 (2015) 362–381.
[2] S.J. Zhu, Y.B. Song, X.H. Zhao, J.R. Shao, J.H. Zhang, B. Yang, The photoluminescence mechanism in carbon dots (graphene quantum dots, carbon nanodots, and polymer dots): current state and future perspective, Nano Res. 8 (2015) 355–381.
[3] K.P. Loh, Q.L. Bao, G. Eda, M. Chhowalla, Graphene oxide as a chemically tunable platform for optical applications, Nat. Chem. 2 (2010) 1015–1024.
[4] V.N. Mochalin, O. Shenderova, D. Ho, Y. Gogotsi, The properties and applications of nanodiamonds, Nat. Nanotechnol. 7 (2012) 11–23.
[5] S.N. Baker, G.A. Baker, Luminescent carbon nanodots: emergent nanolights, Angew. Chem. Int. Ed. 49 (2010) 6726–6744.
[6] H.T. Li, Z.H. Kang, Y. Liu, S.T. Lee, Carbon nanodots: synthesis, properties and applications, J. Mater. Chem. 22 (2012) 24230–24253.
[7] P.C. Hsu, Z.Y. Shih, C.H. Lee, H.T. Chang, Synthesis and analytical applications of photoluminescent carbon nanodots, Green Chem. 14 (2012) 917–920.
[8] P. Roy, P.C. Chen, A.P. Periasamy, Y.N. Chen, H.T. Chang, Photoluminescent carbon nanodots: synthesis, physicochemical properties and analytical applications, Mater. Today 18 (2015) 447–458.
[9] Y.Q. Zhang, D.K. Ma, Y. Zhuang, X. Zhang, W. Chen, L.L. Hong, Q.X. Yan, K. Yu, S.M. Huang, One-pot synthesis of N-doped carbon dots with tunable luminescence properties, J. Mater. Chem. 22 (2012) 16714–16718.
[10] P.J.G. Luo, S. Sahu, S.T. Yang, S.K. Sonkar, J.P. Wang, H.F. Wang, G.E. LeCroy, L. Cao, Y.P. Sun, Carbon "quantum" dots for optical bioimaging, J. Mater. Chem. B 1 (2013) 2116–2127.
[11] Z.L. Wu, P. Zhang, M.X. Gao, C.F. Liu, W. Wang, F. Leng, C.Z. Huang, One-pot hydrothermal synthesis of highly luminescent nitrogen-doped amphoteric carbon dots for bioimaging from *Bombyx mori* silk-natural proteins, J. Mater. Chem. B 1 (2013) 2868–2873.
[12] L. Cao, X. Wang, M.J. Meziani, F.S. Lu, H.F. Wang, P.J.G. Luo, Y. Lin, B.A. Harruff, L.M. Veca, D. Murray, S.Y. Xie, Y.P. Sun, Carbon dots for multiphoton bioimaging, J. Am. Chem. Soc. 129 (2007) 11318–11319.
[13] V.N. Mochalin, Y. Gogotsi, Wet chemistry route to hydrophobic blue fluorescent nanodiamond, J. Am. Chem. Soc. 131 (2009) 4594–4595.
[14] S.T. Yang, L. Cao, P.G.J. Luo, F.S. Lu, X. Wang, H.F. Wang, M.J. Meziani, Y.F. Liu, G. Qi, Y.P. Sun, Carbon dots for optical imaging in vivo, J. Am. Chem. Soc. 131 (2009) 11308–11309.
[15] P. Juzenas, A. Kleinauskas, P.G. Luo, Y.P. Sun, Photoactivatable carbon nanodots for cancer therapy, Appl. Phys. Lett. 103 (2013).
[16] S.J. Zhuo, M.W. Shao, S.T. Lee, Upconversion and downconversion fluorescent graphene quantum dots: ultrasonic preparation and photocatalysis, ACS Nano 6 (2012) 1059–1064.
[17] Z.X. Gan, X.L. Wu, G.X. Zhou, J.C. Shen, P.K. Chu, Is there real upconversion photoluminescence from graphene quantum dots? Adv. Opt. Mater. 1 (2013) 554–558.
[18] L. Wang, S.J. Zhu, H.Y. Wang, Y.F. Wang, Y.W. Hao, J.H. Zhang, Q.D. Chen, Y.L. Zhang, W. Han, B. Yang, H.B. Sun, Unraveling bright molecule-like state and dark intrinsic state in green-fluorescence graphene quantum dots via ultrafast spectroscopy, Adv. Opt. Mater. 1 (2013) 264–271.
[19] B. Kong, A.W. Zhu, C.Q. Ding, X.M. Zhao, B. Li, Y. Tian, Carbon dot-based inorganic–organic nanosystem for two-photon imaging and biosensing of pH variation in living cells and tissues, Adv. Mater. 24 (2012) 5844–5848.

[20] S.J. Zhu, Q.N. Meng, L. Wang, J.H. Zhang, Y.B. Song, H. Jin, K. Zhang, H.C. Sun, H.Y. Wang, B. Yang, Highly photoluminescent carbon dots for multicolor patterning, sensors, and bioimaging, Angew. Chem. Int. Ed. 52 (2013) 3953–3957.

[21] W.P. Wang, Y.C. Lu, H. Huang, A.J. Wang, J.R. Chen, J.J. Feng, Facile synthesis of N, S-codoped fluorescent carbon nanodots for fluorescent resonance energy transfer recognition of methotrexate with high sensitivity and selectivity, Biosens. Bioelectron. 64 (2015) 517–522.

[22] H.T. Li, R.H. Liu, S.Y. Lian, Y. Liu, H. Huang, Z.H. Kang, Near-infrared light controlled photocatalytic activity of carbon quantum dots for highly selective oxidation reaction, Nanoscale 5 (2013) 3289–3297.

[23] M.C. Ortega-Liebana, J.L. Hueso, A. Larrea, V. Sebastian, J. Santamaria, Feroxyhyte nanoflakes coupled to up-converting carbon nanodots: a highly active, magnetically recoverable, Fenton-like photocatalyst in the visible–NIR range, Chem. Commun. (Camb.) 51 (2015) 16625–16628.

[24] H.C. Zhang, H. Huang, H. Ming, H.T. Li, L.L. Zhang, Y. Liu, Z.H. Kang, Carbon quantum dots/Ag$_3$PO$_4$ complex photocatalysts with enhanced photocatalytic activity and stability under visible light, J. Mater. Chem. 22 (2012) 10501–10506.

[25] H.T. Li, R.H. Liu, Y. Liu, H. Huang, H. Yu, H. Ming, S.Y. Lian, S.T. Lee, Z.H. Kang, Carbon quantum dots/Cu$_2$O composites with protruding nanostructures and their highly efficient (near) infrared photocatalytic behavior, J. Mater. Chem. 22 (2012) 17470–17475.

[26] G.P. Gao, Y. Jiao, F.X. Ma, Y.L. Jiao, E. Waclawik, A.J. Du, Carbon nanodot decorated graphitic carbon nitride: new insights into the enhanced photocatalytic water splitting from ab initio studies, Phys. Chem. Chem. Phys. 17 (2015) 31140–31144.

[27] C. Chen, W.M. Cai, M.C. Long, B.X. Zhou, Y.H. Wu, D.Y. Wu, Y.J. Feng, Synthesis of visible-light responsive graphene oxide/TiO$_2$ composites with p/n heterojunction, ACS Nano 4 (2010) 6425–6432.

[28] L. Zhang, M.S. Tse, O.K. Tan, Y.X. Wang, M.D. Han, Facile fabrication and characterization of multi-type carbon-doped TiO$_2$ for visible light-activated photocatalytic mineralization of gaseous toluene, J. Mater. Chem. A 1 (2013) 4497–4507.

[29] C. Chen, M.C. Long, H. Zeng, W.M. Cai, B.X. Zhou, J.Y. Zhang, Y.H. Wu, D.W. Ding, D.Y. Wu, Preparation, characterization and visible-light activity of carbon modified TiO$_2$ with two kinds of carbonaceous species, J. Mol. Catal. A Chem. 314 (2009) 35–41.

[30] M. Pelaez, N.T. Nolan, S.C. Pillai, M.K. Seery, P. Falaras, A.G. Kontos, P.S.M. Dunlop, J.W.J. Hamilton, J.A. Byrne, K. O'Shea, M.H. Entezari, D.D. Dionysiou, A review on the visible light active titanium dioxide photocatalysts for environmental applications, Appl. Catal. B Environ. 125 (2012) 331–349.

[31] P. Fernandez-Ibanez, M.I. Polo-Lopez, S. Malato, S. Wadhwa, J.W.J. Hamilton, P.S.M. Dunlop, R. D'Sa, E. Magee, K. O'Shea, D.D. Dionysiou, J.A. Byrne, Solar photocatalytic disinfection of water using titanium dioxide graphene composites, Chem. Eng. J. 261 (2015) 36–44.

[32] S. Banerjee, S.C. Pillai, P. Falaras, K.E. O'Shea, J.A. Byrne, D.D. Dionysiou, New insights into the mechanism of visible light photocatalysis, J. Phys. Chem. Lett. 5 (2014) 2543–2554.

[33] M.J. Sampaio, L.M. Pastrana-Martinez, A.M.T. Silva, J.G. Buijnsters, C. Han, C.G. Silva, S.A.C. Carabineiro, D.D. Dionysiou, J.L. Faria, Nanodiamond–TiO$_2$ composites for photocatalytic degradation of microcystin-LA in aqueous solutions under simulated solar light, RSC Adv. 5 (2015) 58363–58370.

[34] C. Lettmann, K. Hildenbrand, H. Kisch, W. Macyk, W.F. Maier, Visible light photodegradation of 4-chlorophenol with a coke-containing titanium dioxide photocatalyst, Appl. Catal. B Environ. 32 (2001) 215–227.

[35] C.H. Fang, H.L. Jia, S. Chang, Q.F. Ruan, P. Wang, T. Chen, J.F. Wang, (Gold core)/(titania shell) nanostructures for plasmon-enhanced photon harvesting and generation of reactive oxygen species, Energy Environ. Sci. 7 (2014) 3431–3438.

[36] J.L. Hueso, V.J. Rico, J. Cotrino, J.M. Jimenez-Mateos, A.R. Gonzalez-Elipe, Water plasmas for the revalorisation of heavy oils and cokes from petroleum refining, Environ. Sci. Technol. 43 (2009) 2557–2562.

[37] X.Y. Zhai, P. Zhang, C.J. Liu, T. Bai, W.C. Li, L.M. Dai, W.G. Liu, Highly luminescent carbon nanodots by microwave-assisted pyrolysis, Chem. Commun. 48 (2012) 7955–7957.

[38] A. Eguizabal, L. Uson, V. Sebastian, J.L. Hueso, M.P. Pina, Efficient and facile tuning of Vulcan XC72 with ultra-small Pt nanoparticles for electrocatalytic applications, RSC Adv. 5 (2015) 90691–90697.

[39] J.L. Hueso, J.P. Espinos, A. Caballero, J. Cotrino, A.R. Gonzalez-Elipe, XPS investigation of the reaction of carbon with NO, O$_2$, N$_2$ and H$_2$O plasmas, Carbon 45 (2007) 89–96.

[40] K. Tokarek, J.L. Hueso, P. Kustrowski, G. Stochel, A. Kyziol, Green synthesis of chitosan-stabilized copper nanoparticles, Eur. J. Inorg. Chem. 2013 (2013) 4940–4947.

[41] W. Li, Z.H. Zhang, B.A. Kong, S.S. Feng, J.X. Wang, L.Z. Wang, J.P. Yang, F. Zhang, P.Y. Wu, D.Y. Zhao, Simple and green synthesis of nitrogen-doped photoluminescent carbonaceous nanospheres for bioimaging, Angew. Chem. Int. Ed. 52 (2013) 8151–8155.

[42] Y. Xu, M. Wu, Y. Liu, X.Z. Feng, X.B. Yin, X.W. He, Y.K. Zhang, Nitrogen-doped carbon dots: a facile and general preparation method, photoluminescence investigation, and imaging applications, Chem. Eur. J. 19 (2013) 2276–2283.

[43] M. Sathish, B. Viswanathan, R.P. Viswanath, C.S. Gopinath, Synthesis, characterization, electronic structure, and photocatalytic activity of nitrogen-doped TiO$_2$ nanocatalyst, Chem. Mater. 17 (2005) 6349–6353.

[44] F. Peng, L.F. Cai, L. Huang, H. Yu, H.J. Wang, Preparation of nitrogen-doped titanium dioxide with visible-light photocatalytic activity using a facile hydrothermal method, J. Phys. Chem. Solids 69 (2008) 1657–1664.

[45] A.P. Bhirud, S.D. Sathaye, R.P. Waichal, J.D. Ambekar, C.J. Park, B.B. Kale, In-situ preparation of N-TiO$_2$/graphene nanocomposite and its enhanced photocatalytic hydrogen production by H2S splitting under solar light, Nanoscale 7 (2015) 5023–5034.

[46] S. Dominguez, P. Ribao, M.J. Rivero, I. Ortiz, Influence of radiation and TiO$_2$ concentration on the hydroxyl radicals generation in a photocatalytic LED reactor. Application to dodecylbenzenesulfonate degradation, Appl. Catal. B Environ. 178 (2015) 165–169.

[47] Z.H. Zhang, F.Y. Yu, L.R. Huang, J. Jiatieli, Y.Y. Li, L.J. Song, N. Yu, D.D. Dionysiou, Confirmation of hydroxyl radicals ((OH)-O-center dot) generated in the presence of TiO$_2$ supported on AC under microwave irradiation, J. Hazard. Mater. 278 (2014) 152–157.

[48] X. Yang, C. Cao, K. Hohn, L. Erickson, R. Maghirang, D. Hamal, K. Klabunde, Highly visible-light active C- and V-doped TiO$_2$ for degradation of acetaldehyde, J. Catal. 252 (2007) 296–302.

[49] L.W. Zhang, H.B. Fu, Y.F. Zhu, Efficient TiO$_2$ photocatalysts from surface hybridization of TiO$_2$ particles with graphite-like carbon, Adv. Funct. Mater. 18 (2008) 2180–2189.

[50] D.Y. Liang, C. Cui, H.H. Hu, Y.P. Wang, S. Xu, B.L. Ying, P.G. Li, B.Q. Lu, H.L. Shen, One-step hydrothermal synthesis of anatase TiO$_2$/reduced graphene oxide nanocomposites with enhanced photocatalytic activity, J. Alloys Compd. 582 (2014) 236–240.

[51] J. Tian, Y.H. Leng, Z.H. Zhao, Y. Xia, Y.H. Sang, P. Hao, J. Zhan, M.C. Li, H. Liu, Carbon quantum dots/hydrogenated TiO$_2$ nanobelt heterostructures and their broad spectrum photocatalytic properties under UV, visible, and near-infrared irradiation, Nano Energy 11 (2015) 419–427.

[52] Z. Hu, Y.D. Huang, S.F. Sun, W.C. Guan, Y.H. Yao, P.Y. Tang, C.Y. Li, Visible light driven photodynamic anticancer activity of graphene oxide/TiO$_2$ hybrid, Carbon 50 (2012) 994–1004.

IV.2.1 Supporting Information of Article 2

Diamond & Related Materials

Nitrogen-doped luminescent carbon nanodots for optimal photo-generation of hydroxyl radicals and visible-light expanded photo-catalysis

M.C. Ortega-Liebana[a,b], Jose L. Hueso[a,b,*], S. Ferdousi[c], K.L. Yeung[c] and Jesus Santamaria[a,b,*]

[a]Institute of Nanoscience of Aragon (INA) and Department of Chemical Engineering and Environmental Technology, University of Zaragoza, 50018 Zaragoza, Spain.

[b]Networking Research Center on Bioengineering, Biomaterials and Nanomedicine (CIBER-BBN), 28029 Madrid, Spain.

[c]Department of Chemical and Biomolecular Engineering, The Hong Kong University of Science and Technology (HKUST), Clear Water Bay, Kowloon, Hong Kong, China.
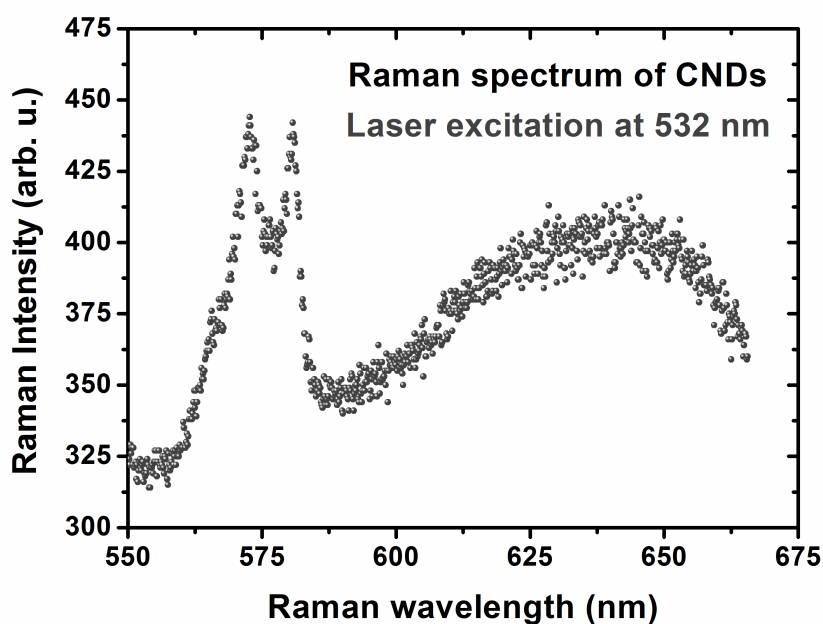
Figure S1: Raman spectrum of the N-CNDs (plotted in wavelength scale) acquired after excitation with an Ar^{+} laser exciting at 532 nm.
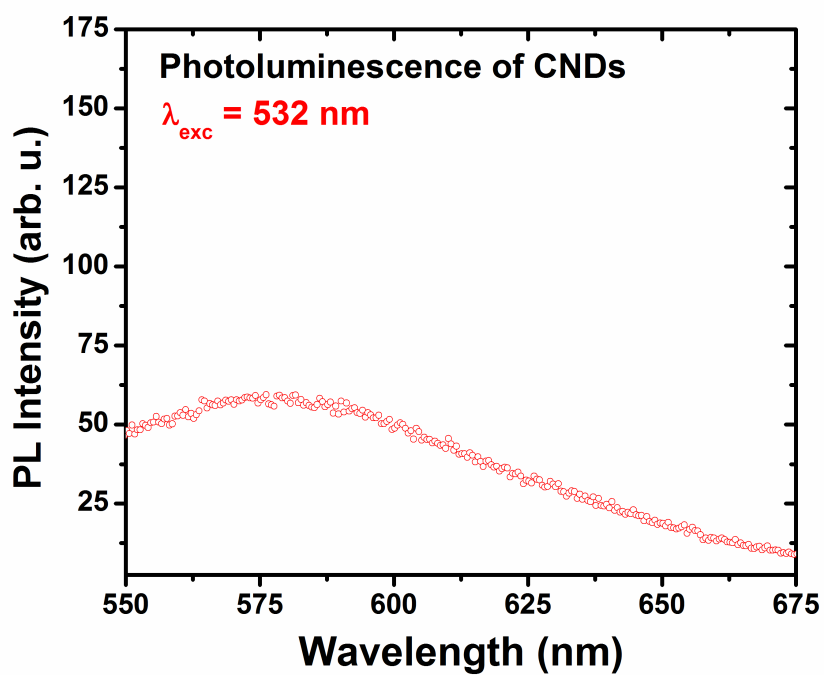
Figure S2: Photoluminescence of the N-CNDs after exciting at 532 nm.
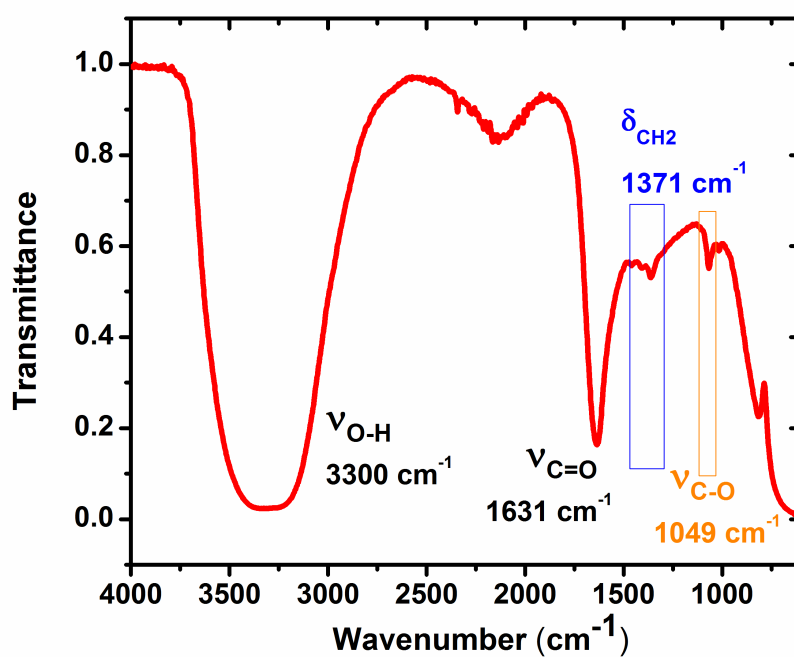
Figure S3: FT-IR spectrum of the carbon nanodots.

166
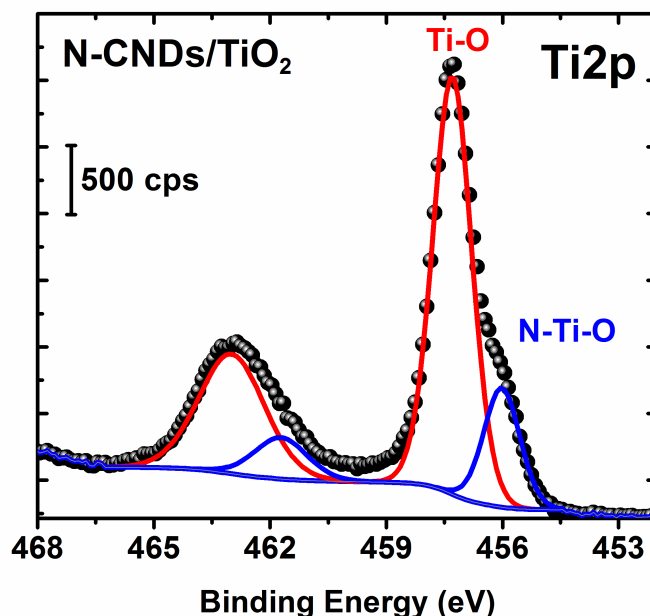
Figure S4: X-ray photoemission spectrum of the Ti2p core level of the CND-TiO$_2$ hybrid catalyst. Interestingly, the spin-orbit split lines of the Ti2p core levels show not only the characteristic peaks of TiO$_2$, but also a second contribution shifted to lower binding energies that corresponds to the interaction of N species with the Ti-O surface. The lower electronegativity of N can promote a higher electron density around the Ti centers thereby contributing to lower BEs (see for instance J. Phys. Chem. Solids 69, 2008, 1657).
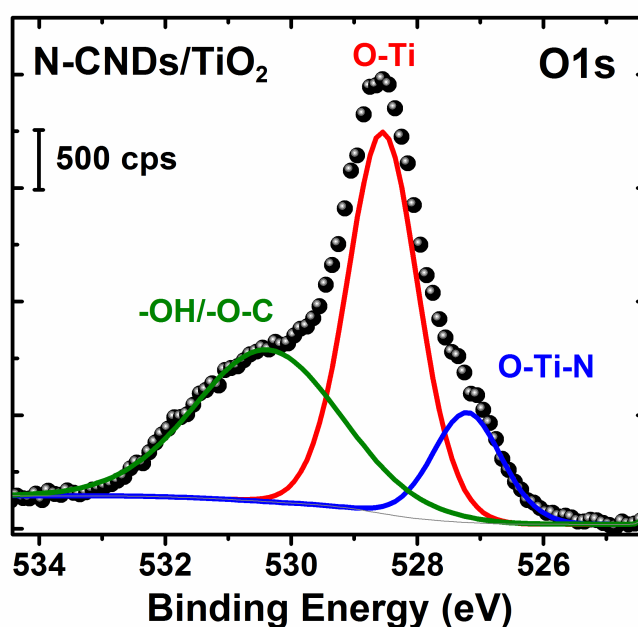
Figure S5: X-ray photoemission spectrum of the O1s core level of the CND-TiO$_2$ hybrid catalyst. the presence of oxygen contributions at 527.3 eV, a relatively low binding energy value, corroborates the formation of novel O-Ti-N linkages previously reported in the literature (see for instance, Chem. Mater. 2005, 17, 6419 or Nanoscale, 2015, 7, 5023) while the contributions at 531-532 eV can be ascribed to the oxidized entities of the deposited carbon dots.
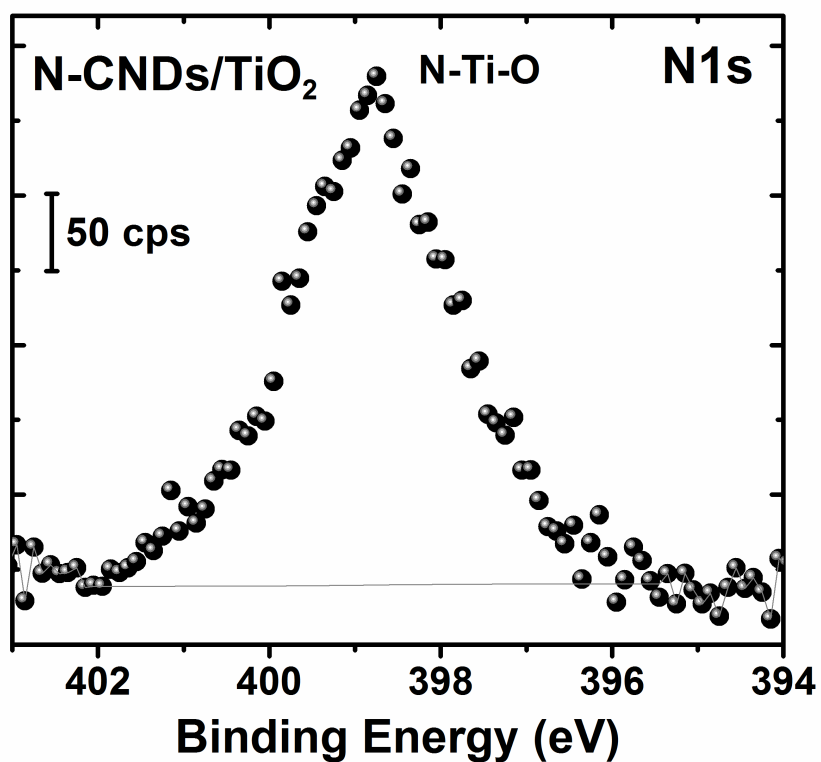
Figure S6: X-ray photoemission spectrum of the N1s core level of the CND-TiO$_2$ hybrid catalyst. The presence of the N1s peak (accounting for 3% atomic wt) is centered at 398.8 eV that has been tentatively assigned to the presence of anionic N$^-$ species that form N-Ti-O linkages thereby confirming the presence of new N entities not present on the surface of the TiO$_2$ before the attachment of the N-CNDs.

IV.3 **Article 3.** Upconverting carbon nanodots as near-infrared activated phototheranostic agents: Dual funtion in bioimaging and photodynamic therapy

IV.4 **Article 4.** Feroxyhyte nanoflakes coupled to up-converting carbon nanodots: a highly active, magnetically recoverable, Fenton-like photocatalyst in the visible-NIR range

ChemComm

CrossMark
← click for updates

Feroxyhyte nanoflakes coupled to up-converting carbon nanodots: a highly active, magnetically recoverable, Fenton-like photocatalyst in the visible-NIR range†

M. C. Ortega-Liebana,[ab] J. L. Hueso,*[ab] A. Larrea,[a] V. Sebastian[ab] and J. Santamaria*[ab]

We demonstrate the enhanced photocatalytic response of a novel Fenton-like heterogeneous catalyst obtained through the assembly of superparamagnetic feroxyhyte nanoflakes synthesized by continuous gas-slug microfluidics and carbon nanodots obtained by pyrolysis from a natural organic source. The novel nanohybrids enable the utilization of the visible and near-infrared ranges due to the active role of the carbon nanodots as up-converting photo-sensitizers. This novel photocatalyst is magnetically recoverable and maintains an excellent response after multiple reutilization cycles. In addition, its synthesis is based on inexpensive and abundant raw materials and its photocatalytic response is evaluated in the presence of energy efficient, affordable light-emitting diodes (LEDs), thereby providing a promising and feasible alternative to the homogeneous Fenton process.

The development of novel catalysts that can be directly activated by sunlight[1] remains a formidable challenge and represents a key step in the realization of processes for the production of environmentally friendly energy (*e.g. via* water splitting to generate hydrogen)[2] or for the remediation of persistent organic pollutants.[3] The photo-Fenton reaction is a well-known example of the advanced oxidation process (AOP) for decontamination that involves the interaction of iron, preferentially Fe(II), and hydrogen peroxide (H_2O_2) to generate highly oxidative radicals in the presence of an external light irradiation source.[4] In recent years, different iron-based heterogeneous catalysts have been investigated to circumvent the major limitations of handling and reutilization associated with the homogeneous reaction.[3–7] Iron (oxyhydro)-oxides either unsupported[2,3,5,8] or deposited onto clay[6,9] or silica supports[10] have been successfully tested for the degradation of multiple pollutants in Fenton-like processes. The photo-catalytic

response of iron-based materials has been improved by the addition of carbon species, the isomorphic substitution of Fe or the combination with matching energy-level semiconductors.[11] Most of these variations have focused on the enhancement of degradation rates in the visible range. Novel nanostructured materials in combination with sensitizers that enable wider utilization of the whole solar spectrum including the near-infrared (NIR) range have not been reported, to the best of our knowledge, for the Fenton reaction. In this work we present the synergistic combination of novel up-converting carbon nanodots (CNDs) and nanoflakes of a relatively unexplored ferrimagnetic feroxyhyte (δ-FeOOH) phase with a graphene-like layered nanostructure.[12,13] We have evaluated the performance of this novel composite as a magnetically recoverable Fenton-like photocatalyst with a high surface area and capable of exhibiting a photocatalytic response beyond the visible range.

Fig. 1a shows a low-magnification TEM image of the ultra-thin nanoflakes synthesized using a continuous microfluidic system segmented by O_2 slugs[13] (see the Experimental section for further details and Fig. S1, ESI,† therein). The obtained nanoflakes exhibited mean sizes of 15 ± 5 nm along the largest width axis and thickness of 2–4 nm. HR-TEM and electron diffraction analysis (Fig. 1b and c) further corroborated the formation of a single and highly anisotropic *P3m*1 crystalline phase corresponding to feroxyhyte (δ-FeOOH). The high availability of exposed area in the suspended feroxyhyte nanoflakes (Fe-NFs) (estimated in 80 m^2 g^{-1} for the pseudo-planar configuration) facilitates both its catalytic role and the assembly of the CNDs, while their superparamagnetic nature (see Fig. S2, ESI†) enables their reutilization *via* magnetic recovery.

On the other hand, carbon nanodots (CNDs) represent an excellent choice as sensitizers due to the abundance of potential precursors for their inexpensive production, their resistance to photo-bleaching and their recently discovered up-converting optical properties.[14–16] We have prepared novel carbon nanodots by pyrolysis of ground leaves obtained from the popular Argentinian *Mate herb* (see the ESI†). Fig. 1d shows a TEM image of the carbon nanodots with an average size

a *Institute of Nanoscience of Aragon (INA) and Department of Chemical Engineering and Environmental Technology, University of Zaragoza, 50018 Zaragoza, Spain.*
E-mail: Jesus.Santamaria@unizar.es, jlhueso@unizar.es

b *Networking Research Center on Bioengineering, Biomaterials and Nanomedicine (CIBER-BBN), 28029 Madrid, Spain.*

† Electronic supplementary information (ESI) available: Experimental details on the synthesis of the catalysts and their photocatalytic activity at different pHs. See DOI: 10.1039/c5cc05387k
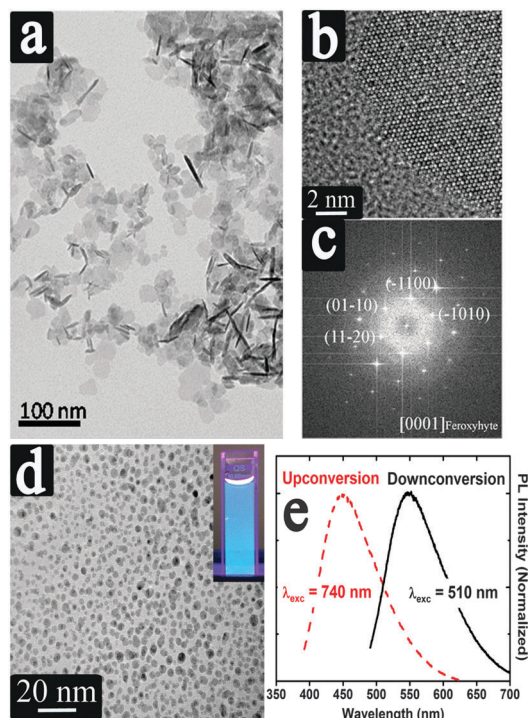
Fig. 1 (a) Low magnification TEM image of the feroxyhyte nanoflakes obtained by oxygen–liquid segmented flows; (b) HR-TEM image of a single feroxyhyte nanoplatelet nanoflake; (c) electron diffraction analysis performed by FFT showing the hexagonal packing with $P3m1$ phase corresponding to the δ-FeOOH layered structure; (d) TEM image of the carbon nanodots obtained after calcination and purification steps; inset: fluorescence observed in a colloidal suspension of the CNDs under a UV lamp (λ_{exc} = 365 nm); (e) normalized photoluminescence emission spectra of the CNDs after excitation at 510 nm (down-conversion) and 740 nm (up-conversion), respectively.

Fig. 2 (a) TEM image of the Fe-NF/CND (0.25 wt%) hybrid photocatalyst after the assembly process; white arrows show spherical CNDs and black arrows remark the presence of the Fe-NF in planar and perpendicular views; (b) band-gap energies for the Fe-NF (circles) and Fe-NF/CNDs (stars) were calculated by extrapolation of the Tauc plots assuming direct transition orders.

distribution of 3.0 ± 1.1 nm (see Fig. S3, ESI†). Notably, these CNDs not only exhibit the expected down-conversion behavior of semiconducting quantum dots (e.g. emission wavelengths at lower energies than the excitation source as shown in Fig. 1e and Fig. S4, ESI†) but also a remarkable up-conversion capability, responding to excitation in the NIR range with emission at higher energies (i.e. shorter wavelengths as shown in Fig. 1e and Fig. S4, ESI†). The facile self-assembly procedure used to form the Fe-NF/CND hybrid photocatalysts involved a simple dispersion of the NFs in a solution of CNDs under vigorous stirring, followed by vacuum-assisted drying (see the ESI†). Fig. 2a shows a TEM image of the resulting composite where CNDs are distributed throughout the pseudo-planar structures of feroxyhyte and further confirmed by STEM-EDX analysis (Fig. S5, ESI†). Tauc plots[11] (Fig. 2b and ESI†) were used to determine band gap energies for the feroxyhyte nanoflakes and the composites containing carbon nanodots, respectively. Assuming direct transitions, band gap energy levels for the feroxyhyte nanoflakes was estimated to be ∼2.25 eV (ca. 550 nm) which is within the range of previously reported nanostructured FeOOH phases.[2,8,11] Likewise, the composite containing the CNDs rendered a band-gap energy extrapolated at ∼2.35 eV (ca. 528 nm).

The effect of the absorbance enhancement on the photocatalytic performance of these nanohybrids was assessed using the decoloration of methyl orange (MO) as model reaction. Two LED sources at specific wavelengths of 532 nm (visible range) and 740 nm (NIR range) were separately used to differentiate the up-converting effect of CNDs and their contribution to expand the photocatalytic activity beyond the visible range. In addition, control experiments of uncatalyzed photolysis (i.e. no solid catalyst) and with Fe-NFs without CNDs were also performed at both LED irradiation wavelengths. None of the control experiments in the absence of catalyst rendered any significant MO decoloration (Fig. 3a–c). On the other hand, the Fenton-like process only occurred with the simultaneous combination of light, hydrogen peroxide (H_2O_2) and feroxyhyte. As expected in the visible irradiation window, and despite using a low power-green emitting LED (10 W), total decoloration of MO was achieved after 90 min with the aid of the feroxyhyte NFs (see Fig. 3a).

As previously reported,[4,7] this iron oxide polymorph and other analogous phases such as goethite are effective photo-Fenton agents after adsorption of the organic contaminant and the formation of photo-responsive surface intermediates (e.g. Fe(III)–OH and Fe(III)–OOH) that react with H_2O_2 to generate highly reactive chemical intermediates that can readily oxidize the organic contaminants:[4,5,8,11]

Scheme 1 Schematic illustration of the electron transfer mechanism between the Fe-NFs and the CNDs acting as sensitizers. CNDs might play the role of providing additional energy levels to reduce recombination events in the Fe-NFs as well as photo-generating additional excitons in both the visible and NIR windows to render highly reactive radicals.
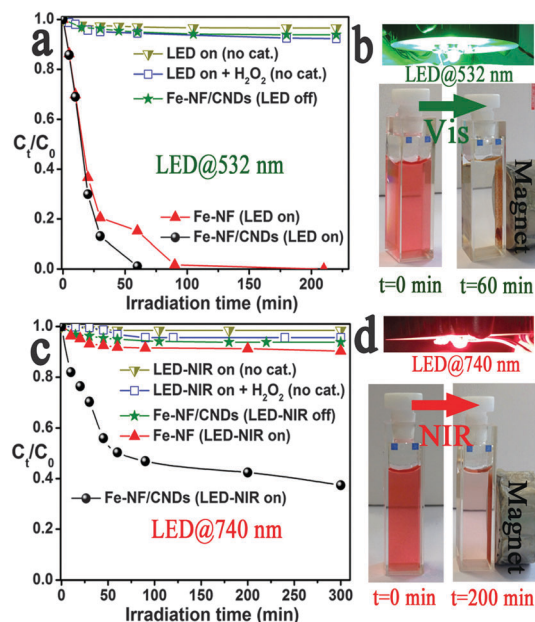
Fig. 3 (a) Time-dependence decoloration of MO in the Fenton-like process carried out under different experimental conditions (see the text) in the presence of a LED exciting at 532 nm; (b) digital images showing details of the green LED and the evolution of the MO decoloration after 60 min in the Fenton-like reaction carried out with the Fe-NF/CND hybrid that is also recovered with a magnet; (c and d) time-dependence decoloration and evolution of the dye under analogous experimental conditions but using a LED-NIR exciting at 740 nm. Experimental conditions: pH = 2.8; [photo-catalysts] = 0.2 g L^{-1}; [H$_2$O$_2$] = 2 mM; [MO] = 25 mM.

$$Fe(III)_{surface} + H_2O_{2(adsorbed)} \rightarrow Fe(II)_{surface} + {}^{\bullet}O_2H + H^+ \quad (1)$$

$$Fe(II)_{surface} + H_2O_{2(adsorbed)} \rightarrow Fe(III)_{surface} + {}^{\bullet}OH + OH^- \quad (2)$$

$$Fe(III)_{surface} + H_2O \rightarrow Fe(II)_{surface} + {}^{\bullet}OH + H^+ \quad (3)$$

$$Fe(III)_{surface} + OH^- \rightarrow Fe(II)_{surface} + {}^{\bullet}OH \quad (4)$$
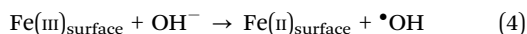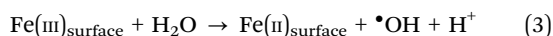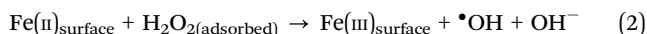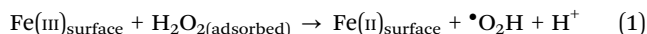
More detailed reaction pathways for heterogeneous Fenton-like processes have been previously addressed elsewhere.[4,6,7] The Fe-NF/CND hybrid photocatalyst was able to enhance the Fenton-like process efficiency, and as a consequence the total decoloration time was reduced to 60 min (Fig. 3a and Fig. S6, ESI†). This improvement can be tentatively attributed to the active role played by carbon nanodots as photo-sensitizers either providing additional exciting photons (Fig. 1e and Scheme 1) to generate more oxidative intermediates or alternatively reducing the electron–hole (e$^-$/h$^+$) recombination rates in the Fe-NFs to enhance the photocatalytic response of Fe-NFs. The latter assumption is based on previous reports on TiO$_2$–CND photocatalytic systems[15] although no direct evidence has been provided in our case. The enhancement produced by the hybrid catalyst was more dramatic when only NIR light was used, with a LED at 740 nm. In this case *ca.* 60% decoloration of MO was achieved in 200 min, while the corresponding figure for the Fe-NFs (feroxyhyte phase alone) was six times lower (Fig. 3c and Fig. S6, ESI†).

These results strongly suggest that CNDs behave as active up-converters able to absorb two-photons that lead to the emission of higher energy photons (Fig. 1e and Scheme 1) *via* an underlying intermediate energy state.[14,17–19] In turn, these high energy photons further excite the feroxyhyte nanoflakes generating new (e$^-$/h$^+$) pairs that initiate the Fenton-like process as described for the NIR irradiation (Scheme 1). An analogous mechanism has been previously claimed for CND/Cu$_2$O composites[20] or libethenite microcrystals[21] using NIR excitation sources. Moreover, unsupported CNDs have also been successfully tested for the selective oxidation of alcohols through the NIR assisted formation of $^{\bullet}$OH radicals.[22] The generation of these hydroxyl radicals in our Fenton-like process was further demonstrated *via* spectroscopic monitoring of a fluorescent probe specifically formed after reaction with $^{\bullet}$OH (see the ESI† and Fig. S7).[23] Alternatively, a scavenging and inhibitory agent such as methanol[8] was also tested to indirectly demonstrate the formation of hydroxyl radicals and their active role in the MO decoloration process beyond a reversible photo-switching mechanism (see the ESI† and Fig. S8).[24] The trend observed in the formation of $^{\bullet}$OH was quite consistent and equivalent to the MO decoloration rates, even at higher pH values where the photocatalytic response progressively diminished (Fig. S7–S10, ESI†). We could not attribute the change in activity to the increasing presence of more photo-active Fe ions leached from the catalyst surface under acidic conditions (based on ICP analysis after 24 h in an acidic solution at pH = 3).[5] As previously reported[7,25] and based on ζ-potential measurements (see Fig. S11, ESI†) and the enhanced adsorption of MO in the dark at lower pH values (see Fig. S12, ESI†), we postulate a better electrostatic interaction between the anionic dye and the solid photocatalyst surface at pH = 2.8 when the composite almost reaches its isoelectric point. Moreover, it has also been postulated that H$_2$O$_2$ loses its oxidizing capabilities in basic media[25] since it decomposes to molecular oxygen and H$_2$O. Also, it has been claimed that the MO dye specifically prefers the quinoid structure at lower pH values and that this form is more prone to

undergo degradation in the presence of $^\bullet$OH and $^\bullet$OOH radicals than the benzenoid form.[25]

Finally, it is worth mentioning that in addition to their main characteristic, *i.e.*, enabling the use of light across a wider spectrum, the Fe-NF/CND hybrids present other significant advantages such as: (i) the inherent magnetic response (see Fig. 3b–d and Fig. S2, ESI†) that allowed the efficient recycl-ability of the catalyst (the same performance was obtained through 4 consecutive MO decoloration cycles using recycled catalysts, see Fig. S13, ESI†); (ii) the excellent response obtained in the presence of highly energy efficient, low power LED sources offers a more environmentally attractive alternative to higher power halogen lamps that are typically used in these studies.

Notes and references

1 A. Kubacka, M. Fernandez-Garcia and G. Colon, *Chem. Rev.*, 2012, **112**, 1555–1614.
2 M. C. Pereira, E. M. Garcia, A. C. da Silva, E. Lorencon, J. D. Ardisson, E. Murad, J. D. Fabris, T. Matencio, T. D. Ramalho and M. V. J. Rocha, *J. Mater. Chem.*, 2011, **21**, 10280–10282.
3 W. Wu, C. Z. Jiang and V. A. L. Roy, *Nanoscale*, 2015, **7**, 38–58.
4 S. S. Lin and M. D. Gurol, *Environ. Sci. Technol.*, 1998, **32**, 1417–1423.
5 M. C. Pereira, L. C. A. Oliveira and E. Murad, *Clay Miner.*, 2012, **47**, 285–302.
6 E. G. Garrido-Ramirez, B. K. G. Theng and M. L. Mora, *Appl. Clay Sci.*, 2010, **47**, 182–192.
7 W. P. Kwan and B. M. Voelker, *Environ. Sci. Technol.*, 2004, **38**, 3425–3431.
8 I. S. X. Pinto, P. Pacheco, J. V. Coelho, E. Lorencon, J. D. Ardisson, J. D. Fabris, P. P. de Souza, K. W. H. Krambrock, L. C. A. Oliveira and M. C. Pereira, *Appl. Catal., B*, 2012, **119**, 175–182.
9 J. H. Ramirez, C. A. Costa, L. M. Madeira, G. Mata, M. A. Vicente, M. L. Rojas-Cervantes, A. J. Lopez-Peinado and R. M. Martin-Aranda, *Appl. Catal., B*, 2007, **71**, 44–56.
10 H. Lim, J. Lee, S. Jin, J. Kim, J. Yoon and T. Hyeon, *Chem. Commun.*, 2006, 463–465.
11 L. V. C. Lima, M. Rodriguez, V. A. A. Freitas, T. E. Souza, A. E. H. Machado, A. O. T. Patrocinio, J. D. Fabris, L. C. A. Oliveira and M. C. Pereira, *Appl. Catal., B*, 2015, **165**, 579–588.
12 P. Z. Chen, K. Xu, X. L. Li, Y. Q. Guo, D. Zhou, J. Y. Zhao, X. J. Wu, C. Z. Wu and Y. Xie, *Chem. Sci.*, 2014, **5**, 2251–2255.
13 A. Larrea, V. Sebastian, A. Ibarra, M. Arruebo and J. Santamaria, *Chem. Mater.*, 2015, **27**, 4254–4260.
14 Z. X. Gan, X. L. Wu, G. X. Zhou, J. C. Shen and P. K. Chu, *Adv. Opt. Mater.*, 2013, **1**, 554–558.
15 S. J. Zhu, Y. B. Song, X. H. Zhao, J. R. Shao, J. H. Zhang and B. Yang, *Nano Res.*, 2015, **8**, 355–381.
16 S. Y. Lim, W. Shen and Z. Q. Gao, *Chem. Soc. Rev.*, 2015, **44**, 362–381.
17 S. N. Baker and G. A. Baker, *Angew. Chem., Int. Ed.*, 2010, **49**, 6726–6744.
18 S. L. Hu, A. Trinchi, P. Atkin and I. Cole, *Angew. Chem., Int. Ed.*, 2015, **54**, 2970–2974.
19 H. T. Li, X. D. He, Z. H. Kang, H. Huang, Y. Liu, J. L. Liu, S. Y. Lian, C. H. A. Tsang, X. B. Yang and S. T. Lee, *Angew. Chem., Int. Ed.*, 2010, **49**, 4430–4434.
20 H. T. Li, R. H. Liu, Y. Liu, H. Huang, H. Yu, H. Ming, S. Y. Lian, S. T. Lee and Z. H. Kang, *J. Mater. Chem.*, 2012, **22**, 17470–17475.
21 G. Wang, B. B. Huang, X. C. Ma, Z. Y. Wang, X. Y. Qin, X. Y. Zhang, Y. Dai and M. H. Whangbo, *Angew. Chem., Int. Ed.*, 2013, **52**, 4810–4813.
22 H. T. Li, R. H. Liu, S. Y. Lian, Y. Liu, H. Huang and Z. H. Kang, *Nanoscale*, 2013, **5**, 3289–3297.
23 C. H. Fang, H. L. Jia, S. Chang, Q. F. Ruan, P. Wang, T. Chen and J. F. Wang, *Energy Environ. Sci.*, 2014, **7**, 3431–3438.
24 W. S. Wang, Y. F. Ye, J. Feng, M. F. Chi, J. H. Guo and Y. D. Yin, *Angew. Chem., Int. Ed.*, 2015, **54**, 1321–1326.
25 N. Panda, H. Sahoo and S. Mohapatra, *J. Hazard. Mater.*, 2011, **185**, 359–365.

IV.4.1 Supporting Information of Article 4

<div align="center">

Chemical Communications

</div>

Feroxyhyte nanoflakes coupled to up-converting carbon nanodots: a highly active, magnetically recoverable, Fenton-like photocatalyst in the visible-NIR range

M.C. Ortega-Liebana[a,b], J.L. Hueso[a,b,*], A. Larrea[a], V. Sebastian[a,b] and J. Santamaria[a,b,*]

[a]Institute of Nanoscience of Aragon (INA) and Department of Chemical Engineering and Environmental Technology, University of Zaragoza, 50018 Zaragoza, Spain.

[b]Networking Research Center on Bioengineering, Biomaterials and Nanomedicine (CIBER-BBN), 28029 Madrid, Spain.

Experimental Section

Chemicals

Potassium nitrate (≥99% KNO_3, Fluka,), Ferrous sulfate heptahydrate (≥99%, $FeSO_4 \cdot 7 H_2O$, Aldrich), Sodium hydroxide (≥98% NaOH, Aldrich), L-lysine crystallized (≥98% $C_6H_{14}N_2O_2$, Aldrich), Sulfuric acid (95-98%, H_2SO_4, Aldrich), Methyl Orange (ACS reagent, 85% dye, Aldrich), Methanol (HPLC >99.9%, Aldrich), Hydrogen peroxide solution (30 wt% in H_2O, Aldrich), Terephthalic acid (98%, Aldrich).

Synthesis of δ-FeOOH nanoflakes

In a typical synthesis, two solutions, namely A and B, were prepared in deionized water and bubbled in Ar for 15 minutes to promote deoxygenation. The solution A consists of 180 mM KNO_3, 162 mM NaOH and 1.85 mM L-lysine. On the other hand, solution B was composed of 13 mM ferrous sulfate heptahydrate and 3,38 mM sulfuric acid. After de-oxygenation, each solution was placed in 60 mL plastic Becton Dickinson syringes. Solutions A and B were injected at a proper flow rate to obtain a 1 minute residence time according to the microfluidic system volume. Solution A and B streams were mixed in a PEEK polymer Y-junction under a constant flow ratio of 1:1 in order to ease the synthesis procedure. The microfluidic system is composed of two PTFE coils

(1/16 inch OD and 0.04 inch ID), which are conceived as mixing and reaction stages, respectively (see Figure S1). The mixing of A and B streams was promoted by sonication in an ultrasonic bath, maintaining the bath temperature in the range of 25-30 ^{o}C using a cooling bath. A pure oxygen gas stream was injected after the mixing coil to obtain a stable gas-liquid segmented flow in the reaction stage. The temperature at the reaction stage was set at 100 ^{o}C maintaining the reactor pressure at 1.4 bar. The synthesized nanoparticles were centrifuged at 10,000 rpm for 10 minutes and re-suspended in distilled water.
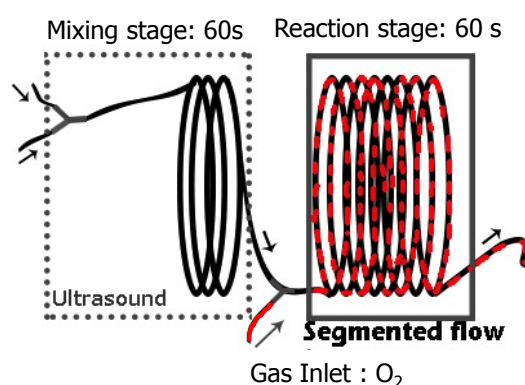
Figure S1: Schematic diagram of the continuous oxygen-liquid segmented flow setup used to prepare the feroxyhyte nanoflakes.

Synthesis of Carbon Nanodots

Mate herb was selected as carbon precursor. The plants were dried out and ground prior to a calcination step at 300 ^{o}C for 2 h in air. The resulting solid was re-suspended in ultrapure water and centrifuged at 6.000 rpm for 10 min to remove large aggregates. The final suspension with a brownish yellow color contained the carbon nanodots and was stored at room temperature.

Synthesis of δ-FeOOH Nanoflakes/Carbon Nanodots hybrids

Fe-NFs/CNDs hybrids were assembled via a drying-vacuum step at low temperature. Typically, 0.2 g Fe-NFs were suspended in a mixture of 1 mL CNDs (0.5 mg/mL) and 1 mL deionized water, and stirred vigorously for 30 min. Then, the suspension was dried at 65 ^{o}C in a vacuum-driven oven during 60 min.

Photo-Fenton catalytic experiments

The Photo-Fenton like activity was evaluated by measuring the decomposition rate of methyl orange (MO) in aqueous solution in the presence of two different LEDs (LED ENGIN, LZ4 models) emitting either at 532 nm (10 W) or 740 nm (6.3 W), respectively. In a typical reaction for decoloration, 0.6 mg of catalyst was dispersed in 3 mL of MO solution (25 mM). Prior to irradiation with LEDs, the suspension was magnetically stirred in the dark for 30 minutes to ensure the establishment of an adsoption/desortion equilibrium, followed by addition of H_2O_2 (2 mM). Different aliquots were taken at selected time intervals and analyzed by UV-Vis spectroscopy (V-67, Jasco Company) after retrieval of the catalyst. The experiments were performed at different pH values for systematic comparison.

Detection of hydroxyl radicals

The generation of hydroxyl radicals (·OH) during the Fenton-like process under LED illumination was monitored with the aid of terephthalic acid (TA). TA can generate a fluorescent derivative (2-hydroxy-terephthalic acid: HTA) emitting at ca. 425 nm after reacting with hydroxyl radicals according to the following reaction:
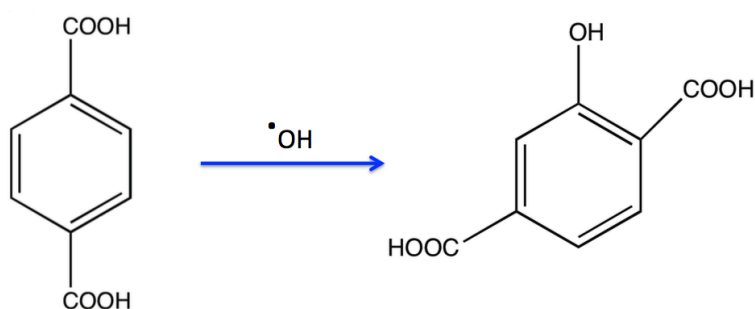
Scheme S1: Reaction of the non-fluorescent terephthalic acid probe with hydroxyl OH radicals to yield a fluorescent derivative emitting at 425 nm.

In a typical experiment, 0.6 mg of catalyst was dispersed in the probe solution containing TA (3 mL, 5 mM, pH at 4.8 or re-adjusted at 7.9 with NaOH) and deposited in a cuvette with 1 cm path length. Prior to irradiation with LEDs, the suspension was magnetically stirred in the dark for 30 minutes followed by addition of H_2O_2 (2 mM).

Different aliquots were taken after selected irradiation time intervals and analyzed by fluorescence spectroscopy without retrieval of the catalyst. The experiments were performed at pH > 4 values to ensure the stability of the HTA fluorescent derivative.

Additionally, a set of experiments with the presence of increasing concentrations of methanol (a well-known hydroxyl radical scavenger) was also carried out for the most favorable conditions (pH = 2.8; LED visible; Fe-NF/CND hybrid). Different volumetric ratios MeOH:H_2O (0:1 / 0.25:0.75 / 0.5: 0.5) were tested under our photocatalytic decoloration conditions in order to evaluate the inhibition of the dye decoloration in the presence of increasing amounts of methanol.

Characterization techniques

The morphologies and particle size distributions were determined with the aid of a T20-FEI microscope with a LaB_6 electron source. Aberration corrected scanning transmission electron microscope images were additionally acquired using a high angle annular dark field detector (STEM-HAADF) in a FEI XFEG TITAN electron microscope operated at 80 kV equipped with a CETCOR Cs-probe corrector and an electron-dispersive spectroscopy (EDS) detector for elemental analysis. At least 200 particles were measured to evaluate the mean diameter of the particles and size distribution. To prepare the sample, the nanoparticle suspension was diluted with water prior to casting on a holey carbon TEM grid. The absorbance spectra of the different nanoparticles and the decoloration of methyl orange (MO) were monitored in a UV-visible-NIR spectrophotometer (V-67, Jasco Company) with a quartz cell of 1 cm light path. Samples were previously filtered through 0.2 µm Millex nylon membrane filters from Millipore. The determination of band gap energies was carried out assuming direct transitions (n) and plotting the following equation: $(\alpha h v) = A (h v - E_g)^{n/2}$ where α, h, v, A and E_g represent the absorption coefficient, Planck´s constant, light frequency, proportionality constant and band gap energy, respectively. Fluorescence measurements were performed using a LS55 Fluorescence Spectrometer (PerkinElmer) equipped with a xenon arc lamp as the light source and a quartz cell (10 x 10 mm). Iron leaching experiments under acidic conditions were quantified by Microwave Plasma-

Atomic Emission Spectrometer (Agilent 4100 MP-AES). The samples (2.5 mL) were digested with 1 mL of an acidic mixture containing HCl:HNO$_3$ (3:1 volumetric ratios) at 65 ºC for 2 h. The digested suspension was diluted with Milli-Q water to a final volume of 5 mL for spectrometric analysis. No traces of leached ionic iron were detected above the threshold detection limit of the equipment (0.05 ppm). The magnetic properties of the different nanoparticles were measured as dried powders after solvent evaporation at different temperatures in a superconducting quantum interference device (SQUID MPMS-5S, Quantum Design) from 0 to 40000 Oe. The samples were measured in a gelatin capsule (a diamagnetic correction for the sample holder was carried out). Magnetic hysteresis loops (plot of the magnetization of the sample as a function of the magnetic field strength) were evaluated at 37 °C.

Additional Figures
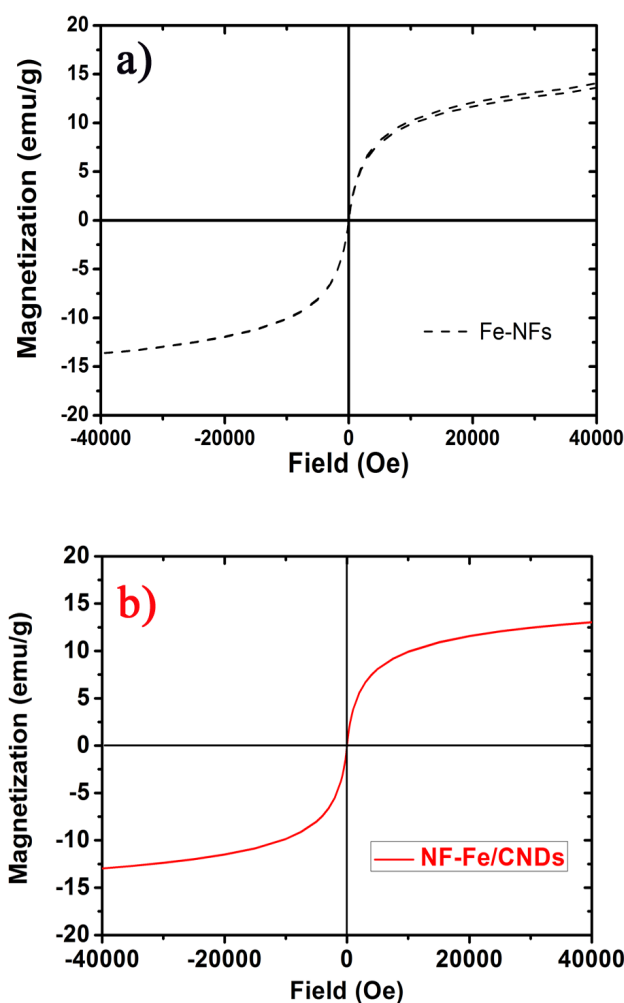
Figure S2. Magnetization curves corresponding to: a) the feroxyhyte nanoflakes and b) the composite photocatalyst measured at 37 °C.
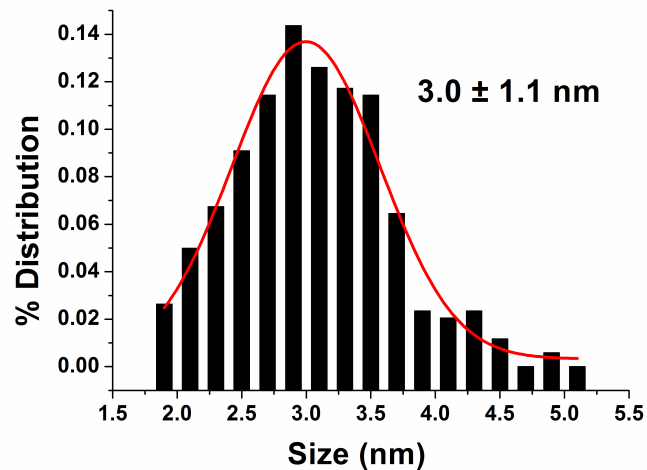
Figure S3. Particle size distribution of carbon nanodots after purification
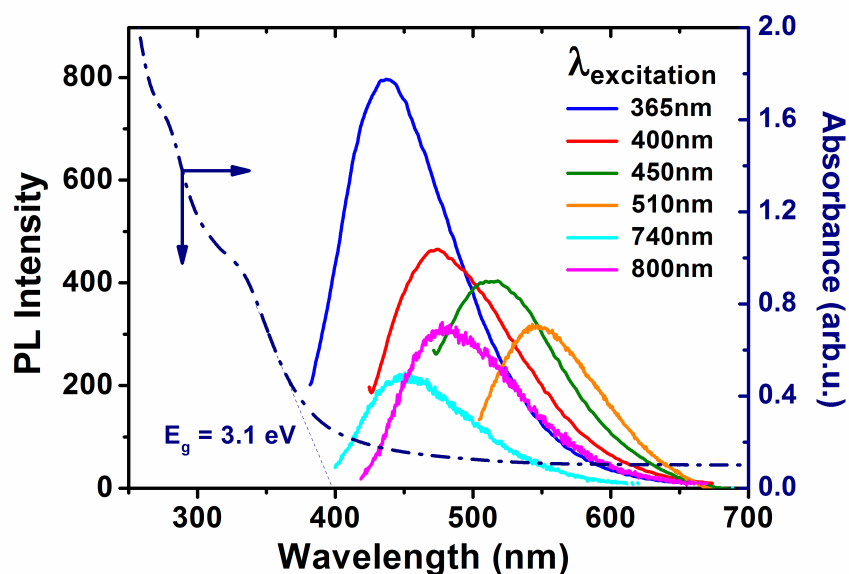
Figure S4. UV-Vis absorbance spectrum and Photoluminescence spectra acquired at room temperature in DI-H$_2$O at different excitation wavelengths corresponding to the upconverting carbon dots. Band gap energy is determined from the extrapolation of the absorbance spectrum. Note that the absorption spectrum does not decay totally and a fraction extends throughout the whole visible range.
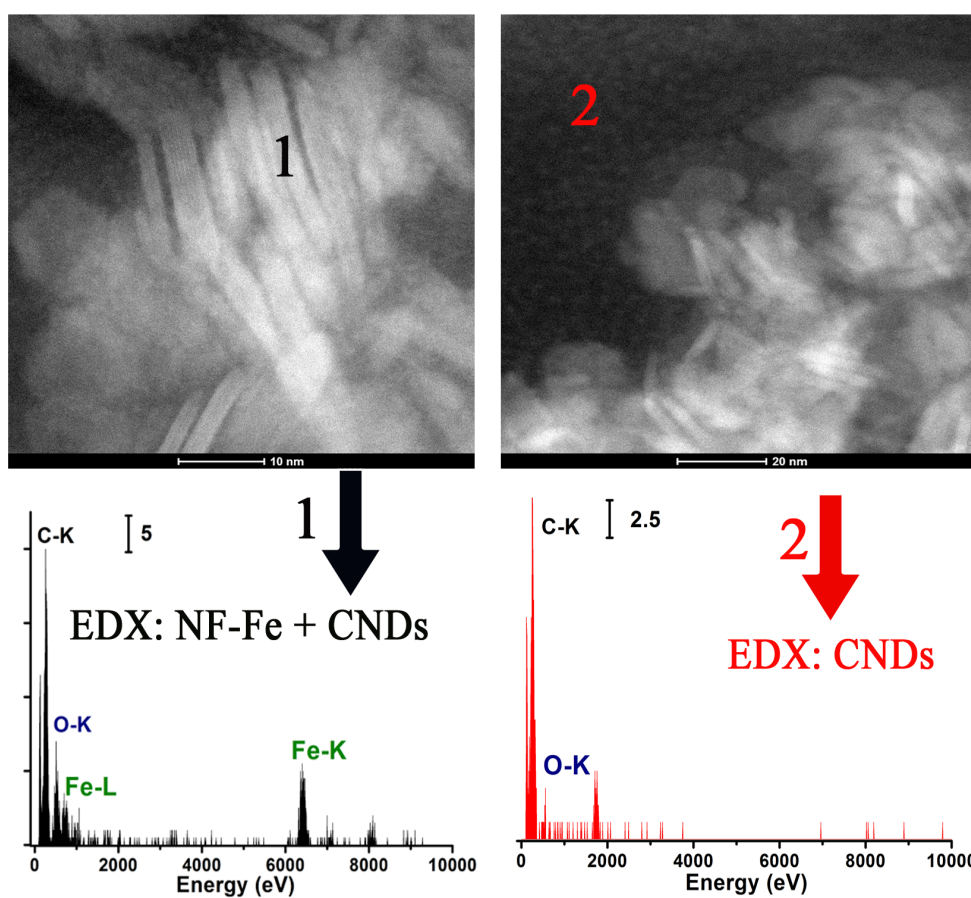
Figure S5. STEM images of the NF-Fe/CNDs composites and EDS analysis corresponding to different areas where CNDs are isolated (spot 2) or in the presence of the Fe-NFs (spot 1).
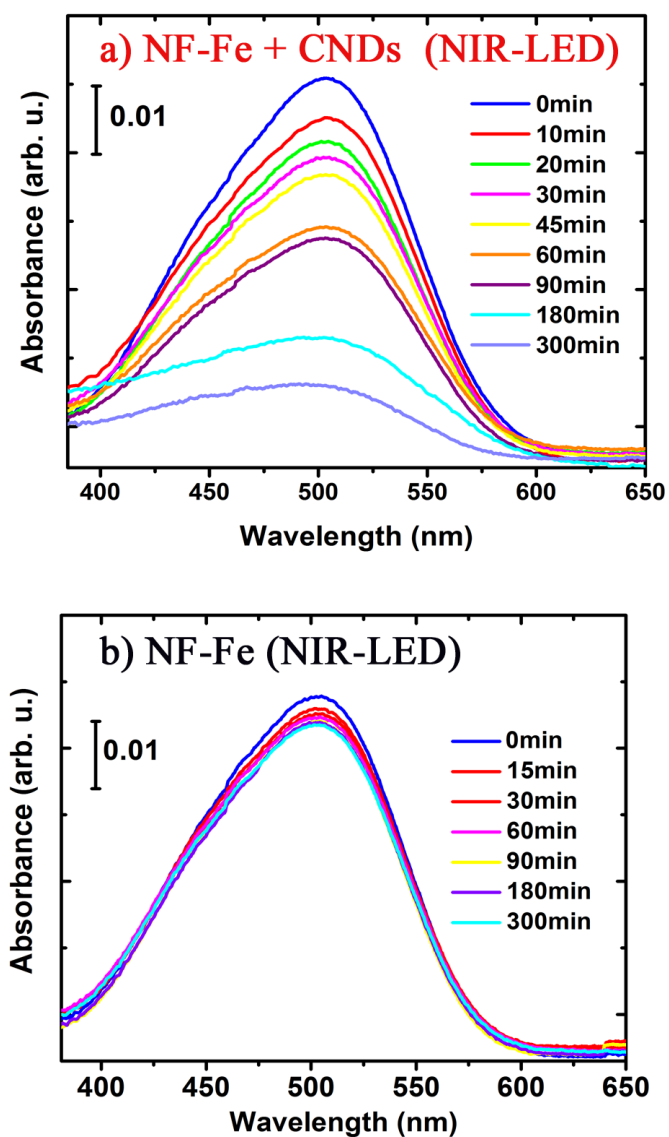
Figure S6. UV-Vis absorption spectra of the MO decoloration induced after different irradiation times under the NIR-LED source: a) in the presence of the NF-Fe/CND composite and b) in the presence of the NF-Fe only.
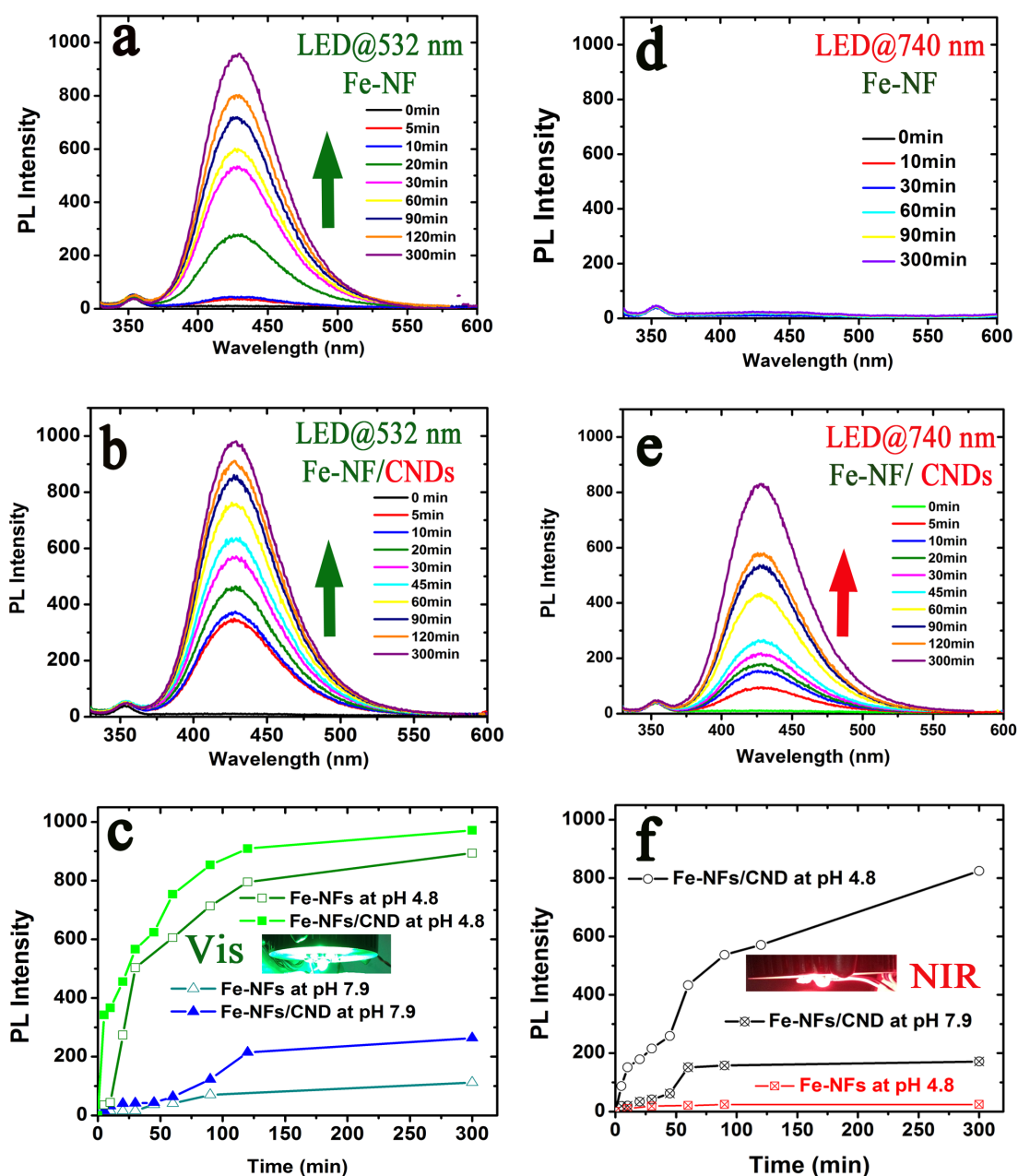
Figure S7. Direct quantification of ·OH radicals formation using terephthalic acid as fluorescent probe that emits in the presence of hydroxyl radicals according to the reaction shown in the Scheme S1; a-b) Fluorescence emission spectra of the terephtalate derivative formed upon different irradiation times under the visible LED at 532 nm and pH = 4.8 for the feroxyhyte nanoflakes and the composite with CNDs, respectively; c) Fluorescence intensity vs time curves corresponding to the experiments carried out at different pH values and the LED-Visible; d-e) Fluorescence emission spectra of the terephtalate derivative formed upon different irradiation times under the NIR-LED at 740 nm and pH = 4.8 for the feroxyhyte nanoflakes and the composite with CNDs, respectively; f) Overview of the evolution of fluorescence intensity vs time corresponding to the experiments carried out at different pH values and the NIR-LED. [MO] = 25 mM; [H$_2$O$_2$] = 2 mM.
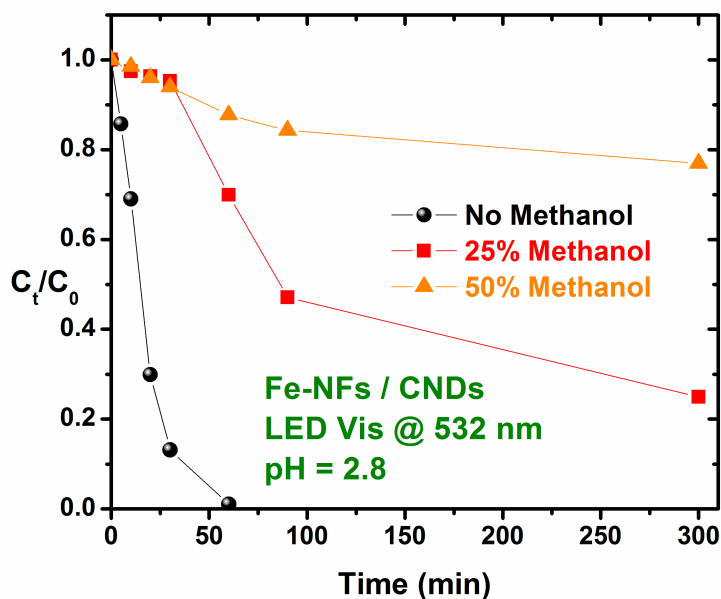
Figure S8. Evaluation of the scavenging effect of increasing amounts of methanol (expressed in % vol. respect to water) on the decoloration of MO using the feroxyhyte/CND composite at pH = 2.8 and under irradiation with the green LED. [MO] = 25 mM; [H_2O_2] = 2 mM.
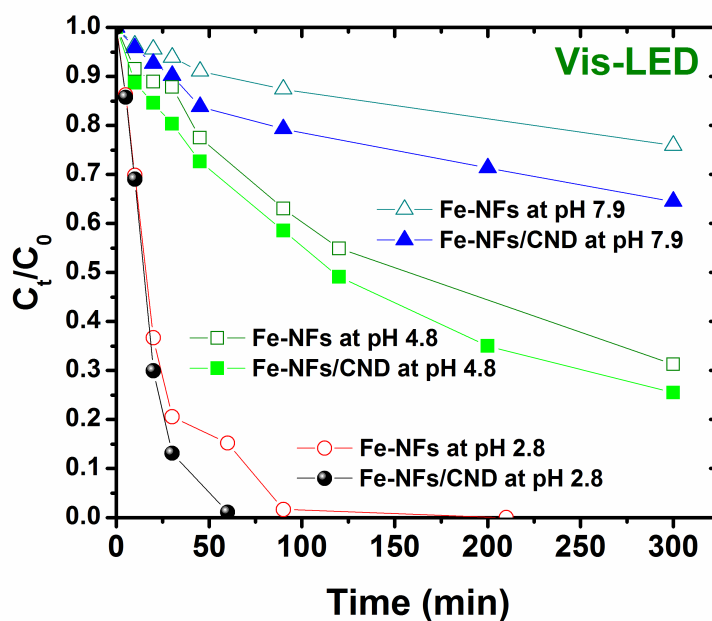
Figure S9. Effect of pH on the decoloration of MO using a 532 nm green LED in the presence of Fe-NFs/CNDs hybrids and Fe-NFs, respectively.
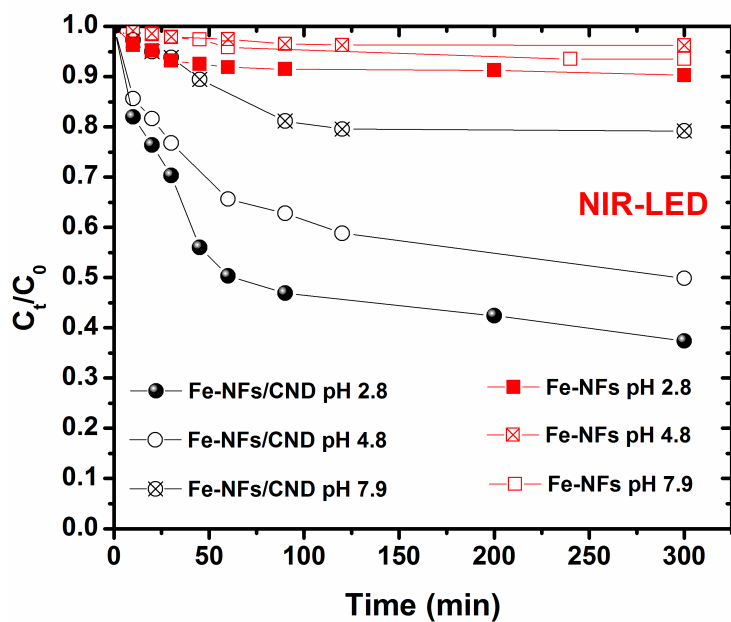
Figure S10. Effect of pH on the decoloration of MO using a 740 nm red-emitting LED in the presence of Fe-NFs/CNDs hybrids and Fe-NFs, respectively.
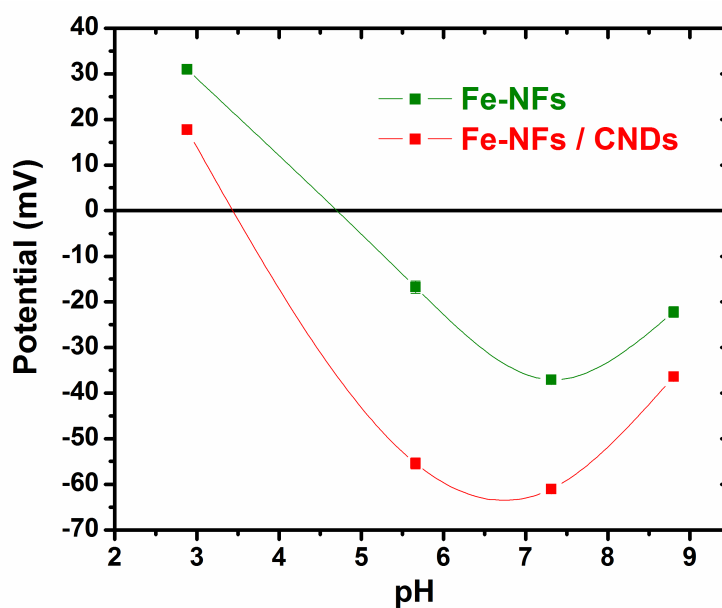
Figure S11. ζ-potential values of the feroxyhyte nanoflakes, the carbon nanodots and the Fenton-like composite catalyst at different pH.
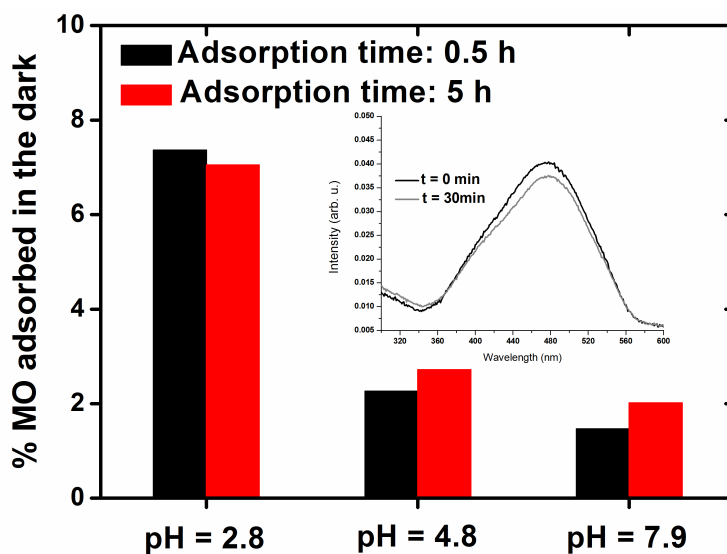
Figure S12. Influence of pH values and adsorption times on the amount of methyl orange adsorbed in the dark by the NF-Fe/CND composite. The inset corresponds to the adsorption carried out at pH = 2.8 after 30 minutes in the dark. The initial concentration of MO was 25 mM.
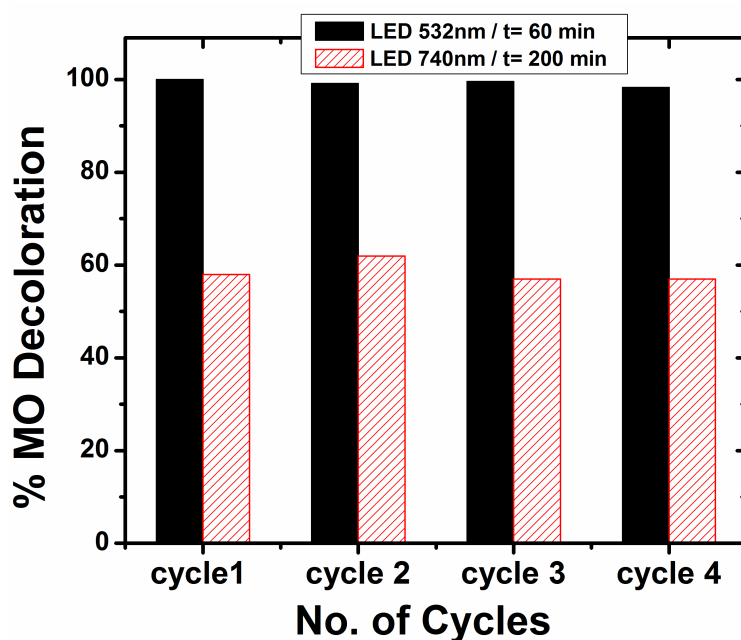
Figure S13. Recyclability of the Fe-NFs/CNDs hybrids after magnetic recovery.

Extraordinary sensitizing effect of co-doped carbon nanodots derived from mate herb: Application to enhanced photocatalytic degradation of chlorinated wastewater compounds under visible light

M. Carmen Ortega-Liebana [a,b], Jose L. Hueso [a,b,*], Shammi Ferdousi [c], Raul Arenal [d,e], Silvia Irusta [a,b], King L. Yeung [c], Jesus Santamaria [a,b,*]

[a] Institute of Nanoscience of Aragon (INA) and Department of Chemical Engineering and Environmental Technology, University of Zaragoza, 50018, Zaragoza, Spain
[b] Networking Research Center on Bioengineering, Biomaterials and Nanomedicine (CIBER-BBN), 28029 Madrid, Spain
[c] Department of Chemical and Biomolecular Engineering, The Hong Kong University of Science and Technology (HKUST), Clear Water Bay, Kowloon, Hong Kong, China
[d] Laboratorio de Microscopías Avanzadas, Instituto de Nanociencia de Aragón, Universidad de Zaragoza, 50018 Zaragoza, Spain
[e] ARAID Foundation, 50018 Zaragoza, Spain

ARTICLE INFO

ABSTRACT

The present work investigates the role of two types of carbon nanodots (CNDs) as novel sensitizers of TiO_2 to create a visible-light driven photo-catalyst that is not only efficient for solar-driven pollution abatement, but also inexpensive, durable and environmentally-friendly. Two widely available green organic precursors, the Argentinean herb Mate and the Stevia plant have been selected as the carbogenic source to thermally induce the formation of different types of CNDs with different levels of N and P doping and tunable photoluminescence response in the UV–vis-near infrared (NIR) ranges. These CNDs have been successfully assembled with TiO_2 to form heterogeneous photocatalysts that are highly active in the visible-light and NIR- driven photodegradation of 2,4-dichlorophenol (2,4-DCP), a persistent chlorinated organic compound present in numerous pesticide formulations.

© 2017 Elsevier B.V. All rights reserved.

1. Introduction

The growing volume of wastes generated by human activities represents one of the most urgent environmental challenges that we face today [1–4]. Persistent and non-biodegradable organics in wastewater are major problems in water management, environmental protection, and water reuse. Traditional treatment methods such as adsorption, coagulation, and secondary biodegradation are often inadequate in treating many of the new, emerging micro-pollutants. They also suffer from high capital and operating costs, and are known to generate undesired secondary pollutants. Advanced oxidation processes (AOPs) [4–9] are capable of efficiently treating a broad range of problematic and refractory organic pollutants in water. The highly reactive radical species and oxidative intermediates (i.e. H_2O_2, $^{\bullet}OH$, $^{\bullet}O_2{}^{-}$, O_3) provide more complete oxidation and mineralization of the pollutants. Heterogeneous photocatalysis is particularly attractive for wastewater treatment with a clear advantage in terms of cost when the process is solar driven [1,5,8,10–12].

Current research is focused mainly on the optimization of the state-of-the-art solid heterogeneous photocatalysts. These materials are typically semiconductors that can be susceptible to photo-corrosion during long-term operation. Titania photocatalysts are remarkably stable under varied operating conditions and due to their abundance are less expensive than alternative materials [2,3,8]. Nevertheless, TiO_2 having a wide electronic band-gap requires UV irradiation. Moreover, rapid recombination of

* Corresponding authors at: Institute of Nanoscience of Aragon (INA) and Department of Chemical Engineering and Environmental Technology, University of Zaragoza, 50018, Zaragoza, Spain.
E-mail addresses: jlhueso@unizar.es (J.L. Hueso), jesus.santamaria@unizar.es (J. Santamaria).
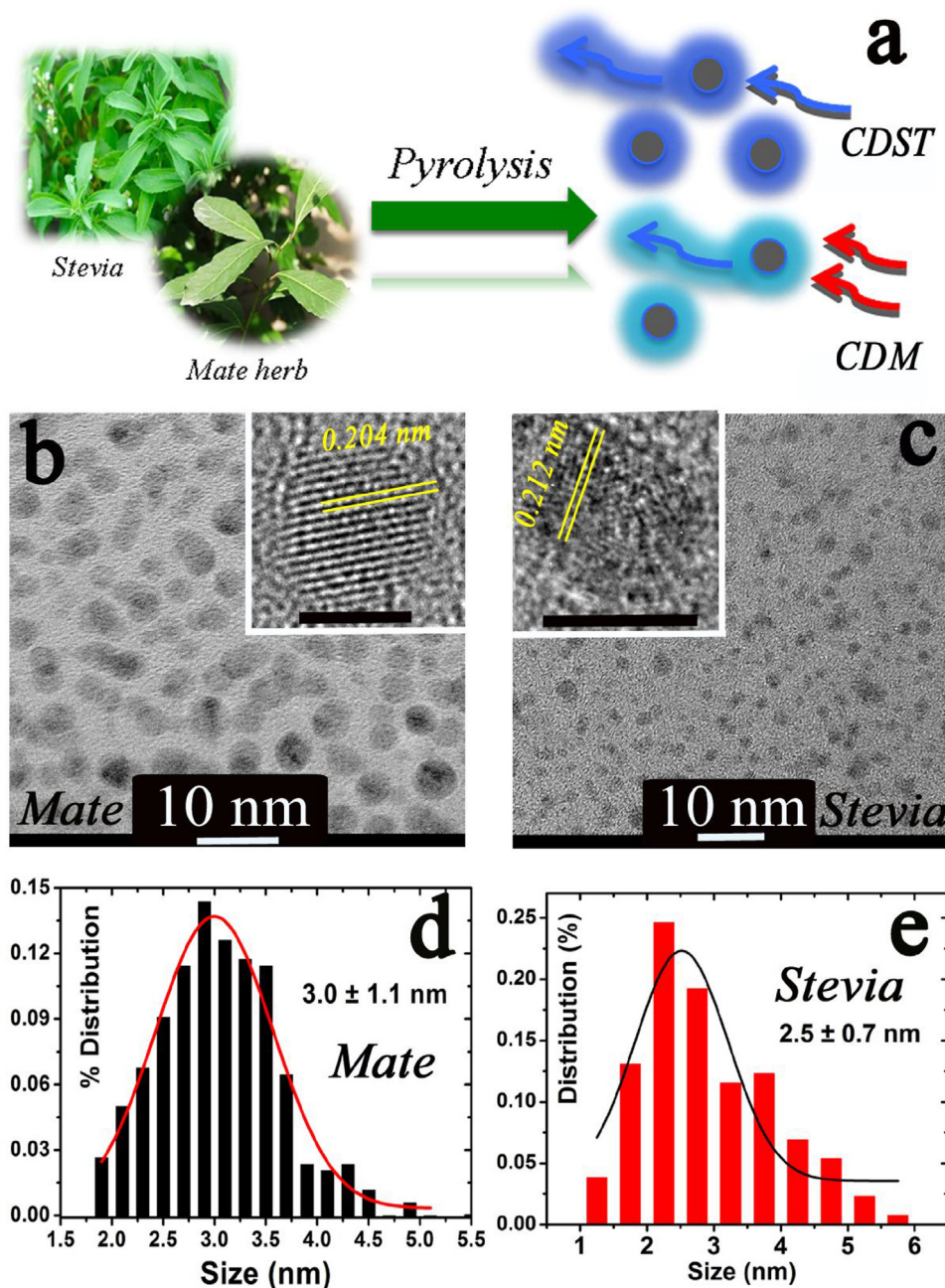
Fig. 1. (a) Scheme of the pyrolysis treatment of Mate and Stevia plant leaves; (b) TEM image of the carbon nanodots retrieved from Mate (inset: HRTEM image of a single CND with (111) orientation corresponding to graphite); (c) TEM image corresponding to the carbon nanodots obtained from the Stevia plant (inset: HRTEM image of a single CND where lattice distances for (020) orientations of graphite are shown); (d) Particle size distribution of the CNDM; (e) Particle size distribution of the CNDST. Scale bars in insets correspond to 3 nm.

the photo-generated electron-hole pair can significantly limit the quantum efficiency. Therefore, narrowing down the band-gap of TiO_2 to increase the visible-light absorption response is an often-used strategy to improve the photocatalyst performance [13,14]. Among the procedures employed are: (i) chemical modifications with light elements such as carbon, nitrogen, boron or sulfur to shift the absorption toward the visible range by creating intermediate energy states that narrow the band gap [13,14]; (ii) addition of plasmonic noble metals that boost absorption in the visible-NIR range due to their surface plasmon resonance (SPR) band [15–21]; (iii) use of sensitizers such as organic dyes and/or narrow band-gap quantum dots that absorb visible light and inject electrons into the conduction band of TiO_2 to suppress the recombination rate of

electron-hole pairs as in the case of quantum dot sensitized solar cells (QDSSCs) [22–25].

This work investigates the use of carbon nanodots (CNDs) in TiO_2 to create a visible-light photo-catalyst that not only is efficient for solar-driven pollution abatement, but also inexpensive, durable and environmentally-friendly [26–34]. Carbon nanodots are luminescent nanomaterials characterized by their broad absorption spectra, resistance to photo-bleaching and low toxicity [30,31,33–39]. They are potentially inexhaustible in view of the abundance of raw materials for their production. CNDs may also exhibit an interesting optical behavior as up-converters, thanks to due to size-dependent quantum confinement effects, expanding their potential applicability as sensitizers in the whole solar

spectrum [27,33,40–47]. Plant leaves and extracts abound with carbon, nitrogen and oxygen elements [47] which may serve as easily available carbon sources for large-scale fabrication of CNDs.

Herein, the preparation of new carbon dots from renewable plant materials has been successfully explored with two low-cost, widely available raw materials: the *Mate* herb (*Ilex paraguariensis*) and the stevia plant (*Stevia rebaudiana*). We have observed that the carbon dots obtained from the different plant sources exhibited unique sensitizing capabilities associated with the specific chemical compositions of the precursors. Furthermore, different levels of doping with nitrogen and phosphor can be achieved depending on the starting plant leaf and it is possible to tailor the resulting green carbon nanodots with different optical response as up-converters or down-converters. Finally, we have easily prepared photocatalytic nanohybrids by self-assembly of our N,P co-doped carbon nanodots onto commercial TiO_2 heterogeneous photocatalysts and used them towards the visible-light driven photodegradation of 2,4-dichlorophenol, a persistent chlorinated organic compound present in numerous pesticide formulations.

2. Experimental

2.1. Materials and reagents

Titanium (IV) dioxide (anatase, 99.8%) terephtalic acid (TA, 98%) and 2,4-dichlorophenol (99%) were purchased from Aldrich. Ethylenediaminetetraacetic acid disodium salt (ACS reagent, 99–101%, EDTA-Na$_2$), 1-butanol (ACS reagent grade) and quinine hemisulphate salt monohydrate (Bioreagent, 98%) were purchased and used without any further purification steps. The mate herb (*Ilex paraguariensis*) was supplied by Cruz Malta and the stevia leaves (*Stevia rebaudiana*) were purchased from Herbalism. Ultrapure water from a Milli-Q ultrapure system was used in this study.

2.2. Synthesis of carbon nanoparticles

CNDs were prepared by pyrolysis of plant leaves (Fig. 1a). The mate herb and the stevia leaves were first dried in an oven at 100 °C prior to grinding into a fine powder. 1.2 g of the dried and powdered mate and stevia leaves were thermally treated in still air for 2 h at 300 °C and 250 °C, respectively. Black carbonized powder was cooled to room temperature, dispersed in ultrapure water (i.e., 15 mL) and centrifuged at 6000 rpm for 10 min to remove large or agglomerated particles. The remaining supernatant was filtered through a 0.1 μm PTFE membrane (WhatmanTH) to give a brownish yellow suspension of CNDs. No presence of additional agglomerates was detected in the final suspension. The CNDs from mate and stevia leaves were named as CNDM and CNDST, respectively. It was observed that other heating temperatures did not render CNDs as indicated by a large decrease in the photoluminescence (PL) intensities and the absence of a representative population of CNDs. According to the literature 250–300 °C is enough for the preparation of CNDs [48].

2.3. Synthesis of CNDs/TiO₂ nanohybrids

CND/TiO$_2$ composites were synthesized by a simple room-temperature process. 0.5 g Anatase TiO$_2$ powders were first dispersed in a mixture of 2.6 mL CNDs solution (1 mg/mL) and 2.4 mL deionized water, and stirred vigorously for 30 min. The resulting suspension was dried under vacuum at 65 °C for 90 min and stored at ambient conditions until further use. The syntheses were performed using the facilities of the NANBIOSIS ICTS, more specifically by the Nanoparticle Synthesis Unit of the CIBER in Bio-Engineering, Biomaterials & Nanomedicine (CIBER-BBN).

2.4. Photocatalytic activity

The photocatalytic activity of the nanohybrids was evaluated by degradation of 2,4-DCP under visible light or under specific near-infrared (NIR) irradiation. A Hg lamp (blanklight blue F6T5BLB, with a cutoff filter λ < 420 nm) for visible light and a light-emitting diode (LED ENGIN, LZ4 model) at 740 nm for NIR experiments, respectively. 20 mg nanohybrids were suspended in 100 mL, 0.025 mM 2,4-DCP aqueous solution and stirred for 12–20 h to approach adsorption equilibrium between 2,4-DCP and photocatalyst before irradiation. Under stirring, a small amount of the suspension (about 3 mL) was taken at different times under irradiation and filtered through a 0.22 μm filter. The liquid was analyzed using an ultra performance liquid chromatography (UPLC) or GC–MS.

2.5. Detection of reactive oxidative species (ROS) generated by NIR illumination

The generation of hydroxyl radical under NIR irradiation was evaluated using terephtalic acid (TA) as a probe, which selectively reacts with ·OH to form a fluorescent derivative [30,49]. In a typical procedure, the detection of hydroxyl radicals (·OH) was carried out with the aid of terephthalic acid (TA, 3 mL, 5 mM) which selectively reacts to generate a fluorescent product (2-hydroxy terephthalic acid) emitting at ca. 425 nm. It is important to note that basic pH conditions (7–9) are first required to promote the stabilization of disodium terephthalate (NaTA). After LED NIR illumination at different time intervals, the mixture solution was centrifuged to remove the catalyst nanoparticles. The fluorescence emission spectrum of the generated 2-hydroxy disodium terephtalate in the supernatant was subsequently measured at an excitation wavelength of 315 nm.

2.6. Characterization techniques

Fluorescence measurements were performed using a LS55 Fluorescence Spectrometer (PerkinElmer) equipped with a xenon arc lamp as the light source and a quartz cell (10 × 10 mm). Absorption and emission spectra of the CNDs suspensions were systematically acquired at different excitation wavelengths in a UV–vis-NIR spectrophotometer (V-67, Jasco Company) with a quartz cell of 1 cm light path. The pH values were measured with GLP22 (CRISON).

The particle morphology and size distribution were examined by transmission electron microscopy (TEM) (FEI Tecnai T20, operated at 200 kV). The energy-filtered transmission electron microscopy (EFTEM) and high-resolution TEM imaging were done in a FEI Tecnai F30 (operated at 300 kV and equipped with a Gatan Image Filter (GIF Tridiem 863)). Electron energy loss spectroscopy (EELS) measurements were performed on probe-corrected scanning TEM (STEM) FEI Titan Low-Base 60–300 operating at 80 KeV (fitted with a X-FEG® gun and Cs-probe corrector (CESCOR from CEOS GmbH)). EEL spectra were recorded using the spectrum-imaging (SPIM) mode [50–52] in a Gatan GIF Tridiem ESR 865 spectrometer. The energy resolution was ~1.1 eV. The functionalization of the CNDs surface was followed by Fourier transform infrared (FTIR) spectroscopy using a Bruker Vertex 70 FTIR spectrometer.

The surface composition of the samples was analyzed by x-ray photoelectron spectroscopy (XPS) with an Axis Ultra DLD (Kratos Tech.). The spectra were excited by a monochromatic Al Kα source (1486.6 eV) run at 12 kV and 10 mA and pass energy of 20 eV was used. The binding energies were referenced to the internal C 1s (284.3 eV) standard. Analyses of the peaks were performed with CasaXPS software, using a weighted sum of Lorentzian and Gaussian component curves after Shirley background subtraction. Raman analysis was carried out with the aid of a Laser Raman
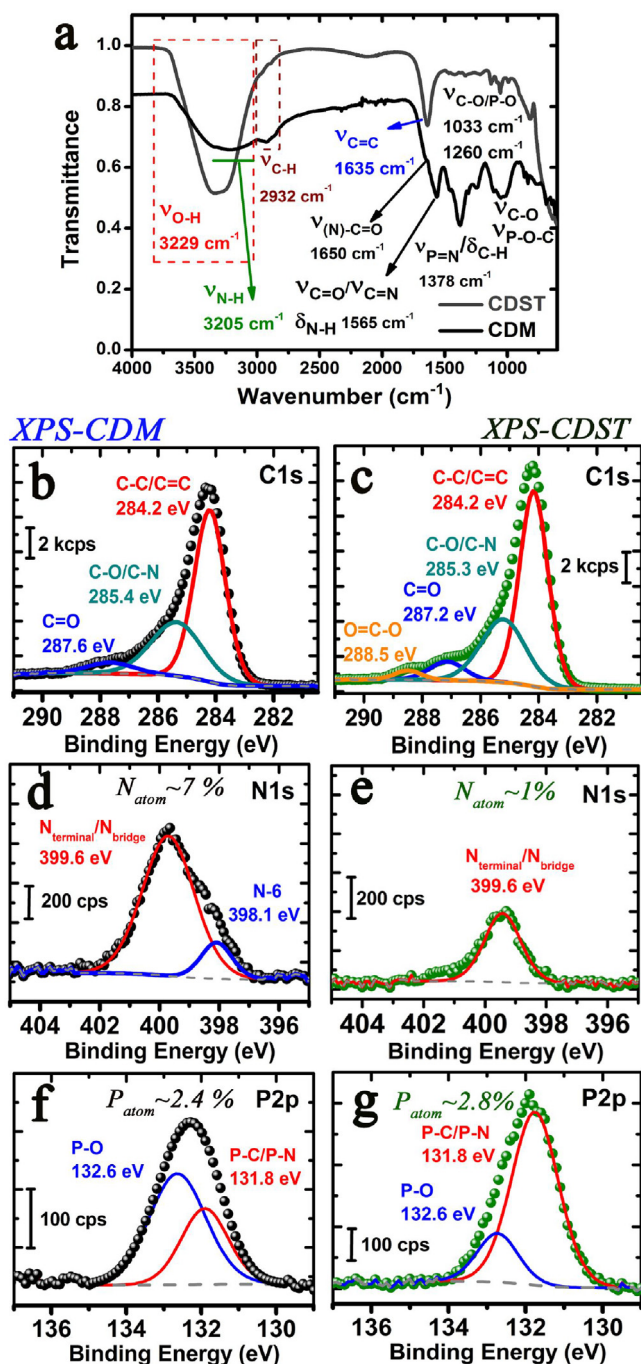
Fig. 2. Surface chemistry analysis of the CNDs: a) FT-IR spectra corresponding to the CDST and the CDM samples, respectively; b)-c) Fitted X-ray photoemission spectra in the C1s region of the CDM and CDST samples, respectively; d)-e) Fitted X-ray photoemission spectra in the N1s region of the CDM and CDST samples, respectively; f)-g) Fitted X-ray photoemission spectra in the P2p region of the CDM and CDST samples, respectively.

WiTec-Alpha 300 spectrometer using an Ar$^+$ ion laser exciting at 532 nm. The Raman light was collected in a backscattering geometry. The instrument was calibrated against the Stokes Raman signal of pure Si at 520 cm^{-1} using a silicon wafer crystal plane surface.

The quantum yield (QY) value of CNDs was calculated by comparing the integrated PL intensities (excited at 360 nm) and absorbance values of CNDs at ~340–345 nm with those of quinine sulphate. Quinine sulphate (QY = 0.54 at 360 nm) was dissolved in 0.1 M H$_2$SO$_4$ (refractive index, 1.33) and CNDs were dissolved in water (refractive index, 1.33). QYs of CDM and CDST were calcu-

lated to be 9.4% and 15.2%, respectively. To minimize re-absorption effects, the absorbance values of the two solutions in 10 mm cuvettes were kept under 0.1 at the excitation wavelength. Excitation and emission slit widths were set at 7.5 nm when recording PL spectra. Elemental analysis rendered similar compositions for both raw carbogenic sources (Mate herb (%) C:H:N:O:P = 48:5:3:38:5 and Stevia plant (%) C:H:N:O:P = 46:6:3:34:5). The GC–MS instrument (GC–MS Shimadzu QP-2010SE) used for the analysis of reaction intermediates was equipped with a Zebron capillary GC column (30 m x 250 μm, 0.25 μm). A NIST/EPA/NIH mass spectral library (NIST14) was used for identification of m/z values. Helium (purity >99.999%) was used as a carrier gas with a flow rate of 1.0 mL min^{-1}, and a 1 μL sample was injected at a split mode. According to previous reports, the temperature of injection was set to 300 °C [53,54]. The column temperature was first kept at 60 °C for 2 min, and raised up to a final temperature of 280 °C at a rate of 10 °C min^{-1}. The detector was a quadrupole mass spectrometer and the temperatures of the ion source and interface were both kept at 250 °C.

2.7. Kinetics of the photodegradation experiments

The kinetics of photocatalytic degradation of 2,4-DCP were adjusted to a Langmuir–Hinshelwood model:

$$r = -\frac{dC}{dt} = \frac{kKC}{1 + KC}$$

where r represents the initial rate of photooxidation, C the concentration of the reactant, t the irradiation time, k the rate constant of the reaction and K is the adsorption coefficient of the reactant. At micromolar concentrations $C \ll 1$, the equation can be simplified to the apparent first rate order equation:

$$\frac{\ln C_0}{C} = kKt = K_{app}t$$

$$C_t = C_0\, e^{-K_{app}t}$$

where K_{app} is the apparent first order rate constant given by the slope of the graph of ln C versus t and intercept C_0 is the initial concentration of the organic pollutant.

3. Results and discussion

3.1. Synthesis and characterization of green N, P-codoped carbon nanodots from natural plant leaves

Dried leaves from Mate and Stevia plants were calcined at 300 °C and 250 °C, respectively (Fig. 1a). After purification (see experimental section for details), stable colloidal suspensions of well-dispersed carbon nanoparticles were obtained. Fig. 1b–c show representative TEM images corresponding to the carbon nanodots rendered from Mate (hereafter labeled as CDM) and Stevia (hereafter denoted as CDST). From TEM images, their average diameters were statistically (N > 100 NPs) estimated as 3.0 ± 1.1 nm and 2.5 ± 0.7 nm respectively (Fig. 1d–e). Both samples exhibit a graphitic crystalline structure as shown in the HRTEM images of individual CNDs (see insets in Fig. 1b–c).

The surface chemistry analysis of the CNDs was carried out by FT-IR and XPS. Fig. 2a shows the FT-IR spectra of the CNDs. The CDST shows absorption contributions at ~3230 cm^{-1} and 1635 cm^{-1} corresponding to characteristic stretching vibration modes of ν (O—H) and ν (C=C), respectively[55]. Some additional contributions at ~1030–1100 cm^{-1} were also detected and tentatively attributed to C—O/P-O stretching modes[56–58]. Remarkably, the CDM sample shows additional features at ~3205 cm^{-1}, ~2930 cm^{-1} that correspond to the stretching bands of ν (N—H) and ν (C—H). Other contributions at ~ 1650 cm^{-1}, ~ 1565 cm^{-1}, ~ 1380 cm^{-1} and in the
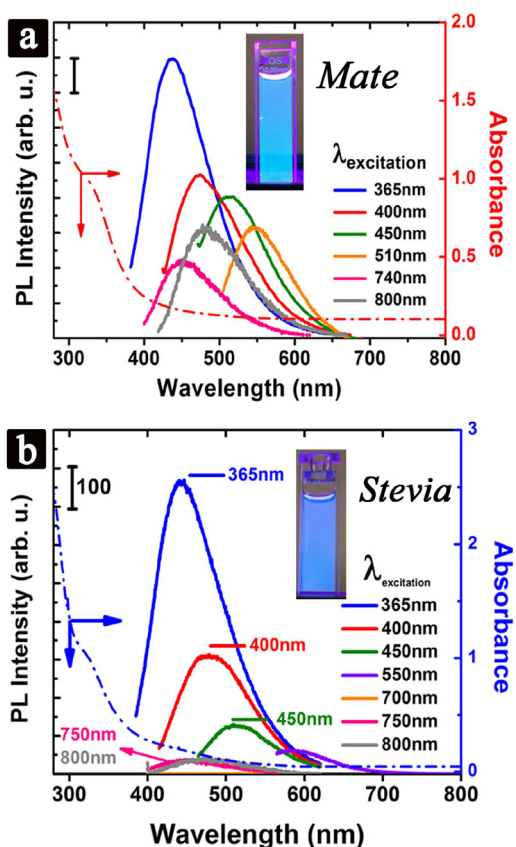
Fig. 3. Optical properties of the CNDs: a) UV–vis absorbance and photoluminescence spectra of the CNDs derived from mate at different excitation wavelengths from 365 to 800 nm; b) UV–vis absorbance and photoluminescence spectra of the CNDs derived from stevia at different excitation wavelengths from 365 to 800 nm; The insets show images of the suspension of the corresponding CNDs under UV light illumination (λ_{exc} = 365 nm). (For interpretation of the references to colour in this figure legend, the reader is referred to the web version of this article.)

1100–1260 cm^{-1} range (Fig. 2a) have been tentatively identified as C=O, C=N, P=N stretching modes corresponding to aromatic amides and aromatic rings containing P groups, thereby accounting for the partial substitution of C atoms by co-doping elements such as N or P [55–58].

XPS results further corroborate the presence of multiple oxidized carbon moieties on the surface of the CNDs such as O—C=O, C=O, C—O/C—N bonds in the C1s region (Fig. 2b–c). The presence of C—C/C=C bonds is predominant (Fig. 2b–c) although the specific contribution of each specific sp^2 or sp^3 bonding types can not be clearly discerned by this technique [34,59–61]. The presence of nitrogen (see Fig. 2d–g), is especially remarkable for the Mate derived carbon dots, accounting for up to 7% N atomic composition in contrast with the CDST that barely reaches 1% N atoms. The main contribution observed at ca. 399.6 eV in the N1s spectra can be an attributed to N—C bonds in terminal or bridged positions within a carbon network according to Pels and Sanchez-Lopez [33,62–64], although it has also been tentatively associated to amides [64]. It is also worth mentioning that both CNDs present an analogous phosphor atomic composition of ∼2.5% P (Fig. 2f–g) with a higher fraction of oxidized P-O species at 132.6 eV in the CDM sample and a higher contribution of P-C/P-N bonds centered at lower BEs (131.8 eV) in the CDST counterpart.

In addition, Raman spectroscopy can be also used as a surface characterization tool of partially ordered carbon materials. The first-order Raman spectra corresponding to both carbon dots samples reveal a similar pattern with two relatively broad bands

centered at ∼1350 cm^{-1} and ∼1580 cm^{-1} with certain overlapping between them that are typically denoted as D band (typical of structural disorder and defects and sp^3 coordination) and G band (typical of graphitic order and sp^2 bonding), respectively (see Fig. S1). Therefore, both CNDs exhibit a slightly higher contribution from the disordered fraction in agreement with the XPS results (see Fig. 2). It is also noteworthy that both samples seem to show a third contribution located at ∼1505 cm^{-1} which has been previously denoted as Dí band and associated with amorphous sp^2-bonded forms of carbon or interstitial defects, thereby pointing out to the existence of outer defective layers in the carbon nanodots [34,65].

Regarding the optical properties of the carbon dots, Fig. 3 displays the UV–vis absorption spectra and the wavelength-dependent photoluminescence (PL) response for both CNDs. These CNDs exhibit a dual behavior as down-converters upon excitation within the 365–510 nm intervals [35] and a more striking up-converting response under NIR irradiation at 750–800 nm [40,41]. The former behavior is traditionally observed in semiconductor-type quantum dots and it is associated with the lower capacity to repopulate the excited states upon excitation with lower energy wavelengths [40,41,43,66,67]. In the particular case of CNDs, the PL emissions in the blue-green range have been attributed to the presence of isolated sp^2 clusters within more extended sp^3 networks [34,68], as suggested from the Raman analysis (Fig. S1).

The up-conversion phenomenon is remarkable for the CNDs derived from mate (Fig. 3a) that display a much stronger PL response in comparison with the stevia counterpart after NIR excitation and a much broader absorption band throughout the whole UV–vis-NIR window (Fig. 3b). Despite continuous efforts to explain this particular behavior, the exact mechanisms behind up-conversion for CNDs have not been unveiled yet. Nevertheless, there is consensus about the influence of doping heteroatoms (i.e. N, S, B, P) [13,68,69] that promote the generation of virtual dopant states close to the LUMO levels of the CNDs thereby enabling longer wavelength multi-photon absorption events and subsequent emissions of single photons at shorter wavelengths during the recombination decay [27,41] (Fig. 3a). Therefore, it seems reasonable to correlate the presence of P and especially N co-dopants in the CDM structure to the broader absorption in the visible range and the enhanced up-converting response in comparison with the CDST sample where the presence of N is rather limited and absorption tail decays at shorter wavelengths than the CDM one (Figs. 2 and 3).

3.2. Synthesis and characterization of CNDs/TiO$_2$ hybrids

Once the optical properties of the CNDs had been established, the next goal was to achieve a successful assembly of both types of CNDs with of the shelf commercial anatase supports to explore their potential capabilities as sensitizers to expand the photocatalytic response beyond the UV range. To do so, both CNDs and TiO$_2$ nanoparticles with anatase phase (Fig. S2) were thoroughly mixed under vigorous stirring for 30 min and then dried under vacuum at 65 °C during 90 min (see Experimental Section). The successful coupling of the CNDs and the TiO$_2$ NPs was confirmed by different TEM analysis approaches. Fig. 4(a) and (c) correspond to low-magnification TEM images of the CNDST decorating the anatase support. Fig. 4(b) and (g) show HRTEM images that clearly corroborate the presence of both CDST and CDM onto the titania particle, respectively. In order to confirm the presence of such nanostructures on the anatase support, an analysis combining high-angle annular dark field (HAADF)-STEM imaging and EDX was performed over the CDM@TiO$_2$ hybrid. The EDX analysis on different regions where CNDs clearly spotted rendered a higher fraction of C signal in comparison with closer areas where CNDs were not apparently deposited (see Fig. 4(e)–(f)).
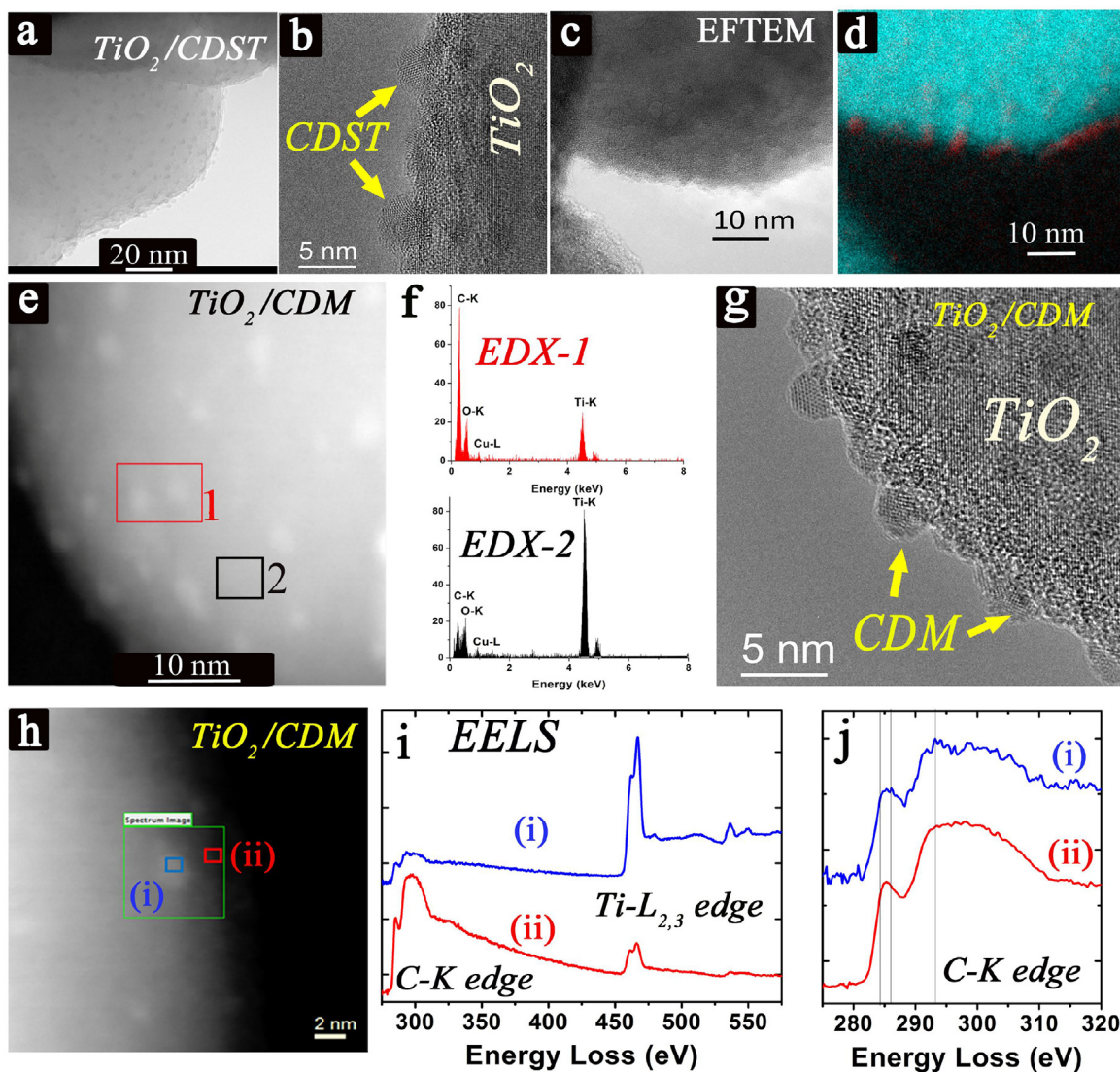
Fig. 4. (a) and (c) Low-magnification TEM micrographs of CDST supported on TiO_2 nanoparticles; (b) and (g) HRTEM images of the CNDs-TiO_2 hybrids including CDST and CDM, respectively; (d) Energy filtered TEM image formed by the superposition of signals stemming from the C-K (in red) and Ti-$L_{2,3}$ edges (in blue and green), respectively. These EFTEM analyses have been performed in the area displayed in the TEM of (c), where the CDST are observed;(e) HAADF-STEM image of the CDM-TiO_2 hybrid including marked areas for EDX analysis; (f) EDX spectra corresponding to the areas analyzed in e; (h) HAADF-STEM image of the CDM-TiO_2 hybrid including marked areas for EELS analysis; (i) EEL spectra extracted from the SPIM recorded in the area marked in the HAADF image displayed in h. C-K, Ti-$L_{2,3}$ and O-K edges are observe;. (j) Zoom of the C-K edge for the two EEL spectra of Fig. 4 (i), see the text. (For interpretation of the references to colour in this figure legend, the reader is referred to the web version of this article.)

In addition, we performed local chemical TEM analyses via energy-filtered transmission electron microscopy imaging-spectrum (EFTEM) and spatially-resolved electron energy-loss spectroscopy (SR-EELS), see Fig. 4(d) and (i)–(j), respectively. From the EFTEM RGB micrograph (Fig. 4(d)), the presence of C nanostructures (C-K map in red) on the top of the TiO_2 particles (Ti-$L_{2,3}$ map in blue and green). This result confirms the presence and the composition of CDSTs spotted by regular TEM in Fig. 4(a)–(c). Analogous results were achieved in the case of CDMs. Furthermore, the hybrids have been analyzed by SR-EELS, which is another very powerful technique to investigate such nanomaterials at sub-nanometer scale [70]. Fig. 4(i) displays two EEL spectra. Each of these two EEL spectra corresponds to the sum of 4 spectra (2×2 probe positions of the spectrum-image (SPIM)) recorded in the areas marked on the high-angle annular dark field (HAADF)–STEM image of Fig. 4(h). This HAADF micrograph also shows the position where the SPIM has been acquired. The C-K, Ti-$L_{2,3}$ and O-K edges are visible, and

these signals correspond to the hybrid nanomaterials (carbonnanodots, other form of C materials and TiO_2 support NPs).

The Fig. 4(j) shows the energy loss near-edge features (ELNES) of the C-K edge for these two EEL spectra. These ELNES signals consist of a π^* peak at ~285 eV and a well-defined σ^* band starting at ~292 eV [51,52,70–72]. These fingerprints are typical for the sp^2 hybridization of the C atoms. However, we can distinguish the signatures of two different types of C materials. The spectrum displayed in Fig. 4(j-ii) corresponds to an amorphous-like C, likely from some adventitious carbon contamination inherent to the TiO_2 nanoparticle. However, the EEL spectrum displayed in Fig. 4(j-i) is closer to the signature of more organized/better structured sp^2C nanomaterial. In addition, this EEL spectrum displays two other signatures: a peak at ~288 eV and another at ~291.8 eV. These peaks can be assigned to: C=C π^* (from CH_2 groups, after reduction by the electron beam), and σ^* contribution from a carbonyl-like group [71,72].
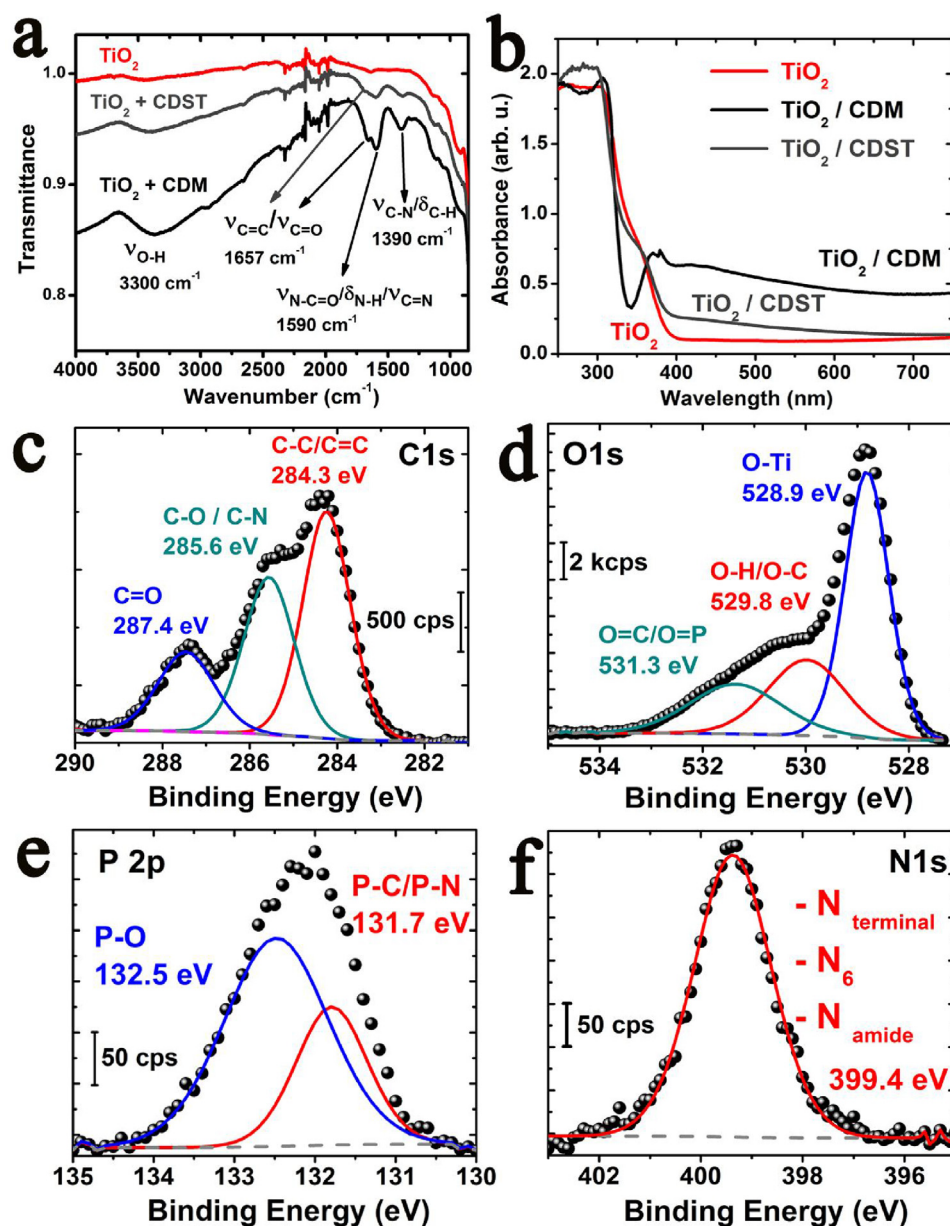
Fig. 5. Surface chemistry analysis of the CND@TiO$_2$ nanohybrids: a) FT-IR spectra comparing the commercial TiO$_2$ nanoparticles before and after assembly with CDST and CDM, respectively; b) UV–vis absorption spectra of the TiO$_2$ anatase nanoparticles before and after the assembly with the CDST and the CDM samples, respectively; Fitted X-ray photoemission spectra of the CDM@TiO$_2$ hybrid corresponding to: c) the C1s region; d) the O1s region; e) the P2p region and f) the N1s region. Analogous XPS analyses can be found in the Electronic Supplementary Information for the CDST@TiO$_2$ sample.

FT-IR spectroscopy analysis was also carried out to determine the nature of the interaction between the CNDs and the anatase. The major differences observed with respect to the bare TiO$_2$ NPs before CNDs assembly are related with the enhanced presence of vibrational bands at 3300 cm^{-1} attributable to —O—H functional groups as well as the bands at 1657 or 1711 cm^{-1} that depending on the CNDs, correspond to C=C and/or C=O stretching vibrations[55]. These features further suggest the effective presence of CNDs with their specific surface oxidized states. Furthermore, the broader and red-shifted absorption bands detected below 1250 cm^{-1} in comparison with the uncoated TiO$_2$ point out to an effective interaction with the supports through the combination of Ti—O—C and Ti—O—Ti vibrational bands or alternatively to the presence of P—O—C stretching contributions associated to aromatic groups [56–58]. Finally, the additional presence of bands at 1590 and 1390 cm^{-1} could suggest the presence of amide groups through the presence of stretching

vibrations of N—H and C—N, respectively [55]. These bands look more pronounced on the CDM@TiO$_2$ hybrids which possess the maximum compositional presence of N species (Fig. 2, Fig. 5a–f). The partial contribution of structural adsorbed water or C—H deformation bands cannot be ruled out [55].

XPS analysis was also performed to study the components and surface chemistry of the CNDs/TiO$_2$ nanohybrids. At a first glance, a clear increment of the presence of carbon atoms was detected on the surface of the nanohybrids (~30–32%) in comparison with the bare TiO$_2$ support (~19%) suggesting the presence of additional carbonaceous entities (CNDs) accompanying the typical adventitious carbon deposits. Raman analysis of the commercial TiO$_2$ support (Fig. S3) and the nanocomposites (Fig. S4) further supported the XPS outcome with a small contribution of carbon species in the 1200–1650 cm^{-1} range in comparison with the strong signal stemming from the anatase phase. The incremental presence of

C—O/C—N bonds at 285.6 eV and especially at 287.4 eV accounting for C=O bonds further corroborates the major presence of surface functional groups associated to the CNDs (Figs. 5c and S5 in SI). Again, the contribution of C—C and especially C≡C features is predominant in the C1 s spectrum of both nanocomposites (Figs. 5c and S5) but the specific differentiation can not be properly resolved by this technique [59–61]. The absence of contributions at 281 eV rules out the direct formation of C-Ti bonds and strongly suggests the interaction via C—O—Ti links [30,73,74]. The contributions in the O1s region at 528.9, 529.8 and 531.3 eV are typically ascribed to O-Ti, (H)O—C and O=C/O = P bonds, respectively (Figs. 5d and S5 in SI) and confirm the presence of modified CNDs. Finally, the signal registered from the N1s and P2p regions in the nanohybrids and the absence of an equivalent signal on the original TiO$_2$ support clearly evidences the successful attachment of the CNDs (Figs. 5e–f and S5 in SI). Both CND@TiO$_2$ hybrids rendered an analogous signal in the P2p region accounting for P-O/P-C bonds at 132.5 and 131.7 eV, respectively and a surface atomic percentage slightly superior for the CDST@TiO$_2$ sample (~1.5% vs. ~1% for hybrid containing CDMs). In contrast, the N1 s region rendered a 2.5-fold higher presence of N entities in the CDM@TiO$_2$ hybrid (~2.6% vs. ~0.9%) with a similar contribution centered at 399.4 eV.

Taking into account the formerly described FTIR results (*vide supra*), the N contributions in the mate-derived hybrids can be likely attributed to the combined presence of amides functionalities and aromatic N—C bonds in terminal positions whilst the stevia-derived hybrids only accounts for heteroatomic substitutions in the carbon network [62,64]. Finally, it is worth mentioning that slight shiftings on the binding energies (B.E.) of the Ti2p$_{3/2}$ and Ti2p$_{1/2}$ contributions observed in the photocatalytic CND@TiO$_2$ hybrids are consistent with a stronger interaction between CNDs and TiO$_2$ via C—O—Ti links [30,73,74]. Likewise, the formation of O—Ti—N linkages via N$^-$ anionic species interacting with the TiO$_2$ lattice previously observed in other N-doped CNDs [30,73,74] can be ruled out due to the absence of lower B.E. contributions, even in the CDST@TiO$_2$ samples with lower N content.

From the optical point of view, the effective assembly of the CNDs was also identified by UV–vis spectroscopy in Fig. 5b. A broader absorption band with a tail extending towards the visible-NIR range was detected for both nanohybrids in comparison with the bare support. These changes account for the effective modification of the band gap properties of the semiconductor support and the positive influence of the N, P heteroatoms and different surface state groups able to create novel conjugated and hybridized energy levels (*vide infra* in the next section for further discussion) [56,68,69,75]. It is especially remarkable the enhanced absorption in the CDM@TiO$_2$ composite that can be attributed to the contribution of extra n-π* transitions provided by additional N energy levels [34,76].

3.3. Visible-light driven photodegradation of 2,4-dichlorophenol in the presence of the CNDs@TiO$_2$ nanohybrids

The photocatalytic activity of the CNDs@TiO$_2$ nanohybrids was tested against the degradation of an aqueous solution containing 2,4-DCP, a recalcitrant and toxic pesticide pollutant, under visible light irradiation. Fig. 6a shows the evolution on the concentration of the chlorinated pollutant at different cumulative irradiation times in the visible-light range using a fluorescent lamp with cut-off filter at λ < 420 nm. The photocatalytic response of anatase NPs before and after the assembly with the two CNDs has been compared. It becomes clear that the CNDs positively contribute to enhance the visible-light driven photocatalytic degradation of 2,4-DCP in comparison with the uncoated TiO$_2$ support. After 60 min of irradiation, only the hybrid containing the carbon dots stemming from mate is able to achieve total degradation of 2,4-DCP.
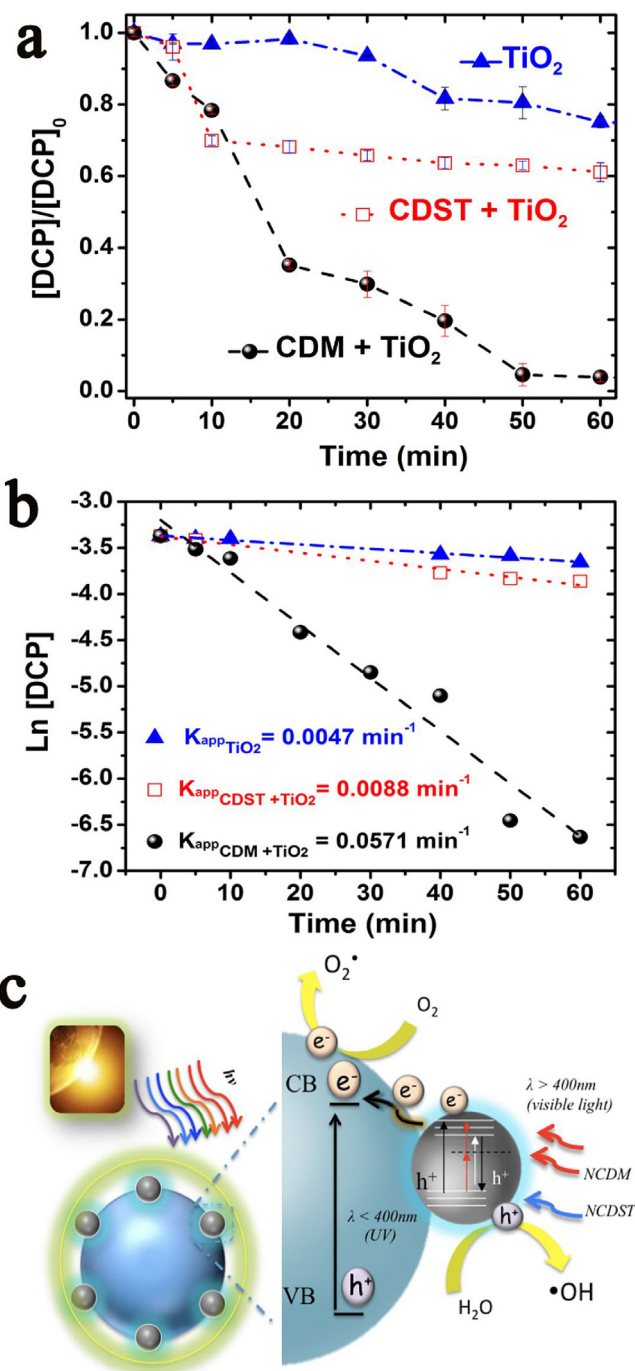
Fig. 6. a) Visible-light driven photocatalytic degradation of 2,4-DCP upon different cumulative irradiation times in the presence of TiO$_2$, CDST@TiO$_2$ and CDM@TiO$_2$, respectively; [2,4-DCP]$_0$ = 0.025 mM; [catalyst] = 0.2 g L^{-1}; b) Apparent kinetic degradation rates (K$_{app}$) for 2,4-DCP obtained from the slope of the semi-log plot for the 2,4-DCP degradation (see Experimental Section for details on the pseudo-first-order kinetic model); c) Schematic view of the most plausible light-induced charge-transfer process occurring on the CNDs@TiO$_2$ nanohybrids.

In contrast, the uncoated TiO$_2$ barely reaches a 30% while the CDST@TiO$_2$ outcome is close to 40% degradation. Therefore, the performance of the CDM@TiO$_2$ clearly exceeds not only that of TiO$_2$, but also the performance of the CDST@TiO$_2$ counterparts accounting for an analogous ~1% wt loading. This is in fact corroborated by the higher apparent rate constants determined for the CDM@TiO$_2$ photocatalyst after the application of a Langmuir-Hinshelwood

Table 1
Summary of recent results related with the visible-light driven photocatalytic degradation of 2,4-dichlorophenol.

Catalyts	Concentration of catalyst or pollutant	Kinetics/Degradation percentages	Irradiation Source	Ref.
GO/g-C_3N_4	10 g/L cat 61 mM DCP	0.008 min^{-1}	Xe short arc lamp (CHF-XM35-150W, Beijing Changtuo Co.) served as the visible light source, ($\lambda > 400$ nm)	[80]
ZnO	0.5 g/L Cat 120 mM DCP	180 min/93%	300 W Xe lamp (PLS-SXE300, Beijing Trusttech Co. Ltd.) equipped with an ultraviolet cutoff filter was employed as the light source to provide visible light ($\lambda \geq 400$ nm)	[83]
TiO_2@C	1 g/L Cat 300 mM DCP	5 h/100%	1000 W halogen lamp was used as the light source of the homemade photoreactor, cooled with flowing water in a quartz cylindrical jacket around the lamp. The short wavelength components were cut-off ($\lambda < 420$ nm)	[82]
BiOI@$Bi_{12}O_{17}Cl_2$	1 g/L Cat 61 mM DCP	2,4-DCP: 47% in 8 h	visible light irradiation (500 W Xe lamp, $\lambda > 420$ nm)	[89]
Graphene	0.2 g/L cat 0.123 mM DCP	87% 180 min second-order kinetics	ozone = 3.188×10^{-3} mol/L	[81]
Au/α-Bi_2O_3	1 g/L cat 0.1 mM DCP	65% 7 h	300 W Xe-arc lamp (CHF-XM150, Beijing Trusttech. Co Ltd.) equipped with a wavelength cutoff filter of $\lambda = 420$ nm,	[90]
N-TiO_2	1 g/L Cat 613 mM DCP	Descomposition rate 55%	A 1000 W halogen lamp was used as the light source of the homemade photoreactor, The short- wavelength components were cut-off ($\lambda < 420$ nm)	[87]
Ag-AgI/Al_2O_3	1.7 g/L Cat 61 mM DCP	81% TOC in 15 min	350 W Xe-arc lamp (Shanghai Photoelectron Device Ltd.) equipped with wavelength cutoff filters for $\lambda > 420$ and 450 nm and focused onto the beaker.	[91]
N-TiO_2	1 g/L Cat 613 mM DCP	50%/5 h	1000 W halogen lamp was used as the light source of the homemade photo-reactor, The short wavelength components ($\lambda < 420$ nm)	[86]
Ag-AgBr/MAP	1.7 g/L Cat 61 mM DCP	100% 20 min	350 W Xe-arc lamp (Shanghai Photoelectron Device Ltd.) equipped with wavelength cutoff filters for $\lambda > 420$ and focused onto the beaker.	[92]
TiO_2/Au NPs	10 g/L cat	0.0095 min^{-1} $R^2 = 0.996$	high pressure xenon short arc lamp (CHFXM35−500W, Beijing Changtuo Co.) was served as the light source, a glass filter (ZUL0422, Asahi Spectra Co.) was added to allow visible light ($\lambda > 420$ nm) to pass through.	[93]
WO_3/TiO_2	1.1 g/L Cat 123 mM DCP	0.2618 min^{-1}	A 1000 W halogen lamp was used as the visible light source (the average light intensity was 60 mW cm−2) and the light from the lamp included beams from ultraviolet and visible light regions. The short-wavelength components ($\lambda < 420$ nm)	[85]
α-Fe_2O_3	1.5 g/L cat 0.5 mM DCP	1.61E^{-4} M/h	The lamp has a wavelength distribution simulating so- lar radiation showing an integrated photons emission of 7% of the total radiation between 290 and 400 nm. The irradiation vessels used were 60 mL cylindrical Pyrex flasks (cutoff $\lambda \approx$ 290 nm)	[88]
V-TiO_2	1 g/L cat 613 mM DCP	8h-90%	300 W high-pressure Hg lamp and a 1000W tungsten halogen lamp equipped with a UV cut-off filters ($\lambda < 420$ nm)	[84]
Mesoporous-TiO_2	1 g/L cat 0.153 mM DCP	K_{app} = 0.004	A 1000 W halogen lamp was used as the light source. The short- wavelength components were cut-off ($\lambda < 420$ nm)	[94]
RGO/$ZnFeO_4$/Ag_3PO_4	2 g/L cat 123 mM DCP	K = 0.0116 min^{-1} $R^2 = 0.9920$	300 W Xe lamp and a 1000W with a UV cut-off filters ($\lambda < 420$ nm)	[54]
P25	0.1 g/L cat 1.5 mM DCP	K = 0.0328 min^{-1}	125 W (Philips HPL-N) Hg lamp	[79]
N-CNDs/TiO_2	0.2 g/L cat 0.025 mM DCP	90% Degradation 7.5 h	Xe lamp with cutoff filter at $\lambda < 420$ nm	[30]

model and the adjustment to a pseudo-first-order kinetics (Fig. 6b). The apparent first order constants (k_{app}), determined by linear fitting to the experimental data, indicate a very limited degrada- tion when TiO_2 was used (k_{app} = 0.0047 min^{-1}) that was duplicated upon the assembly of the CDST (k_{app} = 0.0088 min^{-1}) and 10-fold enhanced in the presence of the CDM (k_{app} = 0.0571 min^{-1}) (Fig. 6b). Analogous kinetic constants have been recently reported by Pas- trana et al. for nanodiamond-TiO_2 composites deposited by atomic layer deposition toward the decomposition of diphenhydramine, a model pharmaceutical pollutant[69,77]. Likewise, these results have been also compared specifically with other photocatalysts reported for the degradation of 2,4-DCP and summarized in Table 1. Although a great number of studies have been previously devoted to UV-light assisted degradation of phenols [78,79], Table 1 is mainly focused on visible-light driven photocatalytic degradation processes assisted by carbon based systems [80,81], C-decorated titania [30,82], undoped [83] or doped semiconductors [84–87],

iron-based Fenton catalysts [54,88] and plasmonic photocatalysts [89–93]. It is worth mentioning that the CDM@TiO_2 kinetics exhibit an analogous or superior performance, even in comparison with P25 operating in the UV range [79] (k = 0.0328 min^{-1}, see Table 1). Hence, our recent results operating with amine-derived CNDs sensitizers did not achieve total degradation even after longer pho- toirradiation periods [30].

Some very recent reports have shown the positive influence of combining carbon structures with TiO_2 to improve its visible- light response, including the direct doping of titania with C atoms and the coating with carbonaceous layers, carbon dots or graphene layers [68], largely using model dyes. In contrast, the number of photocatalytic studies devoted to chlorinated wastewater samples or pharmaceutical pollutants has been scarce or more focused on Fenton catalysts and other AOPs [4,68,69,95,96]. Other analogous systems containing carbon-based sensitizing materials in the form of CNDs, Graphene Oxide or C_3N_4 did not outperform our mate-
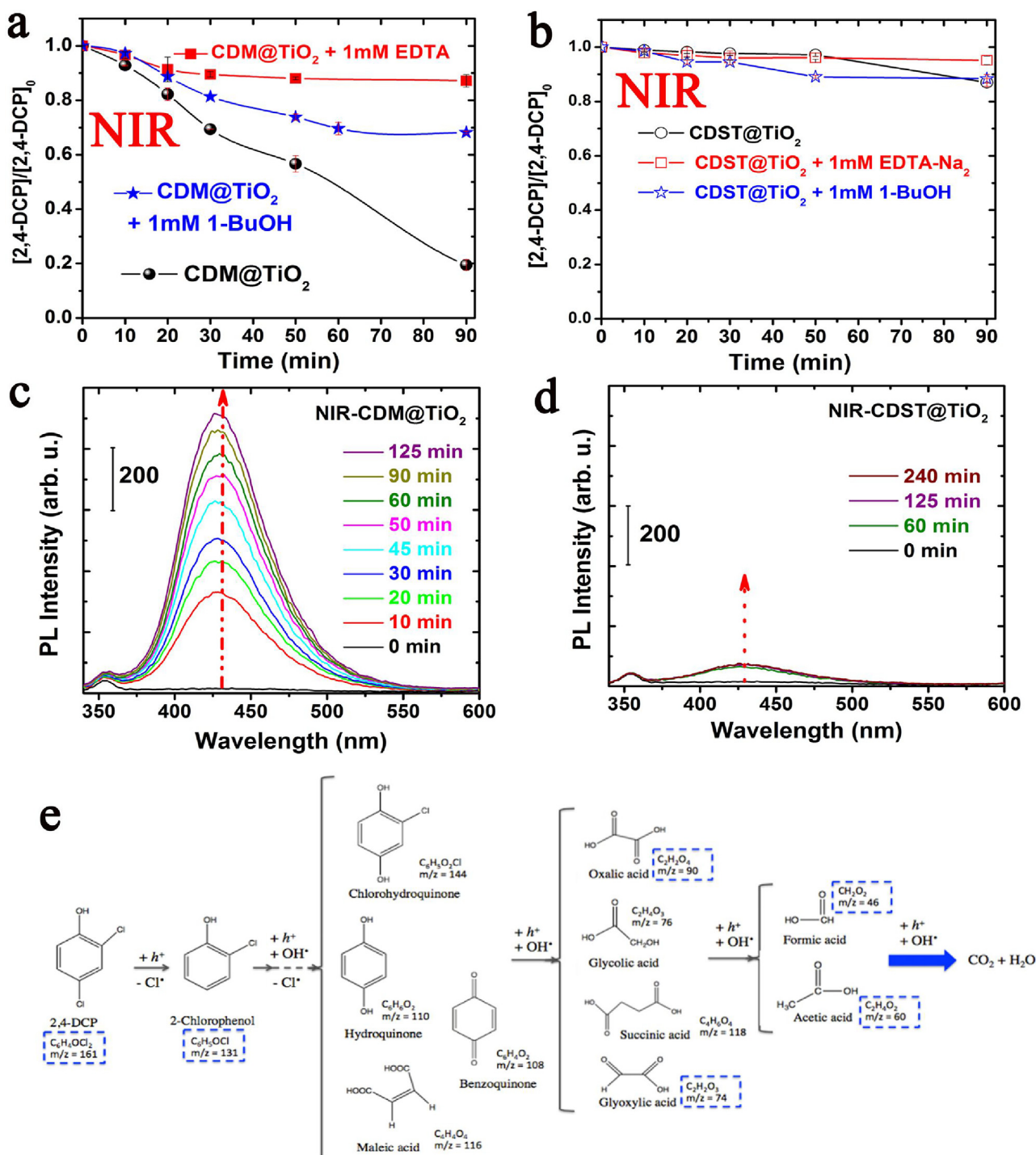
Fig. 7. a) NIR-light driven photocatalytic degradation of 2,4-DCP upon different cumulative irradiation times in the presence of CDM@TiO$_2$ and comparative quenching experiments in the presence of 1-butanol or EDTA-Na$_2$; b) NIR-light driven photocatalytic degradation of 2,4-DCP upon different cumulative irradiation times in the presence of CDST@TiO$_2$ and comparative quenching experiments in the presence of 1-butanol or EDTA-Na$_2$; [2,4-DCP]$_0$ = 0.025 mM; [catalyst] = 0.2 g L^{-1}; c) Fluorescence spectra of the different solutions of the hydroxylated derivative of terephthalic acid after different irradiation times of CDM@TiO$_2$ under NIR-LED light; d) Fluorescence spectra of the different solutions of the hydroxylated derivative of terephthalic acid after different irradiation times of CDST@TiO$_2$ under NIR-LED light; Experimental conditions describe in the Experimental section; e) Proposed reaction and degradation mechanism of 2,4-DCP based on previous results on the literature and the reaction intermediates detected by GC–MS analysis (highlighted with dashed rectangles).

based photocatalytic nanocomposite (see Table 1). Here we not only show that the combination of carbon structures with anatase can be used for the efficient photocatalytic degradation of recalcitrant pollutants (2,4-DCP), but also that these carbon structures must have certain physicochemical properties to be effective, i.e.,

not all carbon dots are alike even when, as in this case, they are of similar size and obtained through analogous routes from natural plants. This accounts for the high charge-transfer efficiency of the CDM in a broader spectral range attributable to their upconversion properties.

The light-induced charge-transfer mechanism likely responsible for the photocatalytic efficiency of the CDM@TiO$_2$ nanohybrid in the visible range, is schematically displayed in Fig. 6c. The presence of N and P heteroatoms in the CNDs favors a broader absorption capacity in the visible range due to the introduction of additional dopant-induced states close to the LUMO level of the CNDs (n → π* transitions caused by C=N, C=P conjugated bonds). Moreover, the presence of surface oxidized groups such as C=O, P=O or COOH can additionally favor band-bending effects and a more effective separation of photocarriers due to the partial hybridation of π levels of carbon and O2p levels located above the HOMO level of the CNDs [68,96]. Therefore, CNDs act as effective photosensitizing agents and electron reservoirs able to improve the charge-transfer photo-induced ability of the anatase NPs by facilitating the mobility of electrons to the conduction band of TiO$_2$ and concomitantly hindering recombination. The electrons can be shuttled freely along the conducting network of CNDs, while the longer-lived holes on TiO$_2$ account for the higher activity of the complex photocatalyst system. The electron/hole pairs then react with the adsorbed oxidants/reducers (usually O$_2$/OH$^-$) to generate reactive oxygen species (e.g. •O$_2^-$, •OH), which cause degradation of the organics contaminant proposed.

In order to corroborate the proposed mechanism and the role of the upconverting CDM, an additional set of photodegradation experiments were carried out upon illumination with a specific NIR-LED operating at 740 nm. In addition, a series of quenching experiments in the presence of 1-butanol and EDTA-Na$_2$ (a hydroxyl and hole scavenger, respectively) [54,97] were also performed to assess the role of these ROS in the overall degradation of 2,4-DCP. Hence, the in-situ and selective generation of ·OH radicals under NIR illumination was also confirmed with the aid of terephthalic acid, a selective probe that becomes fluorescent only when interacts with these hydroxyl radicals [30,49]. Fig. 7a–b shows the clear differences between the photocatalytic performance of the CDM@TiO$_2$ composites and the CDST@TiO$_2$ ones. This result further supports the expanded sensitizing action of the upconverting nanodots even beyond the visible range. It also demonstrates the active role of the OH radicals in the effective photodegradation of the pollutant (Fig. 7c–d). More importantly, it attributes a very active and important role to the presence of holes given the detrimental effect of EDTA-Na$_2$ on the photodegradation effectiveness (Fig. 7a).

A plausible degradation pathway for the 2,4-DCP is proposed and depicted in Fig. 7e. This scheme is based on previous works in the literature [53,54,98,99] and the intermediates detected by GC–MS analysis in our system at different irradiation times. These analyses detected that the 2-Chlorophenol ($m/z = 131$, exact mass 128) is the aromatic intermediate formed, and its concentration decreases sharply at the beginning the photocatalytic time, giving rise to the appearance of other acidic reaction intermediates of low molecular weight, such as glyoxylic acid ($m/z = 74$), oxalic acid ($m/z = 90$), formic acid ($m/z = 46$), and acetic acid ($m/z = 60$), suggesting that CNDM@TiO$_2$ system is effective towards the degradation of 2,4-DCP.

Finally, it is also worth mentioning that both CDM@TiO$_2$ and CDST@TiO$_2$ catalysts could be easily recycled by simple centrifugation and replacement of the pollutant solution. The results (Fig. S6 in SI) showed no loss of activity over 4 reuse cycles and the TEM inspection of the reused photocatalysts did not show any relevant morphological modification on the catalysts after multiple reaction cycles (Fig. S7). Interestingly, the stevia based nanocomposites revealed an apparently major fraction of a carbonaceous layer covering the outer surface of the catalyst particles that we attribute as one potential cause for the deactivation observed in their photocatalytic activity (Fig. 6a) as a result of the formation and/or co-deposition of a competing reaction intermediate that modified the degradation kinetics of the 2,4-DCP [100,101].

4. Conclusions

Upconverting carbon nanodots prepared by pyrolysis of Mate herb leaves have shown excellent response as photosensitizers to expand the photocatalytic activity of anatase supports into the visible range. Interestingly, carbon nanodots with a similar or smaller size prepared from Stevia plant leaves using the same process did not show upconverting properties and displayed a considerably smaller photocatalytic activity (though they were still more active than commercial anatase or P25 under visible light). Both types of CND/TiO$_2$ hybrids show similar presence of oxygenated species on their surface, and analogous content of P. The main difference in the physicochemical characterization is the higher content of N-containing species on the CDM@TiO$_2$. This higher presence of N heteroatoms seems to be determinant on the broader absorption capabilities of the CDM spanning from visible to NIR and their enhanced up-converting behavior. Thus, the much higher photocatalytic activity of this nanohybrid can be explained as the result of the capacity of the CDM@TiO$_2$ to absorb light in a broader range (including NIR) and inject electrons in the conduction band of anatase to generate highly reactive holes and hydroxyl radicals.

Appendix A. Supplementary data

Supplementary data associated with this article can be found, in the online version, at **http://dx.doi.org/10.1016/j.apcatb.2017.06.021**.

References

[1] C.C. Wang, J.R. Li, X.L. Lv, Y.Q. Zhang, G.S. Guo, Energy Environ. Sci. 7 (2014) 2831–2867.

[2] M.C. Ortega-Liebana, E. Sanchez-Lopez, J. Hidalgo-Carrillo, A. Marinas, J.M. Marinas, F.J. Urbano, Appl. Catal. B Environ. 127 (2012) 316–322.

[3] M. Pelaez, N.T. Nolan, S.C. Pillai, M.K. Seery, P. Falaras, A.G. Kontos, P.S.M. Dunlop, J.W.J. Hamilton, J.A. Byrne, K. O'Shea, M.H. Entezari, D.D. Dionysiou, Appl. Catal. B-Environ. 125 (2012) 331–349.

[4] U.I. Gaya, A.H. Abdullah, J. Photochem. Photobiol. C Photochem. Rev. 9 (2008) 1–12.
[5] H. Barndok, M. Pelaez, C. Han, W.E. Platten, P. Campo, D. Hermosilla, A. Blanco, D.D. Dionysiou, Environ. Sci. Pollut. Res. 20 (2013) 3582–3591.
[6] A.O. Ibhadon, P. Fitzpatrick, Catalysts 3 (2013) 189–218.
[7] J.L. Wang, L.J. Xu, Crit. Rev. Environ. Sci. Technol. 42 (2012) 251–325.
[8] A. Kubacka, M. Fernandez-Garcia, G. Colon, Chem. Rev. 112 (2012) 1555–1614.
[9] A.L. Linsebigler, G.Q. Lu, J.T. Yates, Chem. Rev. 95 (1995) 735–758.
[10] A. Dhakshinamoorthy, S. Navalon, A. Corma, H. Garcia, Energy Environ. Sci. 5 (2012) 9217–9233.
[11] E.M. Rodriguez, G. Fernandez, P.M. Alvarez, R. Hernandez, F.J. Beltran, Appl. Catal. B-Environ. 102 (2011) 572–583.
[12] G. Zhang, G. Kim, W. Choi, Energy Environ. Sci. 7 (2014) 954–966.
[13] S. Banerjee, S.C. Pillai, P. Falaras, K.E. O'Shea, J.A. Byrne, D.D. Dionysiou, J. Phys. Chem. Lett. 5 (2014) 2543–2554.
[14] M. Miyauchi, H. Irie, M. Liu, X.Q. Qiu, H.G. Yu, K. Sunada, K. Hashimoto, J. Phys. Chem. Lett. 7 (2016) 75–84.
[15] N. Hintsho, I. Petrik, A. Nechaev, S. Titinchi, P. Ndungu, Appl. Catal. B Environ. 156 (2014) 273–283.
[16] S. Sarina, E.R. Waclawik, H.Y. Zhu, Green Chem. 15 (2013) 1814–1833.
[17] X. Chen, H.Y. Zhu, J.C. Zhao, Z.T. Zheng, X.P. Gao, Angew. Chem. Int. Ed. 47 (2008) 5353–5356.
[18] P.Y. Zhang, T. Song, T.T. Wang, H.P. Zeng, Appl. Catal. B Environ. 206 (2017) 328–335.
[19] J.Y. Qin, H.P. Zeng, Appl. Catal. B Environ. 209 (2017) 161–173.
[20] J.Y. Qin, J.P. Huo, P.Y. Zhang, J. Zeng, T.T. Wang, H.P. Zeng, Nanoscale 8 (2016) 2249–2259.
[21] P.Y. Zhang, T.T. Wang, H.P. Zeng, Appl. Surf. Sci. 391 (2017) 404–414.
[22] T. Ohno, M. Akiyoshi, T. Umebayashi, K. Asai, T. Mitsui, M. Matsumura, Appl. Catal. A Gen. 265 (2004) 115–121.
[23] X.P. Wang, Y.X. Tang, M.Y. Leiw, T.T. Lim, Appl. Catal. A Gen. 409 (2011) 257–266.
[24] Y. Huang, W.K. Ho, Z.H. Ai, X.A. Song, L.Z. Zhang, S.C. Lee, Appl. Catal. B Environ. 89 (2009) 398–405.
[25] G.W. Cui, W.L. Wang, M.Y. Ma, M. Zhang, X.Y. Xia, F.Y. Han, X.F. Shi, Y.Q. Zhao, T.S. Dong, B. Tang, Chem. Commun. 49 (2013) 6415–6417.
[26] Z.P. Zhang, J. Zhang, N. Chen, L.T. Qu, Energy Environ. Sci. 5 (2012) 8869–8890.
[27] H.T. Li, Z.H. Kang, Y. Liu, S.T. Lee, J. Mater. Chem. 22 (2012) 24230–24253.
[28] A. Tarasov, G. Trusov, A. Minnekhanov, D. Gil, E. Konstantinova, E. Goodilin, Y. Dobrovolsky, J. Mater. Chem. A 2 (2014) 3102–3109.
[29] L. Cao, S. Sahu, P. Anilkumar, C.E. Bunker, J.A. Xu, K.A.S. Fernando, P. Wang, E.A. Guliants, K.N. Tackett, Y.P. Sun, J. Am. Chem. Soc. 133 (2011) 4754–4757.
[30] M.C. Ortega-Liebana, J.L. Hueso, S. Ferdousi, K.L. Yeung, J. Santamaria, Diam. Relat. Mater. 65 (2016) 176–182.
[31] M.C. Ortega-Liebana, J.L. Hueso, A. Larrea, V. Sebastian, J. Santamaria, Chem. Commun. 51 (2015) 16625–16628.
[32] P.C. Hsu, Z.Y. Shih, C.H. Lee, H.T. Chang, Green Chem. 14 (2012) 917–920.
[33] M.C. Ortega-Liebana, M.M. Encabo-Berzosa, M.J. Ruedas-Rama, J.L. Hueso, Chem. Eur. J. 23 (2017) 3067–3073.
[34] M.C. Ortega-Liebana, N.X. Chung, R. Limpens, L. Gomez, J.L. Hueso, J. Santamaria, T. Gregorkiewicz, Carbon 117 (2017) 437–446.
[35] S.N. Baker, G.A. Baker, Angew. Chem. Int. Ed. 49 (2010) 6726–6744.
[36] S.T. Yang, L. Cao, P.G.J. Luo, F.S. Lu, X. Wang, H.F. Wang, M.J. Meziani, Y.F. Liu, G. Qi, Y.P. Sun, J. Am. Chem. Soc. 131 (2009) 11308.
[37] R.L. Liu, D.Q. Wu, S.H. Liu, K. Koynov, W. Knoll, Q. Li, Angew. Chem. Int. Ed. 48 (2009) 4598–4601.
[38] L. Cao, X. Wang, M.J. Meziani, F.S. Lu, H.F. Wang, P.J.G. Luo, Y. Lin, B.A. Harruff, L.M. Veca, D. Murray, S.Y. Xie, Y.P. Sun, J. Am. Chem. Soc. 129 (2007) 11318.
[39] Y.P. Sun, B. Zhou, Y. Lin, W. Wang, K.A.S. Fernando, P. Pathak, M.J. Meziani, B.A. Harruff, X. Wang, H.F. Wang, P.J.G. Luo, H. Yang, M.E. Kose, B.L. Chen, L.M. Veca, S.Y. Xie, J. Am. Chem. Soc. 128 (2006) 7756–7757.
[40] S.J. Zhuo, M.W. Shao, S.T. Lee, ACS Nano 6 (2012) 1059–1064.
[41] Z.X. Gan, X.L. Wu, G.X. Zhou, J.C. Shen, P.K. Chu, Adv. Opt. Mater. 1 (2013) 554–558.
[42] A. Salinas-Castillo, M. Ariza-Avidad, C. Pritz, M. Camprubi-Robles, B. Fernandez, M.J. Ruedas-Rama, A. Megia-Fernandez, A. Lapresta-Fernandez, F. Santoyo-Gonzalez, A. Schrott-Fischer, L.F. Capitan-Vallvey, Chem. Commun. 49 (2013) 1103–1105.
[43] Y. Xu, M. Wu, Y. Liu, X.Z. Feng, X.B. Yin, X.W. He, Y.K. Zhang, Chem. Eur. J. 19 (2013) 2276–2283.
[44] C.F. Wang, X. Wu, X.P. Li, W.T. Wang, L.Z. Wang, M. Gu, Q. Li, J. Mater. Chem. 22 (2012) 15522–15525.
[45] W.L. Ong, M. Gao, G.W. Ho, Nanoscale 5 (2013) 11283–11290.
[46] J. Wang, Y.F. Lim, G.W. Ho, Nanoscale 6 (2014) 9673–9680.
[47] J. Wang, Y.H. Ng, Y.F. Lim, G.W. Ho, RSC Adv. 4 (2014) 44117–44123.
[48] M.J. Krysmann, A. Kelarakis, P. Dallas, E.P. Giannelis, J. Am. Chem. Soc. 134 (2012) 747–750.
[49] M.C. Ortega-Liebana, J.L. Hueso, R. Arenal, J. Santamaria, Nanoscale 9 (2017) 1787–1792.
[50] C. Jeanguillaume, C. Colliex, Ultramicroscopy 28 (1989) 252–257.
[51] R. Arenal, F. de la Pena, O. Stephan, M. Walls, M. Tence, A. Loiseau, C. Colliex, Ultramicroscopy 109 (2008) 32–38.
[52] Francis Leonard Deepak, Alvaro Mayoral, R. Arenal, Advanced Transmission Electron Microscopy: Applications to Nanomaterials, Springer, 2015.
[53] L.J. Xu, J.L. Wang, Appl. Catal. B Environ. 123 (2012) 117–126.
[54] X.J. Chen, Y.Z. Dai, J. Guo, T.H. Liu, X.Y. Wang, Ind. Eng. Chem. Res. 55 (2016) 568–578.
[55] E. Pretsch, P. Bühlmann, C. Affolter, A. Herrera, R. Martinez, Structure Determination of Organic Compounds, Springer, New York, 2000.
[56] C.F. Wang, D. Sun, K.L. Zhuo, H.C. Zhang, J.J. Wang, RSC Adv. 4 (2014) 54060–54065.
[57] X.C. Sun, C. Bruckner, Y. Lei, Nanoscale 7 (2015) 17278–17282.
[58] X.J. Gong, W.J. Lu, Y. Liu, Z.B. Li, S.M. Shuang, C. Dong, M.M.F. Choi, J. Mater. Chem. B 3 (2015) 6813–6819.
[59] H. Fu, Z.J. Du, W. Zou, H.Q. Li, C. Zhang, Carbon 65 (2013) 112–123.
[60] W.J. Peng, H.Q. Li, S.X. Song, ACS Appl. Mater. Interfaces 9 (2017) 5204–5212.
[61] B. Xie, L. Hong, P. Chen, B. Zhu, Bull. Polym. 73 (2016) 891–908.
[62] J.R. Pels, F. Kapteijn, J.A. Moulijn, Q. Zhu, K.M. Thomas, Carbon 33 (1995) 1641–1653.
[63] J.C. Sanchez-Lopez, C. Donnet, F. Lefebvre, C. Fernandez-Ramos, A. Fernandez, J. Appl. Phys. 90 (2001) 675–681.
[64] J.L. Hueso, J.P. Espinos, A. Caballero, J. Cotrino, A.R. Gonzalez-Elipe, Carbon 45 (2007) 89–96.
[65] J.P. Boudou, J.I. Paredes, A. Cuesta, A. Martinez-Alonso, J.M.D. Tascon, Carbon 41 (2003) 41–56.
[66] L. Wang, S.J. Zhu, H.Y. Wang, Y.F. Wang, Y.W. Hao, J.H. Zhang, Q.D. Chen, Y.L. Zhang, W. Han, B. Yang, H.B. Sun, Adv. Opt. Mater. 1 (2013) 264–271.
[67] J.H. Shen, Y.H. Zhu, C. Chen, X.L. Yang, C.Z. Li, Chem. Commun. 47 (2011) 2580–2582.
[68] H.J. Yu, R. Shi, Y.F. Zhao, G.I.N. Waterhouse, L.Z. Wu, C.H. Tung, T.R. Zhang, Adv. Mater. 28 (2016) 9454–9477.
[69] S. Yu, H.J. Yun, Y.H. Kim, J. Yi, Appl. Catal. B Environ. 144 (2014) 893–899.
[70] A.C.Y. Liu, R. Arenal, D.J. Miller, X.D. Chen, J.A. Johnson, O.L. Eryilmaz, A. Erdemir, J.B. Woodford, Phys. Rev. B (2007) 75.
[71] R. Arenal, L. De Matteis, L. Custardoy, A. Mayoral, M. Tence, V. Grazu, J.M. De La Fuente, C. Marquina, M.R. Ibarra, ACS Nano 7 (2013) 4006–4013.
[72] R. Arenal, K. March, C.P. Ewels, X. Rocquefelte, M. Kociak, A. Loiseau, O. Stephan, Nano Lett. 14 (2014) 5509–5516.
[73] A.P. Bhirud, S.D. Sathaye, R.P. Waichal, J.D. Ambekar, C.J. Park, B.B. Kale, Nanoscale 7 (2015) 5023–5034.
[74] M. Sathish, B. Viswanathan, R.P. Viswanath, C.S. Gopinath, Chem. Mater. 17 (2005) 6349–6353.
[75] X.J. Yu, J.J. Liu, Y.C. Yu, S.L. Zuo, B.S. Li, Carbon 68 (2014) 718–724.
[76] Y.Q. Dong, H.C. Pang, H.B. Yang, C.X. Guo, J.W. Shao, Y.W. Chi, C.M. Li, T. Yu, Angew. Chem. Int. Ed. 52 (2013) 7800–7804.
[77] L.M. Pastrana-Martinez, S. Morales-Torres, S.A.C. Carabineiro, J.G. Buijnsters, J.L. Faria, J.L. Figueiredo, A.M.T. Silva, ChemPlusChem 78 (2013) 801–807.
[78] M. Pera-Titus, V. Garcia-Molina, M.A. Banos, J. Gimenez, S. Esplugas, Appl. Catal. B Environ. 47 (2004) 219–256.
[79] W.F. Jardim, S.G. Moraes, M.M.K. Takiyama, Water Res. 31 (1997) 1728–1732.
[80] G.Z. Liao, S. Chen, X. Quan, H.T. Yu, H.M. Zhao, J. Mater. Chem. 22 (2012) 2721–2726.
[81] H.Q. Sun, S.Z. Liu, G.L. Zhou, H.M. Ang, M.O. Tade, S.B. Wang, ACS Appl. Mater. Interfaces 4 (2012) 5466–5471.
[82] J. Zhong, F. Chen, J.L. Zhang, J. Phys. Chem. C 114 (2010) 933–939.
[83] J.P. Wang, Z.Y. Wang, B. Huang, Y.D. Ma, Y.Y. Liu, X.Y. Qin, X.Y. Zhang, Y. Dai, ACS Appl. Mater. Interfaces 4 (2012) 4024–4030.
[84] B.Z. Tian, C.Z. Li, F. Gu, H.B. Jiang, Y.J. Hu, J.L. Zhang, Chem. Eng. J. 151 (2009) 220–227.
[85] S.A.K. Leghari, S. Sajjad, F. Chen, J.L. Zhang, Chem. Eng. J. 166 (2011) 906–915.
[86] M.Y. Xing, J.L. Zhang, F. Chen, Appl. Catal. B Environ. 89 (2009) 563–569.
[87] Y. Cong, J.L. Zhang, F. Chen, M. Anpo, J. Phys. Chem. C 111 (2007) 6976–6982.
[88] J. Bandara, J.A. Mielczarski, A. Lopez, J. Kiwi, Appl. Catal. B Environ. 34 (2001) 321–333.
[89] H.W. Huang, K. Xiao, Y. He, T.R. Zhang, F. Dong, X. Du, Y.H. Zhang, Appl. Catal. B Environ. 99 (2016) 75–86.
[90] H.Y. Jiang, K. Cheng, J. Lin, Phys. Chem. Chem. Phys. 14 (2012) 12114–12121.
[91] C. Hu, T.W. Peng, X.X. Hu, Y.L. Nie, X.F. Zhou, J.H. Qu, H. He, J. Am. Chem. Soc. 132 (2010) 857–862.
[92] X.F. Zhou, C. Hu, X.X. Hu, T.W. Peng, J.H. Qu, J. Phys. Chem. C 114 (2010) 2746–2750.
[93] Y. Lu, H.T. Yu, S. Chen, X. Quan, H.M. Zhao, Environ. Sci. Technol. 46 (2012) 1724–1730.
[94] S. Shamaila, A.K.L. Sajjad, F. Chen, J.L. Zhang, Appl. Catal. B Environ. 94 (2010) 272–280.
[95] M.J. Sampaio, L.M. Pastrana-Martinez, A.M.T. Silva, J.G. Buijnsters, C. Han, C.G. Silva, S.A.C. Carabineiro, D.D. Dionysiou, J.L. Faria, RSC Adv. 5 (2015) 58363–58370.
[96] T.F. Yeh, C.Y. Teng, S.J. Chen, H.S. Teng, Adv. Mater. 26 (2014) 3297.
[97] H. Chen, Z.L. Zhang, Z.L. Yang, Q. Yang, B. Li, Z.Y. Bai, Chem. Eng. J. 273 (2015) 481–489.
[98] S.P. Li, X.L. Ma, L.J. Liu, X.H. Cao, RSC Adv. 5 (2015) 1902–1909.
[99] Q. Huang, M.H. Cao, Z.H. Ai, L.Z. Zhang, Appl. Catal. B Environ. 162 (2015) 319–326.
[100] P. Fernandez-Ibanez, M.I. Polo-Lopez, S. Malato, S. Wadhwa, J.W.J. Hamilton, P.S.M. Dunlop, R. D'Sa, E. Magee, K. O'Shea, D.D. Dionysiou, J.A. Byrne, Chem. Eng. J. 261 (2015) 36–44.
[101] M. Romero, J. Blanco, B. Sanchez, A. Vidal, S. Malato, A.I. Cardona, E. Garcia, Sol. Energy 66 (1999) 169–182.

IV.5.1 Supporting Information of Article 5

Applied Catalysis B: Environmental

Extraordinary Sensitizing Effect Of Co-Doped Carbon Nanodots Derived From Mate Herb. Application to Enhanced Photocatalytic Degradation of Chlorinated Wastewater Compounds Under Visible Light

M.Carmen Ortega-Liebana,[ab] Jose L. Hueso,*[ab] Shammi Fersousi,[c] Raul Arenal, [de] Silvia Irusta, [ab] King L. Yeung[c] and Jesus Santamaria*[ab]

[a]Institute of Nanoscience of Aragon (INA) and Department of Chemical Engineering and Environmental Technology, University of Zaragoza, 50018 Zaragoza, Spain.
[b]Networking Research Center on Bioengineering, Biomaterials and Nanomedicine (CIBER-BBN), 28029 Madrid, Spain.
[c]Department of Chemical and Biomolecular Engineering, The Hong Kong University of Science and Technology (HKUST), Clear Water Bay, Kowloon, Hong Kong, China.
[d]Advanced Microscopy Laboratory (LMA) and Institute of Nanoscience of Aragon (INA), University of Zaragoza, 50018 Zaragoza, Spain.
[e]*ARAID* Foundation, 50018 Zaragoza, Spain.

a

b
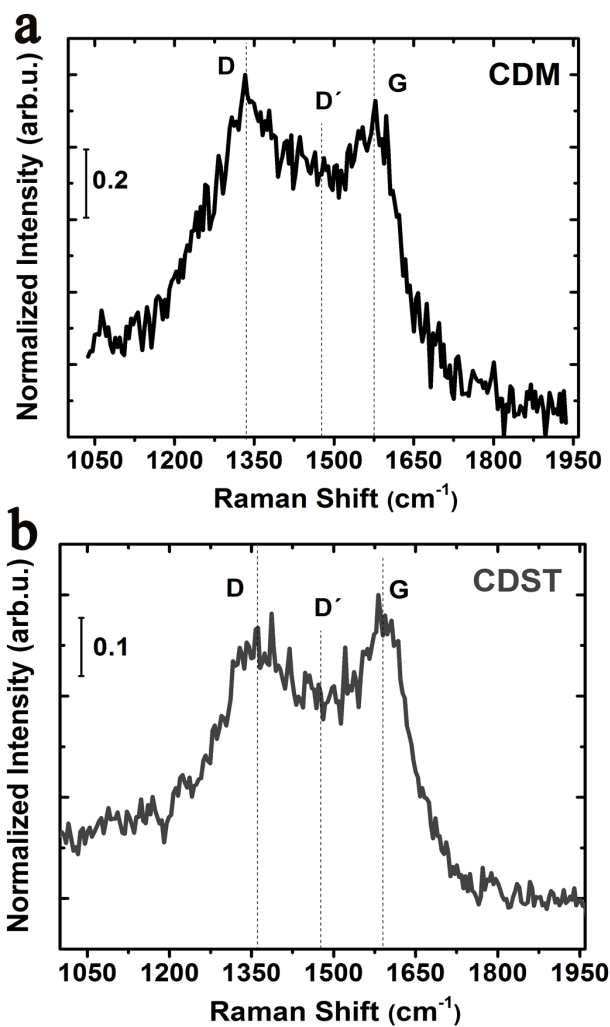
Figure S1. Raman spectra corresponding to the carbon nanodots derived from (a) Mate herb and (b) Stevia plant.
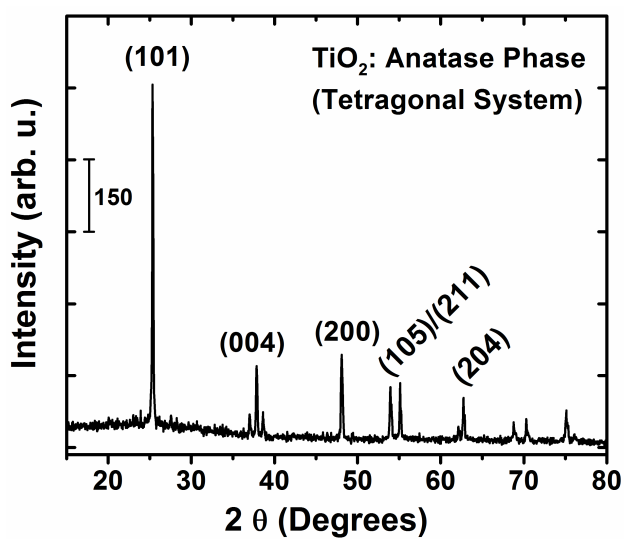
Figure S2. X-ray diffractogram of the as-received TiO_2 particles with anatase phase.
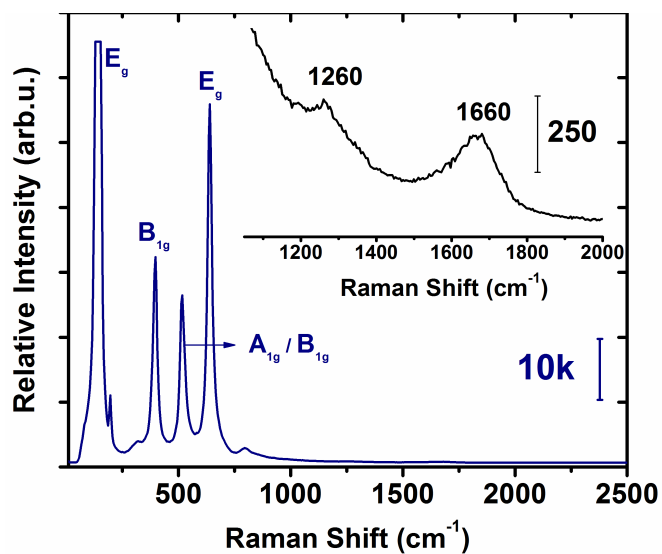
Figure S3. Raman spectra corresponding to the as-received commercial TiO_2 particles.
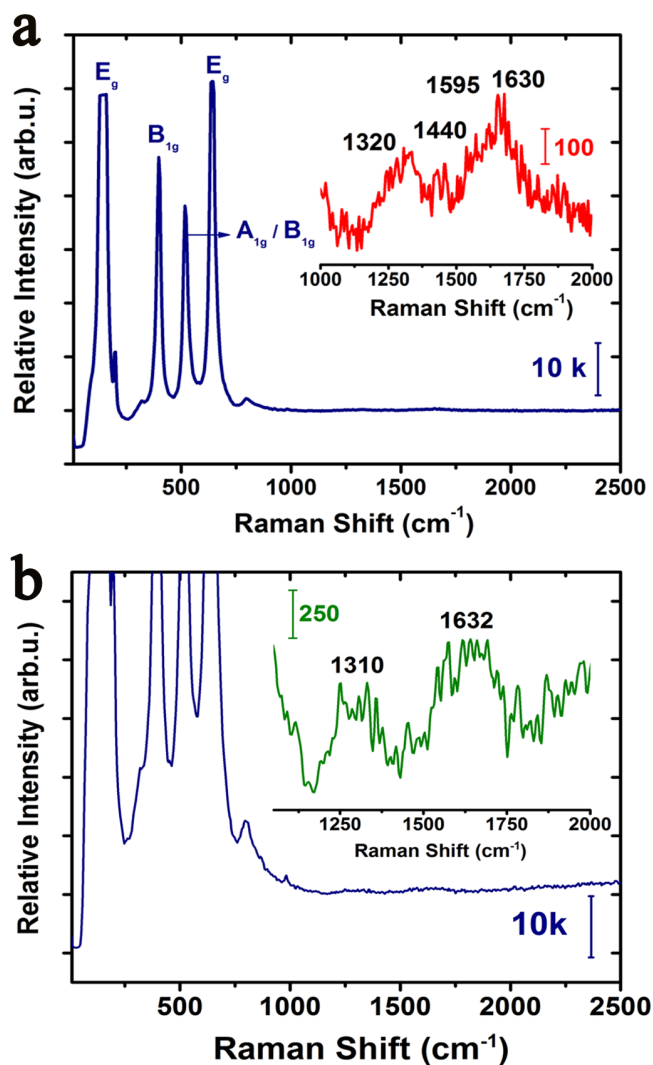
Figure S4. Raman spectra corresponding to the CND@TiO_2 nanocomposites: a) Mate-derived CNDs@TiO_2; b) Stevia-derived CNDs@TiO_2.

229
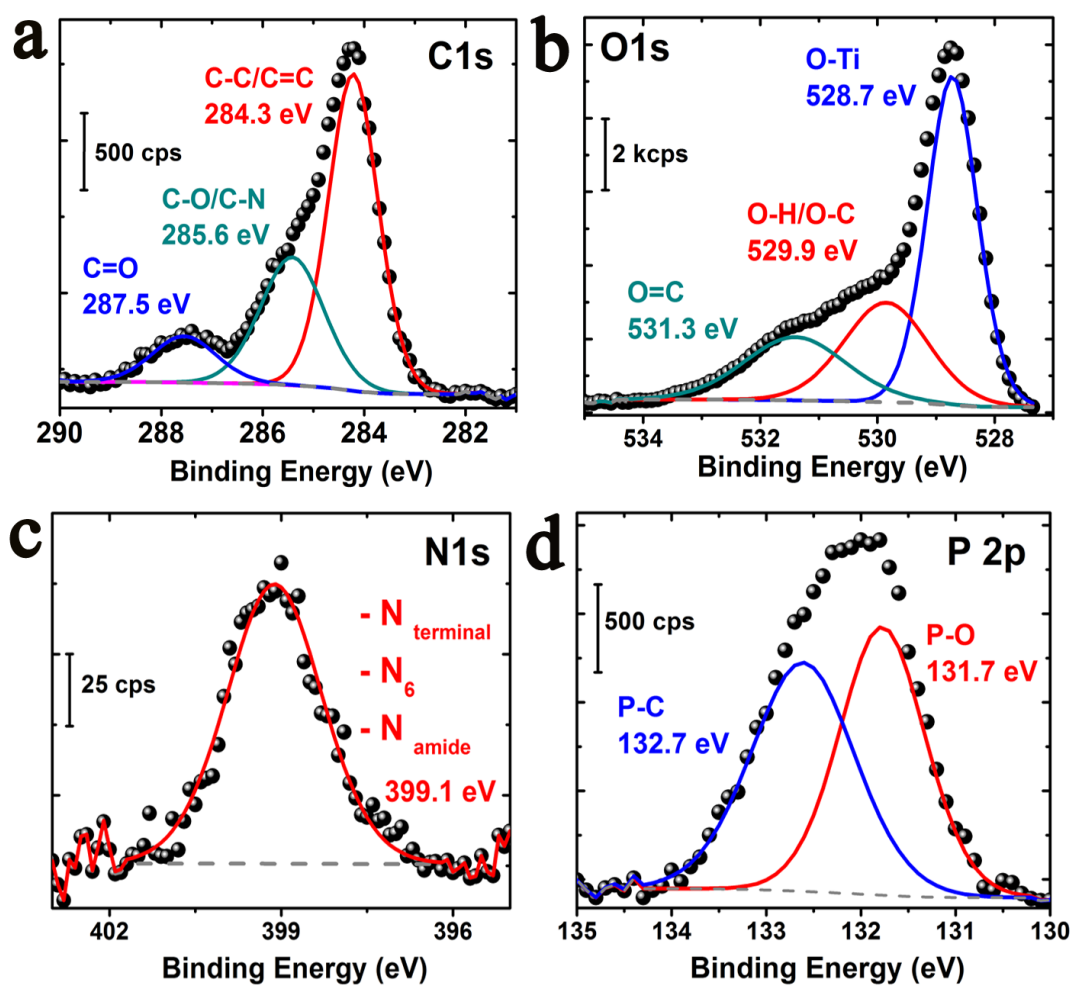
Figure S5. XP spectra corresponding to the C1s, O1s, N1s and P2p region of the CNDST@TiO$_2$ hybrid photocatalysts
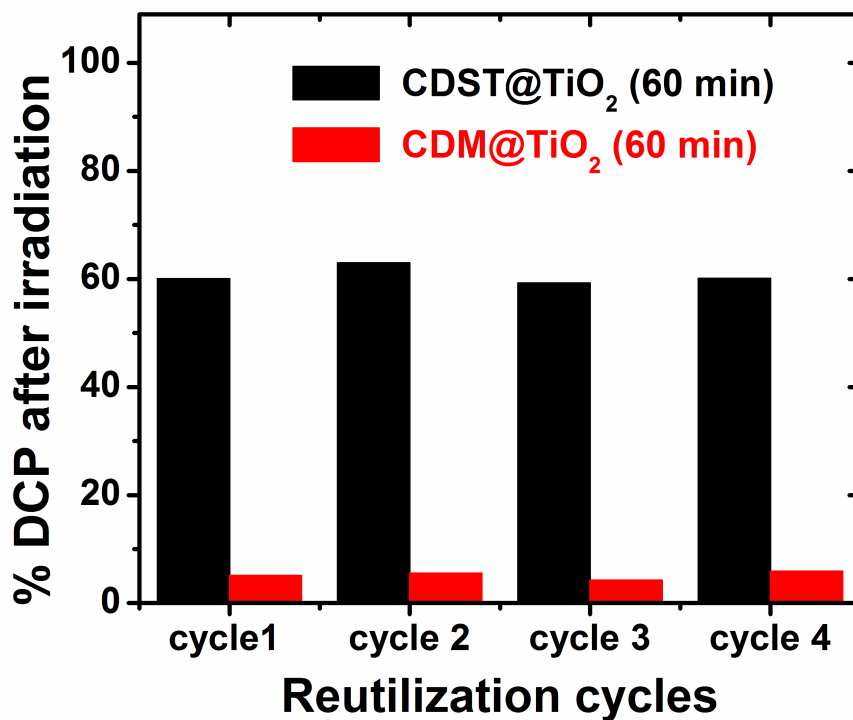
Figure S6. Influence of the reutilization cycles on the degradation of 2,4-DCP.
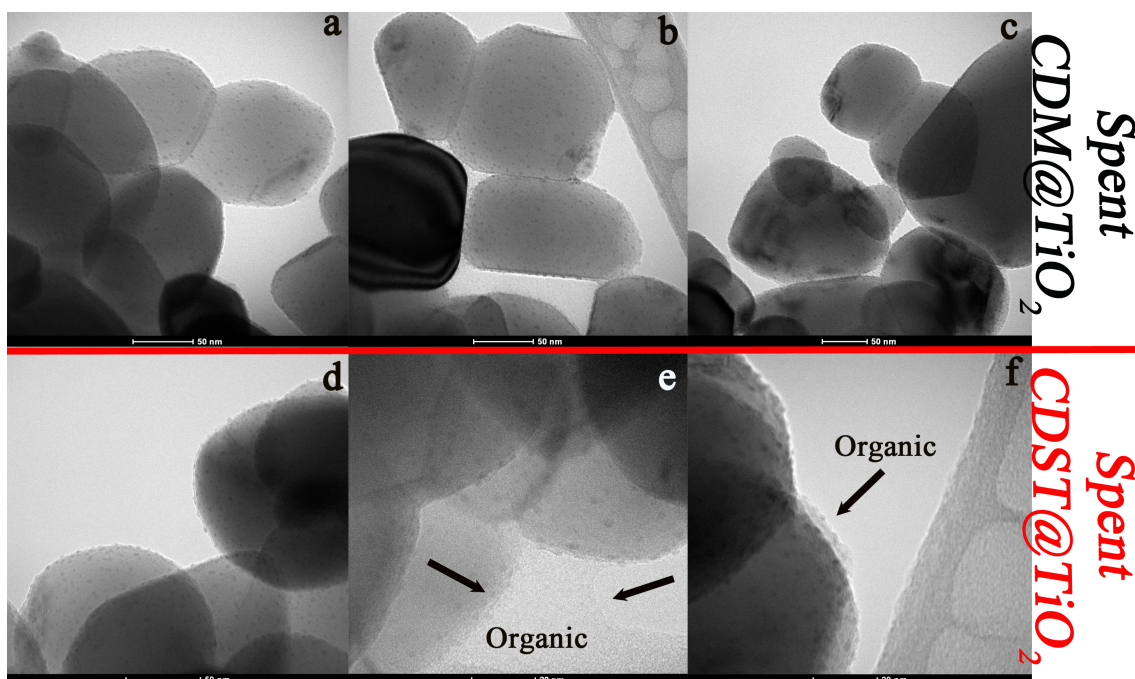
Figure S7. TEM images corresponding to the photocatalysts after multiple reuse cycles: a-c) CDM@TiO$_2$ photocatalyst after reuse; d-f) CDST@TiO$_2$ photocatalyst after multiple uses.

IV.6 **Article 6.** Uniform luminescent carbon nanodots prepared by rapid pyrolysis of organic precursors confined within nanoporous templating structures

Uniform luminescent carbon nanodots prepared by rapid pyrolysis of organic precursors confined within nanoporous templating structures

CrossMark

M.C. Ortega-Liebana [a, b, 1], N.X. Chung [c, 1], R. Limpens [c], L. Gomez [c, *], J.L. Hueso [a, b, **], J. Santamaria [a, b], T. Gregorkiewicz [c]

[a] Institute of Nanoscience of Aragon (INA) and Department of Chemical Engineering and Environmental Technology, Edificio I+D+i, Campus Rio Ebro, 50018, Zaragoza, Spain
[b] Networking Research Center on Bioengineering, Biomaterials and Nanomedicine (CIBER-BBN), 28029, Madrid, Spain
[c] Institute of Physics, University of Amsterdam, Science Park 904, 1098 XH, Amsterdam, The Netherlands

A B S T R A C T

Although several methods on the preparation of carbon nanodots (CNDs) emitting throughout the visible have been recently reported, in most of the processes the product suffers from inhomogeneity in size and shape limiting their impact. Here, we report the synthesis of undoped and nitrogen-doped luminescent carbon nanodots by rapid pyrolysis using ordered mesoporous silica nanorods as confining templates. A rapid thermal decomposition (pyrolysis) within the confined dimensions of their pores leads to a highly uniform size distribution of CNDs with average sizes below 4 nm. These CNDs are synthesized in an extremely short time period (5 min of reaction) by immersion in a fluidized-bed reactor that provides heating homogeneity and ensures fast heat transfer. In addition, a rapid release of the homogeneous CNDs can be easily achieved by a simple ultrasonication-filtration step that prevents further chemical action on the mesoporous templates. The emission of both undoped and N-doped CNDs in colloidal and solid state (with an efficiency of 1−5%) originates from a combination of quantum confinement effects and the presence of oxidized surface states; N-doping introduces resonant absorption states which participate in emission. Furthermore, we present a simple model to describe the excitation-dependent/-independent mechanism of carbon nanodots.

1. Introduction

Carbon nanomaterials (graphene, fullerenes, nanotubes, and carbon nanodots (CNDs) in particular) have been widely studied during the past years due to their optoelectronic properties and their potential applications [1]. The most exciting property of CNDs is their photoluminescence (PL), which can be tuned by varying the excitation wavelength [2,3]. Furthermore, they show low toxicity and can be synthesized from an unlimited number of carbon sources, with feasible large scale production and excellent chemical- and photo-stability [4−6]. CNDs have been successfully used for different purposes, such as sensing, bio-imaging, drug delivery, photocatalysis, and photovoltaics [7−10].

The PL mechanism of CNDs and its excitation dependence have been studied in-depth and related to numerous effects, such as quantum confinement (QCE), surface traps and solvent polarity (or "giant red-edge effect"). However, a clear and unified theory is still missing [11]. One of the issues is the CNDs' variability as their composition, structure and properties depend on the raw materials used as carbon sources and the production method (temperature, pressure, solvent) employed.

Numerous synthetic routes have been reported for the production of CNDs, such as laser ablation [12], electrochemical oxidation [13], electrochemical etching [14−16], microwave assisted reaction [17] and hydrothermal synthesis [18]. Nonetheless, the control of the process to yield a product homogeneous in size and shape is still challenging. Also, clean and efficient methods to reduce processing times are needed. A possible approach to obtain a uniform material is to use an external template able to restrict the

* Corresponding author. Institute of Physics, University of Amsterdam, Science Park 904, 1098 XH, Amsterdam, The Netherlands.
** Corresponding author. Institute of Nanoscience of Aragon (INA) and Department of Chemical Engineering and Environmental Technology, Edificio I+D+i, Campus Rio Ebro, 50018, Zaragoza, Spain.
E-mail addresses: L.gomeznavascues@uva.nl (L. Gomez), jlhueso@unizar.es (J.L. Hueso).
1 Equal contribution.

size and shape of the generated nanostructures. In this regard, micelles [19], mesoporous silica [20] and zeolites [21] have already been used as confining nanoreactors in the production of CNDs. On the other hand, the production of CNDs by pyrolysis (thermal decomposition at high temperatures in the absence of oxygen) is revealed as a simple and efficient method [22]. Therefore, an ideal methodology to synthesize CNDs would be to place the carbon precursor within the pores of an inorganic structure able to withstand the conditions required for pyrolysis. Baldovi *et al.* [21] proposed this idea using zeolites. However, this required long reaction times of up to 24 h and restricted pore sizes to the sub-nanometric range that involved additional chemical or purification steps to retrieve the CNDs.

Here, we report the synthesis of undoped and N-doped CNDs obtained by a rapid pyrolysis method using ordered mesoporous silica nanorods as hosting nanotemplates. These silica-based nanostructures have been successfully used to: (i) load two different organic precursors such as citric acid (CA) or ethylenediaminetetraacetic acid (EDTA), (ii) induce their thermal decomposition (pyrolysis) within the confined dimensions of their porous walls, and (iii) render a highly uniform size distribution of CNDs. This work attempts to shed light on the PL behavior of CNDs without incurring into the necessity of dissolving the mesoporous silica structure. In many of the common CNDs synthesis methods, a variety of shapes and compositions are possible, due to: (i) the gradients of temperature and concentration that inevitably appear in the batch processes leading to different growth rates for different regions of the reactor and (ii) the possibility of agglomeration of growing nanoparticles during the long synthesis processes. By confining the precursors into a porous structure we expect to alleviate both problems. Also, by accelerating the synthesis process, the opportunity for agglomeration would also be minimized. In addition, the rapid pyrolysis method used allows the syntheses to be completed in a short period of time (5 min of reaction) by immersion in a fluidized-bed reactor that provides a fast heating and a high homogeneity in the heating environment [23,24]. The structure of the silica hosting matrix allowed the synthesis of undoped and N-doped CNDs simply by changing the nature of the precursor hosted in the pores. On the other hand, the high aspect ratio of the nanorods provides a longer diffusion path favoring a high degree of pyrolysis within the pores. Furthermore, the CNDs were successfully retrieved from the mesoporous template by simple ultrasonication and in the absence of additional chemical treatments involving the digestion of the template. The influence of the incorporation of dopants such as nitrogen, which is known to alter the optoelectronic characteristics of CNDs [25,26], has been evaluated by a thorough analysis of the chemical and optical properties of both products, undoped and N-doped CNDs.

2. Experimental

2.1. Chemicals

Tetraethylorthosilicate (TEOS, 98%), hydrochloric acid (HCl, 37%), ammonium fluoride (NH_4F, 98%), heptane (99%), poly(-ethylene glycol)-block-poly(propylene glycol)-block-poly(ethylene glycol) average M_n ~5800 (Pluronic® P-123), lithium chloride anhydrous (LiCl, 99%), sodium chloride (NaCl, 99%), potassium nitrate (KNO_3, 99%), citric acid (CA, 99.5%) and ethylenediaminetetraacetic acid (EDTA, 99.995%) were obtained from Sigma-Aldrich. All chemicals were of analytical purity grade.

2.2. Synthesis of ordered mesoporous silica nanorods

Ordered mesoporous silica nanorods were prepared by a slightly

modified hydrothermal synthesis according to previously reported procedure [27]. In a typical synthesis, 1.2 g of P-123 and 0.014 g of NH_4F were first dissolved at 20 °C in 40 mL of HCl (1.75 M) solution under stirring. Upon complete dissolution, 2.75 mL of TEOS and 8.5 mL of heptane were added drop wise and left under stirring for 8 min. The aged precursor mixture was hydrothermally heated at 100 °C for 24 h in a Teflon-lined autoclave. The solid product was then filtered, washed three times with distilled water, and dried at 60 °C overnight. The removal of the organic template was carried out by calcination with a heating ramp of 1 °C min^{-1} up to 550 °C and a dwell time of 6 h in flowing air.

2.3. Synthesis of undoped and N-doped carbon nanodots

In a typical experiment, 200 mg of the calcined silica nanorods and 100 mg of the selected organic precursor (citric acid or EDTA) were mixed and sonicated in 0.5 mL of a solution containing NaCl, LiCl and KNO_3 (mass ratio 20:5:5). The mixture was dried in an oven at 60 °C for 10 min and a fraction of the resulting powder (20 mg) was placed in a quartz capillary (Ø$_{in}$ = 8 mm) designed with inlet-outlet outfits (Ø$_{in}$ = 6 mm) for inert gas feeding (nitrogen flow rate 3 L h^{-1}). The capillary tube was introduced inside a sand fluidized bed (8 cm bed height) used to induce the formation of a bubbling fluidized bed via air bubbling (flow feeding rate 15 L h^{-1}) (see Fig. 1). This fluidized bed configuration promotes a rapid and homogeneous heating during the rapid pyrolysis process carried out by immersion of the tubular reactor containing the mesoporous solids inside the bubbling fluidized bed set at 500 °C under the inert atmosphere provided by nitrogen. The fluidized bed was kept at 500 °C for 5 min and allowed to cool down to room temperature. After the flash pyrolysis process, a brownish-pale yellow solid was obtained. This powdered solid was extensively rinsed and ultrasonicated in water for 15 min to facilitate the release of the carbon nanostructures generated within the silica nanoreactor. The supernatant containing the CNDs was passed through a 10 nm cutoff filter. The final yellow solution containing the CNDs was stored without any further treatment prior to use. The experiments have been performed by the platform of Production of Biomaterials and Nanoparticles of the NANBIOSIS ICTS, more specifically by the Nanoparticle Synthesis Unit of the CIBER in BioEngineering, Biomaterials & Nanomedicine (CIBER-BBN).

2.4. Characterization techniques

The morphologies and particle size distributions were determined by transmission electron microscopy (TEM) (FEI Tecnai T20 and Titan³ High-Base operated at 200 kV and 300 kV, respectively). To prepare the samples, the nanoparticle suspensions were diluted with water prior drop-casting on a holey copper grid. The average size distribution of CNDs was statistically estimated over 200 particle counts. The surface chemistry analysis of the nanoparticles was carried out by Fourier transform infrared (FTIR) spectroscopy using a Bruker Vertex 70 FTIR spectrometer using the horizontal attenuated total reflectance (ATR) mode and by X-ray photoelectron spectroscopy (XPS) with an Axis Ultra DLD (Kratos Tech.). A monochromatic Al Kα source (1486.6 eV) was employed with multiple runs at 12 kV, 10 mA and pass energy of 20 eV. The binding energies were calibrated to the internal C1s (284.2 eV) standard. Curve-fittings were performed with CasaXPS software, using a weighted sum of Lorentzian and Gaussian components after Shirley background subtraction. Raman spectra were acquired with a Laser Raman WiTec Alpha 300 spectrometer using the green exciting radiation (532 nm) from an Ar⁺ ion laser. All measurements were performed at room temperature.

The PLE spectra of concentrated undoped and N-doped CNDs
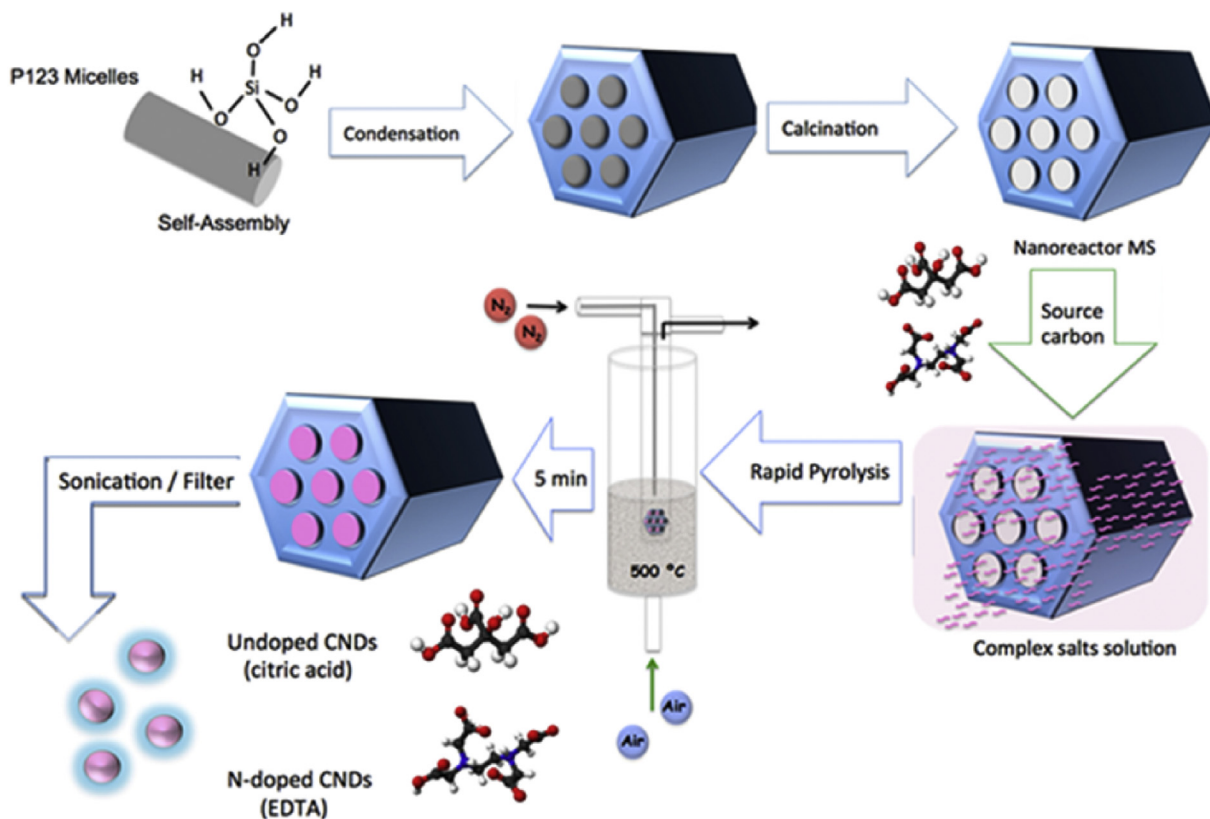
Fig. 1. Scheme describing the different steps carried out to synthesize the mesoporous silica nanorod templates, the nanochannels loading with either citric acid or EDTA, and the rapid pyrolysis treatment carried out in the fluidized bed reactor at 500 °C to render confined undoped and N-doped CNDs, respectively. (A colour version of this figure can be viewed online.)

samples were measured using a Horiba Fluorolog-21 spectrofluorometer with a xenon lamp as an excitation source. Absorption measurements of these samples were conducted with a Perkin Elmer UV–Vis Lambda 950 spectrometer. To prevent absorption saturation in the high absorption regime, we diluted the above undoped and N-doped colloidal samples 15 and 10 times, respectively. The absolute photoluminescence quantum yield (PL QY) measurements were performed in a Newport integrating sphere in order to avoid problems dealing with directionality of reflectance, scattering and emission from these samples; a xenon lamp coupled to a Solar MSA130 monochromator was used to reach a stable and low excitation intensity regime. We used the 7.5 cm and 10 cm integrating spheres to measure PL QY of solid state and colloidal samples, respectively. The details can be found in the Supporting Information.

The nanosecond PL dynamics were measured by using the frequency-doubled output of a tunable Ti:sapphire laser system (Chameleon Ultra, Coherent) providing 140 fs pulses at $\lambda_{exc} = 360$ nm with the repetition frequency of 8 MHz, and the PL emission was detected using a Newport CS260-02 monochromator coupled to a MCP Hamamatsu detector Hamamatsu (R3809U-51).

The PL dynamics were investigated at 430, 445 and 460 nm. For each of them, 2 different excitation powers were employed to validate the linear excitation regime in terms of the relevant parallel PL dynamic traces (in logarithmic scale), as can be seen in Fig. S1. To calculate the lifetime from the dynamics traces, we divide the time window into 2 parts:

(1) For relatively long delay times (multiple nanoseconds), the decay dynamics trace follows a single exponential decay:

$$I_{PL}^{part1} = I_0 \exp\left(-\frac{t}{\tau_{single}} \right) + I_{BGN}$$

With I_0 the initial amplitude, t the delay time, I_{BGN} the background signal and τ_{single} is the single exponential lifetime.

(2) For short time delays, directly after the pulse, the PL mechanism is fitted in terms of the sum of a stretch exponential and the before mentioned single exponential function:

$$I_{PL}^{part2} = I_0 \exp\left(-\frac{t}{\tau_{single}} \right) + I_1 \exp\left[-\left(\frac{t}{\tau_{stretch}}\right)^{\beta} \right] + I_{BGN}$$

With I_1 is the amplitude of the stretch exponential function, β the stretching exponent and $\tau_{stretch}$ the lifetime of the stretched function.

3. Results and discussion

3.1. Rapid pyrolysis of organic precursors hosted within rod-shaped mesoporous silica templates and morpho-chemical characterization of undoped and N-doped CNDs

Fig. 1 shows a scheme of the different synthesis steps carried out to obtain the CNDs. SBA-15 rod-shaped silica mesostructures with straight parallel porous channels were synthesized in first place following a hydrothermal approach previously reported by Oden *et al.* where reaction times were shortened to ensure the formation of rods in the nanoscale [27] (see Fig. 2a and b for SEM and TEM
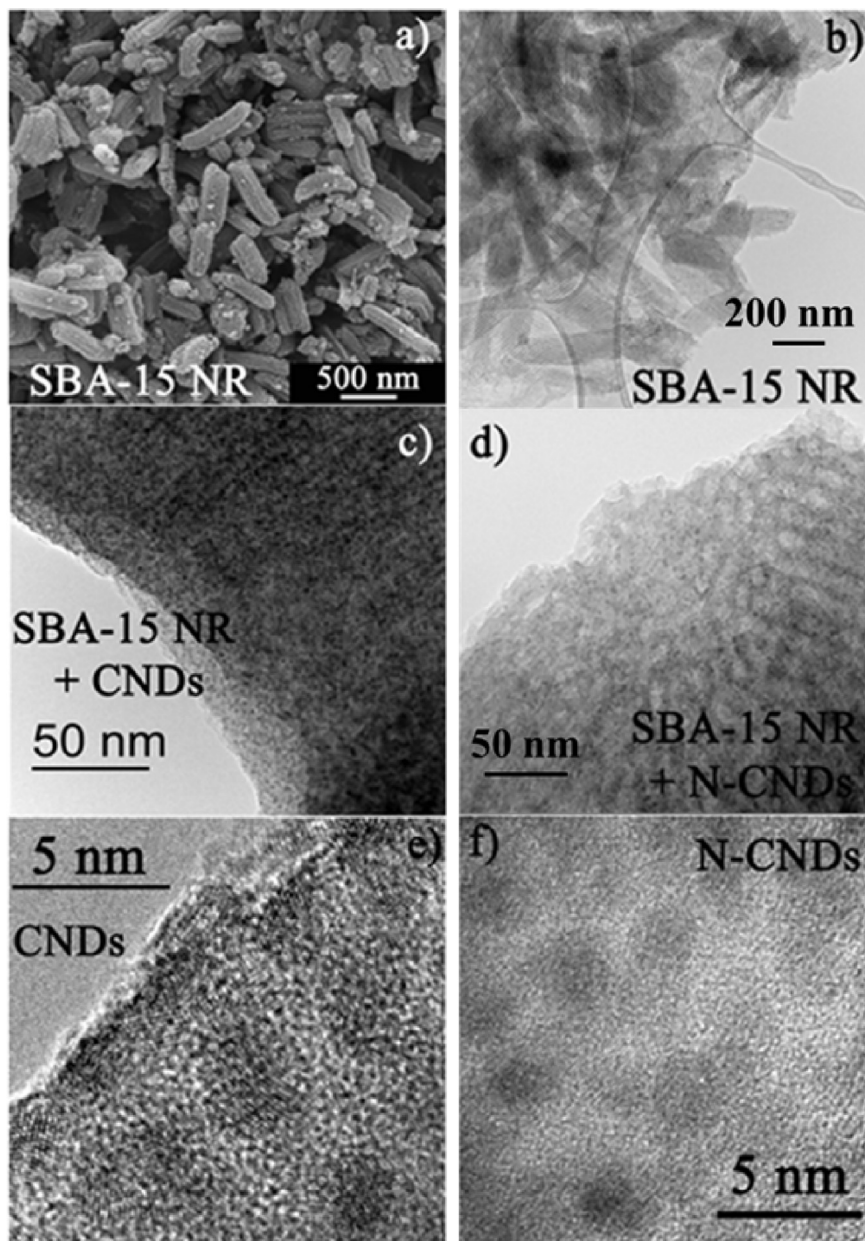
Fig. 2. (a) SEM and (b) TEM images of SBA-15 nanorods after calcination without carbon precursor. (c, d) TEM images showing the loading and confining of CNDs within the mesochannels of SBA-15 nanorods after the flash pyrolysis treatment of CA and EDTA in the fluidized-bed reactor, respectively. (e, f) High-resolution TEM detail of the CNDs encased within the mesoporous SBA-15 nanorods.

images of the SBA-15 nanorods, respectively). Calcination was required to remove the P-123 surfactant used as structuring agent and release the pores. After calcination, the SBA-15 nanorods were immersed in a suspension containing different salts (see Experimental Section) and the organic precursors to be loaded within the channels of the porous support (either citric acid or EDTA containing amine groups to promote N-doping). Subsequently, the loaded SBA-15 pellets were subjected to rapid pyrolysis treatment by immersion within a bubbling fluidized sand bed at 500 °C in the presence of an inert atmosphere of nitrogen. Thermogravimetric analysis revealed that an effective loading of the organic precursors was successfully achieved (up to 33% wt. loading that diminished to approximately 25% wt. after the pyrolysis treatment).

This reactor configuration enabled the effective pyrolysis of the

organic precursors selected as carbon sources and the formation of multiple CNDsencased within the channels of the silica nanoreactor after only 5 min of reaction, as shown in Fig. 2c and d. High-resolution TEM analysis of the freestanding CNDs further corroborates their crystalline structure (Figs. 2e, f and 3c, d). Lattice spacings of 0.210 nm and 0.180 nm corresponding to (100) and (102) diffraction planes of graphite have been identified in Fig. 3c. Likewise, the N-doped CNDs also exhibited a similar crystallinity in spite of their lower mean sizes and 0.204 nm spacings of the (101) diffraction planes in graphite have been also identified in selected nanoparticles (Fig. 3d). In addition, Fig. 3a and b and S4 show the extremely good self-assembly layers of the freestanding CNDs successfully retrieved from the rod-shaped SBA-15 nanotemplates after rinsing, ultrasonication and filtration steps (see Fig. 1 and Experimental Section). This is attributable to the narrow size
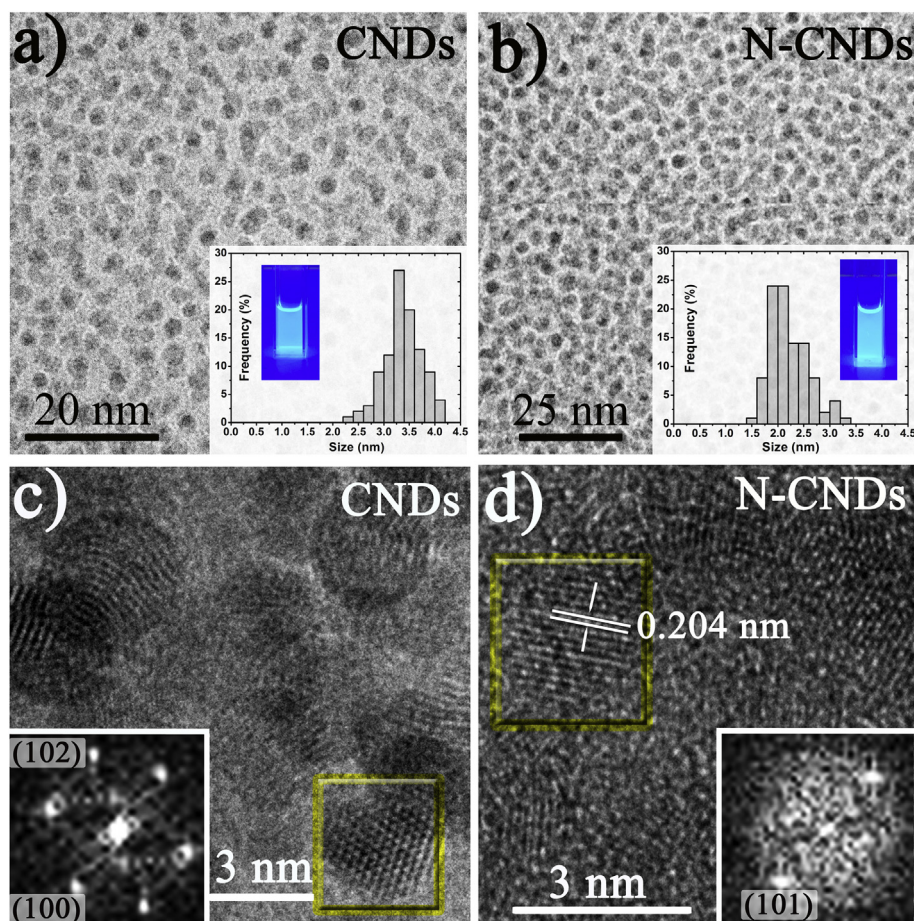
Fig. 3. Low magnification TEM images of the freestanding carbon nanodots after their release from the rod-shaped templates via ultrasonication and filtration: a) Undoped and b) N-doped CNDs, respectively. The insets in (a) and (b) reveal the particle size distribution determined for each type of CNDs and their emission under UV lamp illumination (365 nm); c-d) High resolution TEM images of the undoped and N-doped CNDs, respectively. The insets refer to the FFT analysis carried out on the nanoparticles highlighted in a yellow square and corresponding to graphitic diffraction spots. (A colour version of this figure can be viewed online.)

distribution of the CNDs estimated as 3.4 ± 0.4 nm and 2.3 ± 0.3 nm for the samples retrieved from CA and EDTA initial carbon precursors, respectively (Fig. 3). The differences observed for both carbon types in terms of average diameters are strongly dependent on the specific carbonization-passivation process for each organic precursor, as demonstrated in previous reports [28,29]. Average CNDs concentrations within the range of $1.00-1.25$ mg mL^{-1} were typically obtained with estimated 80% extraction efficiencies. No evidences of other organic aggregates could be detected by TEM inspection. Furthermore, the high pore diameter of the synthesized SBA-15 nanorods (8.43 nm determined by BET) has probably enabled a more straightforward release of the newly formed CNDs in contrast with former silica supports where chemical attacks and digestions were necessary to dissolve the inorganic templates and free the carbogenic cores [20,21]. The sample derived from CA will be hereafter labeled as undoped CNDs and the dots obtained from EDTA will be referred as N-doped CNDs.

The surface chemical composition of the CNDs was analyzed by X-ray photoelectron spectroscopy (XPS) resulting in 73.5% C and 26.5% O for the undoped CNDs and 71.5% C, 27.6% O and 0.9% N for the N-doped counterparts. Fig. 4 compares the high resolution C1s, O1s and N1s X-ray photoemission spectra corresponding to the undoped and the N-doped CNDs, respectively. Using curve-fitting analysis, the C1s contribution of the undoped CNDs can be mainly assigned to C−C bonds at 284.2 eV (37% intensity contribution) and to C−O (hydroxyl, ether-like) groups at 285.5 eV (28%

contribution). An additional and minor contribution of more oxidized species (i.e. carbonyl and carboxylic) at 287 and 288.9 eV further confirms the high presence of surface oxidized moieties dominating the first layers of the undoped CNDs. On the contrary, the N-CND sample shows a much lower contribution of highly oxidized species and its second major contribution is broader and shifted to higher binding energies (BEs). This can be attributed to the presence of C−O−C, C−OH and/or C−N species [30]. The O1s spectra show two main contributions of C/O species. The first one located at ~532.8 eV is usually associated to oxygen atoms bonded to C through sp^2 orbitals (i.e. aromatic species, carboxylic species) while the second is centered at ~531.5 eV and it is tentatively assigned to oxygen bonded to carbon through aliphatic sp^3 orbitals [31,32]. The relative contribution of each peak further corroborates the major presence of sp^3 bond-type in the N-doped sample. Finally, the evaluation of the N1s region confirms the presence of N within the carbon nanostructure prepared from the EDTA source and the negligible presence of any type of species in the undoped CNDs generated from CA. The peak at 399.3 eV can be attributed to N intercalated in terminal or bridge positions of the carbon network according to the criteria of Pels and Sanchez-Lopez [33,34].

Raman spectroscopy can be also used as a tool for the surface characterization of partially ordered carbon materials with an estimated analysis depth of 100 nm. The first-order Raman spectra corresponding to both CND samples reveal a similar pattern with two relatively broad bands centered at ~1350 cm^{-1} and ~1580 cm^{-1}
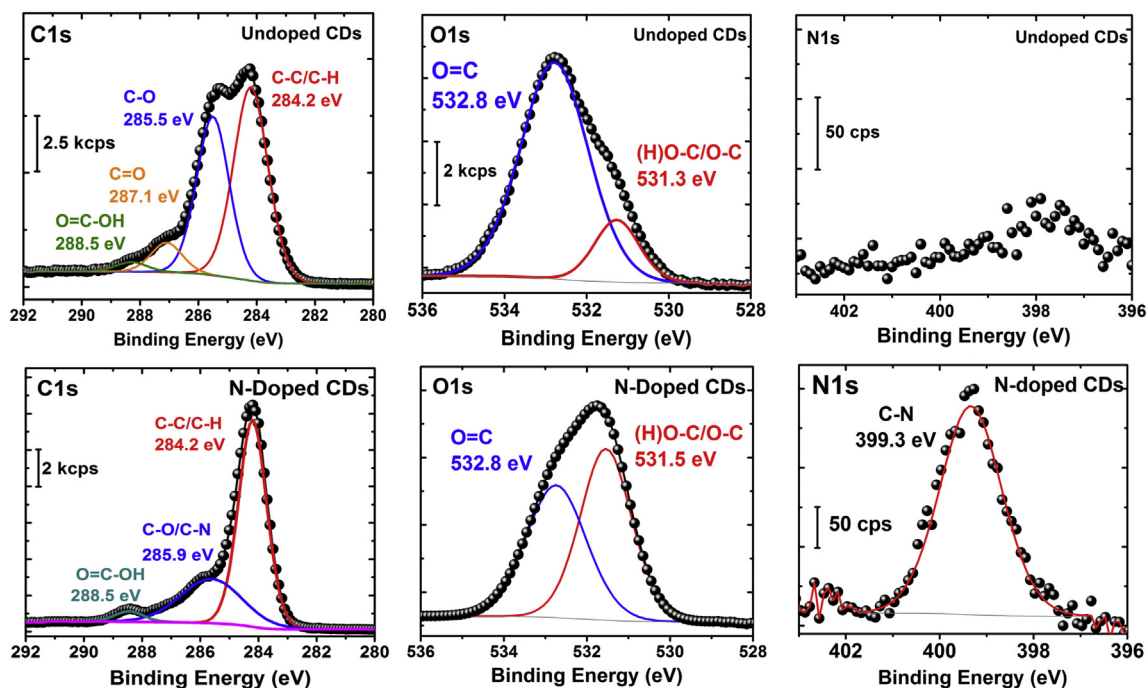
Fig. 4. Fitted X-ray photoelectron spectra (XPS) of the C1s, O1s and N1s regions corresponding to the undoped (upper row graphs) and N-doped CNDs (down row graphs). The result shows the atomic percentage of elements in each sample: O:C = 26.4:73.6 for the pure sample, and O:C:N = 27.6:71.5:0.9 for the N-doped one. (A colour version of this figure can be viewed online.)

with certain overlapping between them that are typically denoted as D band (typical of structural disorder and defects and sp³ coordination) and G band (typical of graphitic order and sp² bonding), respectively (see Fig. S5). It is noteworthy that both samples seem to show a third contribution located at ~1505 cm⁻¹ which has been previously denoted as D band and associated with amorphous sp²-bonded forms of carbon interstitial defects, thereby pointing out to the existence of outer defective layers in CNDs [32]. The FTIR spectrum (Fig. S6) shows peaks around 3369 cm⁻¹ corresponding to the stretching mode of the OH group. In undoped CNDs, the stretching vibrations of C=O and C−O at about 1634 and 1219 cm⁻¹, respectively, and the absorbance peak at 1053 cm⁻¹ can be assigned to the epoxide group (C−O), thereby confirming the existence of oxidized species pointed out by XPS analysis. On the other hand, the N-doped CNDs exhibit peaks at 1627, 1387 and 1079 cm⁻¹ belong to the stretching vibration, indicating that the existence of C=O, C−O−O⁻ and C−O−C group, indicative to the presence of carboxylic group, and the stretch peak of C−C appears at 1347 cm⁻¹. The C−N stretch was also observed at 1310 cm⁻¹ and the deformation vibration of −NH assigned at 1493 cm⁻¹, confirms the presence of N-doped species potentially attributable to amide, secondary amine or carbamate groups [30,33,34].

3.2. Optical characterization of colloidal undoped and N-doped CNDs

In Fig. 5 we present the optical characterization of the water-dispersed CNDs. Both undoped (Fig. 5a) and N-doped (Fig. 5c) CNDs show a strong optical absorption for UV excitations (<320 nm) with an absorption tail extending to the visible regime (absorption spectra depicted by the black dashed lines), as often observed for CNDs [1]. Typically, π-π* (C=C), n-π* (C=O) and σ -π* transitions can be found around excitation wavelengths of 230−250, 300, and 330 nm, respectively [35,36]. While we could not separate the contributions of these transitions, a distinct band

appears at around 320 nm for the N-doped CNDs, which is attributed to the n-π* transition induced by the amino groups at the surface [37]. The absorption enrichment due to the extra n-π* transition is functional for photonic properties as it leads to emission enhancement (Fig. S7). Both colloidal systems show identical blue emission with the PL maximum around 420 nm. The origin of the emission of CNDs remains under debate, and could be the (combined) result of the following mechanisms: (i) the carbon core-related origin of emission resulting from the π-π* transition of sp² clusters assisted by the QCE [1,38], (ii) the functional groups, surface states which behave as energy traps [39]. On one hand, we note that oxygen functional groups are generally considered to facilitate green-shifted emissions [40]. On the other hand, in first instance, the QCE model seems to be tackled by the size-independent emission as the undoped and N-doped CNDs have different average sizes. This can however be explained by the formation of several isolated sp² clusters within the carbon matrix which are responsible for the emission, with their size being independent of the total CND size. This is expected from the existence of both sp² and sp³ bonded carbon (as observed by Raman spectroscopy in Fig. S5) and it is in line with other studies [36,41].

Furthermore, the PL tunability with excitation wavelength (visualized by the blue dashed lines in Fig. 5b and d) is generally found in carbon nanostructures [42,43]. It is attributed to multiple effects, such as the QCE,[33] surface traps,[39] or reorganization of the solvent's polarization [42−45], and is therefore still under debate [11]. According with our results, we tend to explain our excitation-dependence behavior from a simple down-shifting perspective; for broad emission spectra (whether originated from the QCE of size-dispersed sp² islands or simply because of surface traps), color tunability is inevitably achieved by down-conversion of excitations within the excitation spectrum. To our knowledge, all observations of excitation-dependent PL on CNDs are achieved by exciting the sample within the PL spectrum. This model, which we actually perceive as a PL shifting artifact, would explain most − if not all −
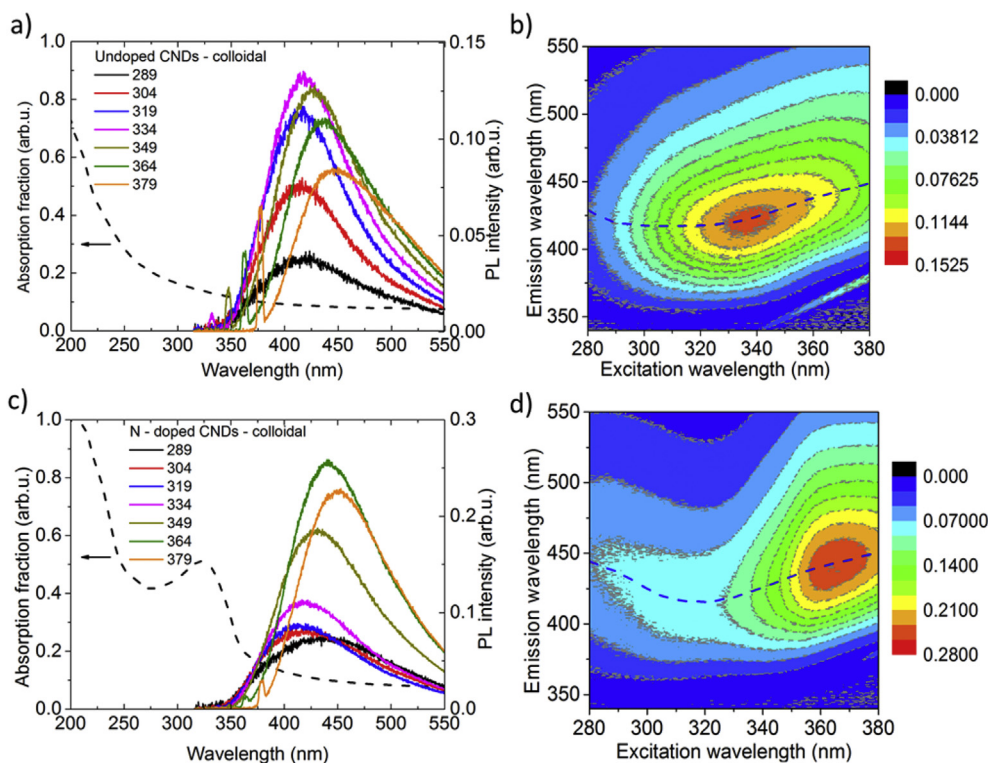
Fig. 5. Optical characterization of undoped (a, b) and N-doped (c, d) CNDs dispersed in water. (a, c) Absorption spectra (black dashed lines) combined with the PL spectra for a range of excitation wavelengths (289–379 nm) with steps of 15 nm, the sharp peaks correspond to the excitation wavelength. (b, d) Contour plot of several PLE spectra with the corresponding peak position of PL (blue dashed lines). (A colour version of this figure can be viewed online.)

interpretations of color tunability upon excitation [46–48]. This hypothesis is further strengthened by the fact that excitation-independent behavior is solely observed for excitations outside the PL spectrum [35,46].

3.3. Comparative optical behavior of colloidal and solid state CNDs

To exclude any potential interference of the solvent's polarity with the data presented in Fig. 5, we will further work with solid state samples. Upon drop casting the samples, the optical density decreases significantly but the feature of the n-π* transition for the N-doped CNDs remains present (black dashed lines in Fig. 6a and c). The PL spectra of both samples, undoped and N-doped CNDs, now show a small red-shift (Fig. 6b and d). The emission at these longer wavelengths is typically related to the hybridized oxygen functional groups with the carbon core [49]. Hence, one possibility is that the oxidized surface states start dominating the emission process upon drop casting, as suggested before [46]. Another scenario that would red-shift the emission of the solid state sample is a change in the photonic mode density. Thirdly, energy transfer, either by re-absorption or by Förster resonant energy transfer (as often observed for semiconductor nanoparticles), could be another reason [50,51]. Since the drop casted CNDs are closely packed, both energy transfer processes would be seriously enhanced. Note that for systems that emit with efficiencies less than 100%, an enhancement of the energy transfer processes would result in a decrease of the PL quantum yield (PL QY); effect that will be addressed in the last part of the Results and Discussion section.

The so-called "giant red-edge effect" is used to explain the violation of Kasha's rule [52] which states that the fluorescence is independent on the excitation energy, by the reorganization of the solvent's polarity perpendicular to the dipole moment of the excited CNDs. We can test this model with our samples, since the

solid state and colloidal forms of the CNDs have similar emission spectra (only a small red-shift appears which might be the result, as we mention earlier, of energy transfer or changes in the functional groups emission). According to the "giant red-edge effect", the excitation-dependent behavior should be completely different (possibly even absent) for the solid state sample due to the absence of the polar solvent. However, both sample forms exhibit similar excitation-dependent PL spectra. This verifies that the excitation-dependent PL shift is not the result of the polarity of the solvent, but seems to result from down-shifting of excitations within the spectrum itself.

The time-resolved PL measurements of CNDs ($\lambda_{exc} = 360$ nm, $\lambda_{det} = 430$ nm) are shown in Fig. 7. Typically, single, double and triple exponential decay fitting curves are used to describe the behavior of CND PL lifetimes [39,49]. We clearly observe that the generated carriers decay through two mechanisms (see details in Supporting Information, Figs. S1 and S2). For short time-scales (up to several ns), the decay has a stretched exponential behavior, with the stretching coefficient β of around 0.7. The average lifetime of the stretched component (derived by making use of Guillois *et al.* [53]) varies from 0.55 to 0.95 ns depending on the sample state and the detection wavelength. At longer time-scales, the decay is single-exponential in nature, with a lifetime of around 5 ns for both solid state samples while it is a bit longer for colloidal samples, and it also increases as consequence of N-doping. The clear distinction of the two decay mechanisms implies that the generated carriers are separated into two different systems. The data can therefore not be explained by two decay paths that work on the same semi-stable state. Hence, a simple model of the competition of radiative and non-radiative recombination is not applicable. To our knowledge, the behavior for longer time-scales (being a single-exponential and the relation to the N-doping) suggests that it is originated from a molecular transition. Actually, single-exponential decay behaviors
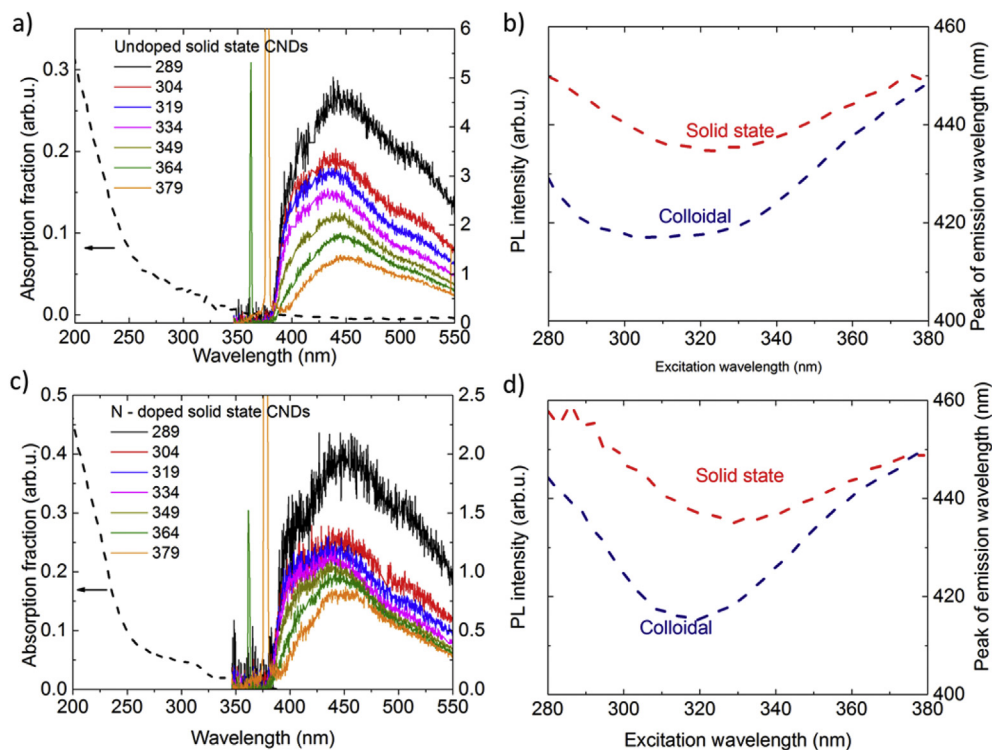
Fig. 6. Optical characterization of undoped (a, b) and N-doped (c, d) CNDs as solid state samples. (a, c) Absorption spectra (black dashed lines) combined with the PL spectra for a range of excitation wavelengths (280–380 nm, the excitation peaks which fall within the spectrum are shown) with steps of 15 nm. (b, d) Excitation dependence of the emission peak of the solid state (red) and the colloidal CNDs (blue). (A colour version of this figure can be viewed online.)
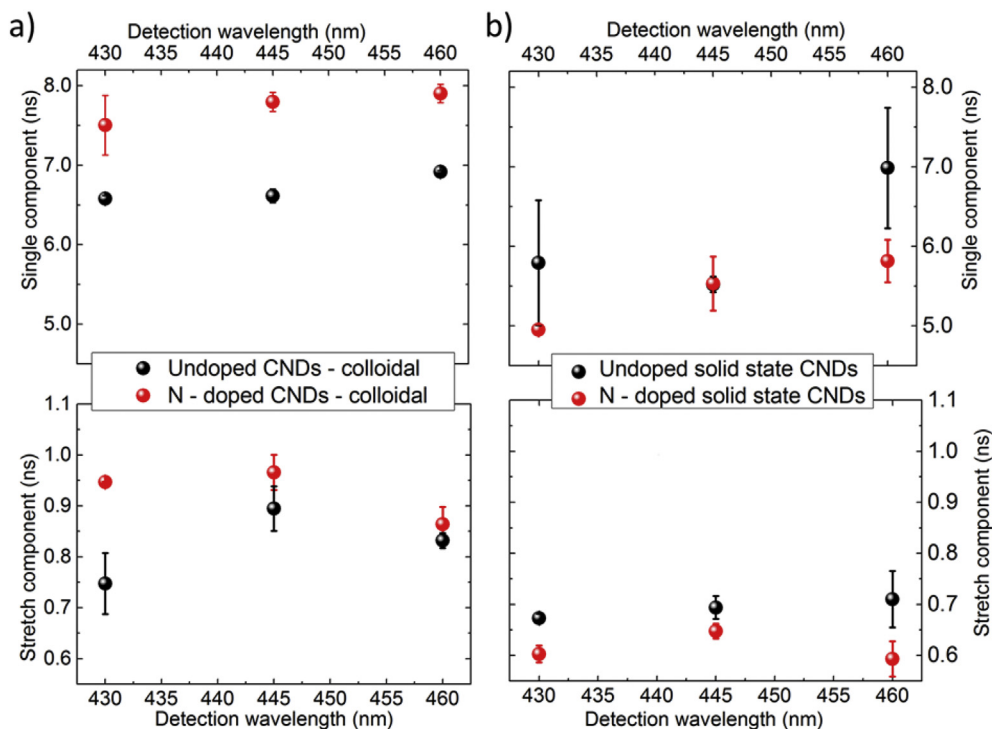
Fig. 7. Time-resolved PL measurements for undoped (black) and N-doped (red) CNDs. (a) Average lifetimes of the single (top) and stretched (bottom) components for water-dispersed CNDs as a function of detection wavelength. (b) Average lifetimes of the single (top) and stretched (bottom) components for the solid state samples as a function of detection wavelength. The depicted error describes the standard deviation of sequential measurements with different excitation powers in linear regime. (A colour version of this figure can be viewed online.)
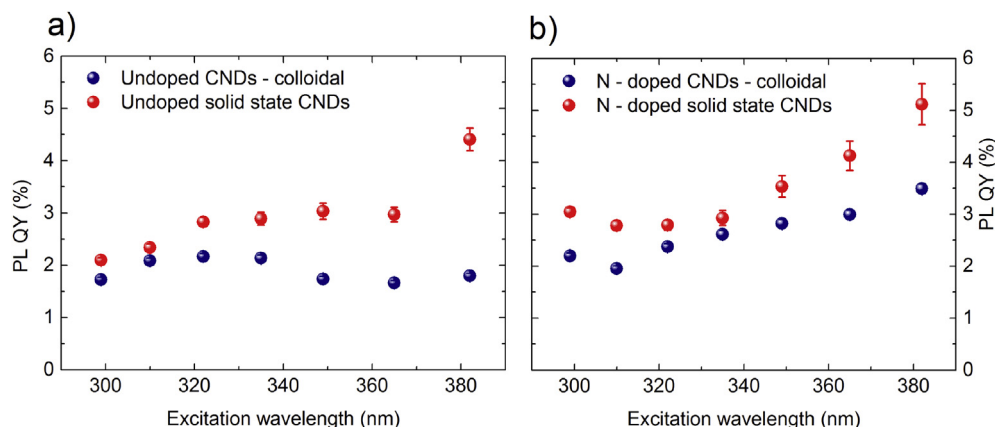
Fig. 8. PL QY of the undoped (a) and N-doped (b) CNDs, as a function of the excitation wavelength. The PL QY values of the colloidal CNDs are denoted in blue, whereas the red circles refer to the solid state CNDs. (A colour version of this figure can be viewed online.)

have been assigned to emission of C=O groups in COOH on N-doped CND surfaces, with lifetimes in the order of 15 ns, quite similar to our results [39].

In Fig. 8, we present the PL QY values as a function of the excitation wavelength, for the undoped and N-doped CNDs in colloidal and solid state. All samples show PL QY values in the range of 1—5%. Two main observations can be made: firstly, the N-doped CNDs (colloidal and solid state) have slightly higher emission efficiencies than their undoped counterparts; secondly, the emission efficiency increases upon drop casting. This latter observation rules out the energy transfer processes as mechanisms responsible for the spectral shifts observed in Fig. 6b and d since they would inevitably decrease the PL QY. We could explain this slight PL QY increase upon drop casting in line with Hao *et al.* [47], who stated that a transition of the PL mechanism arises due to more emission-efficient oxidized surface states. This also agrees with the slight red-shift observed in Fig. 6b and d. Regarding the first observation, it is well known that core emission can be improved by the incorporation of nitrogen [25,26]. Hence, the observed slight increase of the PL QY values of the N-doped CNDs suggests that the emission is still partly originated from the carbon core π-π^* transition of the sp^2 clusters (facilitated by the QCE).

4. Conclusions

The combination of a fluidized bed-assisted rapid pyrolysis with the confinement of precursors within an ordered nanoporous structure has been successfully validated as an efficient route to obtain highly uniform blue emissive undoped and N-doped CNDs with average sizes below 4 nm. This provided a uniform distribution of nanoparticles that allowed us to perform an in-depth study of their PL properties. The fluidized-bed assisted rapid pyrolysis represents a very convenient and appealing method given the short reactions required (below 6 min) and the highly reproducible reaction conditions afforded by the fluidizing environment. Furthermore, a thorough optical characterization of the generated CNDs both in colloidal and solid state has demonstrated that their emission (with an efficiency of 1—5%) originates from a combination of the QCE and the oxidized surface states. In addition, N-doping introduces resonant absorption states which participate in emission. By studying the behavior of different CNDs sample forms, colloidal and solid state, we have been able to explain the excitation-dependent/-independent mechanism with a simple model based on down-converting excitations in a broad emission spectrum, also valid for other CNDs reported in the literature.

Competing financial interests

The authors declare no competing financial interests.

References

[1] S. Zhu, Y. Song, X. Zhao, J. Shao, J. Zhang, B. Yang, The photoluminescence mechanism in carbon dots (graphene quantum dots, carbon nanodots, and polymer dots): current state and future perspective, Nano Res. 8 (2015) 355—381.
[2] S. Hu, A. Trinchi, P. Atkin, I. Cole, Tunable photoluminescence across the entire visible spectrum from carbon dots excited by white light, Angew. Chem. Int. Ed. 54 (2015) 2970—2974.
[3] H. Ding, S.-B. Yu, J.-S. Wei, H.-M. Xiong, Full-color light-emitting carbon dots with a surface-state-controlled luminescence mechanism, ACS Nano 10 (2016) 484—491.
[4] L. Himaja, P.S. Karthik, S.P. Singh, Carbon dots: the newest member of the carbon nanomaterials family, Chem. Rec. 15 (2015) 595—615.
[5] P. Miao, K. Han, Y. Tang, B. Wang, T. Linc, W. Chenga, Recent advances in carbon nanodots: synthesis, properties and biomedical applications, Nanoscale 7 (2015) 1586—1595.

[6] M. Havrdova, K. Hola, J. Skopalik, K. Tomankova, M. Petr, K. Cepe, et al., Toxicity of carbon dots e Effect of surface functionalization on the cell viability, reactive oxygen species generation and cell cycle, Carbon 99 (2016) 238—248.

[7] C.M. Zhang, J. Lin, Defect-related luminescent materials: synthesis, emission properties and applications, Chem. Soc. Rev. 41 (2012) 7938—7961.

[8] S.Y. Lim, W. Shen, Z.Q. Gao, Carbon quantum dots and their applications, Chem. Soc. Rev. 44 (2015) 362—381.

[9] M.C. Ortega-Liebana, J.L. Hueso, A. Larrea, V. Sebastian, J. Santamaria, Feroxyhyte nanoflakes coupled to up-converting carbon nanodots: a highly active, magnetically recoverable, fenton-like photocatalyst in the visible-nir range, Chem. Commun. 51 (2015) 16625—16628.

[10] M.C. Ortega-Liebana, J.L. Hueso, S. Ferdousi, K.L. Yeung, J. Santamaria, Nitrogen-doped luminescent carbon nanodots for optimal photo-generation of hydroxyl radicals and visible-light expanded photo-catalysis, Diam. Relat. Mater. 65 (2016) 176—182.

[11] Z. Gan, H. Xu, Y. Hao, Mechanism for excitation-dependent photoluminescence from graphene quantum dots and other graphene oxide derivates: consensus, debates and challenges, Nanoscale 8 (2016) 7794—7807.

[12] V. Nguyen, L. Yan, J. Si, X. Hou, Femtosecond laser-induced size reduction of carbon nanodots in solution: effect of laser fluence, spot size, and irradiation time, J. Appl. Phys. 117 (2015), 084304—1-084304-6.

[13] J. Deng, Q. Lu, N. Mi, H. Li, M. Liu, M. Xu, et al., Electrochemical synthesis of carbon nanodots directly from alcohols, Chem. Eur. J. 20 (2014) 4993—4999.

[14] J. Zhou, C. Booker, R. Li, X. Zhou, T.-G. Sham, X. Sun, Z. Ding, An Electrochemical avenue to blue luminescent nanocrystals from multiwalled carbon nanotubes (MWCNTs), J. Am. Chem. Soc. 129 (2007) 744—745.

[15] H. Li, X. He, Z. Kang, H. Huang, Y. Liu, J. Liu, S. Lian, C.H.A. Tsang, X. Yang, S.-T. Lee, Water-soluble fluorescent carbon quantum dots and photocatalyst design, Angew. Chem. 122 (2010) 4532—4536.

[16] M. Favaro, S. Agnoli, M. Cattelan, A. Moretto, C. Durante, S. Leonardi, J. Kunze-Liebhauser, O. Schneider, A. Gennaro, G. Granozzi, Shaping graphene oxide by electrochemistry: from foams to self-assembled molecular materials, Carbon 77 (2014) 405—415.

[17] Y. Liu, N. Xiao, N. Gong, H. Wang, X. Shi, W. Gu, L. Ye, One-step microwave-assisted polyol synthesis of green luminescent carbon dots as optical nanoprobes, Carbon 68 (2014) 259—264.

[18] Z. Wang, B. Fu, S. Zou, B. Duan, C. Chang, B. Yang, et al., Facile construction of carbon dots via acid catalytic hydrothermal method and their application for target imaging of cancer cells, Nano Res. 9 (2016) 214—223.

[19] J. Zhang, F. Abbasi, J. Claverie, An efficient templating approach for the synthesis of redispersible size-controllable carbon quantum dots from graphitic polymeric micelles, Chem. Eur. J. 21 (2015) 15142—15147.

[20] J. Zong, Y. Zhu, X. Yang, J. Shen, C. Li, Synthesis of photoluminescent carbogenic dots using mesoporous silica spheres as nanoreactors, Chem. Commun. 47 (2011) 764—766.

[21] H.G. Baldovi, S. Valencia, M. Alvaro, A.M. Asirib, H. Garcia, Highly fluorescent C-dots obtained by pyrolysis of quaternary ammonium ions trapped in all-silica ITQ-29 zeolite, Nanoscale 7 (2015) 1744—1752.

[22] C.E. Machado, L. Gazola Tartuci, H. de Fátima Gorgulho, L.F. Cappa de Oliveira, J. Bettini, D. Pereira dos Santos, et al., Influence of inert and oxidizing atmospheres on the physical and optical properties of luminescent carbon dots prepared through pyrolysis of a model molecule, Chem. Eur. J. 22 (2016) 4556—4563.

[23] R. Ramos, M.P. Pina, M. Menendez, J. Santamaria, G.S. Patience, Oxidative dehydrogenation of propane to propene: simulation of a commercial inert membrane reactor immersed in a fluidized bed, Can. J. Chem. Eng. 79 (2001) 902—912.

[24] J. Herguido, M. Menendez, J. Santamaria, On the use of fluidized bed catalytic reactors where reduction and oxidation zones are present simultaneously, Catal. Tod. 100 (2005) 181—189.

[25] H. Ding, J.-S. Wei, H.-M. Xiong, Nitrogen and sulfur co-doped carbon dots with strong blue luminescence, Nanoscale 6 (2014) 13817—13823.

[26] Y. Choi, B. Kang, J. Lee, S. Kim, G.T. Kim, H. Kang, et al., Integrative approach toward uncovering the origin of photoluminescence in dual heteroatom-doped carbon nanodots, Chem. Mater. 28 (2016) 6840—6847.

[27] E.M. Johansson, M.A. Ballem, J.M. Cordoba, M. Odén, Rapid synthesis of SBA-15 rods with variable lengths, widths, and tunable large pores, Langmuir 27 (2011) 4994—4999.

[28] Y.-P. Sun, B. Zhou, Y. Lin, W. Wang, K.A.S. Fernando, P. Pathak, M.J. Meziani, B.A. Harruff, X. Wang, H. Wang, P.G. Luo, H. Yang, M.E. Kose, B. Chen, L.M. Veca, S.-Y. Xie, Quantum-sized carbon dots for bright and colorful photoluminescence, J. Am. Chem. Soc. 128 (2006) 7756—7757.

[29] P.-C. Hsua, H.-T. Chang, Synthesis of high-quality carbon nanodots from hydrophilic compounds: role of functional groups, Chem. Commun. 48 (2012) 3984—3986.

[30] J.L. Hueso, J.P. Espinos, A. Caballero, J. Cotrino, A.R. Gonzalez-Elipe, XPS investigation of the reaction of carbon with NO, O₂, N₂ and H₂O plasmas, Carbon 45 (2007) 89—96.

[31] J.P. Boudou, A. Martinez-Alonzo, J.M.D. Tascon, Introduction of acidic groups at the surface of activated carbon by microwave-induced oxygen plasma at low pressure, Carbon 38 (2000) 1021—1029.

[32] J.P. Boudou, A. Martinez-Alonzo, J.M.D. Tascon, Oxygen plasma modification of pitch-based isotropic carbon fibres, Carbon 41 (2003) 41—56.

[33] J.R. Pels, F. Kapteijn, J.A. Moulijn, Q. Zhu, K.M. Thomas, Evolution of nitrogen functionalities in carbonaceous materials during pyrolysis, Carbon 33 (1995) 1641—1653.

[34] J.C. Sanchez-Lopez, C. Donnet, F. Lefebvre, C. Fernandez-Ramos, A. Fernandez, Bonding structure in amorphous carbon nitride: a spectroscopic and nuclear magnetic resonance study, J. Appl. Phys. 90 (2001) 675—681.

[35] Z.X. Gan, S.J. Xiong, X.L. Wu, T. Xu, X.B. Zhu, X. Gan, et al., Mechanism of photoluminescence from chemically derived graphene oxide: role of chemical reduction, Adv. Opt. Mater. 1 (2013) 926—932.

[36] Y. Wang, S. Kalytchuk, Y. Zhang, H. Shi, S.V. Kershaw, A.L. Rogach, Thickness-dependent full-color emission tunability in a flexible carbon dot ionogel, J. Phys. Chem. Lett. 5 (2014) 1412—1420.

[37] Y. Dong, H. Pang, H.B. Yang, C. Guo, J. Shao, Y. Chi, et al., Carbon-based dots co-doped with nitrogen and sulfur for high quantum yield and excitation-independent emission, Angew. Chem. Int. Ed. 52 (2013) 7800—7804.

[38] M.A. Sk, A. Ananthanarayanan, L. Huang, K.H. Lim, P. Chen, Revealing the tunable photoluminescence properties of graphene quantum dots, J. Mater. Chem. C 2 (2014) 6954—6960.

[39] H. Ding, H.-M. Xiong, Exploring the blue luminescence origin of nitrogen-doped carbon dots by controlling the water amount in synthesis, RSC Adv. 5 (2015) 66528—66533.

[40] H. Nie, M. Li, Q. Li, S. Liang, Y. Tan, L. Sheng, et al., Carbon dots with continuously tunable full-color emission and their application in ratiometric pH sensing, Chem. Mater. 26 (2014) 3104—3112.

[41] J.R. Rani, J. Lim, J. Oh, J.-W. Kim, H.S. Shin, J.H. Kim, et al., Epoxy to carbonyl group conversion in graphene oxide thin films: effect on structural and luminescent characteristics, J. Phys. Chem. C 116 (2012) 19010—19017.

[42] S. Khan, A. Gupta, N.C. Verma, C.K. Nandi, Time-resolved emission reveals ensemble of emissive states as the origin of multicolor fluorescence in carbon dots, Nano Lett. 15 (2015) 8300—8305.

[43] Y. Deng, X. Chen, F. Wang, X. Zhang, D. Zhao, D. Shen, Environment-dependent photon emission from solid state carbon dots and its mechanism, Nanoscale 6 (2014) 10388—10393.

[44] L. Cao, M.J. Meziani, S. Sahu, Y.P. Sun, Photoluminescence properties of graphene versus other carbon nanomaterials, Acc. Chem. Res. 46 (2013) 171—180.

[45] S.K. Cushing, M. Li, F. Huang, N. Wu, Origin of strong excitation wavelength dependent fluorescence of graphene oxide, ACS Nano 8 (2014) 1002—1013.

[46] S.J. Zhu, Q.N. Meng, L. Wang, J.H. Zhang, Y.B. Song, H. Jin, et al., Highly photoluminescent carbon dots for multicolor patterning, sensors, and bioimaging, Angew. Chem. Int. Ed. 52 (2013) 3953—3957.

[47] Y. Hao, Z. Gan, J. Xu, X. Wu, P.K. Chu, Poly(ethylene glycol)/carbon quantum dot composite solid films exhibiting intense and tunable blue-red emission, Appl. Surf. Sci. 311 (2014) 490—497.

[48] L. Pan, S. Sun, A. Zhang, K. Jiang, L. Zhang, C. Dong, et al., Truly Fluorescent excitation-dependent carbon dots and their applications in multicolor cellular imaging and multidimensional sensing, Adv. Mater. 27 (2015) 7782—7787.

[49] S.H. Jin, D.H. Kim, G.H. Jun, S.H. Hong, S. Jeon, Tuning the photoluminescence of graphene quantum dots through the charge transfer effect of functional groups, ACS Nano 7 (2013) 1239—1245.

[50] R. Limpens, A. Lesage, P. Stallinga, A.N. Poddubny, M. Fujii, T. Gregorkiewicz, Resonant energy transfer in Si nanocrystal solids, J. Phys. Chem. C 119 (2015) 19565—19570.

[51] C. De Weerd, L. Gomez, H. Zhang, W.J. Buma, G. Nedelcu, M.V. Kovalenko, T. Gregorkiewicz, Energy transfer between inorganic perovskite nanocrystals, J. Phys. Chem. C 120 (2016) 13310—13315.

[52] M. Kasha, Characterization of electronic transitions in complex molecules, Discuss. Faraday Soc. 9 (1950) 14—19.

[53] O. Guillos, N. Herlin-Boime, C. Reynaud, G. Ledoux, F. Huisken, Photoluminescence decay dynamics of noninteracting silicon nanocrystals, J. Appl. Phys. 95 (2004) 3677—3682.

IV.6.1 Supporting Information of Article 6

Carbon

Uniform luminescent carbon nanodots prepared by rapid pyrolysis of organic precursors confined within nanoporous templating structures

M. C. Ortega-Liebana[a,b,#], X. N. Chung[c,#], R. Limpens[c], L. Gomez[c,*], J. L. Hueso[a,b,*], J. Santamaria[a,b] and T. Gregorkiewicz[c]

[a]Institute of Nanoscience of Aragon (INA) and Department of Chemical Engineering and Environmental Technology, Edificio I+D+i, Campus Rio Ebro, 50018, Zaragoza, Spain
[b]Networking Research Center on Bioengineering, Biomaterials and Nanomedicine (CIBER-BBN), 28029, Madrid, Spain
[c]Institute of Physics, University of Amsterdam, Science Park 904, 1098 XH Amsterdam, The Netherlands

[#] Equal contribution

*Corresponding authors: L. Gomez – L.gomeznavascues@uva.nl

J.L. Hueso – jlhueso@unizar.es

Additional Figures: lifetime dependence on power (Figure S1), lifetime fitting components (Figure S2), emission intensity according with the different measurements necessary to get pure PL QY (Figure S3), explanation on the error bars of PL QY measurements, TEM images of CNDs (Figure S4), Raman spectrum (Figure S5), FTIR (Figure S6), nitrogen absorption feature in N-doped CNDs (Figure S7).
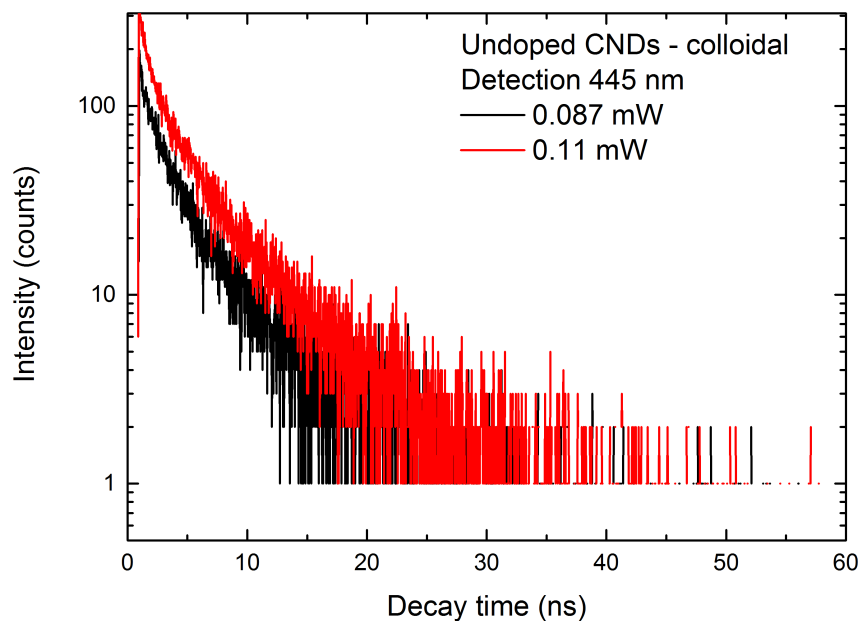
Figure S1. The power dependence of PL dynamics detected at 445 nm upon an excitation wavelength of 360 nm. The parallel traces correspond to high and low excitation powers (0.11 and 0.087 mW) and they validate the linear excitation regime for the undoped CNDs sample in colloidal state.
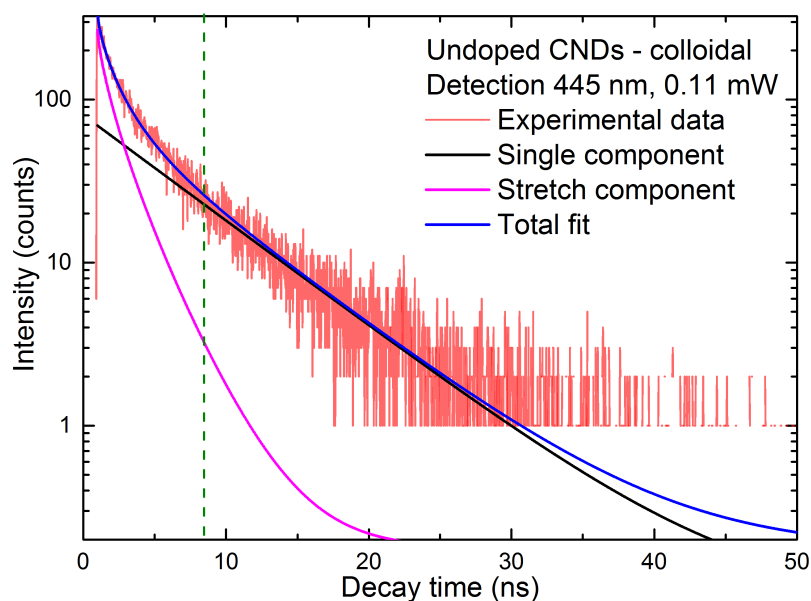
Figure S2. The fitting components, namely single (black) and stretch components (magenta) with lifetimes around 6-8 and 0.5-1 ns, respectively, contribute to the total fitting curve (blue curve) which is suitable for the experimental data (red curve). The broken line shows the border between part 1 and part 2 (see the method to calculate lifetime in the Experimental section of the main manuscript).

246
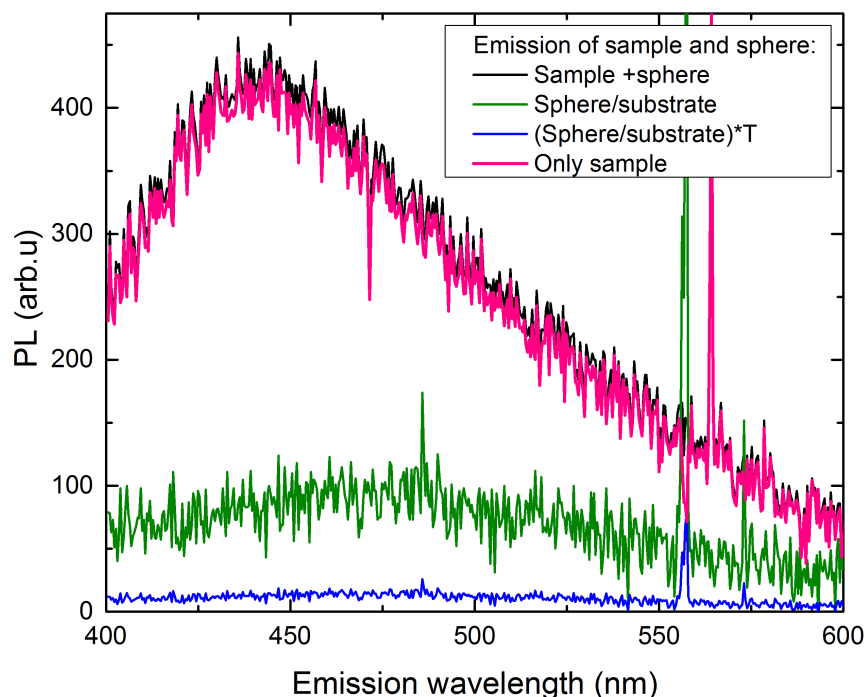
Figure S3. Graph to show how to exclude the emission of the integrating sphere and to correct the PL spectra of the sample. In the sample measurement (sample is inside the integrating sphere), the excitation intensity on the sphere wall is lower than T (transmittance of the sample) times itself in the substrate measurement; therefore, the emission of the sphere (blue and olive curves for sample and substrate measurement, respectively) also reduces T times. Subtracting the blue curve from the ensemble emission (sample + sphere, black curve), we get the "pure" PL spectra of the sample (pink).

In the excitation window: I_0 and I_1 are the excitation intensity hitting the sphere wall in the substrate and in the sample measurements, respectively. If we suppose that most of the excitation intensity hits the sphere wall in the first time, then the scattering of the excitation light is minor. Then, we have:

$$I_1(\lambda_{exc}) = I_0(\lambda_{exc}) \times T(\lambda_{exc}) \tag{1}$$

In the emission window: $I_{sphere/substrate}(\lambda_{em})$ and $I_{sphere/sample}(\lambda_{em})$ are the emission intensity of the sphere in the substrate and in the sample measurements, respectively. In the sample measurement, the signal $I_{sphere+sample}(\lambda_{em})$ originates from both emission of the sphere ($I_{sphere/sample}(\lambda_{em})$) and pure PL from the sample ($I_{pure\ sample}(\lambda_{em})$).

$$I_{sphere+sample}(\lambda_{em}) = I_{sphere/sample}(\lambda_{em}) + I_{pure\ sample}(\lambda_{em}) \tag{2}$$

The emission of the sphere is proportional to the coming intensity, from (1) we have:

247

$$I_{sphere/sample}(\lambda_{em}) = I_{sphere/substrate}(\lambda_{em}) \times T(\lambda_{exc}) \tag{3}$$

Then, the emission of the sample will be:

$$I_{pure\ sample}(\lambda_{em}) = I_{sphere+sample}(\lambda_{em}) - I_{sphere/quartz}(\lambda_{em}) \times T(\lambda_{exc}) \tag{4}$$

The error bars of PL QY:

The method to calculate the uncertainty of PL QY has been established on the previous publication from *Chung et al.* [1] Here, the total error of PL QY responds to the statistical error, the fluctuation of the excitation lamp and the tolerance of the used spectrometers. The individual relative error is obtained as follows:

- The relative statistical error σ_S [2] error comes from both the excitation and the emission measurements.
- The relative sensitivity error of the spectrometer can be deduced:

$$\sigma_{RS}(\lambda_{exc}) = \frac{\alpha_{RS(\lambda_{exc})}}{RS} = \frac{1}{\sqrt{N_{calibration}(\lambda_{exc})}}$$

Where, $N_{calibration}(\lambda_{exc})$ is the number of emitted photons with the wavelength of λ_{exc} of the calibration lamps.

- The relative error of PL QY originated from the excitation power fluctuation has been calculated as follows:

$$\sigma_{lamp}(\lambda_{exc}) = \frac{\beta(\lambda_{exc})}{\alpha(\lambda_{exc})}$$

Here, β and α are relative fluctuations of the excitation intensity and absorption fraction of the sample at the excitation wavelength of λ_{exc}.

Finally, the total relative error of PL QY will be:

$$\sigma_{total}(\lambda_{exc}) = \sqrt{\sigma_S^2(\lambda_{exc}) + \sigma_{RS}^2(\lambda_{exc}) + \sigma_{lamp}^2(\lambda_{exc})}$$
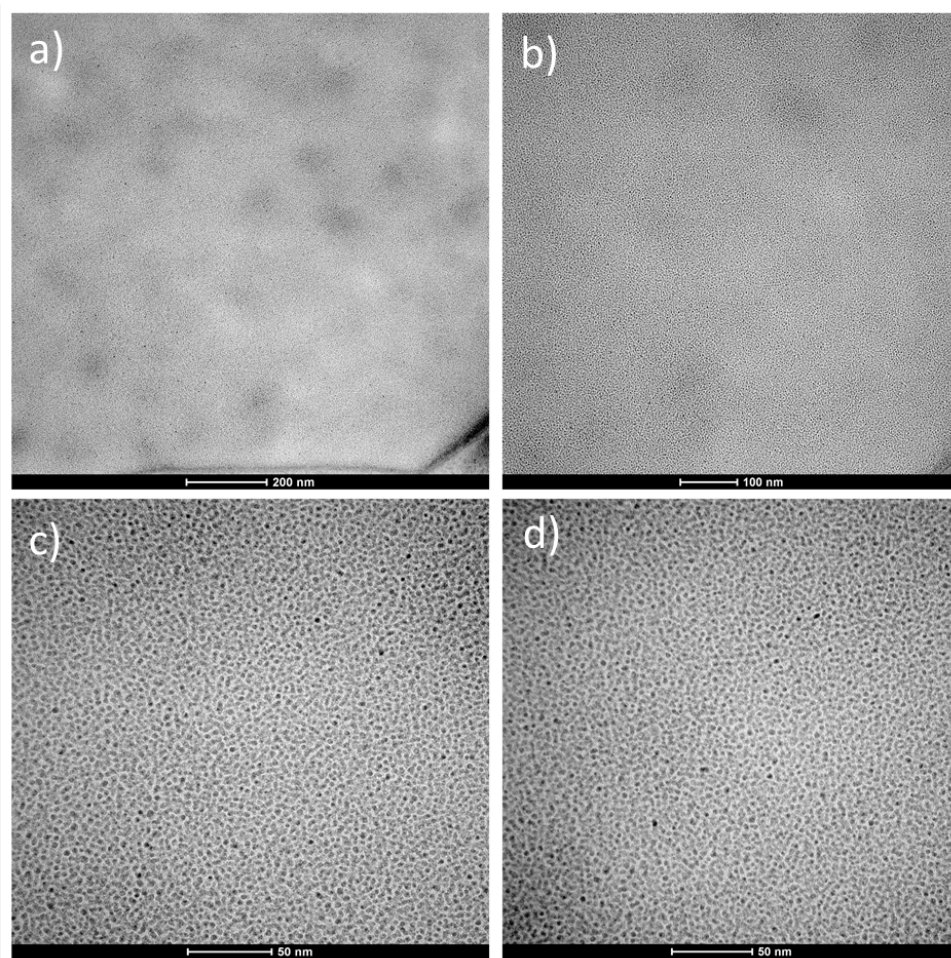
Figure S4. Additional TEM images of CNDs synthesized using CA (a, c) and EDTA (b, d) as carbon source.
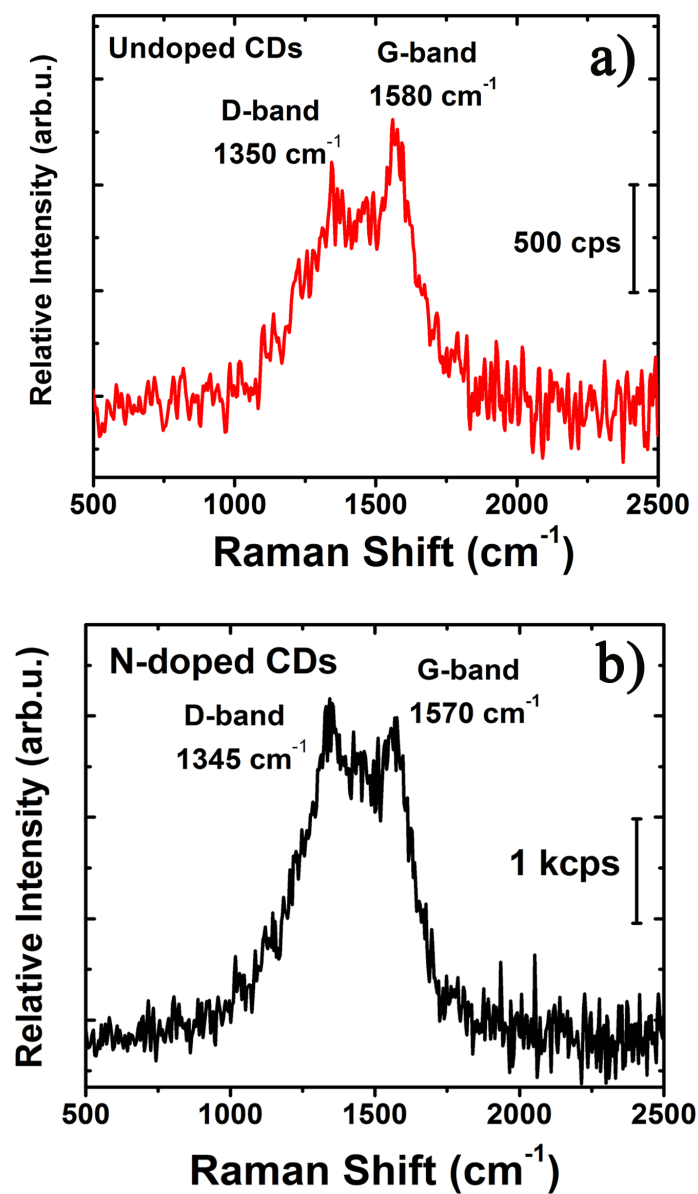
Figure S5. Raman spectrum of undoped (a) and N-doped (b) CNDs. In both samples there are two peaks at 1340 and 1580 cm^{-1} corresponding to D and G band, respectively. They represent diamond (D) and graphite (G) structures.
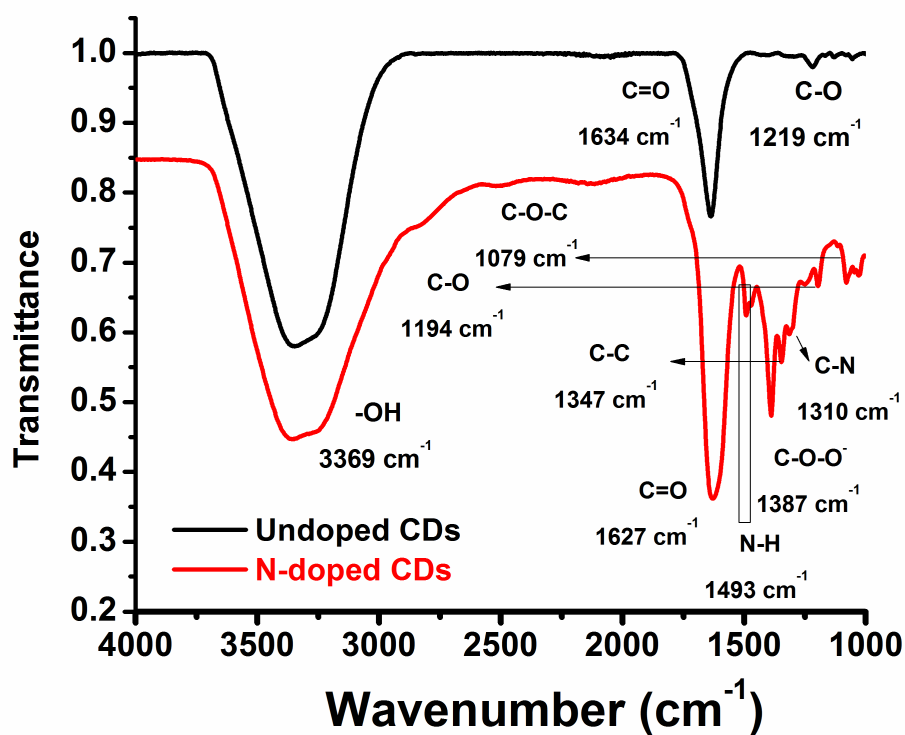
Figure S6. FTIR analysis of undoped (black) and N-doped (red) CNDs.
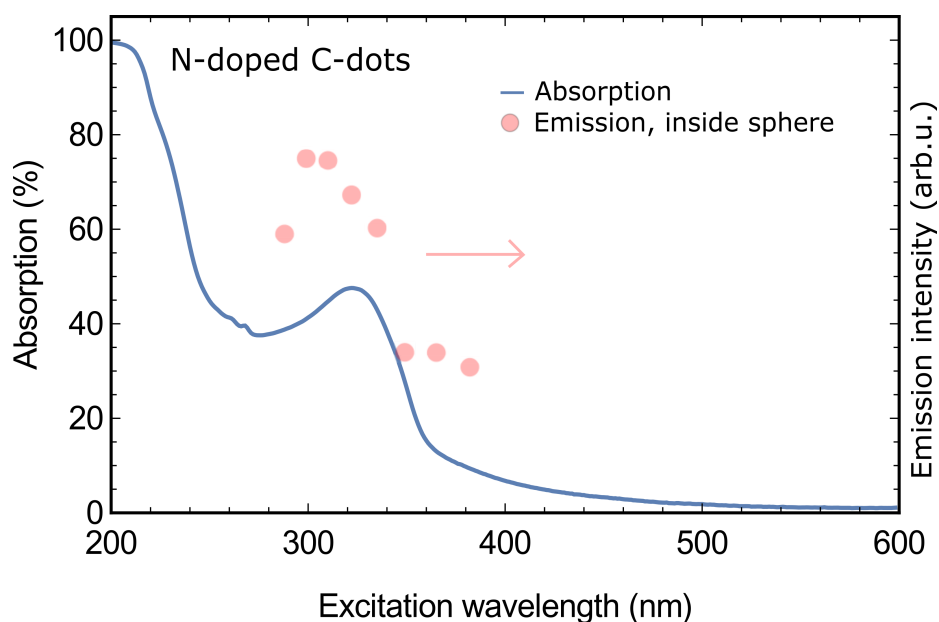
Figure S7. N-doped absorption feature. The blue line represents the absorption spectrum as shown in Figure 3c in the main text. The red transparent closed circles depict the emission intensity scaled by the number of incident photons for the measurement inside the sphere.

In Figure S7, we investigate the effect of the N-doped absorption feature, at an excitation wavelength of around 320 nm (depicted in Figure 5c, in the main text). By making use of the measurements that were performed in an integrating sphere (originally for the PL QY measurements), we can resolve the effect of the enhanced absorption on the emission. In Figure S7 we depict the absorption spectrum by the blue line (as shown in Figure 5c), emission intensities (the red transparent closed circles) normalized by the number of incident photons for the measurements with the sample inside the integrating sphere. We notice that the enhanced resonant absorption is leading to enhanced emission. The latter was actually expected from Figure 8 where the slight change in the PL QY along this excitation wavelength range was observed. Hence we conclude that the carriers generated by the resonant N-doped absorption participate in the normal emission process. Hence, the enhanced absorption is beneficial for photonic applications.

References:

1. N. X. Chung, R. Limpens and T. Gregorkiewicz, Proc. SPIE 9562, DOI: 10.1117/12.2191105 (2015).

2. J. Valenta, Nanoscience Methods (3), 11-27, 2014.

IV.7   **Article 7.** Luminescent mesoporous nanorods as photocatalytic enzyme-like peroxidase surrogates

V. CONCLUSIONS . CONCLUSIONES

The main conclusions regarding the synthesis of CNDs are:

1. Water-soluble CNDs with high luminescence can be obtained by hydrothermal synthesis from low cost and easily available natural precursors, wides the conditions described in this works.

2. By using precursors that include heteroatoms in their structure, N-doping of the CNDs could be achieved by the hydrothermal carbonization (HTC) method.

3. The pyrolytic carbonization of natural plants method can extend the doping categories (i.e. N, P), greatly shortening the reaction time. It is considered to be more cost effective, compared to the HTC route because it does not need special equipment or solvents.

4. The process based on flash thermal treatment and the use of inorganic mesoporous silica nanorods as confining templates, developed on this work yields highly uniform blue emissive undoped and N-doped CNDs and also induce luminescent silicon-based centers in the mesoporous template.

The main conclusions regarding the surface chemistry/characterization of CNDs are:

5. The light emission in CNDs is governed by the interplay between the absorption due to the carbon cores and the surface functional groups.

6. The CNDs obtained had excitation-dependent/-independent PL properties, where a slight PL QY increase was due to more emission-efficient oxidized surface states and the incorporation of nitrogen in them.

7. Doping the CNDs with nitrogen heteroatoms enhanced their optical response in the visible-NIR range (down and up-conversion behavior).

The main conclusions regarding the applications of CNDs are:

Theranostics Agents (Bioimaging and Photodynamic Therapy) and Nanosensors

8. The CNDs show very low cytotoxicity and are efficiently taken up by the cells.

9. The CNDS are capable of a therapeutic response by *in situ* activation upon NIR irradiation light. An increased generation of highly reactive oxidative species (ROS) succefully was responsible for the death of cancer cells where the CNDs had been internalized.

10. CNDs are sensitive fluorescent probes that allow selective detection of: (a) copper ions, even in the presence of highly interfering ion counterparts such as iron, solving in the NIR detection range, and (b) changes of pH, due to its pH-dependent lifetime decay response.

Environmental Catalysis

11. N-doped CNDs can act as nanosensitizers to maximize the solar light harvesting for photocatalytic applications *via* an enhanced production of highly reactive hydroxyl radicals.

12. They enable the use of light across a wider spectrum, and conformed a novel Fenton-like heterogeneous catalyst, obtained through the assembly of superparamagnetic feroxyhyte nanoflakes (Fe-NFs) and CNDs.

13. The inherent magnetic response of Fe-FN, allowed the efficient recovery and recyclability of the catalyst.

14. The photo-catalytic activity of the TiO_2-based nanohybrid can be explained as the result of the capacity of the CNDs to absorb light in a broader range (including NIR) and inject electrons in the conduction band of anatase TiO_2 to generate highly reactive holes and hydroxyl radicals.

15. The up-conversion properties of the CNDs with higher content of N species increased the collection of sunlight in the TiO_2 support, resulting in greater efficiency for photocatalytic degradation of persistent organic compound.

Biocatalysis

16. Carbon and silicon-based luminescent platforms can be activated by light and behave as inorganic peroxidase-like surrogates in a wider range of pH than natural peroxidases.

………………………………………….

Las principales conclusiones respecto a la <u>síntesis de los CNDs</u> son:

1. Se pueden obtener CND solubles en agua con alta luminiscencia mediante síntesis hidrotermal a partir de precursores naturales de bajo coste y fácilmente disponibles, abarcando las condiciones descritas en este trabajo.

2. Usando precursores que incluyen heteroátomos en su estructura, se obtubieron CNDs dopados con grupos amino mediante el método de carbonización hidrotermal.

3. El método de carbonización pirolítica de plantas naturales puede extender las categorías de dopaje (es decir, con N y P), acortando en gran medida el tiempo de reacción. Se considera que es más rentable, en comparación con la ruta sintética hidrotermal, ya que no necesita equipos especiales ni disolventes.

4. El proceso basado en el tratamiento térmico instantáneo y el uso de nanoestructuras de sílice mesoporosas inorgánicas como plantillas de confinamiento, desarrollado en este trabajo, produce no dopados y N dopados CNDs emisores de luz azul altamente uniformes, y también induce centros basados en silicio luminiscente en el templante mesoporoso.

Las principales conclusiones respecto a la <u>química y caracterización superficial</u> de los CND son:

5. La emisión de luz en los CNDs se rige por la interacción entre la absorción debida a los núcleos de carbono y a los grupos funcionales de su superficie.

6. Los CNDs obtenidos tenían propiedades de fotoluminiscencia dependientes e independientes de la excitacion, donde un ligero aumento de rendimiento cuántico de fotoluminiscencia fue debió a una mayor eficiencia de emisión proveniente de los estados oxidados y a la incorporación de nitrógeno en ellos.

7. El dopaje de los CNDs con heteroátomos de nitrógeno mejoró su respuesta óptica en el rango visible (Vis) e infrarrojo cercano (NIR).

Las principales conclusiones con respecto a las aplicaciones de los CND son:

Agentes Teranosticos (Bioimagen y Terápia Fotodinámica) y Nanosensores

8. Los CNDs muestran baja citotoxicidad y se internalizan eficientemente en las células.

9. Los CNDs son capaces de tener respuesta terapéutica por activación *in situ* con irradiacion NIR. Una mayor generación de especies de oxígeno altamente reactivas (acrónimo en inglés, ROS) fue responsable de la muerte de las células cancerosas donde se habían internalizado las nanopartículas.

10. Los CND son sondas fluorescentes sensibles que permiten la detección selectiva de: (a) iones de cobre, incluso en presencia de otros iones altamente interferentes como el hierro, resolviendose estas interferencias en su deteccion bajo excitacion en el rango NIR, y (b) cambios de pH, debido a su respuesta de tiempo de vida media dependiente del pH.

Catálisis Medioambiental

11. Los CND dopados con N pueden actuar como nanosensibilizadores para maximizar la recolección de luz solar para aplicaciones fotocatalíticas a través de una producción mejorada de radicales hidroxilos altamente reactivos.

12. Los CNDs permiten el uso de la luz en un espectro más amplio y conforman un novedoso catalizador heterogéneo tipo Fenton, obtenido a través del ensamblaje de nanoláminas de ferroxihita superparamagnéticas (Fe-NF) y los CNDs.

13. La respuesta magnética inherente del Fe-FN permitió la recuperación y reciclado eficientes del catalizador nanohíbrido.

14. La actividad fotocatalítica de los nanohíbridos basado en TiO_2 se puede explicar como el resultado de la capacidad de los CND de absorber luz en un rango más amplio (incluido NIR) e inyectar electrones en la banda de conducción del TiO_2, fase

15. Las propiedades de "up-conversion" de los CNDs con mayor contenido de especies nitrogenadas aumentaron la recolección de luz solar en el soporte de TiO_2, lo que resultó en una mayor eficiencia para la degradación fotocatalítica del compuesto orgánico persistente de interés.

Biocatálisis

16. Las plataformas mesoporosas luminiscentes a base de carbón y silicio pueden activarse bajo irradiación con luz y comportarse como sustitutos inorgánicos de la enzima peroxidasa natural en un rango de pH amplio.

VI. REFERENCES

1.   Fitzpatrick, J. A. J.; Inouye, Y.; Manley, S.; Moerner, W. E., From "There's Plenty of Room at the Bottom" to Seeing What is Actually There. *Chemphyschem* **2014,** *15* (4), 547-549.

2.   Baird, D.; Shew, A., Probing the history of scanning tunneling microscopy. *Discovering the Nanoscale* **2004**, 145-156.

3.   Junk, A.; Riess, F., From an idea to a vision: There's plenty of room at the bottom. *American Journal of Physics* **2006,** *74* (9), 825-830.

4.   Arico, A. S.; Bruce, P.; Scrosati, B.; Tarascon, J. M.; Van Schalkwijk, W., Nanostructured materials for advanced energy conversion and storage devices. *Nature Materials* **2005,** *4* (5), 366-377.

5.   LesliePelecky, D. L.; Rieke, R. D., Magnetic properties of nanostructured materials. *Chemistry of Materials* **1996,** *8* (8), 1770-1783.

6.   Suryanarayana, C., Recent developments in nanostructured materials. *Advanced Engineering Materials* **2005,** *7* (11), 983-992.

7.   Dreaden, E. C.; Alkilany, A. M.; Huang, X. H.; Murphy, C. J.; El-Sayed, M. A., The golden age: gold nanoparticles for biomedicine. *Chemical Society Reviews* **2012,** *41* (7), 2740-2779.

8.   Niemeyer, C. M., Nanoparticles, proteins, and nucleic acids: Biotechnology meets materials science. *Angewandte Chemie-International Edition* **2001,** *40* (22), 4128-4158.

9.   Zhang, C. M.; Lin, J., Defect-related luminescent materials: synthesis, emission properties and applications. *Chemical Society Reviews* **2012,** *41* (23), 7938-7961.

10.   Kumar, P.; Singh, S.; Gupta, B. K., Future prospects of luminescent nanomaterial based security inks: from synthesis to anti-counterfeiting applications. *Nanoscale* **2016,** *8* (30), 14297-14340.

11.   Braslavsky, S. E., Glossary of terms used in Photochemistry 3(rd) Edition (IUPAC Recommendations 2006). *Pure and Applied Chemistry* **2007,** *79* (3), 293-465.

12.   Valeur, B.; Berberan-Santos, M. N., A Brief History of Fluorescence and Phosphorescence before the Emergence of Quantum Theory. *Journal of Chemical Education* **2011,** *88* (6), 731-738.

13.   Efros, A. L., INTERBAND ABSORPTION OF LIGHT IN A SEMICONDUCTOR SPHERE. *Soviet Physics Semiconductors-Ussr* **1982,** *16* (7), 772-775.

14.   Hotzer, B.; Medintz, I. L.; Hildebrandt, N., Fluorescence in Nanobiotechnology: Sophisticated Fluorophores for Novel Applications. *Small* **2012,** *8* (15), 2297-2326.

15.   Pellegrino, T.; Kudera, S.; Liedl, T.; Javier, A. M.; Manna, L.; Parak, W. J., On the development of colloidal nanoparticles towards multifunctional structures and their possible use for biological applications. *Small* **2005,** *1* (1), 48-63.

16. Lan, X. Z.; Masala, S.; Sargent, E. H., Charge-extraction strategies for colloidal quantum dot photovoltaics. *Nature Materials* **2014,** *13* (3), 233-240.

17. Cadmium Telluride Quantum Dots: Advances and Applications. *Cadmium Telluride Quantum Dots: Advances and Applications* **2013,** 1-229.

18. Medintz, I. L.; Uyeda, H. T.; Goldman, E. R.; Mattoussi, H., Quantum dot bioconjugates for imaging, labelling and sensing. *Nature Materials* **2005,** *4* (6), 435-446.

19. Han, M. Y.; Gao, X. H.; Su, J. Z.; Nie, S., Quantum-dot-tagged microbeads for multiplexed optical coding of biomolecules. *Nature Biotechnology* **2001,** *19* (7), 631-635.

20. Chan, W. C. W.; Maxwell, D. J.; Gao, X. H.; Bailey, R. E.; Han, M. Y.; Nie, S. M., Luminescent quantum dots for multiplexed biological detection and imaging. *Current Opinion in Biotechnology* **2002,** *13* (1), 40-46.

21. Zhou, J.; Yang, Y.; Zhang, C. Y., Toward Biocompatible Semiconductor Quantum Dots: From Biosynthesis and Bioconjugation to Biomedical Application. *Chemical Reviews* **2015,** *115* (21), 11669-11717.

22. Fan, J.; Chu, P. K., Group IV Nanoparticles: Synthesis, Properties, and Biological Applications. *Small* **2010,** *6* (19), 2080-2098.

23. Wu, X.; Zhang, Y. W.; Takle, K.; Bilsel, O.; Li, Z. J.; Lee, H.; Zhang, Z. J.; Li, D. S.; Fan, W.; Duan, C. Y.; Chan, E. M.; Lois, C.; Xiang, Y.; Han, G., Dye-Sensitized Core/Active Shell Upconversion Nanoparticles for Optogenetics and Bioimaging Applications. *Acs Nano* **2016,** *10* (1), 1060-1066.

24. Zhu, X. J.; Su, Q. Q.; Feng, W.; Li, F. Y., Anti-Stokes shift luminescent materials for bio-applications. *Chemical Society Reviews* **2017,** *46* (4), 1025-1039.

25. Chen, G. Y.; Damasco, J.; Qiu, H. L.; Shao, W.; Ohulchanskyy, T. Y.; Valiev, R. R.; Wu, X.; Han, G.; Wang, Y.; Yang, C. H.; Agren, H.; Prasad, P. N., Energy-Cascaded Upconversion in an Organic Dye-Sensitized Core/Shell Fluoride Nanocrystal. *Nano Letters* **2015,** *15* (11), 7400-7407.

26. Zou, W. Q.; Visser, C.; Maduro, J. A.; Pshenichnikov, M. S.; Hummelen, J. C., Broadband dye-sensitized upconversion of near-infrared light. *Nature Photonics* **2012,** *6* (8), 560-564.

27. Xu, J. T.; Yang, P. P.; Sun, M. D.; Bi, H. T.; Liu, B.; Yang, D.; Gai, S. L.; He, F.; Lin, J., Highly Emissive Dye-Sensitized Upconversion Nanostructure for Dual-Photosensitizer Photodynamic Therapy and Bioimaging. *Acs Nano* **2017,** *11* (4), 4133-4144.

28. Liz-Marzan, L. M.; Murphy, C. J.; Wang, J. F., Nanoplasmonics. *Chemical Society Reviews* **2014,** *43* (11), 3820-3822.

29. Eustis, S.; El-Sayed, M. A., Why gold nanoparticles are more precious than pretty gold: Noble metal surface plasmon resonance and its enhancement of the radiative and nonradiative properties of nanocrystals of different shapes. *Chemical Society Reviews* **2006,** *35* (3), 209-217.

30.   Zheng, J.;   Nicovich, P. R.; Dickson, R. M., Highly fluorescent noble-metal quantum dots. *Annual Review of Physical Chemistry* **2007,** *58*, 409-431.

31.   Choi, S.;   Dickson, R. M.; Yu, J. H., Developing luminescent silver nanodots for biological applications. *Chemical Society Reviews* **2012,** *41* (5), 1867-1891.

32.   Chen, H. N.; Xiang, S. S.; Li, W. P.; Liu, H. C.; Zhu, L. Q.; Yang, S. H., Inorganic Perovskite Solar Cells: A Rapidly Growing Field. *Solar Rrl* **2018,** *2* (2).

33.   Wang, H. C.; Wang, W. G.; Tang, A. C.; Tsai, H. Y.; Bao, Z.; Ihara, T.; Yarita, N.; Tahara, H.; Kanemitsu, Y.; Chen, S. M.; Liu, R. S., High-Performance CsPb1-xSnxBr3 Perovskite Quantum Dots for Light-Emitting Diodes. *Angewandte Chemie-International Edition* **2017,** *56* (44), 13650-13654.

34.   Wang, H. C.; Bao, Z.; Tsai, H. Y.; Tang, A. C.; Liu, R. S., Perovskite Quantum Dots and Their Application in Light-Emitting Diodes. *Small* **2018,** *14* (1).

35.   Wang, Y.; Sun, H. D., All-Inorganic Metal Halide Perovskite Nanostructures: From Photophysics to Light-Emitting Applications. *Small Methods* **2018,** *2* (1).

36.   Protesescu, L.; Yakunin, S.; Bodnarchuk, M. I.; Krieg, F.; Caputo, R.; Hendon, C. H.; Yang, R. X.; Walsh, A.; Kovalenko, M. V., Nanocrystals of Cesium Lead Halide Perovskites (CsPbX3, X = Cl, Br, and I): Novel Optoelectronic Materials Showing Bright Emission with Wide Color Gamut. *Nano Letters* **2015,** *15* (6), 3692-3696.

37.   Nedelcu, G.; Protesescu, L.; Yakunin, S.; Bodnarchuk, M. I.; Grotevent, M. J.; Kovalenko, M. V., Fast Anion-Exchange in Highly Luminescent Nanocrystals of Cesium Lead Halide Perovskites (CsPbX3, X = Cl, Br, I). *Nano Letters* **2015,** *15* (8), 5635-5640.

38.   Hwang, I.; Jeong, I.; Lee, J.; Ko, M. J.; Yong, K., Enhancing Stability of Perovskite Solar Cells to Moisture by the Facile Hydrophobic Passivation. *Acs Applied Materials & Interfaces* **2015,** *7* (31), 17330-17336.

39.   Jin, J. J.; Chen, C.; Li, H.; Cheng, Y.; Xu, L.; Dong, B.; Song, H. W.; Dai, Q. L., Enhanced Performance and Photostability of Perovskite Solar Cells by Introduction of Fluorescent Carbon Dots. *Acs Applied Materials & Interfaces* **2017,** *9* (16), 14518-14524.

40.   Koscher, B. A.; Swabeck, J. K.; Bronstein, N. D.; Alivisatos, A. P., Essentially Trap-Free CsPbBr3 Colloidal Nanocrystals by Postsynthetic Thiocyanate Surface Treatment. *Journal of the American Chemical Society* **2017,** *139* (19), 6566-6569.

41.   Canham, L. T., SILICON QUANTUM WIRE ARRAY FABRICATION BY ELECTROCHEMICAL AND CHEMICAL DISSOLUTION OF WAFERS. *Applied Physics Letters* **1990,** *57* (10), 1046-1048.

42.   Miura, S.; Nakamura, T.; Fujii, M.; Inui, M.; Hayashi, S., Size dependence of photoluminescence quantum efficiency of Si nanocrystals. *Physical Review B* **2006,** *73* (24).

43.   Belomoin, G.; Therrien, J.; Smith, A.; Rao, S.; Twesten, R.; Chaieb, S.; Nayfeh, M. H.; Wagner, L.; Mitas, L., Observation of a magic discrete family of ultrabright Si nanoparticles. *Applied Physics Letters* **2002,** *80* (5), 841-843.

44.   Rogozhina, E.; Belomoin, G.; Smith, A.; Abuhassan, L.; Barry, N.; Akcakir, O.; Braun, P. V.; Nayfeh, M. H., Si-N linkage in ultrabright, ultrasmall Si nanoparticles. *Applied Physics Letters* **2001,** *78* (23), 3711-3713.

45.   Kang, Z. H.; Liu, Y.; Tsang, C. H. A.; Ma, D. D. D.; Fan, X.; Wong, N. B.; Lee, S. T., Water-Soluble Silicon Quantum Dots with Wavelength-Tunable Photoluminescence. *Advanced Materials* **2009,** *21* (6), 661-+.

46.   Vasiliev, I.; Chelikowsky, J. R.; Martin, R. M., Surface oxidation effects on the optical properties of silicon nanocrystals. *Physical Review B* **2002,** *65* (12).

47.   Godefroo, S.; Hayne, M.; Jivanescu, M.; Stesmans, A.; Zacharias, M.; Lebedev, O. I.; Van Tendeloo, G.; Moshchalkov, V. V., Classification and control of the origin of photoluminescence from Si nanocrystals. *Nature Nanotechnology* **2008,** *3* (3), 174-178.

48.   Li, Q.; Luo, T. Y.; Zhou, M.; Abroshan, H.; Huang, J. C.; Kim, H. J.; Rosi, N. L.; Shao, Z. Z.; Jin, R. C., Silicon Nanoparticles with Surface Nitrogen: 90% Quantum Yield with Narrow Luminescence Bandwidth and the Ligand Structure Based Energy Law. *Acs Nano* **2016,** *10* (9), 8385-8393.

49.   Li, Q.; Jin, R. C., Photoluminescence from colloidal silicon nanoparticles: significant effect of surface. *Nanotechnology Reviews* **2017,** *6* (6), 601-612.

50.   Warner, J. H.; Hoshino, A.; Yamamoto, K.; Tilley, R. D., Water-soluble photoluminescent silicon quantum dots. *Angewandte Chemie-International Edition* **2005,** *44* (29), 4550-4554.

51.   Yang, C. S.; Bley, R. A.; Kauzlarich, S. M.; Lee, H. W. H.; Delgado, G. R., Synthesis of alkyl-terminated silicon nanoclusters by a solution route. *Journal of the American Chemical Society* **1999,** *121* (22), 5191-5195.

52.   Hessel, C. M.; Rasch, M. R.; Hueso, J. L.; Goodfellow, B. W.; Akhavan, V. A.; Puvanakrishnan, P.; Tunnel, J. W.; Korgel, B. A., Alkyl Passivation and Amphiphilic Polymer Coating of Silicon Nanocrystals for Diagnostic Imaging. *Small* **2010,** *6* (18), 2026-2034.

53.   Shor, J. S.; Bemis, L.; Kurtz, A. D.; Grimberg, I.; Weiss, B. Z.; Macmillian, M. F.; Choyke, W. J., CHARACTERIZATION OF NANOCRYSTALLITES IN POROUS P-TYPE 6H-SIC. *Journal of Applied Physics* **1994,** *76* (7), 4045-4049.

54.   Konstantinov, A. O.; Henry, A.; Harris, C. I.; Janzen, E., PHOTOLUMINESCENCE STUDIES OF POROUS SILICON-CARBIDE. *Applied Physics Letters* **1995,** *66* (17), 2250-2252.

55.   Morkoc, H.; Strite, S.; Gao, G. B.; Lin, M. E.; Sverdlov, B.; Burns, M., LARGE-BAND-GAP SIC, III-V NITRIDE, AND II-VI ZNSE-BASED SEMICONDUCTOR-DEVICE TECHNOLOGIES. *Journal of Applied Physics* **1994,** *76* (3), 1363-1398.

56.   Carmen Ortega-Liebana, M.; Hueso, J. L.; Arenal, R.; Lahoz, R.; de la Fuente, G. F.; Santamaria, J., Continuous-Mode Laser Ablation at the Solid Liquid Interface of Pelletized Low-Cost Materials for the Production of Luminescent Silicon Carbide Nanocrystals. *Journal of Physical Chemistry C* **2015,** *119* (4), 2158-2165.

57.   Beke, D.; Szekrenyes, Z.; Balogh, I.; Veres, M.; Fazakas, E.; Varga, L. K.; Kamaras, K.; Czigany, Z.; Gali, A., Characterization of luminescent silicon carbide nanocrystals prepared by reactive bonding and subsequent wet chemical etching. *Applied Physics Letters* **2011,** *99* (21).

58.   Fan, J. Y.; Li, H. X.; Wang, J.; Xiao, M., Fabrication and photoluminescence of SiC quantum dots stemming from 3C, 6H, and 4H polytypes of bulk SiC. *Applied Physics Letters* **2012,** *101* (13).

59.   Fan, J. Y.; Wu, X. L.; Chu, P. K., Low-dimensional SiC nanostructures: Fabrication, luminescence, and electrical properties. *Progress in Materials Science* **2006,** *51* (8), 983-1031.

60.   Wei, G. D.; Qin, W. P.; Wang, G. F.; Sun, J. B.; Lin, J. J.; Kim, R. J.; Zhang, D. S.; Zheng, K. Z., The synthesis and ultraviolet photoluminescence of 6H-SiC nanowires by microwave method. *Journal of Physics D-Applied Physics* **2008,** *41* (23).

61.   Fan, J. Y.; Li, H. X.; Cui, W. N.; Dai, D. J.; Chu, P. K., Excitation and recombination photodynamics in colloidal cubic SiC nanocrystals. *Applied Physics Letters* **2010,** *97* (19).

62.   Fan, J. Y.; Wu, X. L.; Li, H. X.; Liu, H. W.; Siu, G. G.; Chu, P. K., Luminescence from colloidal 3C-SiC nanocrystals in different solvents. *Applied Physics Letters* **2006,** *88* (4).

63.   Wang, J.; Xiong, S. J.; Wu, X. L.; Li, T. H.; Chu, P. K., Glycerol-Bonded 3C-SiC Nanocrystal Solid Films Exhibiting Broad and Stable Violet to Blue-Green Emission. *Nano Letters* **2010,** *10* (4), 1466-1471.

64.   Angelov, S.; Stoyanova, R.; Dafinova, R.; Kabasanov, K., LUMINESCENCE AND ELECTRON-PARAMAGNETIC-RES STUDIES ON STRONTIUM CARBONATE OBTAINED BY THERMAL-DECOMPOSITION OF STRONTIUM OXALATE. *Journal of Physics and Chemistry of Solids* **1986,** *47* (4), 409-412.

65.   Green, W. H.; Le, K. P.; Grey, J.; Au, T. T.; Sailor, M. J., White phosphors from a silicate-carboxylate sol-gel precursor that lack metal activator ions. *Science* **1997,** *276* (5320), 1826-1828.

66.   Dresselhaus, M. S.; Terrones, M., Carbon-Based Nanomaterials From a Historical Perspective. *Proceedings of the Ieee* **2013,** *101* (7), 1522-1535.

67.   Shamsipur, M.; Barati, A.; Karami, S., Long-wavelength, multicolor, and white-light emitting carbon-based dots: Achievements made, challenges remaining, and applications. *Carbon* **2017,** *124*, 429-472.

68.   Lim, S. Y.; Shen, W.; Gao, Z., Carbon quantum dots and their applications. *Chemical Society Reviews* **2015,** *44* (1), 362-381.

69.   Xu, X. Y.; Ray, R.; Gu, Y. L.; Ploehn, H. J.; Gearheart, L.; Raker, K.; Scrivens, W. A., Electrophoretic analysis and purification of fluorescent single-walled carbon nanotube fragments. *Journal of the American Chemical Society* **2004,** *126* (40), 12736-12737.

70.   Sun, Y. P.; Zhou, B.; Lin, Y.; Wang, W.; Fernando, K. A. S.; Pathak, P.; Meziani, M. J.; Harruff, B. A.; Wang, X.; Wang, H. F.; Luo, P. J. G.; Yang, H.; Kose, M. E.; Chen, B. L.; Veca, L. M.; Xie, S. Y., Quantum-sized carbon dots for bright and colorful photoluminescence. *Journal of the American Chemical Society* **2006,** *128* (24), 7756-7757.

71.   Baker, S. N.; Baker, G. A., Luminescent Carbon Nanodots: Emergent Nanolights. *Angewandte Chemie-International Edition* **2010,** *49* (38), 6726-6744.

72.   Avouris, P.; Freitag, M.; Perebeinos, V., Carbon-nanotube photonics and optoelectronics. *Nature Photonics* **2008,** *2* (6), 341-350.

73.   He, M. S.; Jiang, H.; Kauppinen, E. I.; Lehtonen, J., Diameter and chiral angle distribution dependencies on the carbon precursors in surface-grown single-walled carbon nanotubes. *Nanoscale* **2012,** *4* (23), 7394-7398.

74.   Hedman, D.; Barzegar, H. R.; Rosen, A.; Wagberg, T.; Larsson, J. A., On the Stability and Abundance of Single Walled Carbon Nanotubes. *Scientific Reports* **2015,** *5.*

75.   Shiraki, T.; Uchimura, S.; Shiraishi, T.; Onitsuka, H.; Nakashima, N., Near infrared photoluminescence modulation by defect site design using aryl isomers in locally functionalized single-walled carbon nanotubes. *Chemical Communications* **2017,** *53* (93), 12544-12547.

76.   Riggs, J. E.; Guo, Z. X.; Carroll, D. L.; Sun, Y. P., Strong luminescence of solubilized carbon nanotubes. *Journal of the American Chemical Society* **2000,** *122* (24), 5879-5880.

77.   O'Connell, M. J.; Bachilo, S. M.; Huffman, C. B.; Moore, V. C.; Strano, M. S.; Haroz, E. H.; Rialon, K. L.; Boul, P. J.; Noon, W. H.; Kittrell, C.; Ma, J. P.; Hauge, R. H.; Weisman, R. B.; Smalley, R. E., Band gap fluorescence from individual single-walled carbon nanotubes. *Science* **2002,** *297* (5581), 593-596.

78.   Schipper, M. L.; Nakayama-Ratchford, N.; Davis, C. R.; Kam, N. W. S.; Chu, P.; Liu, Z.; Sun, X. M.; Dai, H. J.; Gambhir, S. S., A pilot toxicology study of single-walled carbon nanotubes in a small sample of mice. *Nature Nanotechnology* **2008,** *3* (4), 216-221.

79.   Eda, G.; Mattevi, C.; Yamaguchi, H.; Kim, H.; Chhowalla, M., Insulator to Semimetal Transition in Graphene Oxide. *Journal of Physical Chemistry C* **2009,** *113* (35), 15768-15771.

80.   Khai, T. V.; Na, H. G.; Kwak, D. S.; Kwon, Y. J.; Ham, H.; Shim, K. B.; Kim, H. W., Significant enhancement of blue emission and electrical conductivity of N-doped graphene. *Journal of Materials Chemistry* **2012,** *22* (34), 17992-18003.

81.   Koos, M.; Veres, M.; Fule, M.; Pocsik, I., Ultraviolet photoluminescence and its relation to atomic bonding properties of hydrogenated amorphous carbon. *Diamond and Related Materials* **2002,** *11* (1), 53-58.

82.   Kozawa, D.; Zhu, X.; Miyauchi, Y.; Mouri, S.; Ichida, M.; Su, H. B.; Matsuda, K., Excitonic Photoluminescence from Nanodisc States in Graphene Oxides. *Journal of Physical Chemistry Letters* **2014,** *5* (10), 1754-1759.

83.   Eda, G.; Lin, Y. Y.; Mattevi, C.; Yamaguchi, H.; Chen, H. A.; Chen, I. S.; Chen, C. W.; Chhowalla, M., Blue Photoluminescence from Chemically Derived Graphene Oxide. *Advanced Materials* **2010,** *22* (4), 505-+.

84.   Tung, V. C.; Allen, M. J.; Yang, Y.; Kaner, R. B., High-throughput solution processing of large-scale graphene. *Nature Nanotechnology* **2009,** *4* (1), 25-29.

85.   Hsiao, W. W. W.; Hui, Y. Y.; Tsai, P. C.; Chang, H. C., Fluorescent Nanodiamond: A Versatile Tool for Long-Term Cell Tracking, Super-Resolution Imaging, and Nanoscale Temperature Sensing. *Accounts of Chemical Research* **2016,** *49* (3), 400-407.

86.   Merchant, K.; Sarkar, S. K., Fluorescent Nanodiamonds for Molecular and Cellular Bioimaging. *Ieee Journal of Selected Topics in Quantum Electronics* **2016,** *22* (3).

87.   Schirhagl, R.; Chang, K.; Loretz, M.; Degen, C. L., Nitrogen-Vacancy Centers in Diamond: Nanoscale Sensors for Physics and Biology. *Annual Review of Physical Chemistry, Vol 65* **2014,** *65*, 83-105.

88.   Mochalin, V. N.; Shenderova, O.; Ho, D.; Gogotsi, Y., The properties and applications of nanodiamonds. *Nature Nanotechnology* **2012,** *7* (1), 11-23.

89.   Davies, G.; Lawson, S. C.; Collins, A. T.; Mainwood, A.; Sharp, S. J., VACANCY-RELATED CENTERS IN DIAMOND. *Physical Review B* **1992,** *46* (20), 13157-13170.

90.   Chang, Y. R.; Lee, H. Y.; Chen, K.; Chang, C. C.; Tsai, D. S.; Fu, C. C.; Lim, T. S.; Tzeng, Y. K.; Fang, C. Y.; Han, C. C.; Chang, H. C.; Fann, W., Mass production and dynamic imaging of fluorescent nanodiamonds. *Nature Nanotechnology* **2008,** *3* (5), 284-288.

91.   Ye, F. M.; Wu, C. F.; Jin, Y. H.; Chan, Y. H.; Zhang, X. J.; Chiu, D. T., Ratiometric Temperature Sensing with Semiconducting Polymer Dots. *Journal of the American Chemical Society* **2011,** *133* (21), 8146-8149.

92.   Wu, C. F.; Schneider, T.; Zeigler, M.; Yu, J. B.; Schiro, P. G.; Burnham, D. R.; McNeill, J. D.; Chiu, D. T., Bioconjugation of Ultrabright Semiconducting Polymer Dots for Specific Cellular Targeting. *Journal of the American Chemical Society* **2010,** *132* (43), 15410-15417.

93.   Wu, C.; Bull, B.; Szymanski, C.; Christensen, K.; McNeill, J., Multicolor Conjugated Polymer Dots for Biological Fluorescence Imaging. *Acs Nano* **2008,** *2* (11), 2415-2423.

94.   Bottini, M.; Balasubramanian, C.; Dawson, M. I.; Bergamaschi, A.; Bellucci, S.; Mustelin, T., Isolation and characterization of fluorescent nanoparticles from pristine and oxidized electric arc-produced single-walled carbon nanotubes. *Journal of Physical Chemistry B* **2006,** *110* (2), 831-836.

95.   Cao, L.; Wang, X.; Meziani, M. J.; Lu, F. S.; Wang, H. F.; Luo, P. J. G.; Lin, Y.; Harruff, B. A.; Veca, L. M.; Murray, D.; Xie, S. Y.; Sun, Y. P., Carbon dots for multiphoton bioimaging. *Journal of the American Chemical Society* **2007,** *129* (37), 11318-+.

96.   Yang, S. T.; Cao, L.; Luo, P. G. J.; Lu, F. S.; Wang, X.; Wang, H. F.; Meziani, M. J.; Liu, Y. F.; Qi, G.; Sun, Y. P., Carbon Dots for Optical Imaging in Vivo. *Journal of the American Chemical Society* **2009,** *131* (32), 11308-+.

97.   Hu, S. L.; Niu, K. Y.; Sun, J.; Yang, J.; Zhao, N. Q.; Du, X. W., One-step synthesis of fluorescent carbon nanoparticles by laser irradiation. *Journal of Materials Chemistry* **2009,** *19* (4), 484-488.

98.   Li, X. Y.; Wang, H. Q.; Shimizu, Y.; Pyatenko, A.; Kawaguchi, K.; Koshizaki, N., Preparation of carbon quantum dots with tunable photoluminescence by rapid laser passivation in ordinary organic solvents. *Chemical Communications* **2011,** *47* (3), 932-934.

99.   Qiao, Z. A.; Wang, Y. F.; Gao, Y.; Li, H. W.; Dai, T. Y.; Liu, Y. L.; Huo, Q. S., Commercially activated carbon as the source for producing multicolor photoluminescent carbon dots by chemical oxidation. *Chemical Communications* **2010,** *46* (46), 8812-8814.

100.   Li, H. T.; He, X. D.; Liu, Y.; Huang, H.; Lian, S. Y.; Lee, S. T.; Kang, Z. H., One-step ultrasonic synthesis of water-soluble carbon nanoparticles with excellent photoluminescent properties. *Carbon* **2011,** *49* (2), 605-609.

101.   Li, H. T.; He, X. D.; Kang, Z. H.; Huang, H.; Liu, Y.; Liu, J. L.; Lian, S. Y.; Tsang, C. H. A.; Yang, X. B.; Lee, S. T., Water-Soluble Fluorescent Carbon Quantum Dots and Photocatalyst Design. *Angewandte Chemie-International Edition* **2010,** *49* (26), 4430-4434.

102.   Bao, L.; Zhang, Z. L.; Tian, Z. Q.; Zhang, L.; Liu, C.; Lin, Y.; Qi, B. P.; Pang, D. W., Electrochemical Tuning of Luminescent Carbon Nanodots: From Preparation to Luminescence Mechanism. *Advanced Materials* **2011,** *23* (48), 5801-+.

103.   Zhou, J. G.; Booker, C.; Li, R. Y.; Zhou, X. T.; Sham, T. K.; Sun, X. L.; Ding, Z. F., An electrochemical avenue to blue luminescent nanocrystals from multiwalled carbon nanotubes (MWCNTs). *Journal of the American Chemical Society* **2007,** *129* (4), 744-745.

104.   Niu, F. S.; Xu, Y. H.; Liu, M. L.; Sun, J.; Guo, P. R.; Liu, J. Q., Bottom-up electrochemical preparation of solid-state carbon nanodots directly from nitriles/ionic liquids using carbon-free electrodes and the applications in specific ferric ion detection and cell imaging. *Nanoscale* **2016,** *8* (10), 5470-5477.

105.   Deng, J. H.; Lu, Q. J.; Mi, N. X.; Li, H. T.; Liu, M. L.; Xu, M. C.; Tan, L.; Xie, Q. J.; Zhang, Y. Y.; Yao, S. Z., Electrochemical Synthesis of Carbon Nanodots Directly from Alcohols. *Chemistry-a European Journal* **2014,** *20* (17), 4993-4999.

106.   Zhu, H.; Wang, X.; Li, Y.; Wang, Z.; Yang, F.; Yang, X., Microwave synthesis of fluorescent carbon nanoparticles with electrochemiluminescence properties. *Chemical Communications* **2009,** (34), 5118-5120.

107.   Tang, L. B.; Ji, R. B.; Cao, X. K.; Lin, J. Y.; Jiang, H. X.; Li, X. M.; Teng, K. S.; Luk, C. M.; Zeng, S. J.; Hao, J. H.; Lau, S. P., Deep Ultraviolet Photoluminescence of Water-Soluble Self-Passivated Graphene Quantum Dots. *Acs Nano* **2012,** *6* (6), 5102-5110.

108.   Wei, W. L.; Xu, C.; Wu, L.; Wang, J. S.; Ren, J. S.; Qu, X. G., Non-Enzymatic-Browning-Reaction: A Versatile Route for Production of Nitrogen-Doped Carbon Dots with Tunable Multicolor Luminescent Display. *Scientific Reports* **2014,** *4*.

109.   Zong, J.; Zhu, Y. H.; Yang, X. L.; Shen, J. H.; Li, C. Z., Synthesis of photoluminescent carbogenic dots using mesoporous silica spheres as nanoreactors. *Chemical Communications* **2011,** *47* (2), 764-766.

110.   Yang, Y. X.; Wu, D. Q.; Han, S.; Hu, P. F.; Liu, R. L., Bottom-up fabrication of photoluminescent carbon dots with uniform morphology via a soft-hard template approach. *Chemical Communications* **2013,** *49* (43), 4920-4922.

111.   Guo, X.; Wang, C. F.; Yu, Z. Y.; Chen, L.; Chen, S., Facile access to versatile fluorescent carbon dots toward light-emitting diodes. *Chemical Communications* **2012,** *48* (21), 2692-2694.

112.   Wang, Y. F.; Dong, L. H.; Xiong, R. L.; Hu, A. G., Practical access to bandgap-like N-doped carbon dots with dual emission unzipped from PAN@PMMA core-shell nanoparticles. *Journal of Materials Chemistry C* **2013,** *1* (46), 7731-7735.

113.   Zhu, B.; Sun, S.; Wang, Y.; Deng, S.; Qian, G.; Wang, M.; Hu, A., Preparation of carbon nanodots from single chain polymeric nanoparticles and theoretical investigation of the photoluminescence mechanism. *Journal of Materials Chemistry C* **2013,** *1* (3), 580-586.

114.   Lai, C. W.; Hsiao, Y. H.; Peng, Y. K.; Chou, P. T., Facile synthesis of highly emissive carbon dots from pyrolysis of glycerol; gram scale production of carbon dots/mSiO(2) for cell imaging and drug release. *Journal of Materials Chemistry* **2012,** *22* (29), 14403-14409.

115.   Hu, Y. P.; Yang, J.; Tian, J. W.; Jia, L.; Yu, J. S., Waste frying oil as a precursor for one-step synthesis of sulfur-doped carbon dots with pH-sensitive photoluminescence. *Carbon* **2014,** *77*, 775-782.

116.   Krysmann, M. J.; Kelarakis, A.; Dallas, P.; Giannelis, E. P., Formation Mechanism of Carbogenic Nanoparticles with Dual Photoluminescence Emission. *Journal of the American Chemical Society* **2012,** *134* (2), 747-750.

117.   Zhou, J.; Sheng, Z.; Han, H.; Zou, M.; Li, C., Facile synthesis of fluorescent carbon dots using watermelon peel as a carbon source. *Materials Letters* **2012,** *66* (1), 222-224.

118.   Hsu, P.-C.; Chang, H.-T., Synthesis of high-quality carbon nanodots from hydrophilic compounds: role of functional groups. *Chemical Communications* **2012,** *48* (33), 3984-3986.

119.   Sahu, S.; Behera, B.; Maiti, T. K.; Mohapatra, S., Simple one-step synthesis of highly luminescent carbon dots from orange juice: application as excellent bio-imaging agents. *Chemical Communications* **2012,** *48* (70), 8835-8837.

120.   Jia, X. F.; Li, J.; Wang, E. K., One-pot green synthesis of optically pH-sensitive carbon dots with upconversion luminescence. *Nanoscale* **2012,** *4* (18), 5572-5575.

121.   Mehta, V. N.; Jha, S.; Kailasa, S. K., One-pot green synthesis of carbon dots by using Saccharum officinarum juice for fluorescent imaging of bacteria (Escherichia coli) and yeast (Saccharomyces cerevisiae) cells. *Materials Science & Engineering C-Materials for Biological Applications* **2014,** *38*, 20-27.

122.   Liu, H. F.; Li, Z. H.; Sun, Y. Q.; Geng, X.; Hu, Y. L.; Meng, H. M.; Ge, J.; Qu, L. B., Synthesis of Luminescent Carbon Dots with Ultrahigh Quantum Yield and Inherent Folate Receptor-Positive Cancer Cell Targetability. *Scientific Reports* **2018,** *8*, 8.

123.   Liang, Q. H.; Ma, W. J.; Shi, Y.; Li, Z.; Yang, X. M., Easy synthesis of highly fluorescent carbon quantum dots from gelatin and their luminescent properties and applications. *Carbon* **2013,** *60*, 421-428.

124.   Wu, H.; Mi, C.; Huang, H.; Han, B.; Li, J.; Xu, S., Solvothermal synthesis of green-fluorescent carbon nanoparticles and their application. *Journal of Luminescence* **2012,** *132* (6), 1603-1607.

125.   Hsu, P.-C.; Chen, P.-C.; Ou, C.-M.; Chang, H.-Y.; Chang, H.-T., Extremely high inhibition activity of photoluminescent carbon nanodots toward cancer cells. *Journal of Materials Chemistry B* **2013,** *1* (13), 1774-1781.

126.   Wang, J.; Wang, C.-F.; Chen, S., Amphiphilic Egg-Derived Carbon Dots: Rapid Plasma Fabrication, Pyrolysis Process, and Multicolor Printing Patterns. *Angewandte Chemie-International Edition* **2012,** *51* (37), 9297-9301.

127.   Lu, W.; Qin, X.; Liu, S.; Chang, G.; Zhang, Y.; Luo, Y.; Asiri, A. M.; Al-Youbi, A. O.; Sun, X., Economical, Green Synthesis of Fluorescent Carbon Nanoparticles and Their Use as Probes for Sensitive and Selective Detection of Mercury(II) Ions. *Analytical Chemistry* **2012,** *84* (12), 5351-5357.

128.   Wang, J.; Ng, Y. H.; Lim, Y.-F.; Ho, G. W., Vegetable-extracted carbon dots and their nanocomposites for enhanced photocatalytic H-2 production. *Rsc Advances* **2014,** *4* (83), 44117-44123.

129.   Liu, S.; Tian, J. Q.; Wang, L.; Zhang, Y. W.; Qin, X. Y.; Luo, Y. L.; Asiri, A. M.; Al-Youbi, A. O.; Sun, X. P., Hydrothermal Treatment of Grass: A Low-Cost, Green Route to Nitrogen-Doped, Carbon-Rich, Photoluminescent Polymer Nanodots as an Effective Fluorescent Sensing Platform for Label-Free Detection of Cu(II) Ions. *Advanced Materials* **2012,** *24* (15), 2037-2041.

130.   Fang, Y. X.; Guo, S. J.; Li, D.; Zhu, C. Z.; Ren, W.; Dong, S. J.; Wang, E. K., Easy Synthesis and Imaging Applications of Cross-Linked Green Fluorescent Hollow Carbon Nanoparticles. *Acs Nano* **2012,** *6* (1), 400-409.

131.   Wang, Q. L.; Huang, X. X.; Long, Y. J.; Wang, X. L.; Zhang, H. J.; Zhu, R.; Liang, L. P.; Teng, P.; Zheng, H. Z., Hollow luminescent carbon dots for drug delivery. *Carbon* **2013,** *59*, 192-199.

132.   Fu, M.; Ehrat, F.; Wang, Y.; Milowska, K. Z.; Reckmeier, C.; Rogach, A. L.; Stolarczyk, J. K.; Urban, A. S.; Feldmann, J., Carbon Dots: A Unique Fluorescent Cocktail of Polycyclic Aromatic Hydrocarbons. *Nano Letters* **2015,** *15* (9), 6030-6035.

133. Sarswat, P. K.; Free, M. L., Light emitting diodes based on carbon dots derived from food, beverage, and combustion wastes. *Physical Chemistry Chemical Physics* **2015,** *17* (41), 27642-27652.

134. Bao, L.; Liu, C.; Zhang, Z. L.; Pang, D. W., Photoluminescence-Tunable Carbon Nanodots: Surface-State Energy-Gap Tuning. *Advanced Materials* **2015,** *27* (10), 1663-+.

135. Ghosh, S.; Chizhik, A. M.; Karedla, N.; Dekaliuk, M. O.; Gregor, I.; Schuhmann, H.; Seibt, M.; Bodensiek, K.; Schaap, I. A. T.; Schulz, O.; Demchenko, A. P.; Enderlein, J.; Chizhik, A. I., Photoluminescence of Carbon Nanodots: Dipole Emission Centers and Electron-Phonon Coupling. *Nano Letters* **2014,** *14* (10), 5656-5661.

136. Kang, Y. F.; Fang, Y. W.; Li, Y. H.; Li, W.; Yin, X. B., Nucleus-staining with biomolecule-mimicking nitrogen-doped carbon dots prepared by a fast neutralization heat strategy. *Chemical Communications* **2015,** *51* (95), 16956-16959.

137. Li, N.; Liu, S. G.; Fan, Y. Z.; Ju, Y. J.; Xiao, N.; Luo, H. Q.; Li, N. B., Adenosine-derived doped carbon dots: From an insight into effect of N/P co-doping on emission to highly sensitive picric acid sensing. *Analytica Chimica Acta* **2018,** *1013*, 63-70.

138. Li, F.; Li, T. Y.; Sun, C. X.; Xia, J. H.; Jiao, Y.; Xu, H. P., Selenium-Doped Carbon Quantum Dots for Free-Radical Scavenging. *Angewandte Chemie-International Edition* **2017,** *56* (33), 9910-9914.

139. Hai, X.; Mao, Q. X.; Wang, W. J.; Wang, X. F.; Chen, X. W.; Wang, J. H., An acid-free microwave approach to prepare highly luminescent boron-doped graphene quantum dots for cell imaging. *Journal of Materials Chemistry B* **2015,** *3* (47), 9109-9114.

140. Dong, Y. Q.; Pang, H. C.; Yang, H. B.; Guo, C. X.; Shao, J. W.; Chi, Y. W.; Li, C. M.; Yu, T., Carbon-Based Dots Co-doped with Nitrogen and Sulfur for High Quantum Yield and Excitation-Independent Emission. *Angewandte Chemie-International Edition* **2013,** *52* (30), 7800-7804.

141. Zhou, J.; Zhou, H.; Tang, J. B.; Deng, S. E.; Yan, F.; Li, W. J.; Qu, M. H., Carbon dots doped with heteroatoms for fluorescent bioimaging: a review. *Microchimica Acta* **2017,** *184* (2), 343-368.

142. Liao, J.; Cheng, Z. H.; Zhou, L., Nitrogen-Doping Enhanced Fluorescent Carbon Dots: Green Synthesis and Their Applications for Bioimaging and Label-Free Detection of Au3+ Ions. *Acs Sustainable Chemistry & Engineering* **2016,** *4* (6), 3053-3061.

143. Borse, V.; Thakur, M.; Sengupta, S.; Srivastava, R., N-doped multi-fluorescent carbon dots for 'turn off-on' silver-biothiol dual sensing and mammalian cell imaging application. *Sensors and Actuators B-Chemical* **2017,** *248*, 481-492.

144. Tetsuka, H.; Asahi, R.; Nagoya, A.; Okamoto, K.; Tajima, I.; Ohta, R.; Okamoto, A., Optically Tunable Amino-Functionalized Graphene Quantum Dots. *Advanced Materials* **2012,** *24* (39), 5333-5338.

145. Hola, K.; Sudolska, M.; Kalytchuk, S.; Nachtigallova, D.; Rogach, A. L.; Otyepka, M.; Zboril, R., Graphitic Nitrogen Triggers Red Fluorescence in Carbon Dots. *Acs Nano* **2017,** *11* (12), 12402-12410.

146. Xu, Q.; Kuang, T. R.; Liu, Y.; Cai, L. L.; Peng, X. F.; Sreeprasad, T. S.; Zhao, P.; Yu, Z. Q.; Li, N., Heteroatom-doped carbon dots: synthesis, characterization, properties, photoluminescence mechanism and biological applications. *Journal of Materials Chemistry B* **2016,** *4* (45), 7204-7219.

147. Jiang, K.; Sun, S.; Zhang, L.; Lu, Y.; Wu, A. G.; Cai, C. Z.; Lin, H. W., Red, Green, and Blue Luminescence by Carbon Dots: Full-Color Emission Tuning and Multicolor Cellular Imaging. *Angewandte Chemie-International Edition* **2015,** *54* (18), 5360-5363.

148. Guo, L.; Ge, J. C.; Liu, W. M.; Niu, G. L.; Jia, Q. Y.; Wang, H.; Wang, P. F., Tunable multicolor carbon dots prepared from well-defined polythiophene derivatives and their emission mechanism. *Nanoscale* **2016,** *8* (2), 729-734.

149. Wang, C. X.; Jiang, K. L.; Wu, Q.; Wu, J. P.; Zhang, C., Green Synthesis of Red-Emitting Carbon Nanodots as a Novel "Turn-on" Nanothermometer in Living Cells. *Chemistry-a European Journal* **2016,** *22* (41), 14475-14479.

150. Yang, C. H.; Zhu, S. J.; Li, Z. L.; Li, Z.; Chen, C.; Sun, L.; Tang, W.; Liu, R.; Sun, Y.; Yu, M., Nitrogen-doped carbon dots with excitationin-dependent long-wavelength emission produced by a room-temperature reaction. *Chemical Communications* **2016,** *52* (80), 11912-11914.

151. Garcia-Calzada, R.; Rodio, M.; Bagga, K.; Intartaglia, R.; Bianchini, P.; Chirvony, V. S.; Martinez-Pastor, J. P., Facile laser-assisted synthesis of inorganic nanoparticles covered by a carbon shell with tunable luminescence. *Rsc Advances* **2015,** *5* (62), 50604-50610.

152. Wang, X.; Cao, L.; Yang, S. T.; Lu, F. S.; Meziani, M. J.; Tian, L. L.; Sun, K. W.; Bloodgood, M. A.; Sun, Y. P., Bandgap-Like Strong Fluorescence in Functionalized Carbon Nanoparticles. *Angewandte Chemie-International Edition* **2010,** *49* (31), 5310-5314.

153. Shen, J. H.; Zhu, Y. H.; Yang, X. L.; Li, C. Z., Graphene quantum dots: emergent nanolights for bioimaging, sensors, catalysis and photovoltaic devices. *Chemical Communications* **2012,** *48* (31), 3686-3699.

154. Gokus, T.; Nair, R. R.; Bonetti, A.; Bohmler, M.; Lombardo, A.; Novoselov, K. S.; Geim, A. K.; Ferrari, A. C.; Hartschuh, A., Making Graphene Luminescent by Oxygen Plasma Treatment. *Acs Nano* **2009,** *3* (12), 3963-3968.

155. Cao, L.; Meziani, M. J.; Sahu, S.; Sun, Y. P., Photoluminescence Properties of Graphene versus Other Carbon Nanomaterials. *Accounts of Chemical Research* **2013,** *46* (1), 171-180.

156. Zhu, S. J.; Song, Y. B.; Zhao, X. H.; Shao, J. R.; Zhang, J. H.; Yang, B., The photoluminescence mechanism in carbon dots (graphene quantum dots, carbon nanodots, and polymer dots): current state and future perspective. *Nano Research* **2015,** *8* (2), 355-381.

157.   Dekaliuk, M. O.; Viagin, O.; Malyukin, Y. V.; Demchenko, A. P., Fluorescent carbon nanomaterials: "quantum dots" or nanoclusters? *Physical Chemistry Chemical Physics* **2014,** *16* (30), 16075-16084.

158.   Nguyen, V.; Si, J. H.; Yan, L. H.; Hou, X., Direct demonstration of photoluminescence originated from surface functional groups in carbon nanodots. *Carbon* **2016,** *108*, 268-273.

159.   Xu, Y.; Wu, M.; Liu, Y.; Feng, X. Z.; Yin, X. B.; He, X. W.; Zhang, Y. K., Nitrogen-Doped Carbon Dots: A Facile and General Preparation Method, Photoluminescence Investigation, and Imaging Applications. *Chemistry-a European Journal* **2013,** *19* (7), 2276-2283.

160.   Qi, B. P.; Hu, H.; Bao, L.; Zhang, Z. L.; Tang, B.; Peng, Y.; Wang, B. S.; Pang, D. W., An efficient edge-functionalization method to tune the photoluminescence of graphene quantum dots. *Nanoscale* **2015,** *7* (14), 5969-5973.

161.   Ding, H.; Yu, S. B.; Wei, J. S.; Xiong, H. M., Full-Color Light-Emitting Carbon Dots with a Surface-State-Controlled Luminescence Mechanism. *Acs Nano* **2016,** *10* (1), 484-491.

162.   Tetsuka, H.; Nagoya, A.; Fukusumi, T.; Matsui, T., Molecularly Designed, Nitrogen-Functionalized Graphene Quantum Dots for Optoelectronic Devices. *Advanced Materials* **2016,** *28* (23), 4632-4638.

163.   Liu, C.; Xiao, G. J.; Yang, M. L.; Zou, B.; Zhang, Z. L.; Pang, D. W., Mechanofluorochromic Carbon Nanodots: Controllable Pressure-Triggered Blue- and Red-Shifted Photoluminescence. *Angewandte Chemie-International Edition* **2018,** *57* (7), 1893-1897.

164.   Cayuela, A.; Soriano, M. L.; Carrillo-Carrion, C.; Valcarcel, M., Semiconductor and carbon-based fluorescent nanodots: the need for consistency. *Chemical Communications* **2016,** *52* (7), 1311-1326.

165.   Sharma, V.; Tiwari, P.; Mobin, S. M., Sustainable carbon-dots: recent advances in green carbon dots for sensing and bioimaging. *Journal of Materials Chemistry B* **2017,** *5* (45), 8904-8924.

166.   Feng, T.; Ai, X. Z.; An, G. H.; Yang, P. P.; Zhao, Y. L., Charge-Convertible Carbon Dots for Imaging Guided Drug Delivery with Enhanced in Vivo Cancer Therapeutic Efficiency. *Acs Nano* **2016,** *10* (4), 4410-4420.

167.   Zheng, X. T.; Ananthanarayanan, A.; Luo, K. Q.; Chen, P., Glowing Graphene Quantum Dots and Carbon Dots: Properties, Syntheses, and Biological Applications. *Small* **2015,** *11* (14), 1620-1636.

168.   Peng, H.; Travas-Sejdic, J., Simple Aqueous Solution Route to Luminescent Carbogenic Dots from Carbohydrates. *Chemistry of Materials* **2009,** *21* (23), 5563-5565.

169.   Yang, Z.-C.; Wang, M.; Yong, A. M.; Wong, S. Y.; Zhang, X.-H.; Tan, H.; Chang, A. Y.;   Li, X.; Wang, J., Intrinsically fluorescent carbon dots with tunable emission

derived from hydrothermal treatment of glucose in the presence of monopotassium phosphate. *Chemical Communications* **2011,** *47* (42), 11615-11617.

170.   Li, X. M.; Zhang, S. L.; Kulinich, S. A.; Liu, Y. L.; Zeng, H. B., Engineering surface states of carbon dots to achieve controllable luminescence for solid-luminescent composites and sensitive Be2+ detection. *Scientific Reports* **2014,** *4*.

171.   Zhou, J.; Liu, Q.; Feng, W.; Sun, Y.; Li, F. Y., Upconversion Luminescent Materials: Advances and Applications. *Chemical Reviews* **2015,** *115* (1), 395-465.

172.   Pawlicki, M.; Collins, H. A.; Denning, R. G.; Anderson, H. L., Two-Photon Absorption and the Design of Two-Photon Dyes. *Angewandte Chemie-International Edition* **2009,** *48* (18), 3244-3266.

173.   Auzel, F., Upconversion and anti-stokes processes with f and d ions in solids. *Chemical Reviews* **2004,** *104* (1), 139-173.

174.   Tian, X. H.; Zhu, Y. Z.; Zhang, Q.; Zhang, R. L.; Wu, J. Y.; Tian, Y. P., Halides tuning the subcellular-targeting in two-photon emissive complexes via different uptake mechanisms. *Chemical Communications* **2017,** *53* (56), 7941-7944.

175.   Liu, Q.; Guo, B. D.; Rao, Z. Y.; Zhang, B. H.; Gong, J. R., Strong Two-Photon-Induced Fluorescence from Photostable, Biocompatible Nitrogen-Doped Graphene Quantum Dots for Cellular and Deep-Tissue Imaging. *Nano Letters* **2013,** *13* (6), 2436-2441.

176.   Wang, L.; Wang, Y. L.; Xu, T.; Liao, H. B.; Yao, C. J.; Liu, Y.; Li, Z.; Chen, Z. W.; Pan, D. Y.; Sun, L. T.; Wu, M. H., Gram-scale synthesis of single-crystalline graphene quantum dots with superior optical properties. *Nature Communications* **2014,** *5*.

177.   Zheng, M.; Xie, Z. G.; Qu, D.; Li, D.; Du, P.; Jing, X. B.; Sun, Z. C., On Off On Fluorescent Carbon Dot Nanosensor for Recognition of Chromium(VI) and Ascorbic Acid Based on the Inner Filter Effect. *Acs Applied Materials & Interfaces* **2013,** *5* (24), 13242-13247.

178.   Wang, J.; Cheng, C. M.; Huang, Y.; Zheng, B. Z.; Yuan, H. Y.; Bo, L.; Zheng, M. W.; Yang, S. Y.; Guo, Y.; Xiao, D., A facile large-scale microwave synthesis of highly fluorescent carbon dots from benzenediol isomers. *Journal of Materials Chemistry C* **2014,** *2* (25), 5028-5035.

179.   Ke, C. C.; Yang, Y. C.; Tseng, W. L., Synthesis of Blue-, Green-, Yellow-, and Red-Emitting Graphene-Quantum-Dot-Based Nanomaterials with Excitation-Independent Emission. *Particle & Particle Systems Characterization* **2016,** *33* (3), 132-139.

180.   Liang, Z. C.; Kang, M. J.; Payne, G. F.; Wang, X. H.; Sun, R. C., Probing Energy and Electron Transfer Mechanisms in Fluorescence Quenching of Biomass Carbon Quantum Dots. *Acs Applied Materials & Interfaces* **2016,** *8* (27), 17478-17488.

181.   Zhang, H. C.; Huang, H.; Ming, H.; Li, H. T.; Zhang, L. L.; Liu, Y.; Kang, Z. H., Carbon quantum dots/Ag3PO4 complex photocatalysts with enhanced photocatalytic activity and stability under visible light. *Journal of Materials Chemistry* **2012,** *22* (21), 10501-10506.

182.   Wang, R.; Lu, K. Q.; Tang, Z. R.; Xu, Y. J., Recent progress in carbon quantum dots: synthesis, properties and applications in photocatalysis. *Journal of Materials Chemistry A* **2017,** *5* (8), 3717-3734.

183.   Wang, X.; Cao, L.; Lu, F. S.; Meziani, M. J.; Li, H.; Qi, G.; Zhou, B.; Harruff, B. A.; Kermarrec, F.; Sun, Y. P., Photoinduced electron transfers with carbon dots. *Chemical Communications* **2009,** (25), 3774-3776.

184.   Hu, Y. L.; Geng, X.; Zhang, L.; Huang, Z. M.; Ge, J.; Li, Z. H., Nitrogen-doped Carbon Dots Mediated Fluorescent on-off Assay for Rapid and Highly Sensitive Pyrophosphate and Alkaline Phosphatase Detection. *Scientific Reports* **2017,** *7*.

185.   Hong, G. S.; Diao, S. O.; Antaris, A. L.; Dai, H. J., Carbon Nanomaterials for Biological Imaging and Nanomedicinal Therapy. *Chemical Reviews* **2015,** *115* (19), 10816-10906.

186.   Choi, H.; Ko, S. J.; Choi, Y.; Joo, P.; Kim, T.; Lee, B. R.; Jung, J. W.; Choi, H. J.; Cha, M.; Jeong, J. R.; Hwang, I. W.; Song, M. H.; Kim, B. S.; Kim, J. Y., Versatile surface plasmon resonance of carbon-dot-supported silver nanoparticles in polymer optoelectronic devices. *Nature Photonics* **2013,** *7* (9), 732-738.

187.   Gowthaman, N. S. K.; Sinduja, B.; Karthikeyan, R.; Rubini, K.; John, S. A., Fabrication of nitrogen-doped carbon dots for screening the purine metabolic disorder in human fluids. *Biosensors & Bioelectronics* **2017,** *94*, 30-38.

188.   Wang, J.; Peng, F.; Lu, Y. M.; Zhong, Y. L.; Wang, S. Y.; Xu, M. F.; Ji, X. Y.; Su, Y. Y.; Liao, L. S.; He, Y., Large-Scale Green Synthesis of Fluorescent Carbon Nanodots and Their Use in Optics Applications. *Advanced Optical Materials* **2015,** *3* (1), 103-111.

189.   Jang, B.; Choi, Y., Photosensitizer-Conjugated Gold Nanorods for Enzyme-Activatable Fluorescence Imaging and Photodynamic Therapy. *Theranostics* **2012,** *2* (2), 190-197.

190.   Koo, H.; Lee, H.; Lee, S.; Min, K. H.; Kim, M. S.; Lee, D. S.; Choi, Y.; Kwon, I. C.; Kim, K.; Jeong, S. Y., In vivo tumor diagnosis and photodynamic therapy via tumoral pH-responsive polymeric micelles. *Chemical Communications* **2010,** *46* (31), 5668-5670.

191.   Bae, B. C.; Na, K., Self-quenching polysaccharide-based nanogels of pullulan/folate-photosensitizer conjugates for photodynamic therapy. *Biomaterials* **2010,** *31* (24), 6325-6335.

192.   Zhang, P. H.; He, Z. M.; Wang, C.; Chen, J. N.; Zhao, J. J.; Zhu, X. N.; Li, C. Z.; Min, Q. H.; Zhu, J. J., In Situ Amplification of Intracellular MicroRNA with MNAzyme Nanodevices for Multiplexed Imaging, Logic Operation, and Controlled Drug Release. *Acs Nano* **2015,** *9* (1), 789-798.

193.   Stewart, M. P.; Sharei, A.; Ding, X. Y.; Sahay, G.; Langer, R.; Jensen, K. F., In vitro and ex vivo strategies for intracellular delivery. *Nature* **2016,** *538* (7624), 183-192.

194.   Chu, K. F.; Dupuy, D. E., Thermal ablation of tumours: biological mechanisms and advances in therapy. *Nature Reviews Cancer* **2014,** *14* (3), 199-208.

195.   Valerio, M.; Cerantola, Y.; Eggener, S. E.; Lepor, H.; Polascik, T. J.; Villers, A.; Emberton, M., New and Established Technology in Focal Ablation of the Prostate: A Systematic Review. *European Urology* **2017,** *71* (1), 17-34.

196.   Li, Z. B.; Ye, E. Y.; David; Lakshminarayanan, R.; Loh, X. J., Recent Advances of Using Hybrid Nanocarriers in Remotely Controlled Therapeutic Delivery. *Small* **2016,** *12* (35), 4782-4806.

197.   Fang, J.; Nakamura, H.; Maeda, H., The EPR effect: Unique features of tumor blood vessels for drug delivery, factors involved, and limitations and augmentation of the effect. *Advanced Drug Delivery Reviews* **2011,** *63* (3), 136-151.

198.   Pansare, V. J.; Hejazi, S.; Faenza, W. J.; Prud'homme, R. K., Review of Long-Wavelength Optical and NIR Imaging Materials: Contrast Agents, Fluorophores, and Multifunctional Nano Carriers. *Chemistry of Materials* **2012,** *24* (5), 812-827.

199.   Weissleder, R., A clearer vision for in vivo imaging. *Nature Biotechnology* **2001,** *19* (4), 316-317.

200.   Thekaekara, M. P., SOLAR-RADIATION MEASUREMENT - TECHNIQUES AND INSTRUMENTATION. *Solar Energy* **1976,** *18* (4), 309-325.

201.   Yun, S. H.; Kwok, S. J. J., Light in diagnosis, therapy and surgery. *Nature Biomedical Engineering* **2017,** *1* (1).

202.   Keereweer, S.; Van Driel, P.; Snoeks, T. J. A.; Kerrebijn, J. D. F.; de Jong, R. J. B.; Vahrmeijer, A. L.; Sterenborg, H.; Lowik, C., Optical Image-Guided Cancer Surgery: Challenges and Limitations. *Clinical Cancer Research* **2013,** *19* (14), 3745-3754.

203.   Ntziachristos, V.; Ripoll, J.; Weissleder, R., Would near-infrared fluorescence signals propagate through large human organs for clinical studies? *Optics Letters* **2002,** *27* (5), 333-335.

204.   Tong, R.; Kohane, D. S., Shedding light on nanomedicine. *Wiley Interdisciplinary Reviews-Nanomedicine and Nanobiotechnology* **2012,** *4* (6), 638-662.

205.   Ackroyd, R.; Kelty, C.; Brown, N.; Reed, M., The history of photodetection and photodynamic therapy. *Photochemistry and Photobiology* **2001,** *74* (5), 656-669.

206.   Li, L. P.; Zhang, R. P.; Lu, C. X.; Sun, J. H.; Wang, L. J.; Qu, B. T.; Li, T. T.; Liu, Y. D.; Li, S. J., In situ synthesis of NIR-light emitting carbon dots derived from spinach for bio-imaging applications. *Journal of Materials Chemistry B* **2017,** *5* (35), 7328-7334.

207.   Bhunia, S. K.; Saha, A.; Maity, A. R.; Ray, S. C.; Jana, N. R., Carbon Nanoparticle-based Fluorescent Bioimaging Probes. *Scientific Reports* **2013,** *3*.

208.   Wang, H.; Mukherjee, S.; Ji, J. H.; Banerjee, P.; Chen, Q. W.; Zhou, S. Q., Biocompatible Chitosan-Carbon Dot Hybrid Nanogels for NIR-Imaging-Guided Synergistic Photothermal-Chemo Therapy. *Acs Applied Materials & Interfaces* **2017,** *9* (22), 18639-18649.

209.   Wang, H.; Wang, K.; Tian, B.; Revia, R.; Mu, Q. X.; Jeon, M.; Chang, F. C.; Zhang, M. Q., Preloading of Hydrophobic Anticancer Drug into Multifunctional Nanocarrier for Multimodal Imaging, NIR-Responsive Drug Release, and Synergistic Therapy. *Small* **2016,** *12* (46), 6388-6397.

210.   Li, D.; Jing, P. T.; Sun, L. H.; An, Y.; Shan, X. Y.; Lu, X. H.; Zhou, D.; Han, D.; Shen, D. Z.; Zhai, Y. C.; Qu, S. N.; Zboril, R.; Rogach, A. L., Near-Infrared Excitation/Emission and Multiphoton-Induced Fluorescence of Carbon Dots. *Advanced Materials* **2018,** *30* (13).

211.   Luo, P. J. G.; Yang, F.; Yang, S. T.; Sonkar, S. K.; Yang, L. J.; Broglie, J. J.; Liu, Y.; Sun, Y. P., Carbon-based quantum dots for fluorescence imaging of cells and tissues. *Rsc Advances* **2014,** *4* (21), 10791-10807.

212.   Fahrenkrog, B.; Aebi, U., The nuclear pore complex: Nucleocytoplasmic transport and beyond. *Nature Reviews Molecular Cell Biology* **2003,** *4* (10), 757-766.

213.   Alam, A. M.; Park, B. Y.; Ghouri, Z. K.; Park, M.; Kim, H. Y., Synthesis of carbon quantum dots from cabbage with down- and up-conversion photoluminescence properties: excellent imaging agent for biomedical applications. *Green Chemistry* **2015,** *17* (7), 3791-3797.

214.   Wang, W. J.; Xia, J. M.; Feng, J.; He, M. Q.; Chen, M. L.; Wang, J. H., Green preparation of carbon dots for intracellular pH sensing and multicolor live cell imaging. *Journal of Materials Chemistry B* **2016,** *4* (44), 7130-7137.

215.   Marin, M. J.; Galindo, F.; Thomas, P.; Russell, D. A., Localized Intracellular pH Measurement Using a Ratiometric Photoinduced Electron-Transfer-Based Nanosensor. *Angewandte Chemie-International Edition* **2012,** *51* (38), 9657-9661.

216.   Kumawat, M. K.; Thakur, M.; Gurung, R. B.; Srivastava, R., Graphene Quantum Dots from Mangifera indica: Application in Near Infrared Bioimaging and Intracellular Nanothermometry. *Acs Sustainable Chemistry & Engineering* **2017,** *5* (2), 1382-1391.

217.   Datta, K. K. R.; Kozak, O.; Ranc, V.; Havrdova, M.; Bourlinos, A. B.; Safarova, K.; Hola, K.; Tomankova, K.; Zoppellaro, G.; Otyepka, M.; Zboril, R., Quaternized carbon dot-modified graphene oxide for selective cell labelling - controlled nucleus and cytoplasm imaging. *Chemical Communications* **2014,** *50* (74), 10782-10785.

218.   Kumawat, M. K.; Thakur, M.; Gurung, R. B.; Srivastava, R., Graphene Quantum Dots for Cell Proliferation, Nucleus Imaging, and Photoluminescent Sensing Applications. *Scientific Reports* **2017,** *7*.

219.   Wang, R.; Zhang, F., NIR luminescent nanomaterials for biomedical imaging. *Journal of Materials Chemistry B* **2014,** *2* (17), 2422-2443.

220.   Hola, K.; Zhang, Y.; Wang, Y.; Giannelis, E. P.; Zboril, R.; Rogach, A. L., Carbon dots-Emerging light emitters for bioimaging, cancer therapy and optoelectronics. *Nano Today* **2014,** *9* (5), 590-603.

221.   Kim, H.; Park, Y.; Beack, S.; Han, S.; Jung, D.; Cha, H. J.; Kwon, W.; Hahn, S. K., Dual-Color-Emitting Carbon Nanodots for Multicolor Bioimaging and Optogenetic Control of Ion Channels. *Advanced Science* **2017,** *4* (11).

222.   Anselmo, A. C.; Gupta, V.; Zern, B. J.; Pan, D.; Zakrewsky, M.; Muzykantov, V.; Mitragotri, S., Delivering Nanoparticles to Lungs while Avoiding Liver and Spleen through Adsorption on Red Blood Cells. *Acs Nano* **2013,** *7* (12), 11129-11137.

223. Yang, W. N.; Zhang, H.; Lai, J. X.; Peng, X. Y.; Hu, Y. P.; Gu, W.; Ye, L., Carbon dots with red-shifted photoluminescence by fluorine doping for optical bio-imaging. *Carbon* **2018,** *128*, 78-85.

224. Chatterjee, D. K.; Fong, L. S.; Zhang, Y., Nanoparticles in photodynamic therapy: An emerging paradigm. *Advanced Drug Delivery Reviews* **2008,** *60* (15), 1627-1637.

225. Voon, S. H.; Kiew, L. V.; Lee, H. B.; Lim, S. H.; Noordin, M. I.; Kamkaew, A.; Burgess, K.; Chung, L. Y., In Vivo Studies of Nanostructure-Based Photosensitizers for Photodynamic Cancer Therapy. *Small* **2014,** *10* (24), 4993-5013.

226. Dolmans, D.; Fukumura, D.; Jain, R. K., Photodynamic therapy for cancer. *Nature Reviews Cancer* **2003,** *3* (5), 380-387.

227. Agostinis, P.; Berg, K.; Cengel, K. A.; Foster, T. H.; Girotti, A. W.; Gollnick, S. O.; Hahn, S. M.; Hamblin, M. R.; Juzeniene, A.; Kessel, D.; Korbelik, M.; Moan, J.; Mroz, P.; Nowis, D.; Piette, J.; Wilson, B. C.; Golab, J., Photodynamic Therapy of Cancer: An Update. *Ca-a Cancer Journal for Clinicians* **2011,** *61* (4), 250-281.

228. Celli, J. P.; Spring, B. Q.; Rizvi, I.; Evans, C. L.; Samkoe, K. S.; Verma, S.; Pogue, B. W.; Hasan, T., Imaging and Photodynamic Therapy: Mechanisms, Monitoring, and Optimization. *Chemical Reviews* **2010,** *110* (5), 2795-2838.

229. Hatz, S.; Lambert, J. D. C.; Ogilby, P. R., Measuring the lifetime of singlet oxygen in a single cell: addressing the issue of cell viability. *Photochemical & Photobiological Sciences* **2007,** *6* (10), 1106-1116.

230. Buytaert, E.; Dewaele, M.; Agostinis, P., Molecular effectors of multiple cell death pathways initiated by photodynamic therapy. *Biochimica Et Biophysica Acta-Reviews on Cancer* **2007,** *1776* (1), 86-107.

231. Ye, R. R.; Tan, C. P.; He, L.; Chen, M. H.; Ji, L. N.; Mao, Z. W., Cyclometalated Ir(III) complexes as targeted theranostic anticancer therapeutics: combining HDAC inhibition with photodynamic therapy. *Chemical Communications* **2014,** *50* (75), 10945-10948.

232. Zhang, D. Y.; Zheng, Y.; Zhang, H.; He, L.; Tan, C. P.; Sun, J. H.; Zhang, W.; Peng, X. Y.; Zhan, Q. Q.; Ji, L. N.; Mao, Z. W., Ruthenium complex-modified carbon nanodots for lysosome-targeted one- and two-photon imaging and photodynamic therapy. *Nanoscale* **2017,** *9* (47), 18966-18976.

233. Zhang, D. Y.; Zheng, Y.; Tan, C. P.; Sun, J. H.; Zhang, W.; Ji, L. N.; Mao, Z. W., Graphene Oxide Decorated with Ru(II)-Polyethylene Glycol Complex for Lysosome-Targeted Imaging and Photodynamic/Photothermal Therapy. *Acs Applied Materials & Interfaces* **2017,** *9* (8), 6761-6771.

234. Green, D. R.; Reed, J. C., Mitochondria and apoptosis. *Science* **1998,** *281* (5381), 1309-1312.

235. Zhang, P.; Steelant, W.; Kumar, M.; Scholfield, M., Versatile photosensitizers for photodynamic therapy at infrared excitation. *Journal of the American Chemical Society* **2007,** *129* (15), 4526-+.

236.   Fan, J. X.; Liu, M. D.; Li, C. X.; Hong, S.; Zheng, D. W.; Liu, X. H.; Chen, S.; Cheng, H.; Zhang, X. Z., A metal-semiconductor nanocomposite as an efficient oxygen-independent photosensitizer for photodynamic tumor therapy. *Nanoscale Horizons* **2017,** *2* (6), 349-355.

237.   Yang, G. B.; Xu, L. G.; Chao, Y.; Xu, J.; Sun, X. Q.; Wu, Y. F.; Peng, R.; Liu, Z., Hollow MnO2 as a tumor-microenvironment-responsive biodegradable nano-platform for combination therapy favoring antitumor immune responses. *Nature Communications* **2017,** *8*, 13.

238.   Guo, W.; Wang, F.; Ding, D. D.; Song, C. Q.; Guo, C. S.; Liu, S. Q., TiO2-x Based Nanoplatform for Bimodal Cancer Imaging and NIR-Triggered Chem/Photodynamic/Photothermal Combination Therapy. *Chemistry of Materials* **2017,** *29* (21), 9262-9274.

239.   Deng, K. R.; Li, C. X.; Huang, S. S.; Xing, B. G.; Jin, D. Y.; Zeng, Q. G.; Hou, Z. Y.; Lin, J., Recent Progress in Near Infrared Light Triggered Photodynamic Therapy. *Small* **2017,** *13* (44), 27.

240.   Zhou, Z. J.; Song, J. B.; Nie, L. M.; Chen, X. Y., Reactive oxygen species generating systems meeting challenges of photodynamic cancer therapy. *Chemical Society Reviews* **2016,** *45* (23), 6597-6626.

241.   Ethirajan, M.; Chen, Y. H.; Joshi, P.; Pandey, R. K., The role of porphyrin chemistry in tumor imaging and photodynamic therapy. *Chemical Society Reviews* **2011,** *40* (1), 340-362.

242.   Li, X.; Yu, S.; Lee, D.; Kim, G.; Lee, B.; Cho, Y.; Zheng, B. Y.; Ke, M. R.; Huang, J. D.; Nam, K. T.; Chen, X. Y.; Yoon, J., Facile Supramolecular Approach to Nucleic-Acid-Driven Activatable Nanotheranostics That Overcome Drawbacks of Photodynamic Therapy. *Acs Nano* **2018,** *12* (1), 681-688.

243.   Zhang, R. Y.; Xing, R. R.; Jiao, T. F.; Ma, K.; Chen, C. J.; Ma, G. H.; Yan, X. H., Carrier-Free, Chemophotodynamic Dual Nanodrugs via Self-Assembly for Synergistic Antitumor Therapy. *Acs Applied Materials & Interfaces* **2016,** *8* (21), 13262-13269.

244.   Chen, Q.; Huang, Z.; Chen, H.; Shapiro, H.; Beckers, J.; Hetzel, F. W., Improvement of tumor response by manipulation of tumor oxygenation during photodynamic therapy. *Photochemistry and Photobiology* **2002,** *76* (2), 197-203.

245.   Cheng, Y. H.; Cheng, H.; Jiang, C. X.; Qiu, X. F.; Wang, K. K.; Huan, W.; Yuan, A.; Wu, J. H.; Hu, Y. Q., Perfluorocarbon nanoparticles enhance reactive oxygen levels and tumour growth inhibition in photodynamic therapy. *Nature Communications* **2015,** *6*.

246.   He, D. G.; Hai, L.; He, X.; Yang, X.; Li, H. W., Glutathione-Activatable and O-2/Mn2+-Evolving Nanocomposite for Highly Efficient and Selective Photodynamic and Gene-Silencing Dual Therapy. *Advanced Functional Materials* **2017,** *27* (46), 12.

247.   Idris, N. M.; Gnanasammandhan, M. K.; Zhang, J.; Ho, P. C.; Mahendran, R.; Zhang, Y., In vivo photodynamic therapy using upconversion nanoparticles as remote-controlled nanotransducers. *Nature Medicine* **2012,** *18* (10), 1580-U190.

248. Zhao, T. T.; Yu, K.; Li, L.; Zhang, T. S.; Guan, Z. P.; Gao, N. Y.; Yuan, P. Y.; Li, S.; Yao, S. Q.; Xu, Q. H.; Xu, G. Q., Gold Nanorod Enhanced Two-Photon Excitation Fluorescence of Photosensitizers for Two-Photon Imaging and Photodynamic Therapy. *Acs Applied Materials & Interfaces* **2014,** *6* (4), 2700-2708.

249. Fan, Y. Y.; Liu, H. L.; Han, R. C.; Huang, L.; Shi, H.; Sha, Y. L.; Jiang, Y. Q., Extremely High Brightness from Polymer-Encapsulated Quantum Dots for Two-photon Cellular and Deep-tissue Imaging. *Scientific Reports* **2015,** *5*.

250. Ortega-Liebana, M. C.; Hueso, J. L.; Arenal, R.; Santamaria, J., Titania-coated gold nanorods with expanded photocatalytic response. Enzyme-like glucose oxidation under near-infrared-illumination. *Nanoscale* **2017,** *9* (5), 1787-1792.

251. Zhang, F.; Zhang, M.; Zheng, X.; Tao, S. Y.; Zhang, Z. Q.; Sun, M. D.; Song, Y. B.; Zhang, J.; Shao, D.; He, K.; Li, J.; Yang, B.; Chen, L., Berberine-based carbon dots for selective and safe cancer theranostics. *Rsc Advances* **2018,** *8* (3), 1168-1173.

252. Huang, P.; Lin, J.; Wang, X. S.; Wang, Z.; Zhang, C. L.; He, M.; Wang, K.; Chen, F.; Li, Z. M.; Shen, G. X.; Cui, D. X.; Chen, X. Y., Light-Triggered Theranostics Based on Photosensitizer-Conjugated Carbon Dots for Simultaneous Enhanced-Fluorescence Imaging and Photodynamic Therapy. *Advanced Materials* **2012,** *24* (37), 5104-5110.

253. Ge, J. C.; Lan, M. H.; Zhou, B. J.; Liu, W. M.; Guo, L.; Wang, H.; Jia, Q. Y.; Niu, G. L.; Huang, X.; Zhou, H. Y.; Meng, X. M.; Wang, P. F.; Lee, C. S.; Zhang, W. J.; Han, X. D., A graphene quantum dot photodynamic therapy agent with high singlet oxygen generation. *Nature Communications* **2014,** *5*.

254. Wang, J.; Zhang, Z. H.; Zha, S.; Zhu, Y. Y.; Wu, P. Y.; Ehrenberg, B.; Chen, J. Y., Carbon nanodots featuring efficient FRET for two-photon photodynamic cancer therapy with a low fs laser power density. *Biomaterials* **2014,** *35* (34), 9372-9381.

255. Zheng, D. W.; Li, B.; Li, C. X.; Fan, J. X.; Lei, Q.; Li, C.; Xu, Z. S.; Zhang, X. Z., Carbon-Dot-Decorated Carbon Nitride Nanoparticles for Enhanced Photodynamic Therapy against Hypoxic Tumor via Water Splitting. *Acs Nano* **2016,** *10* (9), 8715-8722.

256. Jia, Q. Y.; Ge, J. C.; Liu, W. M.; Zheng, X. L.; Chen, S. Q.; Wen, Y. M.; Zhang, H. Y.; Wang, P. F., A Magnetofluorescent Carbon Dot Assembly as an Acidic H2O2-Driven Oxygenerator to Regulate Tumor Hypoxia for Simultaneous Bimodal Imaging and Enhanced Photodynamic Therapy. *Advanced Materials* **2018,** *30* (13).

257. Kim, H. N.; Ren, W. X.; Kim, J. S.; Yoon, J., Fluorescent and colorimetric sensors for detection of lead, cadmium, and mercury ions. *Chemical Society Reviews* **2012,** *41* (8), 3210-3244.

258. Arora, M.; Kiran, B.; Rani, S.; Rani, A.; Kaur, B.; Mittal, N., Heavy metal accumulation in vegetables irrigated with water from different sources. *Food Chemistry* **2008,** *111* (4), 811-815.

259. Smith, D. G.; Topolnicki, I. L.; Zwicker, V. E.; Jolliffe, K. A.; New, E. J., . Fluorescent sensing arrays for cations and anions. *Analyst* **2017,** *142* (19), 3549-3563.

260.   Ullah, N.;   Mansha, M.;   Khan, I.; Qurashi, A., Nanomaterial-based optical chemical sensors for the detection of heavy metals in water: Recent advances and challenges. *Trac-Trends in Analytical Chemistry* **2018,** *100,* 155-166.

261.   Li, M.;   Gou, H. L.;   Al-Ogaidi, I.; Wu, N. Q., Nanostructured Sensors for Detection of Heavy Metals: A Review. *Acs Sustainable Chemistry & Engineering* **2013,** *1* (7), 713-723.

262.   Liu, Y.;   Liu, C. Y.; Zhang, Z. Y., Synthesis of highly luminescent graphitized carbon dots and the application in the Hg2+ detection. *Applied Surface Science* **2012,** *263,* 481-485.

263.   Liu, J. Y.;   Lv, G. C.;   Gu, W. L.;   Li, Z. H.;   Tang, A. W.; Mei, L. F., A novel luminescence probe based on layered double hydroxides loaded with quantum dots for simultaneous detection of heavy metal ions in water. *Journal of Materials Chemistry C* **2017,** *5* (20), 5024-5030.

264.   Xie, J. P.;   Zheng, Y. G.; Ying, J. Y., Highly selective and ultrasensitive detection of Hg2+ based on fluorescence quenching of Au nanoclusters by Hg2+-Au+ interactions. *Chemical Communications* **2010,** *46* (6), 961-963.

265.   Iqbal, A.;   Tian, Y. J.;   Wang, X. D.;   Gong, D. Y.;   Guo, Y. L.;   Iqbal, K.;   Wang, Z. P.; Liu, W. S.; Qin, W. W., Carbon dots prepared by solid state method via citric acid and 1,10-phenanthroline for selective and sensing detection of Fe2+ and Fe3+. *Sensors and Actuators B-Chemical* **2016,** *237,* 408-415.

266.   Gedda, G.;   Lee, C. Y.;   Lin, Y. C.; Wu, H. F., Green synthesis of carbon dots from prawn shells for highly selective and sensitive detection of copper ions. *Sensors and Actuators B-Chemical* **2016,** *224,* 396-403.

267.   Bandi, R.;   Gangapuram, B. R.;   Dadigala, R.;   Eslavath, R.;   Singh, S. S.; Guttena, V., Facile and green synthesis of fluorescent carbon dots from onion waste and their potential applications as sensor and multicolour imaging agents. *Rsc Advances* **2016,** *6* (34), 28633-28639.

268.   Escudero, D., Revising Intramolecular Photoinduced Electron Transfer (PET) from First-Principles. *Accounts of Chemical Research* **2016,** *49* (9), 1816-1824.

269.   Miura, T.;   Urano, Y.;   Tanaka, K.;   Nagano, T.;   Ohkubo, K.; Fukuzumi, S., Rational design principle for modulating fluorescence properties of fluorescein-based probes by photoinduced electron transfer. *Journal of the American Chemical Society* **2003,** *125* (28), 8666-8671.

270.   Vlcek, A.;   Kvapilova, H.;   Towrie, M.; Zalis, S., Electron-Transfer Acceleration Investigated by Time Resolved Infrared Spectroscopy. *Accounts of Chemical Research* **2015,** *48* (3), 868-876.

271.   Kumar, A.;   Chowdhuri, A. R.;   Laha, D.;   Mahto, T. K.;   Karmakar, P.; Sahu, S. K., Green synthesis of carbon dots from Ocimum sanctum for effective fluorescent sensing of Pb2+ ions and live cell imaging. *Sensors and Actuators B-Chemical* **2017,** *242,* 679-686.

272.   Chen, Y. M.; Shang, P. X.; Dong, Y. Q.; Chi, Y. W., Regulating the overlap between the absorption spectrum of metal ion-chromogenic agent and the emission spectrum of carbon-based dots to improve the sensing performance for metal ions. *Sensors and Actuators B-Chemical* **2017,** *242*, 1210-1215.

273.   Chen, J.; Li, Y.; Lv, K.; Zhong, W.; Wang, H.; Wu, Z.; Yi, P.; Jiang, J., Cyclam-functionalized carbon dots sensor for sensitive and selective detection of copper(II) ion and sulfide anion in aqueous media and its imaging in live cells. *Sensors and Actuators B-Chemical* **2016,** *224*, 298-306.

274.   Zhang, R. Z.; Chen, W., Nitrogen-doped carbon quantum dots: Facile synthesis and application as a "turn-off' fluorescent probe for detection of Hg2+ ions. *Biosensors & Bioelectronics* **2014,** *55*, 83-90.

275.   Pu, F.; Huang, Z. Z.; Ren, J. S.; Qu, X. G., DNA/Ligand/Ion-Based Ensemble for Fluorescence Turn on Detection of Cysteine and Histidine with Tunable Dynamic Range. *Analytical Chemistry* **2010,** *82* (19), 8211-8216.

276.   Zhou, L.; Lin, Y. H.; Huang, Z. Z.; Ren, J. S.; Qu, X. G., Carbon nanodots as fluorescence probes for rapid, sensitive, and label-free detection of Hg2+ and biothiols in complex matrices. *Chemical Communications* **2012,** *48* (8), 1147-1149.

277.   Dong, Y. Q.; Wang, R. X.; Li, G. L.; Chen, C. Q.; Chi, Y. W.; Chen, G. N., Polyamine-Functionalized Carbon Quantum Dots as Fluorescent Probes for Selective and Sensitive Detection of Copper Ions. *Analytical Chemistry* **2012,** *84* (14), 6220-6224.

278.   Salinas-Castillo, A.; Ariza-Avidad, M.; Pritz, C.; Camprubi-Robles, M.; Fernandez, B.; Ruedas-Rama, M. J.; Megia-Fernandez, A.; Lapresta-Fernandez, A.; Santoyo-Gonzalez, F.; Schrott-Fischer, A.; Capitan-Vallvey, L. F., Carbon dots for copper detection with down and upconversion fluorescent properties as excitation sources. *Chemical Communications* **2013,** *49* (11), 1103-1105.

279.   Chen, J. C.; Liu, J. H.; Li, J. Z.; Xu, L. Q.; Qiao, Y. J., One-pot synthesis of nitrogen and sulfur co-doped carbon dots and its application for sensor and multicolor cellular imaging. *Journal of Colloid and Interface Science* **2017,** *485*, 167-174.

280.   Wen, X. P.; Shi, L. H.; Wen, G. M.; Li, Y. Y.; Dong, C.; Yang, J.; Shuang, S. M., Green and facile synthesis of nitrogen-doped carbon nanodots for multicolor cellular imaging and Co2+ sensing in living cells. *Sensors and Actuators B-Chemical* **2016,** *235*, 179-187.

281.   Wang, Z.; Xu, C.; Lu, Y. X.; Chen, X.; Yuan, H. T.; Wei, G. Y.; Ye, G.; Chen, J., Fluorescence sensor array based on amino acid derived carbon dots for pattern-based detection of toxic metal ions. *Sensors and Actuators B-Chemical* **2017,** *241*, 1324-1330.

282.   Varma, R. S., Journey on greener pathways: from the use of alternate energy inputs and benign reaction media to sustainable applications of nano-catalysts in synthesis and environmental remediation. *Green Chemistry* **2014,** *16* (4), 2027-2041.

283.   Narayanan, R.; Tabor, C.; El-Sayed, M. A., Can the observed changes in the size or shape of a colloidal nanocatalyst reveal the nanocatalysis mechanism type: Homogeneous or heterogeneous? *Topics in Catalysis* **2008,** *48* (1-4), 60-74.

284.   Chen, C. C.; Ma, W. H.; Zhao, J. C., Semiconductor-mediated photodegradation of pollutants under visible-light irradiation. *Chemical Society Reviews* **2010,** *39* (11), 4206-4219.

285.   Kong, X. Y.; Tan, W. L.; Ng, B. J.; Chai, S. P.; Mohamed, A. R., Harnessing Vis-NIR broad spectrum for photocatalytic CO2 reduction over carbon quantum dots-decorated ultrathin Bi2WO6 nanosheets. *Nano Research* **2017,** *10* (5), 1720-1731.

286.   Huang, Y.; Liang, Y. L.; Rao, Y. F.; Zhu, D. D.; Cao, J. J.; Shen, Z. X.; Ho, W. K.; Lee, S. C., Environment-Friendly Carbon Quantum Dots/ZnFe2O4 Photocatalysts: Characterization, Biocompatibility, and Mechanisms for NO Removal. *Environmental Science & Technology* **2017,** *51* (5), 2924-2933.

287.   Malato, S.; Fernandez-Ibanez, P.; Maldonado, M. I.; Blanco, J.; Gernjak, W., Decontamination and disinfection of water by solar photocatalysis: Recent overview and trends. *Catalysis Today* **2009,** *147* (1), 1-59.

288.   Oturan, M. A.; Aaron, J. J., Advanced Oxidation Processes in Water/Wastewater Treatment: Principles and Applications. A Review. *Critical Reviews in Environmental Science and Technology* **2014,** *44* (23), 2577-2641.

289.   Kudo, A.; Miseki, Y., Heterogeneous photocatalyst materials for water splitting. *Chemical Society Reviews* **2009,** *38* (1), 253-278.

290.   Xie, S. J.;   Zhang, Q. H.;   Liu, G. D.; Wang, Y., Photocatalytic and photoelectrocatalytic reduction of CO2 using heterogeneous catalysts with controlled nanostructures. *Chemical Communications* **2016,** *52* (1), 35-59.

291.   Zhang, H. C.; Ming, H.; Lian, S. Y.; Huang, H.; Li, H. T.; Zhang, L. L.; Liu, Y.; Kang, Z. H.; Lee, S. T., Fe2O3/carbon quantum dots complex photocatalysts and their enhanced photocatalytic activity under visible light. *Dalton Transactions* **2011,** *40* (41), 10822-10825.

292.   Di, J.; Xia, J. X.; Ji, M. X.; Wang, B.; Yin, S.; Zhang, Q.; Chen, Z. G.; Li, H. M., Carbon Quantum Dots Modified BiOCl Ultrathin Nanosheets with Enhanced Molecular Oxygen Activation Ability for Broad Spectrum Photocatalytic Properties and Mechanism Insight. *Acs Applied Materials & Interfaces* **2015,** *7* (36), 20111-20123.

293.   Di, J.; Xia, J. X.; Ji, M. X.; Li, H. P.; Xu, H.; Li, H. M.; Chen, R., The synergistic role of carbon quantum dots for the improved photocatalytic performance of Bi2MoO6. *Nanoscale* **2015,** *7* (26), 11433-11443.

294.   Chai, N. N.; Wang, H. X.; Hu, C. X.; Wang, Q.; Zhang, H. L., Well-controlled layer-by-layer assembly of carbon dot/CdS heterojunctions for efficient visible-light-driven photocatalysis. *Journal of Materials Chemistry A* **2015,** *3* (32), 16613-16620.

295.   Cao, L.; Sahu, S.; Anilkumar, P.; Bunker, C. E.; Xu, J. A.; Fernando, K. A. S.; Wang, P.; Guliants, E. A.; Tackett, K. N.; Sun, Y. P., Carbon Nanoparticles as Visible-Light Photocatalysts for Efficient CO2 Conversion and Beyond. *Journal of the American Chemical Society* **2011,** *133* (13), 4754-4757.

296.   Martindale, B. C. M.; Hutton, G. A. M.; Caputo, C. A.; Reisner, E., Solar Hydrogen Production Using Carbon Quantum Dots and a Molecular Nickel Catalyst. *Journal of the American Chemical Society* **2015,** *137* (18), 6018-6025.

297.   Guo, Y.; Yao, P. J.; Zhu, D. Q.; Gu, C., A novel method for the development of a carbon quantum dot/carbon nitride hybrid photocatalyst that responds to infrared light irradiation. *Journal of Materials Chemistry A* **2015,** *3* (25), 13189-13192.

298.   Zhao, Z. F.; Butburee, T.; Peerakiatkhajohn, P.; Lyu, M. Q.; Wang, S. C.; Wang, L. Z.; Zheng, H. J., Carbon Quantum Dots sensitized Vertical WO3 Nanoplates with Enhanced Photoelectrochemical Properties. *Chemistryselect* **2016,** *1* (11), 2772-2777.

299.   Pan, J. Q.; Sheng, Y. Z.; Zhang, J. X.; Wei, J. M.; Huang, P.; Zhang, X.; Feng, B. X., Preparation of carbon quantum dots/TiO2 nanotubes composites and their visible light catalytic applications. *Journal of Materials Chemistry A* **2014,** *2* (42), 18082-18086.

300.   Wang, W. S.; Wang, D. H.; Qu, W. G.; Lu, L. Q.; Xu, A. W., Large Ultrathin Anatase TiO2 Nanosheets with Exposed {001} Facets on Graphene for Enhanced Visible Light Photocatalytic Activity. *Journal of Physical Chemistry C* **2012,** *116* (37), 19893-19901.

301.   Li, H. T.; Liu, R. H.; Lian, S. Y.; Liu, Y.; Huang, H.; Kang, Z. H., Near-infrared light controlled photocatalytic activity of carbon quantum dots for highly selective oxidation reaction. *Nanoscale* **2013,** *5* (8), 3289-3297.

302.   Sharma, R.; Bansal, S.; Singhal, S., Tailoring the photo-Fenton activity of spinel ferrites (MFe2O4) by incorporating different cations (M = Cu, Zn, Ni and Co) in the structure. *Rsc Advances* **2015,** *5* (8), 6006-6018.

303.   Sakthivel, S.; Kisch, H., Daylight photocatalysis by carbon-modified titanium dioxide. *Angewandte Chemie-International Edition* **2003,** *42* (40), 4908-4911.

304.   Pelaez, M.; Baruwati, B.; Varma, R. S.; Luque, R.; Dionysiou, D. D., Microcystin-LR removal from aqueous solutions using a magnetically separable N-doped TiO2 nanocomposite under visible light irradiation. *Chemical Communications* **2013,** *49* (86), 10118-10120.

305.   Furube, A.; Du, L.; Hara, K.; Katoh, R.; Tachiya, M., Ultrafast plasmon-induced electron transfer from gold nanodots into TiO2 nanoparticles. *Journal of the American Chemical Society* **2007,** *129* (48), 14852-+.

306.   Lu, Z. Y.; Yu, Z. H.; Dong, J. B.; Song, M. S.; Liu, Y.; Liu, X. L.; Ma, Z. F.; Su, H.; Yan, Y. S.; Huo, P. W., Facile microwave synthesis of a Z-scheme imprinted ZnFe2O4/Ag/PEDOT with the specific recognition ability towards improving photocatalytic activity and selectivity for tetracycline. *Chemical Engineering Journal* **2018,** *337*, 228-241.

307.   Guo, J. J.; Wang, K.; Wang, X. T., Photocatalytic reduction of CO2 with H2O vapor under visible light over Ce doped ZnFe2O4. *Catalysis Science & Technology* **2017,** *7* (4), 6013-6025.

308.   Devi, L. G.; Kumar, S. G., Exploring the critical dependence of adsorption of various dyes on the degradation rate using Ln(3+)-TiO2 surface under UV/solar light. *Applied Surface Science* **2012,** *261*, 137-146.

309.   Liu, L.; Chen, X. B., Titanium Dioxide Nanomaterials: Self-Structural Modifications. *Chemical Reviews* **2014,** *114* (19), 9890-9918.

310.   Kocher, J.; Kumar, A.; Priya, S.; Kumar, J., Nickel-induced structural, optical, magnetic, and electrical behavior of alpha-Fe2O3. *Physica Status Solidi B-Basic Solid State Physics* **2014,** *251* (8), 1552-1557.

311.   Bai, L. J.; Jiang, W. Y.; Gao, C. X.; Zhong, S. X.; Zhao, L. H.; Li, Z. Q.; Bai, S., Facet engineered interface design of NaYF4:Yb, Tm upconversion nanocrystals on BiOCl nanoplates for enhanced near-infrared photocatalysis. *Nanoscale* **2016,** *8* (45), 19014-19024.

312.   Tian, Q. Y.; Yao, W. J.; Wu, Z. H.; Liu, J.; Liu, L.; Wu, W.; Jiang, C. Z., Full-spectrum-activated Z-scheme photocatalysts based on NaYF4:Yb3+/Er3+, TiO2 and Ag6Si2O7. *Journal of Materials Chemistry A* **2017,** *5* (45), 23566-23576.

313.   Li, L.; Zhang, M. Y.; Zhao, Z. Y.; Sun, B. D.; Zhang, X. T., Visible/near-IR-light-driven TNFePc/BiOCl organic-inorganic heterostructures with enhanced photocatalytic activity. *Dalton Transactions* **2016,** *45* (23), 9497-9505.

314.   Gao, W. W.; Liu, W. X.; Leng, Y. H.; Wang, X. W.; Wang, X. Q.; Hu, B.; Yu, D. H.; Sang, Y. H.; Liu, H., In2S3 nanomaterial as a broadband spectrum photocatalyst to display significant activity. *Applied Catalysis B-Environmental* **2015,** *176*, 83-90.

315.   Yu, H. J.; Zhao, Y. F.; Zhou, C.; Shang, L.; Peng, Y.; Cao, Y. H.; Wu, L. Z.; Tung, C. H.; Zhang, T. R., Carbon quantum dots/TiO2 composites for efficient photocatalytic hydrogen evolution. *Journal of Materials Chemistry A* **2014,** *2* (10), 3344-3351.

316.   Zhang, J.; Tang, Y. L.; Hu, G.; Gao, B. L.; Gan, Z. X.; Chu, P. K., Carbon nanodots-based nanocomposites with enhanced photocatalytic performance and photothermal effects. *Applied Physics Letters* **2017,** *111* (1), 5.

317.   Markad, G. B.; Kapoor, S.; Haram, S. K.; Thakur, P., Metal free, carbon-TiO2 based composites for the visible light photocatalysis. *Solar Energy* **2017,** *144*, 127-133.

318.   Cheng, C.; Lu, D.; Shen, B.; Liu, Y. D.; Lei, J. Y.; Wang, L. Z.; Zhang, J. L.; Matsuoka, M., Mesoporous silica-based carbon dot/TiO2 photocatalyst for efficient organic pollutant degradation. *Microporous and Mesoporous Materials* **2016,** *226*, 79-87.

319.   Sun, M.; Ma, X.; Chen, X.; Sun, Y.; Cui, X.; Lin, Y., A nanocomposite of carbon quantum dots and TiO2 nanotube arrays: enhancing photoelectrochemical and photocatalytic properties. *Rsc Advances* **2014,** *4* (3), 1120-1127.

320.   Zhang, Y.-Q.; Ma, D.-K.; Zhang, Y.-G.; Chen, W.; Huang, S.-M., N-doped carbon quantum dots for TiO2-based photocatalysts and dye-sensitized solar cells. *Nano Energy* **2013,** *2* (5), 545-552.

321.   Kim, Y. K.; Kang, E. B.; Kim, S. H.; Sharker, S. M.; Kong, B. Y.; In, I.; Lee, K. D.; Park, S. Y., Visible-Light-Driven Photocatalysts of Perfluorinated Silica-Based

Fluorescent Carbon Dot/TiO2 for Tunable Hydrophilic-Hydrophobic Surfaces. *Acs Applied Materials & Interfaces* **2016,** *8* (43), 29827-29834.

322. Wang, Q.; Zhu, N. X.; Liu, E. G.; Zhang, C. L.; Crittenden, J. C.; Zhang, Y.; Cong, Y. Q., Fabrication of visible-light active Fe2O3-GQDs/NF-TiO2 composite film with highly enhanced photoelectrocatalytic performance. *Applied Catalysis B-Environmental* **2017,** *205*, 347-356.

323. Miao, R.; Luo, Z.; Zhong, W.; Chen, S. Y.; Jiang, T.; Dutta, B.; Nasr, Y.; Zhang, Y. S.; Suib, S. L., Mesoporous TiO2 modified with carbon quantum dots as a high-performance visible light photocatalyst. *Applied Catalysis B-Environmental* **2016,** *189*, 26-38.

324. Ke, J.; Li, X. Y.; Zhao, Q. D.; Liu, B. J.; Liu, S. M.; Wang, S. B., Upconversion carbon quantum dots as visible light responsive component for efficient enhancement of photocatalytic performance. *Journal of Colloid and Interface Science* **2017,** *496*, 425-433.

325. Gligorovski, S.; Strekowski, R.; Barbati, S.; Vione, D., Environmental Implications of Hydroxyl Radicals (center dot OH). *Chemical Reviews* **2015,** *115* (24), 13051-13092.

326. Su, M. H.; He, C.; Sharma, V. K.; Abou Asi, M.; Xia, D.; Li, X. Z.; Deng, H. Q.; Xiong, Y., Mesoporous zinc ferrite: Synthesis, characterization, and photocatalytic activity with H2O2/visible light. *Journal of Hazardous Materials* **2012,** *211*, 95-103.

327. Chandra, S.; Chowdhuri, A. R.; Mahto, T. K.; Sahu, S. K., Nanostructured Fe3O4@Fe2O3/Carbon Dots Heterojunction for Efficient Photocatalyst Under Visible Light. *Journal of Nanoscience and Nanotechnology* **2017,** *17* (2), 1116-1124.

328. Chen, H. B.; Liu, W. X.; Qin, Z. Z., ZnO/ZnFe2O4 nanocomposite as a broadspectrum photo-Fenton-like photocatalyst with near-infrared activity. *Catalysis Science & Technology* **2017,** *7* (11), 2236-2244.

329. Reedy, C. J.; Gibney, B. R., Heme protein assemblies. *Chemical Reviews* **2004,** *104* (2), 617-649.

330. Li, M. L.; Liu, L.; Shi, Y.; Yang, Y. F.; Zheng, H. Z.; Long, Y. J., Dichlorofluorescein as a peroxidase mimic and its application to glucose detection. *New Journal of Chemistry* **2017,** *41* (15), 7578-7582.

331. Garg, B.; Bisht, T., Carbon Nanodots as Peroxidase Nanozymes for Biosensing. *Molecules* **2016,** *21* (12).

332. Wei, H.; Wang, E. K., Nanomaterials with enzyme-like characteristics (nanozymes): next-generation artificial enzymes. *Chemical Society Reviews* **2013,** *42* (14), 6060-6093.

333. Liu, L.; Du, B. J.; Shang, C. S.; Wang, J.; Wang, E. K., Construction of surface charge-controlled reduced graphene oxide-loaded Fe3O4 and Pt nanohybrid for peroxidase mimic with enhanced catalytic activity. *Analytica Chimica Acta* **2018,** *1014*, 77-84.

334.   Wang, X. R.;   Hu, J. M.;   Zhang, G. Y.; Liu, S. Y., Highly Selective Fluorogenic Multianalyte Biosensors Constructed via Enzyme-Catalyzed Coupling and Aggregation-Induced Emission. *Journal of the American Chemical Society* **2014,** *136* (28), 9890-9893.

335.   Li, D. Y.;   Ying, Y. B.;   Wu, J.;   Niessner, R.; Knopp, D., Comparison of monomeric and polymeric horseradish peroxidase as labels in competitive ELISA for small molecule detection. *Microchimica Acta* **2013,** *180* (7-8), 711-717.

336.   Fanjul-Bolado, P.;   Gonzalez-Garia, M. B.; Costa-Garcia, A., Amperometric detection in TMB/HRP-based assays. *Analytical and Bioanalytical Chemistry* **2005,** *382* (2), 297-302.

337.   Duran, N.;   Esposito, E., Potential applications of oxidative enzymes and phenoloxidase-like compounds in wastewater and soil treatment: a review. *Applied Catalysis B-Environmental* **2000,** *28* (2), 83-99.

338.   Ju, Y.;   Kim, J., Dendrimer-encapsulated Pt nanoparticles with peroxidase-mimetic activity as biocatalytic labels for sensitive colorimetric analyses. *Chemical Communications* **2015,** *51* (72), 13752-13755.

339.   Jv, Y.;   Li, B. X.; Cao, R., Positively-charged gold nanoparticles as peroxidiase mimic and their application in hydrogen peroxide and glucose detection. *Chemical Communications* **2010,** *46* (42), 8017-8019.

340.   Gao, L. Z.;   Fan, K. L.; Yan, X. Y., Iron Oxide Nanozyme: A Multifunctional Enzyme Mimetic for Biomedical Applications. *Theranostics* **2017,** *7* (13), 3207-3227.

341.   Gao, L. Z.;   Zhuang, J.;   Nie, L.;   Zhang, J. B.;   Zhang, Y.;   Gu, N.;   Wang, T. H.;   Feng, J.;   Yang, D. L.;   Perrett, S.;   Yan, X., Intrinsic peroxidase-like activity of ferromagnetic nanoparticles. *Nature Nanotechnology* **2007,** *2* (9), 577-583.

342.   Liu, B. W.;   Sun, Z. Y.;   Huang, P. J. J.; Liu, J. W., Hydrogen Peroxide Displacing DNA from Nanoceria: Mechanism and Detection of Glucose in Serum. *Journal of the American Chemical Society* **2015,** *137* (3), 1290-1295.

343.   Chen, Q.;   Liu, M.;   Zhao, J.;   Peng, X.;   Chen, X.;   Mi, N.;   Yin, B.;   Li, H.;   Zhang, Y.; Yao, S., Water-dispersible silicon dots as a peroxidase mimetic for the highly-sensitive colorimetric detection of glucose. *Chemical Communications* **2014,** *50* (51), 6771-6774.

344.   Wang, H. W.;   Jiang, W. W.;   Wang, Y. W.;   Liu, X. L.;   Yao, J. L.;   Yuan, L.;   Wu, Z. Q.;   Li, D.;   Song, B.; Chen, H., Catalase-like and Peroxidase-like Catalytic Activities of Silicon Nanowire Arrays. *Langmuir* **2013,** *29* (1), 3-7.

345.   Shi, W.;   Wang, Q.;   Long, Y.;   Cheng, Z.;   Chen, S.;   Zheng, H.; Huang, Y., Carbon nanodots as peroxidase mimetics and their applications to glucose detection. *Chemical Communications* **2011,** *47* (23), 6695-6697.

346.   Song, Y. J.;   Qu, K. G.;   Zhao, C.;   Ren, J. S.; Qu, X. G., Graphene Oxide: Intrinsic Peroxidase Catalytic Activity and Its Application to Glucose Detection. *Advanced Materials* **2010,** *22* (19), 2206-2210.

347.   Zhu, W. F.; Zhang, J.; Jiang, Z. C.; Wang, W. W.; Liu, X. H., High-quality carbon dots: synthesis, peroxidase-like activity and their application in the detection of H2O2, Ag+ and Fe3+. *Rsc Advances* **2014,** *4* (33), 17387-17392.

348.   Wang, B.; Liu, F.; Wu, Y. Y.; Chen, Y. F.; Weng, B.; Li, C. M., Synthesis of catalytically active multielement-doped carbon dots and application for colorimetric detection of glucose. *Sensors and Actuators B-Chemical* **2018,** *255*, 2601-2607.

349.   Dong, Y. M.; Zhang, J. J.; Jiang, P. P.; Wang, G. L.; Wu, X. M.; Zhao, H.; Zhang, C., Superior peroxidase mimetic activity of carbon dots-Pt nanocomposites relies on synergistic effects. *New Journal of Chemistry* **2015,** *39* (5), 4141-4146.

350.   Guo, Y. L.; Liu, X. Y.; Yang, C. D.; Wang, X. D.; Wang, D.; Iqbal, A.; Liu, W. S.; Qin, W. W., Synthesis and Peroxidase-Like Activity of Cobalt@Carbon-Dots Hybrid Material. *Chemcatchem* **2015,** *7* (16), 2467-2474.

351.   Zheng, C.; Ke, W. J.; Yin, T. X.; An, X. Q., Intrinsic peroxidase-like activity and the catalytic mechanism of gold@carbon dots nanocomposites. *Rsc Advances* **2016,** *6* (42), 35280-35286.

352.   Choudhury, S. D.; Chethodil, J. M.; Gharat, P. M.; Praseetha, P. K.; Pal, H., pH-Elicited Luminescence Functionalities of Carbon Dots: Mechanistic Insights. *Journal of Physical Chemistry Letters* **2017,** *8* (7), 1389-1395.

353.   Simpson, A.; Pandey, R. R.; Chusuei, C. C.; Ghosh, K.; Patel, R.; Wanekaya, A. K., Fabrication characterization and potential applications of carbon nanoparticles in the detection of heavy metal ions in aqueous media. *Carbon* **2018,** *127*, 122-130.

354.   Chhabra, V. A.; Kaur, R.; Kumar, N.; Deep, A.; Rajesh, C.; Kim, K. H., Synthesis and spectroscopic studies of functionalized graphene quantum dots with diverse fluorescence characteristics. *Rsc Advances* **2018,** *8* (21), 11446-11454.

355.   Hu, S. L.; Wang, Y. B.; Zhang, W. Y.; Chang, Q.; Yang, J. L., Multicolour Emission States from Charge Transfer between Carbon Dots and Surface Molecules. *Materials* **2017,** *10* (2).

356.   Anjana, R. R.; Devi, J. S. A.; Jayasree, M.; Aparna, R. S.; Aswathy, B.; Praveen, G. L.; Lekha, G. M.; Sony, G., S,N-doped carbon dots as a fluorescent probe for bilirubin. *Microchimica Acta* **2018,** *185* (1).

357.   Yang, M.; Li, B. Y.; Zhong, K. L.; Lu, Y., Photoluminescence properties of N-doped carbon dots prepared in different solvents and applications in pH sensing. *Journal of Materials Science* **2018,** *53* (4), 2424-2433.

358.   Wang, C.; Hu, T. T.; Wen, Z. Q.; Zhou, J. D.; Wang, X. J.; Wu, Q.; Wang, C. X., Concentration-dependent color tunability of nitrogen-doped carbon dots and their application for iron(III) detection and multicolor bioimaging. *Journal of Colloid and Interface Science* **2018,** *521*, 33-41.

359.   Travlou, N. A.; Secor, J.; Bandosz, T. J., Highly luminescent S-doped carbon dots for the selective detection of ammonia. *Carbon* **2017,** *114*, 544-556.

360.   Baldovi, H. G.; Valencia, S.; Alvaro, M.; Asiri, A. M.; Garcia, H., Highly fluorescent C-dots obtained by pyrolysis of quaternary ammonium ions trapped in all-silica ITQ-29 zeolite. *Nanoscale* **2015,** *7* (5), 1744-1752.

361.   Tang, C. B.; Qi, K.; Wooley, K. L.; Matyjaszewski, K.; Kowalewski, T., Well-defined carbon nanoparticles prepared from water-soluble shell cross-linked micelles that contain polyacrylonitrile cores. *Angewandte Chemie-International Edition* **2004,** *43* (21), 2783-2787.

362.   Johansson, E. M.; Ballem, M. A.; Cordoba, J. M.; Oden, M., Rapid Synthesis of SBA-15 Rods with Variable Lengths, Widths, and Tunable Large Pores. *Langmuir* **2011,** *27* (8), 4994-4999.

363.   Uson, L.; Hueso, J. L.; Sebastian, V.; Arenal, R.; Florea, I.; Irusta, S.; Arruebo, M.; Santamaria, J., In-situ preparation of ultra-small Pt nanoparticles within rod-shaped mesoporous silica particles: 3-D tomography and catalytic oxidation of n-hexane. *Catalysis Communications* **2017,** *100*, 93-97.

364.   He, Q. J.; Shi, J. L.; Cui, X. Z.; Wei, C. Y.; Zhang, L. X.; Wu, W.; Bu, W. B.; Chen, H. R.; Wu, H. X., Synthesis of oxygen-deficient luminescent mesoporous silica nanoparticles for synchronous drug delivery and imaging. *Chemical Communications* **2011,** *47* (28), 7947-7949.

365.   Ishikawa, Y.; Vasin, A. V.; Salonen, J.; Muto, S.; Lysenko, V. S.; Nazarov, A. N.; Shibata, N.; Lehto, V. P., Color control of white photoluminescence from carbon-incorporated silicon oxide. *Journal of Applied Physics* **2008,** *104* (8).

366.   Carbonaro, C. M.; Corpino, R.; Ricci, P. C.; Salis, M.; Anedda, A., Changing the environment of mesoporous silica to investigate the origin of UV and visible photoluminescence of surface centers. *Journal of Materials Science* **2013,** *48* (12), 4452-4458.

367.   Wang, J.; Gao, M.; Ho, G. W., Bidentate-complex-derived TiO2/carbon dot photocatalysts: in situ synthesis, versatile heterostructures, and enhanced H-2 evolution. *Journal of Materials Chemistry A* **2014,** *2* (16), 5703-5709.

368.   Brouwer, A. M., Standards for photoluminescence quantum yield measurements in solution (IUPAC Technical Report). *Pure and Applied Chemistry* **2011,** *83* (12), 2213-2228.

369.   Chen, X. J.; Dai, Y. Z.; Guo, J.; Liu, T. H.; Wang, X. Y., Novel Magnetically Separable Reduced Graphene Oxide (RGO)/ZnFe2O4/Ag3PO4 Nanocomposites for Enhanced Photocatalytic Performance toward 2,4-Dichlorophenol under Visible Light. *Industrial & Engineering Chemistry Research* **2016,** *55* (3), 568-578.

370.   Pinto, I. S. X.; Pacheco, P.; Coelho, J. V.; Lorencon, E.; Ardisson, J. D.; Fabris, J. D.; de Souza, P. P.; Krambrock, K. W. H.; Oliveira, L. C. A.; Pereira, M. C., Nanostructured delta-FeOOH: An efficient Fenton-like catalyst for the oxidation of organics in water. *Applied Catalysis B-Environmental* **2012,** *119*, 175-182.

371. Fu, J.; Shao, Y.; Wang, L.; Zhu, Y., Lysosome-controlled efficient ROS overproduction against cancer cells with a high pH-responsive catalytic nanosystem. *Nanoscale* **2015,** *7* (16), 7275-7283.

372. Krainer, F. W.; Glieder, A., An updated view on horseradish peroxidases: recombinant production and biotechnological applications. *Applied Microbiology and Biotechnology* **2015,** *99* (4), 1611-1625.

373. Algarra, M.; Campos, B. B.; Radotic, K.; Mutavdzic, D.; Bandosz, T.; Jimenez-Jimenez, J.; Rodriguez-Castellon, E.; da Silva, J., Luminescent carbon nanoparticles: effects of chemical functionalization, and evaluation of Ag+ sensing properties. *Journal of Materials Chemistry A* **2014,** *2* (22), 8342-8351.

374. Kalyanaraman, B.; Hardy, M.; Podsiadly, R.; Cheng, G.; Zielonka, J., Recent developments in detection of superoxide radical anion and hydrogen peroxide: Opportunities, challenges, and implications in redox signaling. *Archives of Biochemistry and Biophysics* **2017,** *617*, 38-47.

VII. ANNEXES: Regulations required to submit a PhD thesis by compendium of publications

According to the specific regulations for the presentation of the PhD Thesis by a compendium of publications (Articles 19, 20 and 21 of the Regulation, of the Agreement of 20/12/2013 of the Governing Council of the University of Zaragoza), the following sections are presented below:

- Subject category and impact factor of the articles reported in this dissertation.
- PhD student´s contributions.
- Resignation to claim authority rights by contributing authors not holding a PhD. degree included in any of the publications of the present dissertation.
- E-mail of submission of articles pending publication (Article 7 of this PhD Thesis).

………………………………………………….

Según la normativa específica para la presentación de Tesis Doctoral como compendio de publicaciones (Artículos 19, 20 y 21 del Reglamento, del Acuerdo de 20/12/2013 del Consejo de Gobierno de la Universidad de Zaragoza), se presentan a continuación los siguientes apartados:

- Áreas temáticas y factor de impacto de las revistas en donde se ha publicado el trabajo realizado.
- Aportaciones del doctorando.
- Renuncia de los coautores no doctores participantes en los trabajos incluidos en esta Tesis Doctoral presentada por la modalidad de compendio de publicaciones.
- E-mail de submisión de los artículos pendientes de publiación (Artículo 7 de esta Tesis Doctoral).

Subject category and impact factor of the articles reported in this dissertation

The characteristics of the journals in which the articles that make up this dissertation have been published are shown. Specifying the journal, the subject category to which they belong, their impact factor (Journal of Citation Reports, Web of Knowledge) and the number of citations.

Article 1. Chemistry A European Journal, 2017, 23: 3067-3073. Hot Paper. IF: 5.317 (29/166 Chemistry Multidisciplinary). Citations: 4.

Article 2. Diamond and Related Materials, 2016, 65: 176-182. IF: 2.561 (91/275 Materials Science, Multidisciplinary). Citations: 10.

Article 3. In preparation for Advanced Functional Materials. IF: 12.124 (7/87 Nanoscience, Nanotechnology)

Article 4. Chemical Communications, 2015, 51: 16625-16628. IF: 6.567 (21/163 Chemistry, Multidisciplinary). Citations: 13.

Article 5. Applied Catalysis B: Environmental, 2017, 218: 68-79. IF: 9.446 (1/49 Engineering Environmental). Citations: 3.

Article 6. Carbon, 2017, 117: 437-446. IF: 6.337 (32/275 Materials Science, Multidisciplinary). Citations: 5.

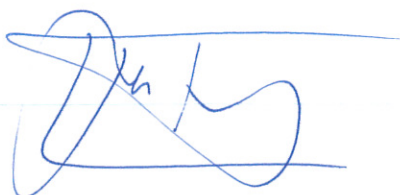***Article 7.*** Under review in Chemical Science. IF: 8.668 (17/166 Chemistry, Multidisciplinary).

Áreas temáticas y factor de impacto de las revistas en donde se ha publicado el trabajo realizado

Se muestran las características de las revistas en las que han sido publicados los manuscritos que conforman esta Tesis Doctoral. Se especifican los nombres de las revistas así como el área temática a las que pertenecen, su índice de impacto (Journal of Citation Reports, Web of Knowledge) y el número de citaciones.

Article 1. Chemistry A European Journal, 2017, 23: 3067-3073. Hot Paper. IF: 5.317 (29/166 Chemistry Multidisciplinary). Citations: 4.

Article 2. Diamond and Related Materials, 2016, 65: 176-182. IF: 2.561 (91/275 Materials Science, Multidisciplinary). Citations: 10.

Article 3. En preparación para Advanced Functional Materials. IF: 12.124 (7/87 Nanoscience, Nanotechnology)

Article 4. Chemical Communications, 2015, 51: 16625-16628. IF: 6.567 (21/163 Chemistry, Multidisciplinary). Citations: 13.

Article 5. Applied Catalysis B: Environmental, 2017, 218: 68-79. IF: 9.446 (1/49 Engineering Environmental). Citations: 3.

Article 6. Carbon, 2017, 117: 437-446. IF: 6.337 (32/275 Materials Science, Multidisciplinary). Citations: 5.

Article 7. En revisión en Chemical Science. IF: 8.668 (17/166 Chemistry, Multidisciplinary).

PhD student's contributions

Professor Jesus Santamaria Ramiro and **Doctor Jose Luis Hueso Martos**, supervisors of the present dissertation,

REPORT

That **Mrs. María del Carmen Ortega Liebana** has actively participated in all the results reported in this Doctoral Thesis and is claimed as principal contributor. The PhD candidate has been the main researcher responsible for the advances and development of the following research aspects: synthesis, characterization of the nanoparticles, development of the catalytic applications, as well as the interpretation of the results achieved during her research period at the University of Zaragoza as well as during her Postgraduate Internship at the Hong Kong University of Science and Technology (HKUST) supervised by Prof. King Lun Yeung. The main contributions from other collaborators have been: the cytotoxicity assays and the evaluation of the internalization of the nanoparticles by confocal microscopy have been carried out by Dr. M.M. Encabo-Berzosa, the synthesis of magnetic nanoparticles by microfluidics have been carried out by Dr. A. Larrea and Dr. V. Sebastian, the measurements of the Time-resolved Photoluminescence decay of the nanoparticles have been carried out by Dr. M.J. Ruedas-Rama, the studies of Electron Energy Loss Spectrocopy (ELLS) have been performed in collaboration with Dr. R. Arenal and Dr. R. Fernandez-Pacheco belonging to the Advanced Microscopy Laboratory (LMA) of the Institute of Nanoscience of Aragon and the evaluation of nanoparticles in Photodynamic Therapy have been carried out in collaboration with the Department of Pharmacology and Physiology (Faculty of Medicine) of the University of Zaragoza, supervised by Prof. J.O. Alda.

And for the record, we sign this document in Zaragoza on 23rd May 2018,

Prof. Jesús Santamaría Ramiro   Dr. José Luis Hueso Martos
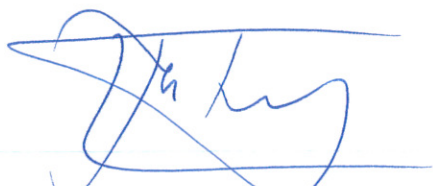
Aportaciones del doctorando

EL **Prof. Jesús Santamaría Ramiro** y el **Dr. José Luis Hueso Martos**, directores de la presente Tesis Doctoral,

CERTIFICAN

Que **Dña. María del Carmen Ortega Liébana** ha participado activamente en los trabajos incluidos en esta memoria como ejecutora y autora principal. Tanto la realización de las síntesis, la caracterización de las nanopartículas, la puesta a punto de las aplicaciones catalíticas, así como la interpretación de los resultados han estado a su cargo tanto en los trabajos realizados en el Instituto de Nanociencia de Aragón como durante su estancia realizada en Hong Kong University of Science and Technology (HKUST) supervisada por el Prof. King Lun Yeung. Las principales excepciones han sido: los ensayos de citotoxicidad y la evaluación de la internalización de las nanopartículas mediante microscopia confocal han sido realizados por la Dra. M.M. Encabo-Berzosa, la síntesis de nanopartículas magnéticas mediante microfluidica han sido realizadas por la Dra. A. Larrea y el Dr. Víctor Sebastián, las medidas del tiempo de vida media de fluorescencia de las nanopartículas han sido realizadas por la Dra. M.J. Ruedas-Rama, los análisis de Espectroscopía Electrónica de pérdidas de energías (EELS) han sido realizados en colaboración con el Dr. R. Arenal y Dr. R. Fernández-Pacheco pertenecientes al Laboratorio de Microscopías Avanzadas (LMA) del Instituto de Nanociencia de Aragón y los estudios de evaluación de las nanopartículas en terapia fotodinámica han sido realizados en colaboración con el Departamento de Farmacología y Fisiología (Facultad de Medicina) de la Universidad de Zaragoza, dirigido por el Prof. J.O. Alda.

Y para que conste, adjuntamos el presente certificado

En Zaragoza a 23 de mayo de 2018

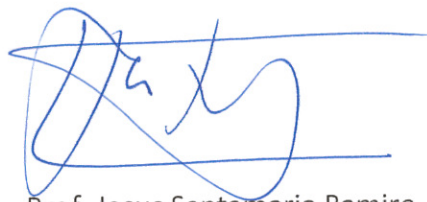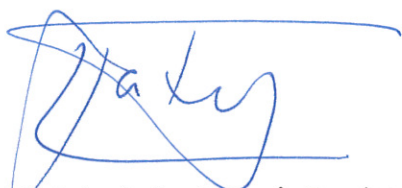Prof. Jesús Santamaría Ramiro

Dr. José Luis Hueso Martos

Resignation to claim authority rights by contributing authors not holding a PhD degree included in any of the publications of the present dissertation.

Professor **Jesus Santamaria Ramiro** and **Doctor Jose Luis Hueso Martos**, supervisors of the present dissertation,

REPORT

That all the authors contributing to the compendium of articles presented in this dissertation already hold a PhD degree and no specific resignation letters are required.

And for the record, we sign this document in Zaragoza on 23rd May 2018,

Prof. Jesus Santamaria Ramiro

Dr. Jose Luis Hueso Martos

Renuncia de los coautores no doctores participantes en los trabajos incluidos en esta Tesis Doctoral presentada por la modalidad de compendio de publicaciones.

El **Prof. Jesús Santamaría Ramiro** y el **Dr. José Luis Hueso Martos**, directores de la presente Tesis Doctoral,

CERTIFICAN

Que todos los coautores de los trabajos incluidos en la presente Tesis Doctoral para su presentación como compendio de publicaciones poseen el título de Doctor y no es necesaria justificar ningún tipo de renuncia de coautores no doctores.

Y para que conste, firmamos el presente certificado,

En Zaragoza, a 23 de mayo de 2018

Prof. Jesús Santamaría Ramiro

Dr. José Luis Hueso Martos

Regulations required to submit a PhD thesis by compendium of publications

- E-mail of submission of articles pending publication (Article 7 of this PhD Thesis).

………………………………………………………….

- E-mail de submisión de los artículos pendientes de publiación (Artículo 7 de esta Tesis Doctoral).

Asunto	**Acknowledgement of your Submission to Chemical Science – SC-EDG-03-2018-001418**
De	Chemical Science <onbehalfof@manuscriptcentral.com>
Destinatario	<jlhueso@unizar.es>
Cc	<mcol88@unizar.es>, <jlhueso@unizar.es>, <pacheco@unizar.es>, <sirusta@unizar.es>, <Jesus.Santamaria@unizar.es>
Responder a	<chemicalscience@rsc.org>
Fecha	2018-03-27 16:43

27-Mar-2018

Dear Dr Hueso:

TITLE: Luminescent mesoporous nanorods as photocatalytic enzyme-like peroxidase surrogates

Thank you for your submission to Chemical Science, published by the Royal Society of Chemistry. This is an automatic acknowledgement that you have uploaded your files to our online submission system. Your manuscript ID is: SC-EDG-03-2018-001418

Your manuscript will be passed to an editor for initial assessment as soon as possible. If there are any problems with your submission we will contact you.

Please indicate the above manuscript ID when you contact us about this submission. You can check the status of your manuscript by logging into your Author Centre (https://mc.manuscriptcentral.com/chemsci).

Why have you chosen to submit to Chemical Science today? Please would you take one minute to answer this question at https://www.surveymonkey.co.uk/r/Q7KMXTP

Do you have an ORCID iD? ORCID (Open Researcher and Contributor iD) is a unique researcher identifier that allows you to link your research output and other professional activities in a single record. We therefore encourage each researcher to sign up for their own ORCID account. Please edit your user account to link your ORCID iD or create a new one, ensuring that you have not linked your account to another researcher's ORCID iD. Please note that we are unable to do this on your behalf. If your article is accepted, you may choose to have your ORCID record updated automatically with details of the publication.

We already have the following information for authors of this manuscript: Ortega-Liebana, M. Carmen – No ORCID iD Available, Hueso, José – http://orcid.org/0000-0002-4546-4111, Fernández-Pacheco, Rodrigo – No ORCID iD Available, Irusta, Silvia – No ORCID iD Available, Santamaria, Jesus – No ORCID iD Available
If this is not how you want your name to appear on an Accepted Manuscript, please amend your ScholarOne account.

The Royal Society of Chemistry is a member of CrossCheck. Your submission may be compared against the CrossCheck database using the iThenticate plagiarism detection software. For further information, please see here: http://www.rsc.org/journals-books-databases/journal-authors-reviewers/processes-policies/#crosscheck

Chemical Science has a policy of sharing reviewer reports. Please note that the Editor's decision and copies of the reports will be shared with all reviewers who provide a recommendation on your manuscript.

Please contact us if we can be of any assistance.

Yours sincerely,
Chemical Science Editorial Office
chemicalscience@rsc.org

****